Towards Adaptive Radiation Therapy—a framework for inclusion of organ deformation in adaptive dose delivery

A Dissertation
SUBMITTED TO THE FACULTY OF
UNIVERSITY OF MINNESOTA
BY

Nagarajan Varadhan M.S, M.Phil

IN PARTIAL FULFILLMENT OF THE REQUIREMENTS
FOR THE DEGREE OF
DOCTOR OF PHILOSOPHY

Susanta Hui PhD

December 2013

Dedication

This dissertation is dedicated to my wonderful supportive family and children here in

Minnesota and my parents in India.

Table of Contents

Chapter 1: Introduction and clinical rationale for adaptive radiation therapy

Chapter 2: Implementation and framework of adaptive radiation therapy for prostate cancer.

Chapter 5: Dose warping and experimental validation of accuracy of dose warping using deformable phantoms.

List of Tables

List of Figures

Cyan line: bladder. Brown line: Rectum. Red line: Prostate.

deformation algorithm.

of the five beam geometries studied.

Acronyms

ART: Adaptive Radiation Therapy

CBCT Cone-beam CT: Computed tomography in which the source describes a helical trajectory relative to the object while a two dimensional array of detectors measures the transmitted radiation on part of a cone of x-rays emanating from the source. Also referred as kvCBCT

CC Cross-correlation

CT Computed tomography: 3D medical imaging based on x-rays.

CT images are expressed in Hounsfield units (HU).

CTV Clinical target volume: volume surrounding the GTV with a margin of tissue at high risk for clinical extension of the tumor.

CUDA Computer Unified Device Architecture used in GPU computing

DLL Dynamically linked libraries

DSC Dice Similarity Coefficient

DVH Dose volume histogram: cumulative dose distribution function on a volume. The dose is expressed in grays (Gy) or cGy

FDG Fludeoxyglucose (18F): glucose analog (using the positron emitting radioactive isotope fluorine-18) used as tracer for PET imaging. Injection doses are measured in megabecquerels (MBq).

FEM Finite element method: numerical technique for finding approximate solutions of partial differential and integral equations on a mesh.

GTV Gross tumor volume: volume of the tumor as it is visible on the images.

GUI Graphical user interface.

GPU Graphics processing unit

HD Hausdorff distance, measures the maximum of the closest distance between two volumes where the closest distance is computed for each vertex of the two volumes. Sometimes 95% HD is reported where outliers are rejected

IGRT: Image Guided Radiation Therapy

IMRT: Intensity Modulated Radiation Therapy

ITK Insight ToolKit: Segmentation and Registration toolkit (by Kitware, Inc.)

ITV Internal target volume, takes into account organ motion

kvCT: kilo voltage CT commonly referred as the treatment planning CT scan

kvCBCT: kilo voltage cone beam CT obtained using the x-ray source mounted on the linear accelerator. (see CBCT definition)

Linac: Medical Linear Accelerator

MI Mutual information:

MRI Magnetic resonance imaging:

MVCT Megavoltage CT obtained using Tomotherapy Hi-ART system

NIST National Institute of Standards and Technology

OAR Organs at risk: organs that must be specially spared during radiotherapy.

PET Positron emission tomography: 3D medical imaging based on the detection of pairs of gamma rays emitted indirectly by a positron-emitting radionuclide (tracer).

PTV Planning target volume: volume surrounding the tumor that is planned to receive the prescribed therapeutic dose based on organ motion and set up uncertainty.

SBRT: Stereotactic Body Radiation Therapy

Slicer RT-Radiation therapy research tool kit for 3D slicer (www.slicer.org)

SSD Sum of squared differences:

SUV Standardized uptake value: ratio of the tissue radioactivity concentration and injected dose (divided by body weight). It is used for quantitative analysis of PET images.

TPS Treatment planning system.

TPS Thin Plate Splines

VTK Visualization Tool Kit (Kitware Inc)

INTRODUCTION:

Cancer is the second leading cause of death in the USA with about 575,000 deaths each year and a disease for which death rates are increasing. Between 2000 and 2050, the elderly population in the USA is projected to increase by 135%[1]. Moreover, the population aged 85 and over, which is the group most likely to need health and long-term care services, including cancer care services is projected to increase by 350%. Approximately 60% of cancer patients are treated with external beam radiotherapy at some point during management of their disease. The goal of radiation therapy (RT) is to maximize the dose to the target while limiting the dose to nearby healthy organs or organ at risk, (OAR), in order to improve tumor control and normal tissue toxicity. Radiation therapy is primarily used to treat cancer by locally targeting radiation to the gross tumor volume (GTV) with added clinical target volume that accounts for microscopic extensions of the disease (CTV) and an additional planning target volume (PTV) that accounts for setup and localization errors . The concept of GTV, CTV and PTV to report dose prescription is discussed in the review paper [2]. Radiation beams are produced by medical linear accelerators which have now imaging capabilities including volumetric imaging using cone beam CT integrated into the treatment delivery process. The linear accelerators are mounted on a gantry with a rotating couch, gantry and collimator to allow for many beam directions to be focused on the target volume. Avoidance of normal tissues is accomplished by directing multiple beams at the target using a beams eye view (BEV) of the target, thus delivering a high dose where the beams intersect at the target, and a relatively lower dose outside of the intersection and also by

1

modulating the intensity of radiation using Multi Leaf Collimator (MLC) so that the maximum dose is delivered to target. Biological sparing of normal tissue is accomplished by fractionating the radiation therapy over several weeks with tumor typically being irradiated 5 days in a week. The tumor tissue lacks repair mechanisms to repair DNA damage from the radiation, whereas normal tissues can repair minor DNA damage. Therefore, by fractionating the treatment, normal tissues are provided time to repair, thus biologically sparing the normal tissue.

Although conventionally fractionated radiotherapy is delivered in a four to eight week time period, radiation therapy treatment planning is carried out based on information that is currently limited to a single 3D anatomical computed tomography (CT) image data set acquired at the onset of treatment design (Fig. 1a). The patient is typically marked for repeated alignment with localization lasers in the treatment room. The treatment planning is then performed on the CT scan where beam geometries, energies, and collimation are determined either by inverse planning using intensity modulation or using conventional 3D conformal therapy techniques, and the resultant dose distribution is computed. This concept may result in significant treatment uncertainties, including geometric miss of target/tumor and resulting in excess irradiation of organs at risk (OAR). An example to highlight this is shown below in Fig 1 in the case of head and neck cancer patient.

Fig 1 a, refers to the planning CT used for treatment planning, fig 1b refers to the CT acquired on first day of treatment showing correspondence to the planning CT. Fig 1c is the CT acquired on the last day of treatment and illustrates how the patient's aquaplast mask does not fit to the external skin due to the weight loss or other changes. A plan

delivered based on planning CT to this CT geometry may result in unacceptable OAR and tumor doses.
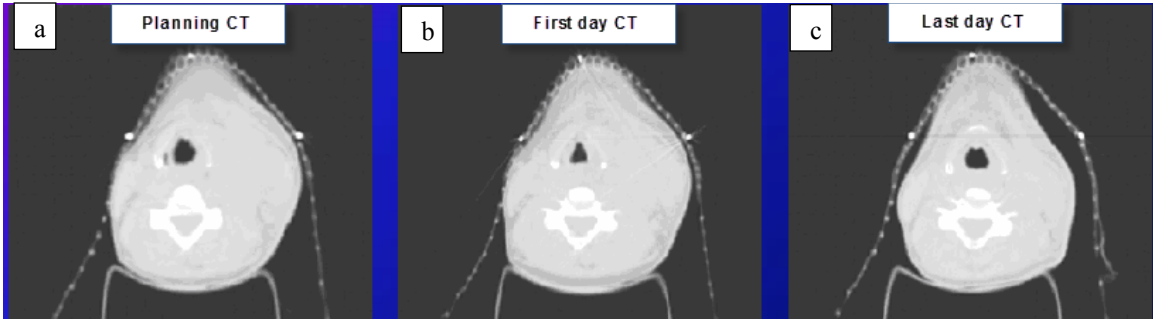
Figs 1.1 a, b, c illustrating the patient's CT anatomy during planning CT, first day of treatment and last day of treatment respectively

1.2 Imaging workflow in radiation oncology:

Imaging is included in the radiation oncology process in a variety of ways. The approach taken depends upon: the type of imaging, the availability of the on board imaging technology on the linear accelerator (kilo voltage x-ray imaging, cone beam CT, CT on rails, MVCT etc...) the clinical objective, and, and the presence of other imaging modalities for multi-modality imaging and registration. The most commonly used imaging modalities of CT, PET and MRI and its workflow process in radiation oncology is discussed in this section.

1.2.1   CT Imaging in Radiotherapy Workflow

CT images are utilized for pre-treatment imaging; treatment planning and treatment verification for radiation treatments can be outlined as in Figure 1 below. It should be noted in the current setting; ART involves the patient being rescanned for a new treatment planning CT in the flow of images from linac to CT as shown in fig 1.
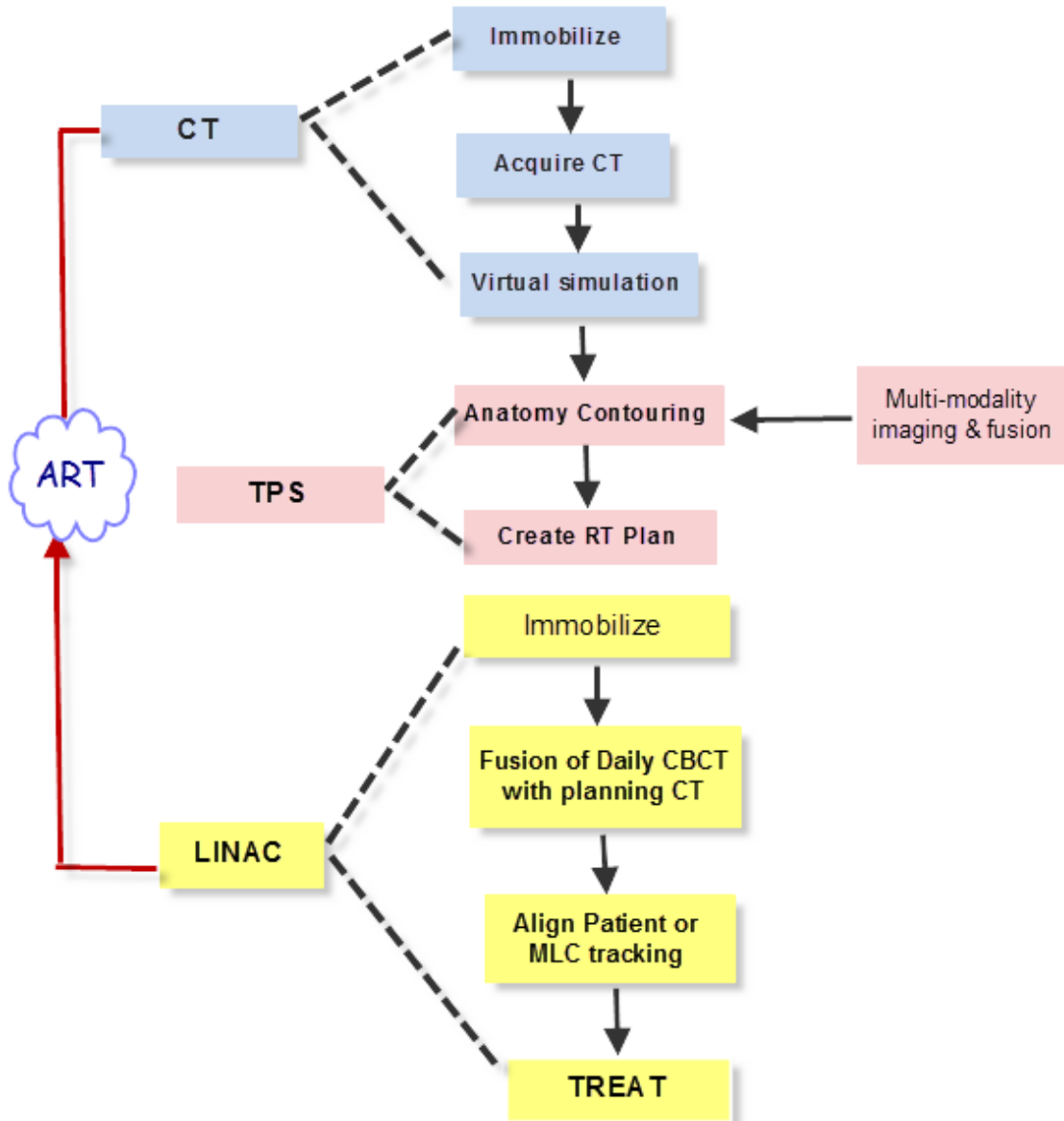
Figure 1.2. Workflow for CT-based radiotherapy. (Adapted from reference 3)

With the availability of multi-modal imaging for diagnosis and therapy response, the

imaging work flow in a modern radiation oncology department [3] can be represented as

shown in Fig 1.3 below.
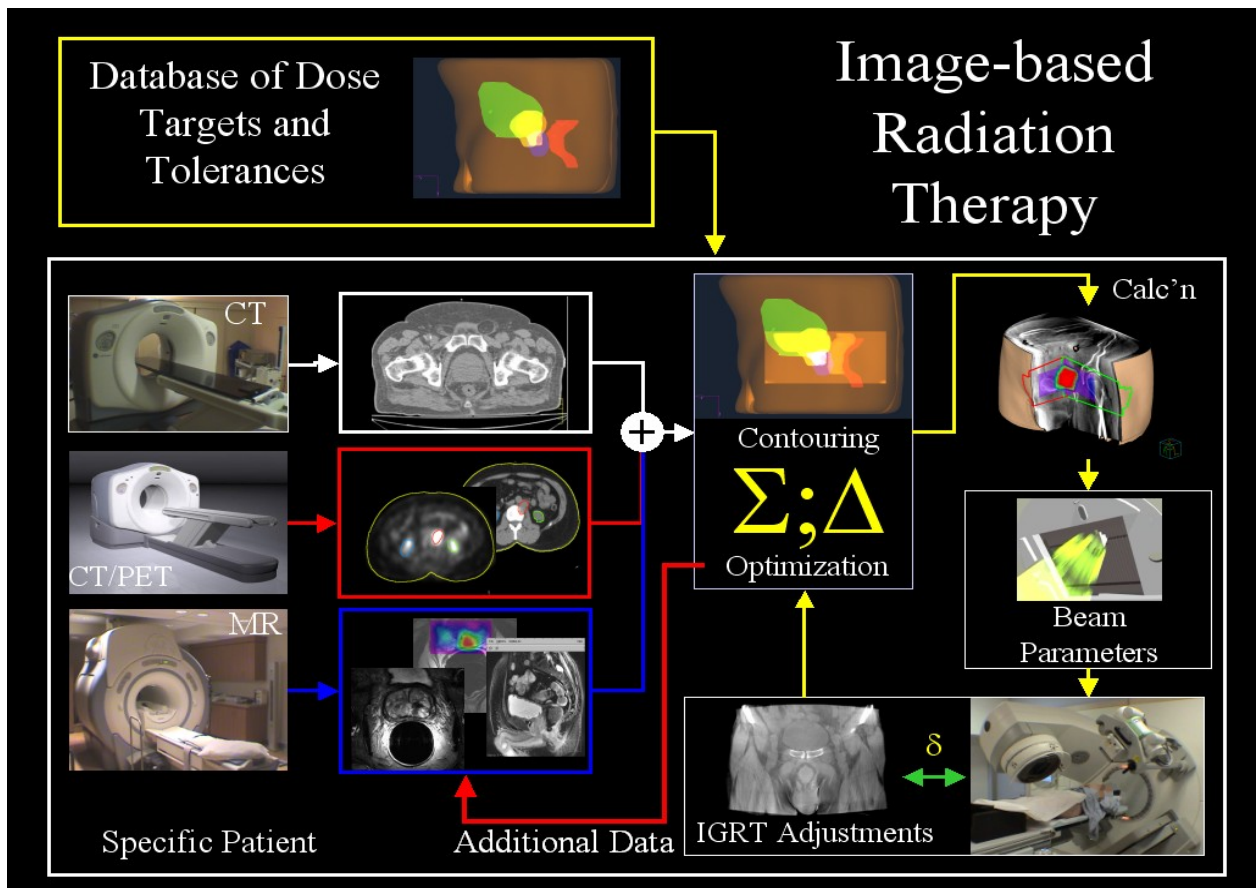
Figure 1.3: Progression of the radiation therapy workflow towards an image guided

radiation therapy process, in which images from a variety of imaging modalities are used

in the design of the therapy. These images are registered using both rigid and non-rigid

methods and used for visualization and manual or automated segmentation. Imaging in

the room is now being more broadly employed to both evaluate geometric targeting (e.g.,

cone-beam CT, MVCT, etc..) and adaptation based on delivered dose (Adaptive radiation therapy)(Adapted from reference 3)

 A treatment plan is developed based on contouring target volume quantified by patient specific imaging i.e. CT, MRI or PET. Appropriate margin expansion for CTV to PTV margins for tumor/target can be defined based on quantifying the systematic (Σ) and random (σ) errors as defined by Van herk's formulae[4]

 Δ(CTV-PTV Expansion) = 2.5 Σ + 0.7 σ

Once a treatment plan has been approved, the plan, isocenter and DRRs or CT scan itself are sent to the linear accelerator. DRRs are used for comparison with megavoltage or kilovoltage planar images for appropriate patient alignment. The CT scan is used to estimate appropriate patient alignment by registration and fusion of the CT scan with volumetric images acquired at the linear accelerator which can be kilovoltage or megavoltage, cone beam or fan beam. CT imaging is the most dominant imaging used in the entire workflow of radiation oncology process.

1.2.2   Positron Emission Tomography (PET) imaging for target Definition and therapy response in Radiation Therapy

Positron emission tomography (PET) provides functional information on tumor, and may also identify the extent and location of active disease. This technique is based on the injection of a radioactive tracer with short half-life. The half-life of radioactive F^{18} to trace glucose metabolism using the fluorodeoxyglucose, (FDG) is two hours. The tracer concentrates on the area of interest with increased metabolic activity and whose activity can be detected using gamma ray detectors. PET/CT scans can be acquired separately

and can be integrated with treatment planning using rigid and non-rigid registration techniques or may be performed as part of radiation therapy simulation to adjust target volumes. PET imaging can also be used to assess tumor response or recurrence after completion of radiation. An example of PET imaging pre and post radiation therapy is shown below in figure 1.4 as discussed in reference[5]. SUV or Standardized Uptake Value is a convenient measure for monitoring and assessing therapy response and is calculated either pixel-wise yielding a parametric image, or over a region of interest (ROI). This may be done for any image acquired at time point *t*, or for all images of a dynamic series acquired at multiple time points. The SUV is commonly defined as the ratio of the tissue radioactivity concentration *c* (e.g. in MBq/kg = kBq/g) at time point *t*, and the *injected activity* (e.g. in MBq, extrapolated to the same time *t*) divided by the *body weight* (e.g. in kg):

$$\text{SUV (t)} = \frac{c(t)}{\{injected\ activity(t)\Big/body\ weight\}}$$
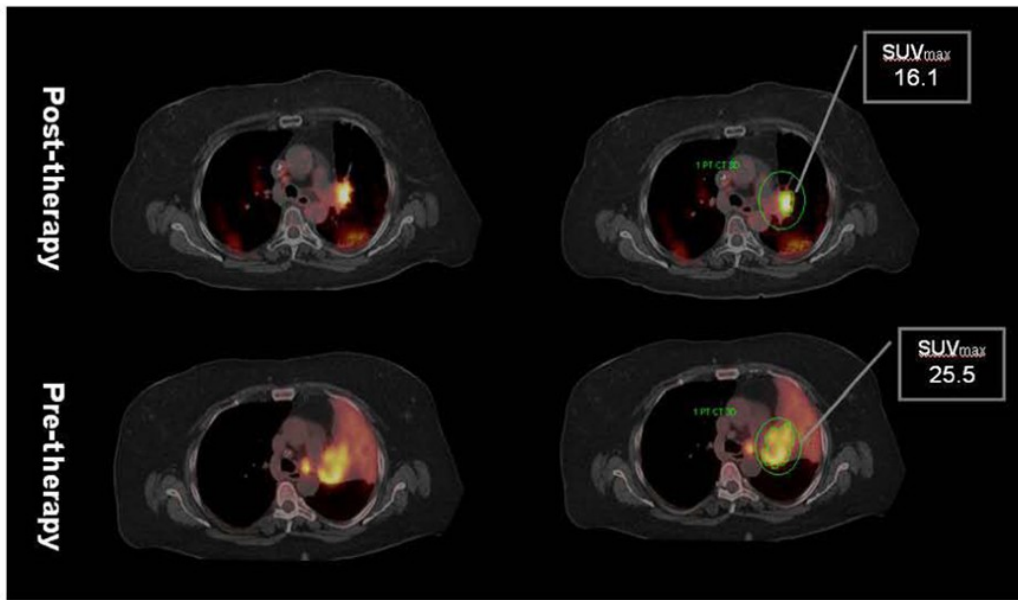
Figure 1.4: PET imaging showing tumor response before and after completion of radiation therapy (see reference 5 for details)

1.2.3   Magnetic Resonance Imaging (MRI) use in Therapy Planning and Response

MRI image data can be used in the radiation therapy treatment planning process in several ways. Currently morphological data from MR based on T1, T2 imaging and similarly weighted images, together with contrast agents can be used to define tumor and organ extent as shown in fig 1.5 for a brain tumor example.
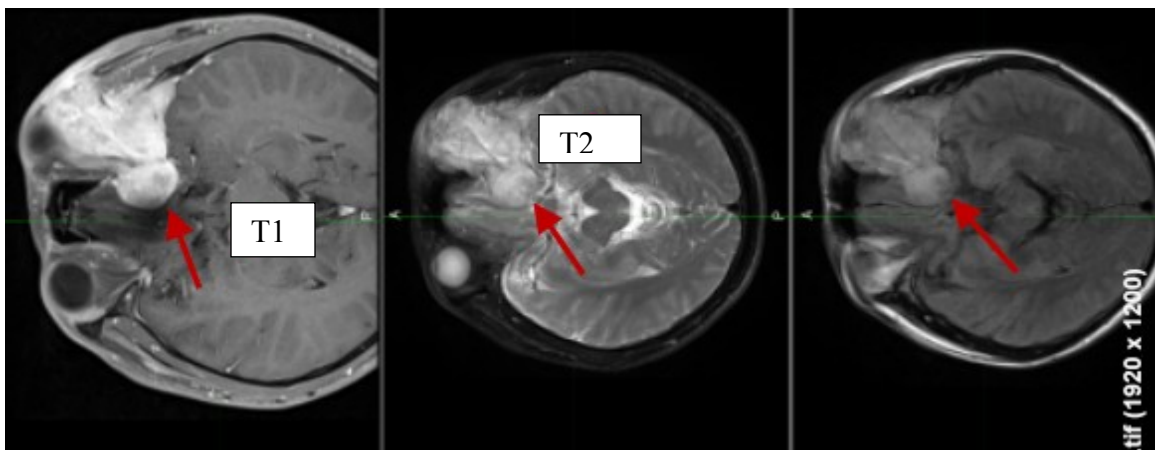
Figure 1.5. T1 and T 2 images of MRI of brain

There is growing use of functional and metabolic information to complement morphological images. These data used can either by digitally transferred to a planning system and co-registered with CT, with and without prior distortion correction. Alternately the data can be used directly for planning after distortion correction and with bulk assignment of attenuation corrections (MR simulation).

MR simulation requires appropriate set up of the patient in the treatment position, registration of surface markers, and assurance of spatial accuracy. Registration to CT also benefits from these steps. MR may also be used to assess changes in target volume during therapy and to assess response and residual disease following treatment.

1.3   Clinical rationale for Adaptive Radiation Therapy:

1.3.1 Introduction to ART

The term adaptive radiation therapy was originally coined by Di Yan [6] . Adaptive radiotherapy has been introduced as a feedback control strategy to include patient-specific treatment variation explicitly in the control of treatment planning and delivering radiation during the treatment course[7]. The goal of adaptive radiation therapy is not only to address inter and intra fraction changes but also to take advantage of treatment variation in the individualized treatment optimization. The potential of adaptive radiotherapy extends beyond the increase of radiation dose delivery accuracy. It could also improve radiotherapy efficacy after patient-specific biological changes are incorporated in the adaptive optimal control process. Most clinical applications of adaptive radiotherapy have been limited to target position correction alone (IGRT), and the extensive feedback information obtained during

the treatment course has not been fully used in treatment optimization. In the following section we present an overview of various approaches to ART and its clinical rationale.

1.3.1 On-line and Off-line Analysis for In-room Image Guidance

Once the technical development and optimization of in-room imaging tools integrated with the actual treatment process, the next important step is the development and implementation of clinical protocols for image-based guidance[8]. There is a variety of information available in the literature describing such protocols for adaptive radiation therapy for different anatomical sites and a nice summary can be found in Seminars in Radiation Oncology[9]. It is well known from daily imaging arising from Image Guided Radiation Therapy (IGRT) that dose delivery to tumor and organs at risk is affected by inter-fraction and intra-fraction motion of organs. Intra-fraction motion defined as motion when the radiation beam is delivered occurs due to variety of physiological changes in anatomy like breathing, cardiac motion, rectal peristalsis and bladder filling etc. Inter-fractional (day-to-day) geometric change occurs over the weeks of radiation therapy, due to digestive processes, change of breathing patterns, difference in patient setup, and treatment response like growth or shrinkage of the tumor or nearby organs at risk. In the past, these changes were taken into account by population-based "uncertainty" margins around the target area, which may be excessive or conservative and are broadly applied to the structures identified before the therapy begins.

Daily imaging from IGRT has provided clinicians and physicists tools to quantify patient specific anatomical changes and thereby devise strategies to incorporate these changes in

plan optimization. This approach has the promise to improve therapeutic ratio by simultaneously incorporating both dose escalation to the tumor and reduction of dose given to organs at risk. This has already resulted in dose escalation strategies using larger fractions size hypo-fractionated regimen (Prostate, Lung etc.) by increasing the chance of local control without increasing toxicity.

Adaptive radiotherapy (ART) is currently mostly based on an off-line approach where the anatomical and biological changes are monitored over the course of treatment, and the treatment is modified when significant changes are identified. However with increased automation, on-line ART (while the patient is still on treatment table) can be achieved in principle. On-line ART has been implemented by select research groups and its potential benefit has been demonstrated for bladder, prostate and head & neck disease sites.[10-12] IGRT is typically an on-line concept where the patient or treatment plan is shifted or modified for each treatment.

Off-line analysis has also been used to quantify and separate random and systematic uncertainties for individual patients. This information can be used to design decision rules to indicate when to correct a set-up deviation for a particular type of treatment, see reference [13] for details using electronic portal imaging devices(EPID). Off-line set-up verification protocols using EPID can be based on decision rules using a shrinking action level (SAL) as discussed in reference [14]. Other approaches are based on average deviations observed during the first number of fractions and assuming these deviations are valid for the whole treatment, *e.g.* the no-action level (NAL) protocol [15].

However the most significant impact for ART necessity has resulted from the volumetric CT (CBCT, MVCT, etc.) acquired at the time of daily treatment. This has resulted in variety of adaptive therapy options that will be discussed next.

By using image information obtained during the first week of treatment, the PTV margin can be adapted for an individual patient. A new plan can then be designed using the average GTV and OAR positions. In the following weeks, new scans are used to monitor the adequacy of the ART treatment plan. It should be noted that the clinically applied GTV-to-PTV margins should compensate for all geometrical uncertainties in the radiotherapy chain including those induced by target definition, which are not improved by in-room image guidance. However 3D image guidance can point to the need for plan adaptation based on soft tissue imaging. An example for a head and neck patient is given below based on CT scans acquired 3 weeks apart. As seen in Figs 1.6 a, and b, there is a significant decrease in tumor volume on the CT scan taken 3 weeks after start of therapy. If the original plan had been delivered to the new patient geometry this would have resulted in a severe overdose of parotid as seen in figure 1.6 d. The parotid in this example would have received 70Gy instead of the 45Gy originally planned, resulting in unacceptable toxicity for the patient. Thus a robust strategy to implement ART is required to improve therapeutic ratio.
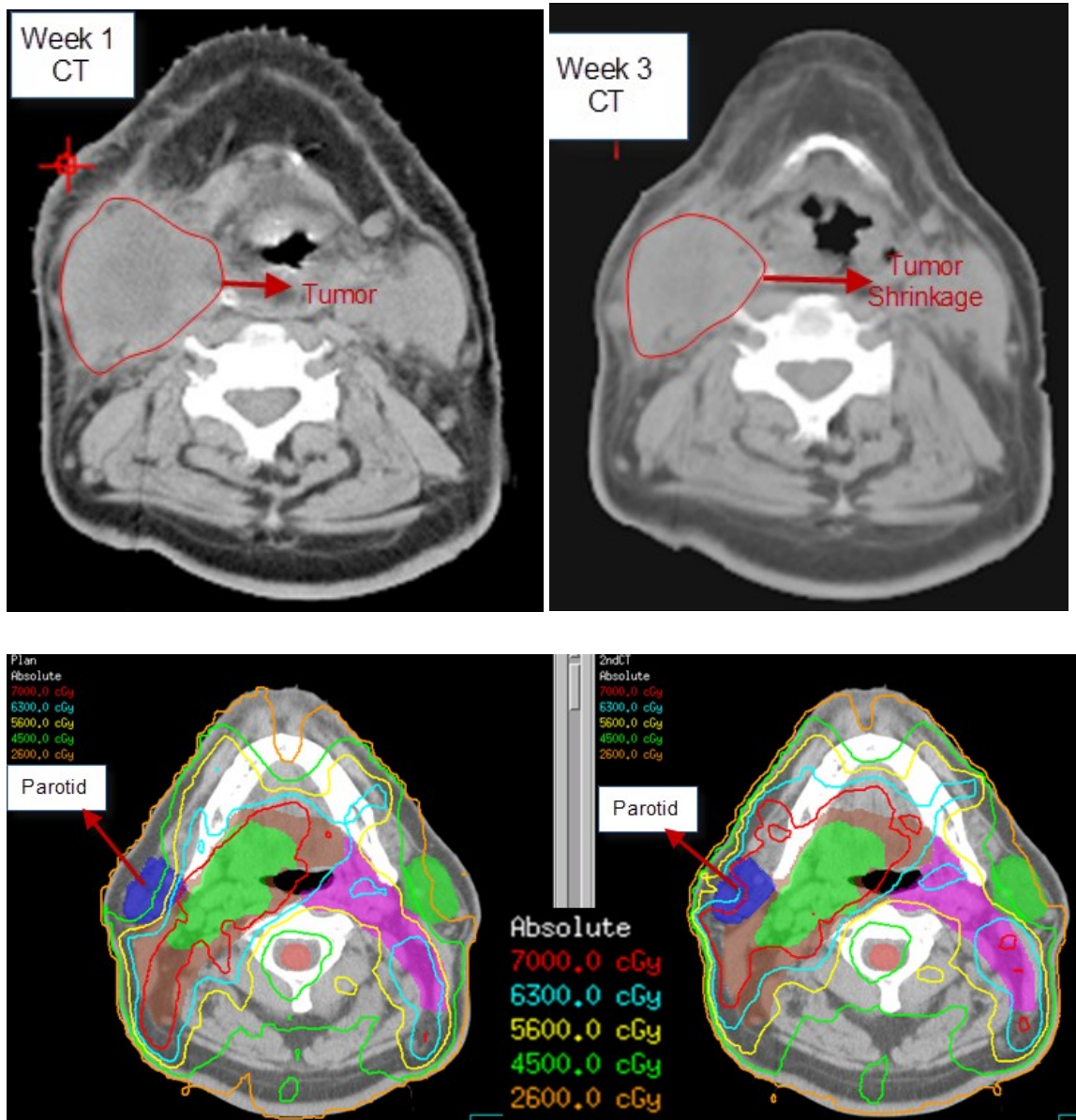
Figure 1.6 a, Tumor volume at the treatment planning CT scan, b, Tumor volume, 3 weeks after start of treatment showing shrinkage of tumor, c) Isodose distribution on original CT , d) isodose distribution on new anatomy if original plan was delivered without adaptation

1.4   Motivation, goals and scientific contribution of this dissertation

This dissertation aims to develop the necessary scientific knowledge to include organ deformation in adaptive dose delivery. Our goal in this dissertation is to develop methods and tools based on scientific insight gained to account organ deformation in the adaptive dose feedback loop that would ultimately help physicians and physicists in the radiation oncology community to better serve their clinical needs. In that context, several scientific concepts have been proposed and validated and will be highlighted in this section.

 It is widely accepted that ART accounting organ deformation is a clinical requisite and would be greatly beneficial to a certain group of patients receiving radiation therapy for different anatomical sites[9]. In this dissertation we first demonstrate the need for ART in the treatment of localized prostate cancer and propose plan adaptation without deformable image registration tools[16]. However implementation of ART is a daunting task as quantifying and accounting anatomical changes manually (without deformable image registration) is extremely time consuming and not practical in a clinical environment[16]. Deformable image registration (DIR) has the potential to map anatomical changes in imaging data between two study sets which exhibit organ deformation. Clearly the challenge in DIR is to account these anatomical changes accurately to ultimately implement cumulative dose tracking on a reference study set.

DIR based voxel mapping being inherently degenerate, (as in there is no unique solution) is a particularly challenging yet extremely important problem in validation

for radiation oncology applications. DIR accuracy in the context of radiation therapy can be separated into two parts a) validation of image registration from various algorithms, b) validation of deformable dose registration (dose warping). Scientific methods for both features are proposed and limitations of existing methods are examined in this dissertation.

This dissertation aims to develop tools to independently perform deformable image registration (DIR) using open source platform[17] (3D Slicer) and propose a frame work to validate the accuracy of DIR with an emphasis on radiation oncology applications[18]. A novel method of verifying DIR accuracy using virtually simulated deformation to mimic clinically observed organ deformation was proposed and validated. Independent validation tools for verifying accuracy of image registration are implemented using open source modules[18]. The second step in implementing ART involves calculating the doses to a deforming anatomy. Again, re-planning and re-optimization of treatment plans as done for treatment planning CT cannot be applied to daily imaging data because of the time and resource constraints. Dose warping defined as applying the deformation vector field (DVF) arising from DIR on the original dose distribution has the potential to account for organ deformation and accumulate doses. However its application and validity in a clinical environment remains controversial[19] .

The vast majority of research work that has been done on dose warping accuracy studies has only examined arbitrary deformations of varying magnitude for dose delivery verification. This dissertation proposes to examine the fundamental science of

deformation linked to its causative physical force. A quantitative relationship between force and deformation may give insight into the deformation characteristics of various organs if the biomechanical properties of tissues like Young's modulus and Poisson ratio are known. This can be potentially used to create simulated deformations of various organs analogous to what has been done for surgical simulations. A database of simulated deformations for various organs in response to applied force can give clinicians insight into how an organ may deform over an entire course of radiation therapy and can be potentially be used to adapt margins in a dose painting /dose escalation scenario.

There is a large growing database in the surgical community that has quantified the biomechanical properties of organs. A force-deformation relationship has important applications in surgical simulations, optimizing surgical tool design, creating "smart" instruments capable of assessing pathology or force-limiting novice surgeons, and understanding tissue injury mechanisms and damage thresholds [20].

In general soft tissue organ deformation can be thought of as a bio-feedback between physics and anatomy & physiology of organs. A medical simulator including soft tissue organ deformation can be thought of in a three generation step model as shown in figure 1.7 and discussed in[21-25]. The first generation of medical simulators only considers the geometric nature of human organs like variations in shape, volume etc... This can be easily quantified using the wide variety of modern imaging methods available. The second generation of medical simulators aims to model the physical interaction of human organs. Clearly for radiation oncology applications, understanding soft tissue deformation and a potential simulation of organ deformation is of paramount importance. This

dissertation aims to study the physical interaction of organ deformation (second generation medical simulator) by quantifying the deformation with its causative physical force which in a clinical scenario may be linked to the influence of neighboring organs. The third generation of medical simulators accounts for the functional nature of organs and are more complicated in design and scope. The flow chart (Figure 1.7) shows how different levels of simulation (anatomy, physics and physiology) interact with one another. In a radiation therapy context, occurrence of tumor in an organ (physiological process) will modify the biomechanical properties of the tissue (physics). For example it is known that the mean density of parotid glands (physics) varies during the course of head and neck IMRT therapy due to changes in tumor size (physiology) and salivary flow (physiology)[26, 27]

To achieve such advanced simulations, it is necessary to model the phenomena occurring at the geometric, physical and physiological levels. Although rapid progress has been made in deformable image registration (DIR), more research effort is needed in physical modeling of organ deformation from a physics perspective. In particular, modeling soft tissue organ deformation is likely to be a key ingredient in creating second and third generation medical simulators from the context of radiation therapy applications.
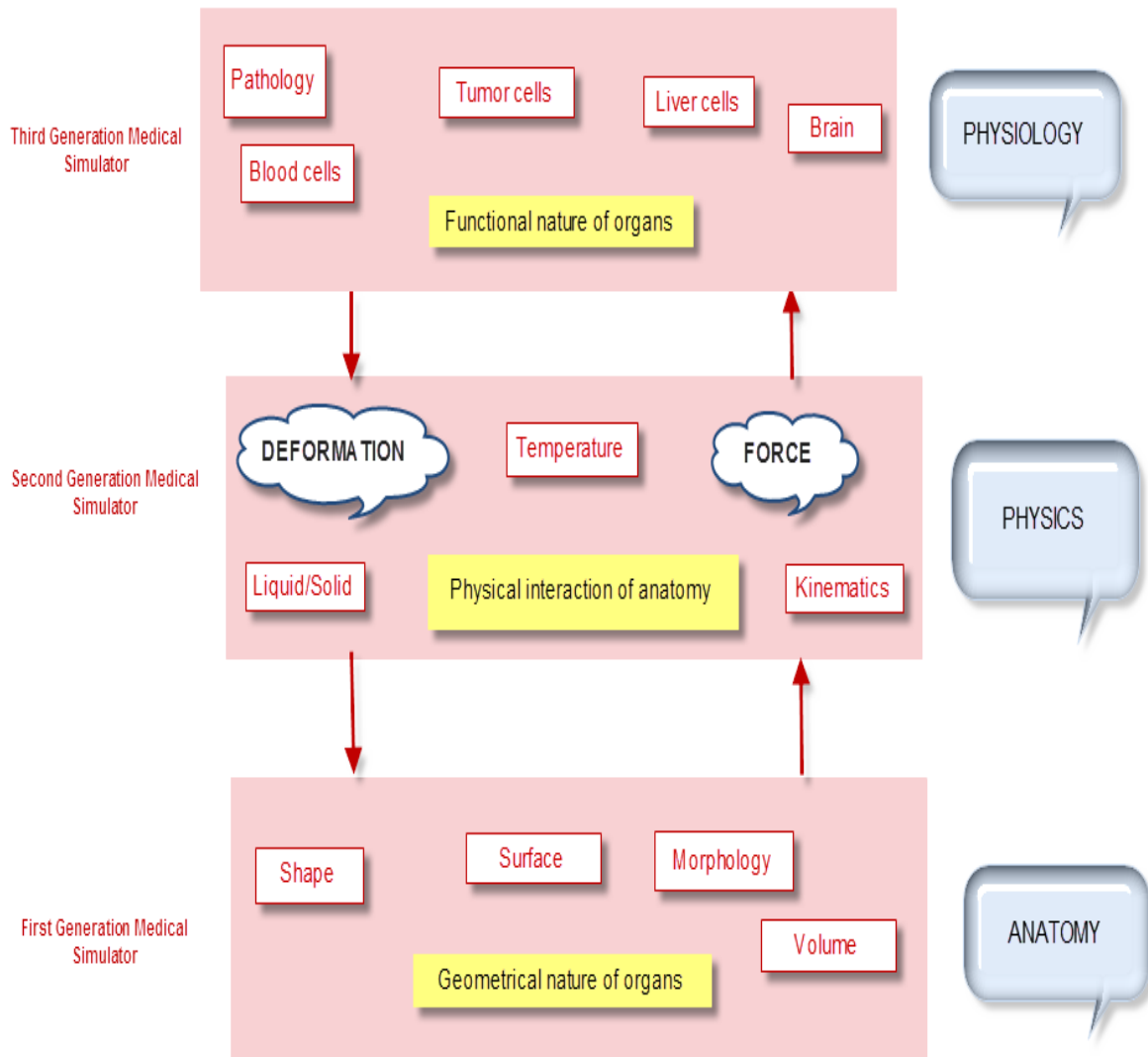
Figure 1.7 Three different generations of medical simulators illustrating the interplay between physics, physiology & geometry of the organs. (Adapted from reference 25)

To explore the relationship between deformation and its causative physical force a deformable bladder phantom with mechanical and tensile properties comparable to an adult human bladder was designed and built using a tissue equivalent viscoelastic polymer substance. Using this fundamental relationship, the accuracy of dose deformation arising from commercial DIR algorithms was investigated. A threshold limit

18

for dose warping was ascertained and established from various commercially available DIR algorithms beyond which dose recalculation is the deformed geometry is necessary. The applicability of dose warping to dose painting scenarios was investigated. This dissertation also highlights the need to validate the volume of dose from dose warping as traditionally used 3D gamma pass rates used by most research studies may not accurately describe dose warping for dose painting.

1.5 Organization of this document

This document is organized as follows.

Chapter 2 details the clinical need for adopting ART in the treatment of localized prostate cancer. Specifically imaging data from 10 patients was analyzed using both kvCBCT from Elekta Synergy and MVCT from Tomotherapy system. The feasibility of direct dose calculation on kvCBCT and MVCT images as well as quantitative soft tissue contrast comparison between the various imaging modalities is discussed. ART options in the absence of DIR using the planned adaptive software on the Tomotherapy system are outlined. Our results clearly demonstrate the need to develop a strategy that includes deformable image registration to adopt ART.

Chapter 3 details the technical principles and physics of DIR and the various approaches of DIR transformation functions with a focus on radiation oncology applications. Details of similarity measures, deformation models and optimization methods for various algorithmic implementations are discussed.

Chapter 4 gives a framework in validating the accuracy of DIR algorithms. The lack of verification scheme is one of the major drawbacks in adoption of DIR into clinical

practice. We propose a novel method by synthetically deforming CT data with a known

applied deformation and using the deformation vector field (DVF) arising from that to

evaluate the accuracy of DIR. Various methods and relative strengths of these methods in

evaluating the accuracy of DIR is presented in Chapter 4. As discussed before, dose

tracking based on dose warping is the next logical step towards implementing ART.

However the accuracy and application of dose warping in a clinical environment remains

controversial as warping the dose with DVF may not represent the physical process of

dose deposition from radiation transport principles in a deformed anatomy.

In Chapter 5 we describe a novel deformable bladder phantom made of a viscoelastic

polymer substance developed in this project towards verifying the accuracy of dose

warping. "Deformable dose" from commercial DIR algorithms was compared against the

"true" dose received by organ in deformed state to illustrate at what deformation, dose

recalculation in deformed anatomy may be clinically necessary. Dose warping was first

evaluated using 1D point dose measurement with implanted MOSFETS in the deformed

anatomy. Five parallel air canals running through the phantom were used to position

the MOSFETS in deformed anatomy. The dose directly measured by MOSFETS in

deformed anatomy was compared to the warped dose from 2 DIR algorithms.

However 1D point dose measurement for an arbitrary deformation cannot be

considered a comprehensive validation of verifying dose in a deforming anatomy.

For this reason we modified our phantom to parameterize deformation with applied

physical force. The importance and scope of quantitative relationship between force

and deformation is highlighted in Chapter 5. Both 1D deformation along the axis of

applied force and 3D deformation of organ were quantified. Using the fundamental

relationship established between force and deformation we assess 3D dose

comparison for dose warping. Details of verification scheme and applicability

methods to dose painting are discussed in Chapter 5.

Chapter 6 gives general summary and conclusions of the dissertation and highlights

the application of current work to other clinical applications in lung cancer and TMI.

A model for on-line adaptive radiotherapy is discussed for future clinical

implementation.

Appendix details the diffeomorphic demons and B-spline algorithms implemented as

part of this dissertation, as plug-in modules using 3Dslicer as the visualization

platform. A detailed procedure manual to perform DIR and evaluate the accuracy of

DIR is presented.

1.6   Scientific output in this dissertation:

1.6.1   **Journal Publications:**

a) **Raj Varadhan**, Susanta Hui, Sarah Way, Kurt Nisi.

Assessing prostate, bladder and rectal doses during image guided radiation

therapy — need for plan adaptation?[16]

Journal of Applied Clinical Medical Physics, Volume 10, (3), 2009

b) **Raj Varadhan**, Grigorios Karangelis, Karthik Krishnan, Susanta Hui.

A framework for deformable image registration validation in

radiotherapy clinical applications [18].

Journal of Applied Clinical Medical Physics, Volume 14, (1), 2013.

c) **Raj Varadhan**, Susanta Hui**.**

Applicability and Limits of Dose Warping - Are There Islands of Deformation

that Fail to Depict Dose Painting?

Manuscript under revision

1.6.2   **Conference presentations**

a)) **R. Varadhan**, S. Hui**.** SU-E-J-204 Experimental validation of dose warp

accuracy arising from deformable image registration algorithms - Medical Physics

40, 198 (2013)American Association of Physicists in Medicine (AAPM) 55th

Annual meeting, Indianapolis 2013[28]

b) **R. Varadhan**, S. Hui. Testing accuracy of deformable image registration

studies using computational modeling and inverse consistency metrics-

International Journal of Radiation Oncology *Biology* Physics Vol **84**, Issue 3,

Supplement, page S763-American Society for Radiation Oncology (ASTRO) 54th Annual meeting, Boston, 2012

c) S.Chaudhari, S.Edlund, L. Cho, **R.Varadhan**, S.Hui SU-E-T-513 Breathing Motion Effects on Chest Wall and Resulting Dose Errors- Medical Physics, **38,** 3607 (2011), American Association of Physicists in Medicine (AAPM) 53rd Annual meeting, Vancouver, BC 2011[29]

d) S.K.Hui, **R.Varadhan**, K.D. Dusenbery, S.H. Levitt. SU-FF-J-109 Conformal Prostate treatment- A closer look at dose delivery uncertainty and adaptive radiotherapy options- Medical Physics **34**, 2393 (2007),American Association of Physicists in Medicine (AAPM) 49th Annual meeting, Minneapolis, MN 2007[30]

e) **) R. Varadhan,** S.Way, K.Nisi, S.Hui.SU-FF-J-111 Assessing prostate, bladder and rectal doses during image guided IMRT using kvCBCT- Medical Physics **34**, 2393 (2007), American Association of Physicists in Medicine (AAPM) 49th Annual meeting, Minneapolis, MN 2007[31]

f)) **R.Varadhan**, S.Hui, D.Roback. SU-FF-J-106 Comparison of IGRT Technologies- Tomotherapy Hi-ART, Varian Trilogy and Elekta Synergy- Medical Physics **34**, 2392 (2007), American Association of Physicists in Medicine (AAPM) 49th Annual meeting, Minneapolis, MN 2007[32]

Chapter 2: Implementation and framework of adaptive radiation therapy for prostate cancer.

2.1 INTRODUCTION

This chapter details the clinical rationale and methodology used in implementing adaptive radiotherapy for prostate cancer. The framework suggested as part of this dissertation were published in peer reviewed journal, Journal of Applied Clinical Medical Physics, Ref [16] and is discussed in this chapter.

The goal of a radiation treatment as discussed before is to ensure that the target receives accurate and adequate dose coverage while the dose to the critical structures is kept as low as possible. Intensity Modulated Radiation Therapy (IMRT) [33-35] and IGRT have led to more precise conformal radiation therapy. Conformal therapy has the potential to enhance the therapeutic ratio (dose to tumor/Organ at Risk (OAR)). However, due to the complexity of treatment delivery and variation in patient/tumor intra-fraction and inter-fraction position, treatment may still pose risks for a geographic miss [36, 37].

The use of CT Imaging in IGRT technology to localize the prostate, bladder and rectum each day has made it possible to deliver the dose to the target more precisely. It is well known that the confirmation of the relative position and shape of the target and organs at risk during daily fractionated treatment is of fundamental importance to accurate dose delivery [38]. Although the primary aim of IGRT technologies in the treatment of prostate cancer is to accurately localize the tumor for precise targeting, these technologies are also capable of monitoring changes in the filling and shape of the bladder and rectum.

The ability to monitor and quantify the daily changes in these critical structures is necessary to track the actual dose delivered to them.

The current study evaluates 10 patients for the dosimetric changes due to inter-fraction organ motion associated with the treatment of prostate cancer. The two IGRT technologies used in the study include Megavoltage CT (MVCT) localization on the Tomotherapy Hi-ART machine and kilovoltage Cone Beam CT (kvCBCT) localization using the Elekta Synergy system. A framework that can be applied to adapt plans for patients treated on the Tomotherapy Hi-ART system was created. The framework includes a method to analyze the cumulative Dose Volume Histogram (DVH) calculated by the Planned Adaptive Software. These evaluations can then be incorporated into a plan modification with the aim of minimizing the differences between planned and delivered doses.

Although previous studies [39] with the Tomotherapy system have demonstrated daily dose recalculations, to the best of our knowledge, our study is the first one to attempt to create a summation dose and evaluate the dosimetric impact of taking into account the changes in daily parameters. The dosimetric information can be used to modify a patient plan or Planning Target Volume (PTV) margins based on the evaluation of actual dose received.

2.2 Methods and Materials

2.2.1 kvCBCT dose calculation accuracy on Elekta Synergy

The actual dose delivered to the prostate, bladder and rectum for 5 patients was investigated by using the daily anatomy information provided by kvCBCT images. The feasibility of direct dose recomputation on the kvCBCT images was investigated using

the ComTom CT Phantom. The ComTom phantom consists of 37 pins, each 1'' in diameter, which are arranged in 3 concentric rings. There are 18 pins in the outer ring, each spaced 20 degrees apart. There are 9 pins in the middle and inner rings respectively, all spaced 40 degrees apart. The CT numbers of the 9 pins plus air encompass the range of x-ray attenuation normally found for human tissue. The relative electron density of the materials in this phantom (compared to a value of 1.0 for water) varied from 1.87 in Teflon to 0.15 for low density polyurethane. The kvCT scan of the phantom is shown in Figure 2.1.

5 patients were randomly chosen for this study. Our standard IMRT treatment for definitive prostate cancer includes seven equally spaced beams using 10 MV photons in a step and shoot delivery. All patients were treated to a dose of 75.6 Gy in 42 fractions. The treatments were planned and optimized using the CMS XiO treatment planning system and the dose calculation was performed using a convolution/superposition algorithm. The PTV margin routinely used at our institution for prostate IMRT is 1 cm in the superior/inferior direction, 8 mm everywhere else except posteriorly where the margin is 5 mm. The patients were instructed to have a "full bladder" at the time of CT simulation and during daily treatment. The current study did not include any analysis of seminal vesicles coverage.

One full volumetric kvCBCT study set was randomly chosen for every patient from each week of treatment. A total of 9 CT study sets (Week 1 to Week 9) were used for each patient to analyze the prostate, bladder and rectal volume changes and their impact on dosimetry. The kvCBCT scans were manually contoured by the same Radiation Oncologist to account for any deformation in the target, rectum and bladder. The

kvCBCT scans were fused with the treatment planning CT scans and the dose was recomputed on the treatment planning CT scan. A two-step process was used in registering the kvCT (primary study set) with the kvCBCT (secondary study set) scans/images. The primary and secondary study sets were transferred to the CMS Focal workstation. An automatic registration was performed to automate the alignment between the two study sets. The software computes the geometric transformation that best registers corresponding anatomic details in the two study sets of the same patient's anatomy. The alignment criterion is mutual information (MI) which is a measure of the statistical similarity of the overlapping data. The transformation that gives the maximum value of MI is considered to be the best registration. In the second step, interactive registration was used to further refine the automatic registration performed by the software. The radiation oncologist manually inspected and refined the alignment of the prostate between the kvCBCT and kvCT study sets based on soft tissue match.
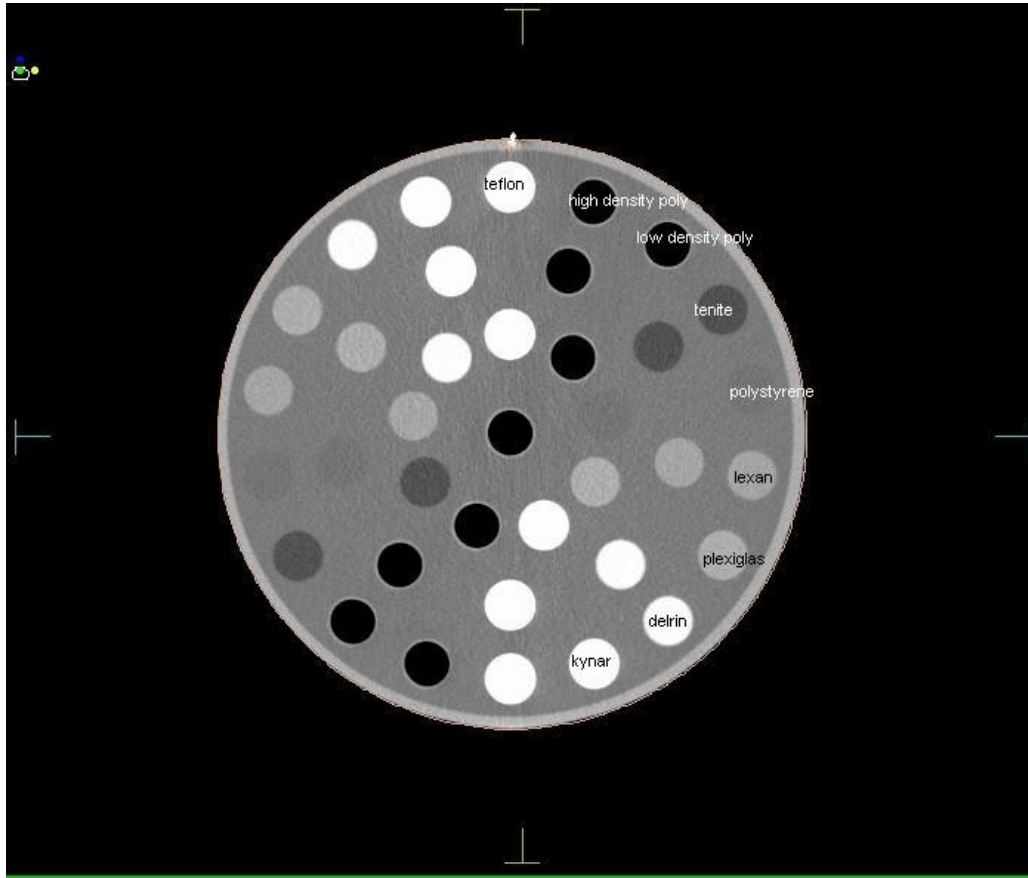
Figure 2.1 kvCT image of the ComTom Phantom.

2.2.2   **Soft tissue contrast comparison of kvCT, kvCBCT, and MVCT scans**

The Catphan 600 phantom (Phantom Laboratory, Salem, NY) was used in order to

quantitatively evaluate and compare the soft tissue contrast between the three imaging

modalities (kvCT, kvCBCT and MVCT). Additionally, the low contrast resolution, image

uniformity and spatial resolution were compared. The kvCT, kvCBCT and MVCT

images of CTP 404 module of Catphan 600 phantom are given below in Figures 2.2a–c.
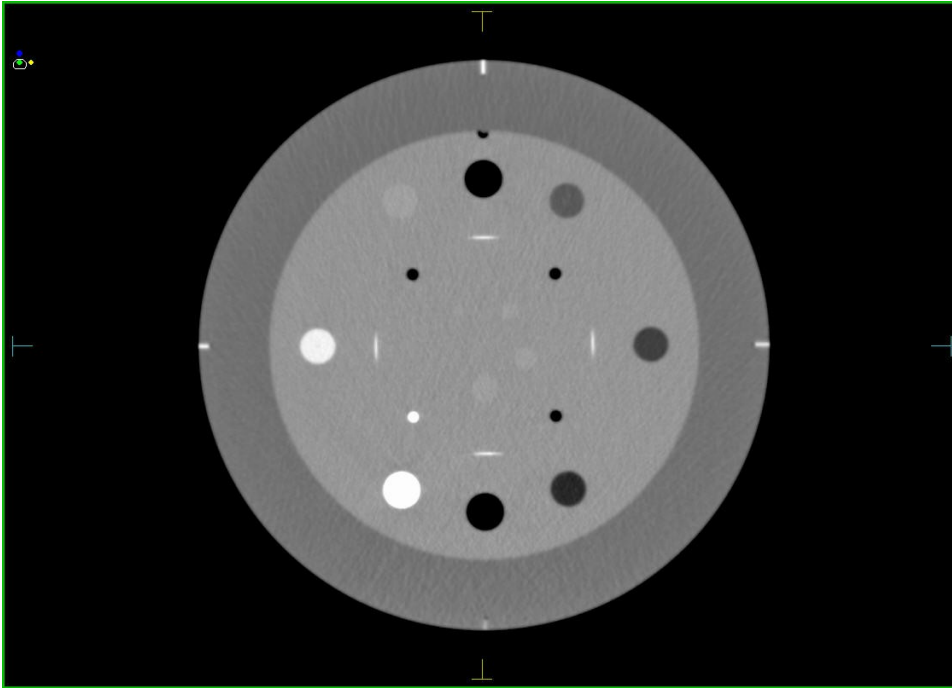
Figure 2.2a. kvCT image of the CTP 404 module of Catphan Phantom.
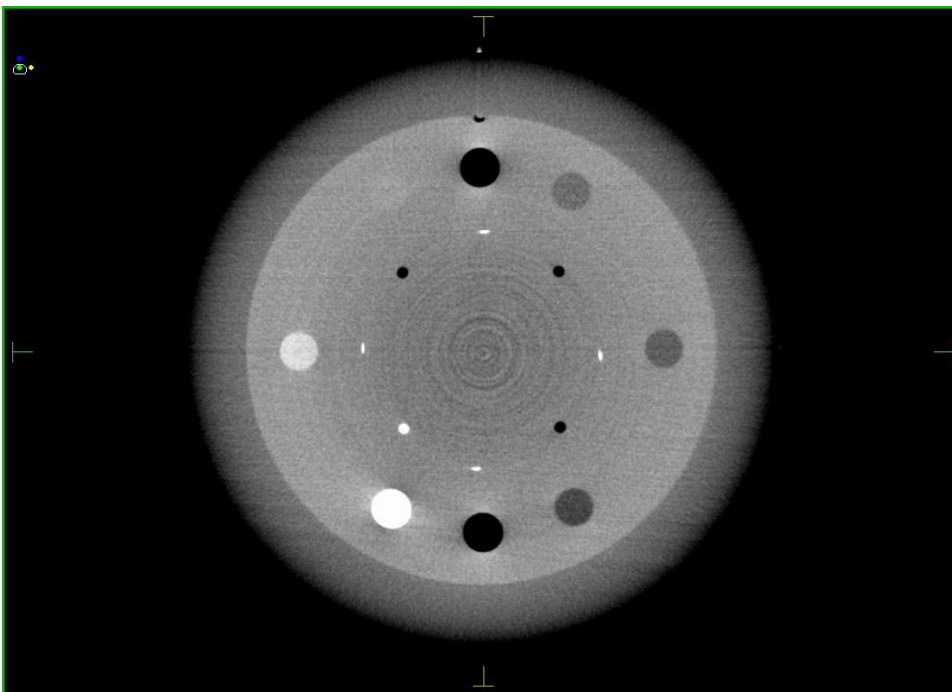
Figure 2.2b. kvCBCT image of the CTP 404 module of Catphan Phantom.
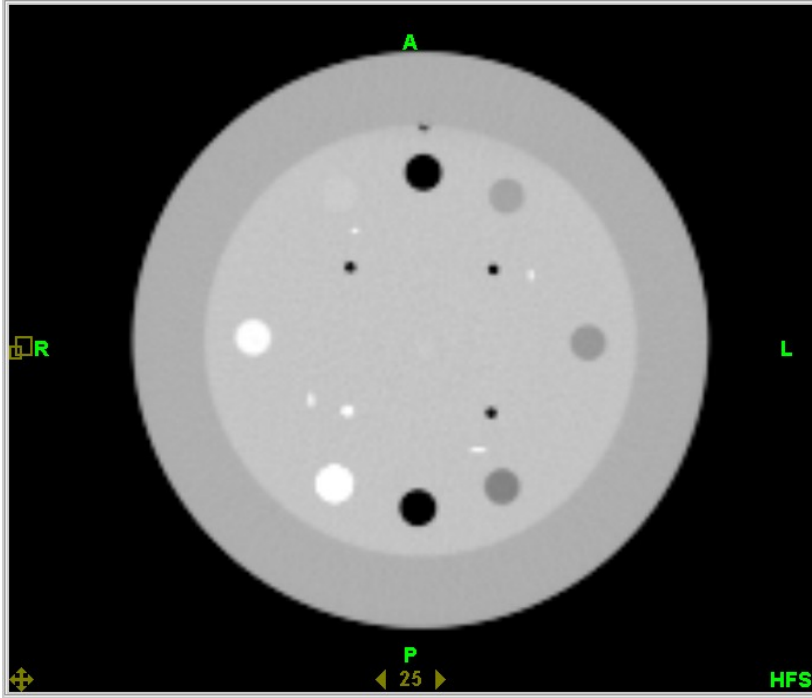
Figure 2.2c. MVCT image of the CTP 404 module of Catphan Phantom.

Low Contrast Resolution is the ability of the imaging system to distinguish between relatively large objects which differ only slightly in density from uniform background[40] .

The 3D Low contrast resolution (LCR) is computed from the mean and standard deviation of the pixel values of polystyrene and LDPE found in the CTP 404 module of the Catphan phantom using the formula [41]

$$LCR = \frac{2.75*(SD_{poly} + SD_{LDPE})}{(Mean_{Poly} - Mean_{LDPE})}$$

where we have assumed

$$5.5 = \frac{(No\min alCTnumberPoly - No\min alCTnumberLDPE)}{10}$$

Image artifacts due to equipment design, beam hardening or image reconstruction software can manifest themselves as systematic CT number variations. Hence, scanning a uniform phantom and sampling CT numbers in the fixed areas can quantify the presence of systematic variations. The 3D uniformity is computed from the pixel values of three locations in the CTP 486 uniformity module of the Catphan 600 phantom using the formula [41]

$$3D\ Uniformity = \frac{Mean(high) - Mean(low)}{Mean(high)} * 100$$

Spatial resolution characterizes the imaging system's ability to distinguish between two very small objects placed closely together. Spatial resolution measurements are performed with objects which have high contrast from uniform background. Spatial resolution is frequently referred to as high contrast resolution [42]. The 3D high contrast or spatial resolution of the three imaging modalities was calculated by imaging and measuring the resolution pattern on the line pair phantom (CTP 528 module) which has a range of spatial frequencies.

2.2.3   Adaptive Tomotherapy

The details of MVCT image reconstruction during Tomotherapy are well known and have been discussed by Ruchala et al. [43]. The energy of the MVCT beam (3.5 MV) is lower than that of the treatment beam (6 MV). The accuracy of dose calculation on the MVCT images was reported by Langen et al and has also been independently verified at our institution [44].

The MVCT images are limited to a 40 cm circle of reconstruction due to the limitation of the maximum Tomotherapy collimator width, whereas, the kvCT studies usually have a

50 cm circle of reconstruction or larger in case of big bore CT scanners. MVCT scans are also typically shorter in the patient's cranio-caudal direction to save time and reduce the imaging dose. Planned Adaptive software inserts the 40 cm field of view MVCT images into the corresponding kvCT treatment planning study by creating a combined MVCT/kvCT image study set. This is referred to as the merged image. Typically kvCT images are acquired with a slice thickness of 3mm and MVCT scanning on Tomotherapy has three possible slice thicknesses: fine (2mm), normal (4mm) and coarse (6mm). Therefore, interpolation within the MVCT image set is required to maintain a uniform 3mm slice thickness. A different image-value-density table (IVDT) is used for performing dose calculations with MVCT images due to the higher beam energy of the Tomotherapy unit (3.5 MV) as compared to the kvCT images. It has already been shown that the dose calculation is accurate using the merged images on the Planned Adaptive Software when compared to the same plan using the kvCT image [45].

In the Planned Adaptive software the original contours used for treatment planning on the kvCT study set are overlaid on the merged images, and they are re-contoured, if necessary, based on anatomy of the day. Using the merged images as the imaging dataset for adaptive plans assumes that the regions of interest outside the MVCT scan in patient anatomy have not significantly changed because the MVCT images cover only limited length in the cranio-caudal direction. Planned Adaptive software calculates verification doses for each patient. This is done by applying the daily delivery sinogram (based on the original kvCT plan) in the calculation of dose distribution on the merged image. Through the Planned Adaptive software, a summation dose, which is the addition of verification doses from each treatment fraction, was generated and compared against the

planned dose. Once the summation doses have been created, a cumulative DVH is constructed in the Planned Adaptive Software. Planned Adaptive software facilitates the modification of structures (based on patterns of accumulated dose that may have resulted in over or under dosage) in the merged image set. The resultant modified structures are then transferred to the Tomotherapy Planning Station for optimization of an "adaptive" plan. Adaptive planning allows adjustment of the remaining treatments to correct for changes that have occurred up to that point in treatment. Depending upon the anatomical site and clinical scenario, additional verifications and adaptive plans can be generated to correct for further anatomy variations. This paradigm is called Adaptive Tomotherapy Planning.

5 prostate patients were randomly chosen for this part of this study. All patients were treated in supine position using the Helical Tomotherapy unit at University of Minnesota. The patients were implanted with three gold seed markers to help align the MVCT study set with the kvCT study set and also to minimize inter-user variability in registering images.

The positional variations of inter-fraction organ motion for each treatment fraction were systematically monitored and characterized using onboard MVCT images. The registration values used to position the patient at the time of treatment were used to correct the MVCT scan when creating the merged scan. The rectum and bladder were re-contoured manually on merged study sets incorporating the bladder and rectal daily variation as determined on the MVCT scan. There were only minimal changes in the prostate target volume definition on the MVCT scans as compared to kvCT scan. The

merged images created with the MVCT scans were then used to create adaptive treatment plans using Tomotherapy Planning Station.

The reconstructed doses were compared with calculated treatment planning doses for individual organs through cumulative dose volume histograms (DVHs). The purpose of the comparison was to determine if treatment plan improvements can be dosimetrically significant and to distinguish between clinically significant and insignificant anatomy changes. Cumulative DVHs from the planned adaptive software were analyzed for each patient and adaptive radiotherapy strategies were formed based on our analysis of these 5 patients.

2.3. RESULTS

2.3.1. CT number vs. electron density using kvCBCT scans with Elekta Synergy

The CT number derived from the kvCBCT image was found to vary considerably (average variation of 283 HU) from the kvCT image as seen in Figure 2. The CT numbers derived from the kvCBCT scans showed the largest deviation from the corresponding values from the kvCT image for low relative electron density materials such as polyurethane with a maximum deviation of 684 HU for the low density polyurethane. Further, the CT number reproducibility for the same material 1 cm superior and inferior to a given central axis slice varied by as much as $\pm$ 200HU compared to the value on the central axis slice. Hence, it was concluded that direct dose re-computation on Elekta kvCBCT scans is not accurate or feasible at this time.
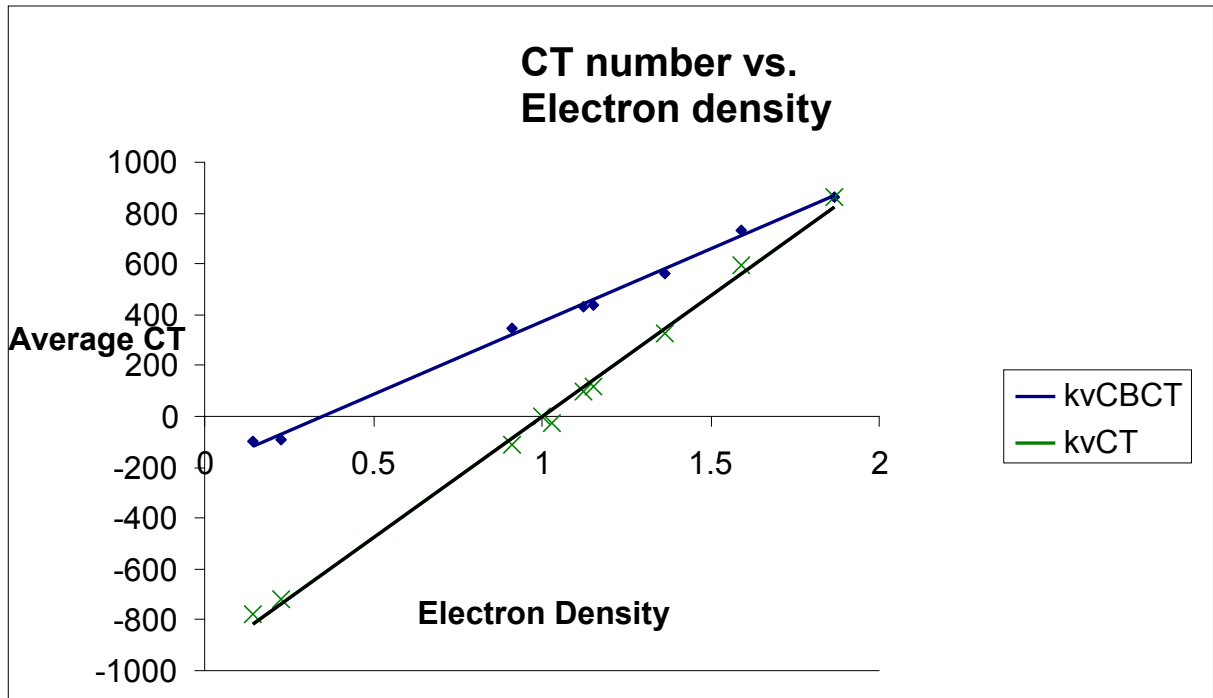
Figure 2.3 Relative Electron density vs. CT number variation for kvCBCT and kvCT

scans of ComTom Phantom.

2.3.2 Prostate, bladder and rectal volume and dose changes using kvCBCT scans on Elekta Synergy

Before each treatment, a kvCBCT scan was acquired and the prostate was aligned to the kvCT. The same physician was present and performed the alignment of kvCBCT with kvCT to eliminate inter-user variability and interpretation of soft tissue images. The CBCT scan for the prostate was imaged at 120 kVp and 1040 mAs. Based on our measurements on the CIRS body phantom, this is equivalent to an imaging dose of 2.8 cGy at the center per day, for a total of 118 cGy over 42 fractions. This dose was not added to the actual treatment dose in dose comparisons.

Figure 4 shows the rectal volume changes in the 5 patients analyzed from each week based on the kvCBCT scans contoured by the same Radiation Oncologist. Week 0

represents the rectal volume from the treatment planning kvCT scan. As seen in Figure 4

below, there is a large variation in the rectal volume over the 9 week period.

Radiation Therapy Oncology Group (RTOG) 0126 criteria of volume of rectum

receiving 75 Gy (V 75 Gy) was chosen to track rectal doses from kvCBCT scans. This

is equivalent to the percentage of rectal volume receiving the daily fraction dose of

180 cGy as compared to the rectal volume from the treatment planning kvCT scan.

This is illustrated in Fig. 5. Due to the changes in rectal filling on the day of treatment,

the maximum variation in rectal volume receiving the percentage of prescribed dose

was as high as 12% (patient 3, Week 3).
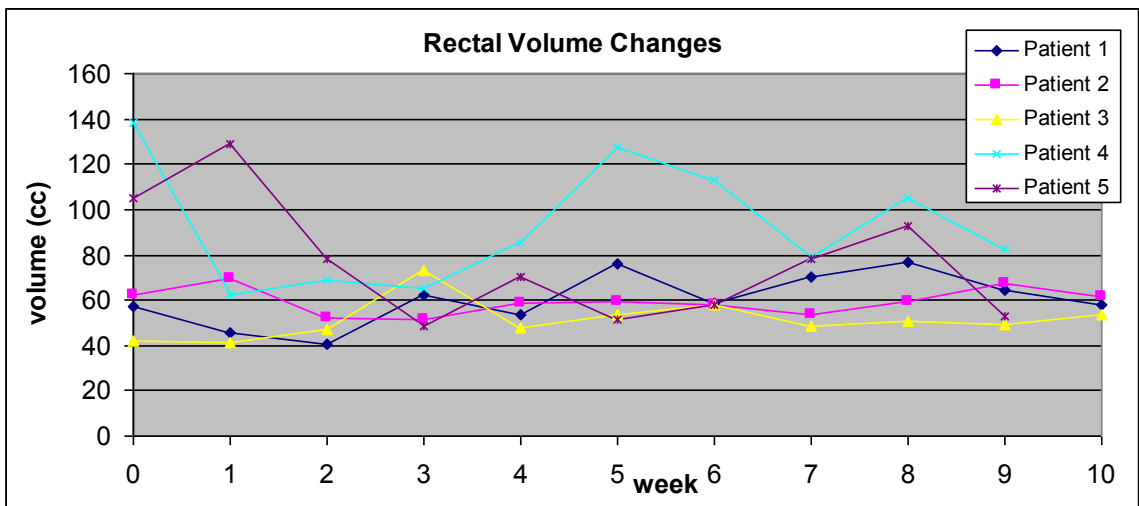
Figure 2.4 Changes in rectal volume over the course of treatment (42 fractions).
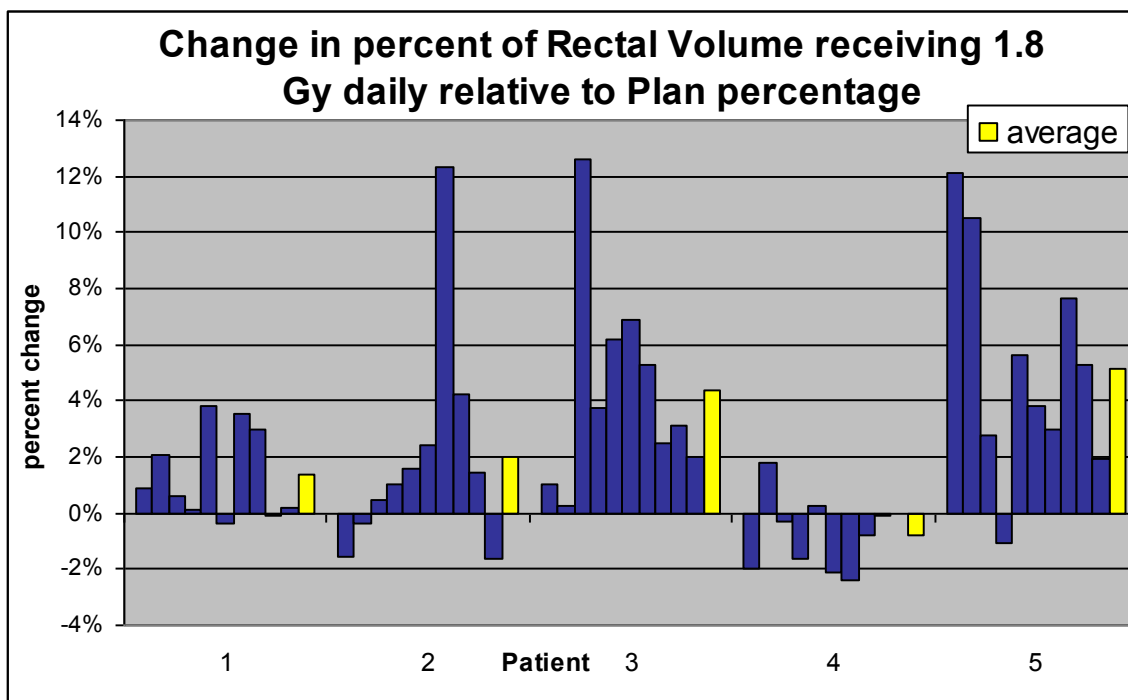
Figure2.5 Change in percentage of rectal volume receiving 1.8 Gy relative to the treatment plan value listed by patient. Positive values indicate an increase in the volume of the rectum receiving 1.8 Gy; negative values indicate a decrease in rectal volume at that dose. Each column represents data from one selected daily cone-beam scan per consecutive week of treatment. The average over these values for the course of treatment is shown by the yellow bars.

Figure 6 shows the bladder volume changes for the 5 patients treated using the Elekta Synergy system. There was a large variation in bladder volume, especially for patient 2, when compared against bladder volumes from the kvCT. In this study sample, the bladder volumes seem to decrease during treatment when compared to kvCT volumes. Radiation Therapy Oncology Group (RTOG) 0126 criteria of volume of bladder receiving 70 Gy (V 70 Gy) was chosen to track bladder doses from kvCBCT scans. This is equivalent to the

percentage of bladder volume receiving the daily fraction dose of 170 cGy as compared to the bladder volume from kvCT scan. The results are reported in Fig. 7. Due to the changes in bladder filling on the day of treatment, the maximum variation in bladder volume receiving the percentage of prescribed dose was as high as 40% (patient 5, Week 3).

Finally, the changes in prostate target dose, based on recomputation of dose using the changes in the target volume as outlined in the kvCBCT images, were evaluated. The target dose change compared to planning dose is minimal as would be expected from positioning with daily image guidance. This is outlined in Fig. 8.
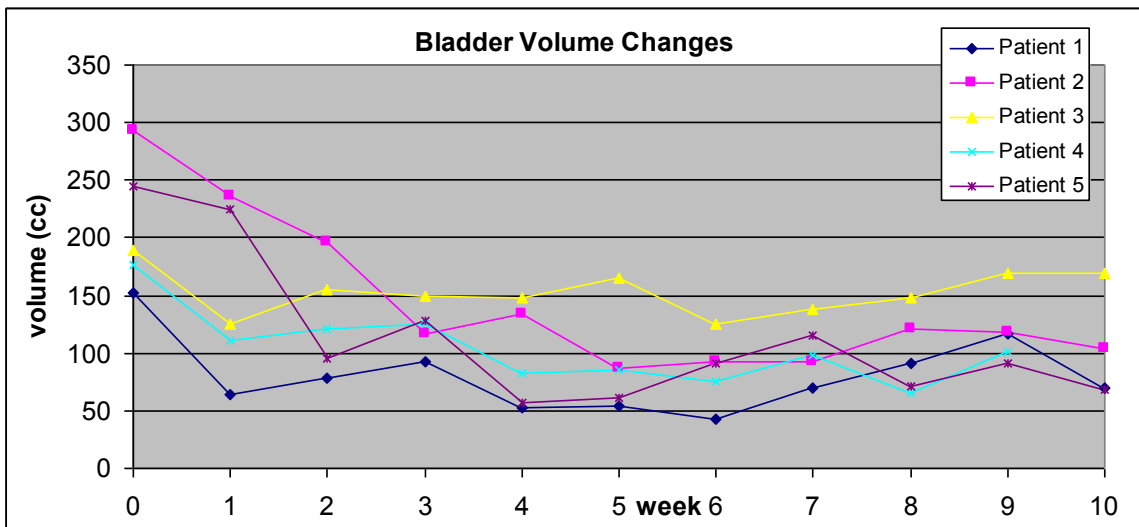
Figure 2.6 Change in bladder volume over the course of treatment (42 fractions) for all 5 patients.
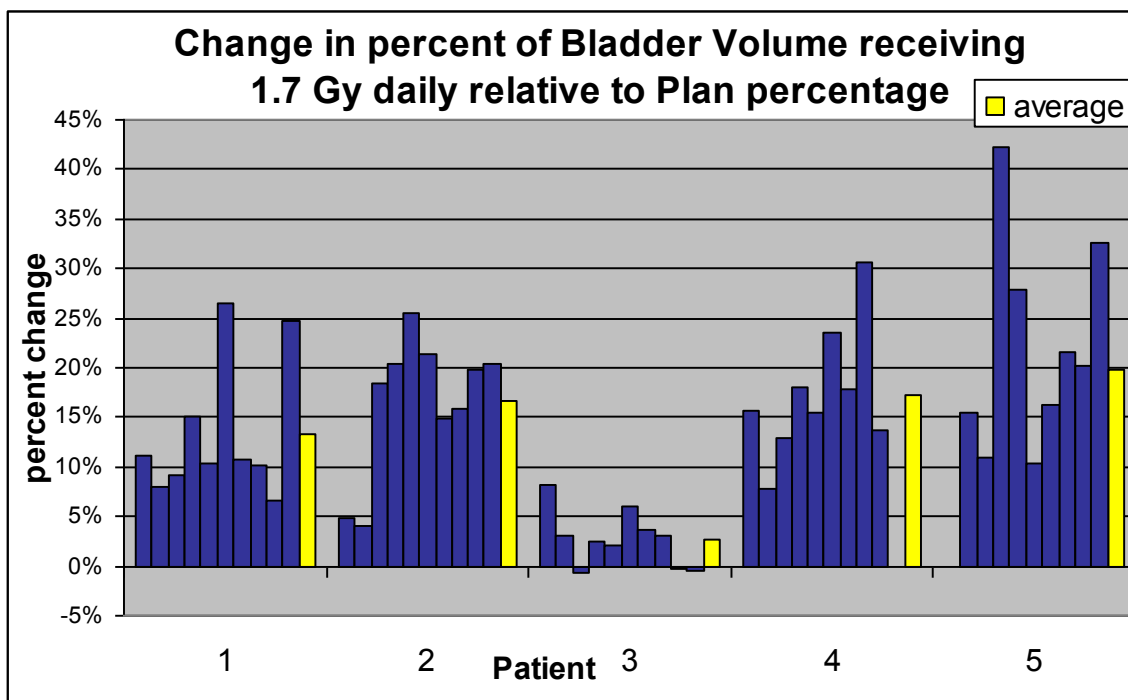
Figure. 2.7 Change in percentage of bladder volume receiving 1.7 Gy relative to the treatment plan value listed by patient. Positive values indicate an increase in the volume of bladder receiving 1.7 Gy, while negative values indicate a decrease in bladder volume at that dose. Each column represents data from one selected daily cone beam scan per consecutive week of treatment. The average for these values over the course of treatment is shown in yellow.
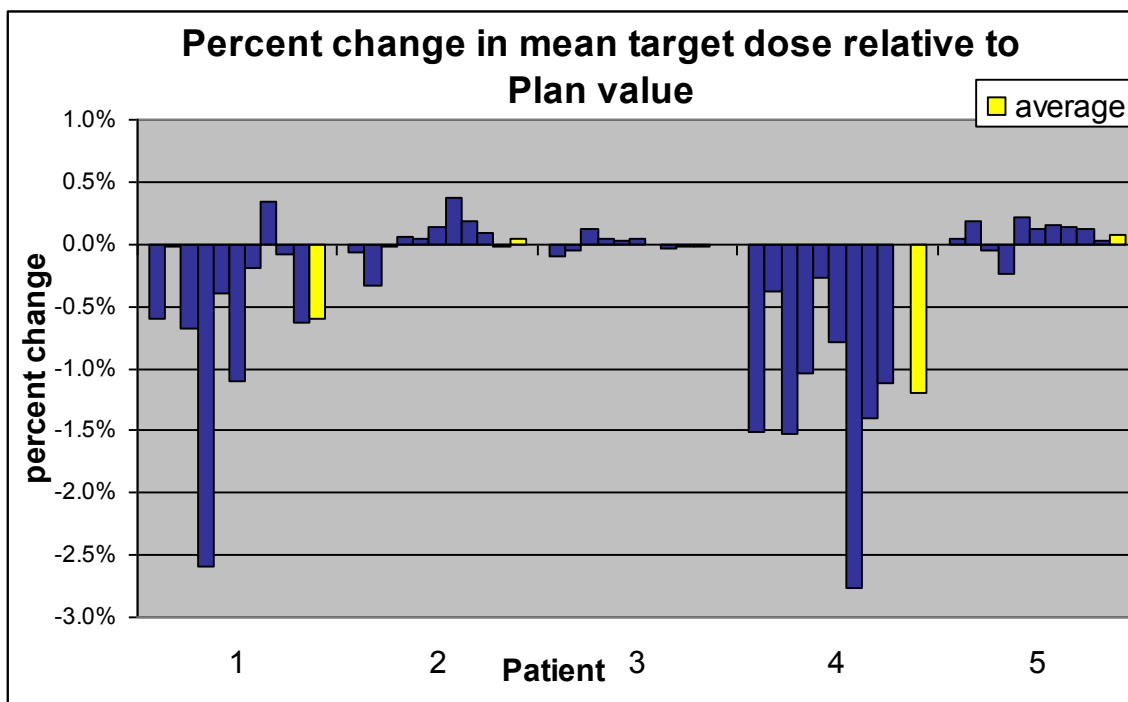
Figure 2.8 Change in mean target dose relative to the plan value for each patient. Each column represents data from one selected daily cone beam scan per consecutive week of treatment. The average for these values over the course of treatment is shown in yellow

2.3.3. Soft tissue contrast comparison of kvCT, kvCBCT, and MVCT scans

As expected, the kvCT images provided the best contrast resolution while the MVCT displayed the poorest. The quantitative values for the 3 imaging modalities are listed in Table 2.1 given below.

Imaging Modality	3D Low contrast Visibility	3D IMAGE UNIFORMITY (%)	3-D SPATIAL RESOLUTION (line pairs)
MVCT	3.19	9.3	4
kvCBCT	1.73	0.9	7
kvCT	0.11	0.044	7

Table 2.1. Quantitative comparison of contrast resolution in the 3 imaging modalities of MVCT, kvCBCT, and kvCT.

2.3.4 . Dose tracking using MVCT on Tomotherapy HI-ART system

Of the 5 patients analyzed using an Adaptive Tomotherapy plan, 3 showed minimal differences between planned and delivered dose in terms of cumulative DVH. Instead of reporting cumulative doses received by each organ, the data was analyzed in terms of cumulative DVH as reported by the Planned Adaptive software. Three different scenarios out of the 5 patient cases analyzed were picked to discuss adaptive radiotherapy strategies. A 10 % difference between planned and delivered mean dose was used as the threshold for target and critical structures in deciding whether or not to re-optimize a given plan.

Scenario I - good agreement between Planned and Delivered dose (Less than 5 % difference between planned and delivered mean doses)

Figure 9 displays a scenario where there is good agreement between planned and delivered doses after manually contouring on 42 study sets to account for volume changes in the bladder, rectum and target. The delivered summation dose for the target is slightly more than the planned dose. Overall, based on the Adaptive Tomotherapy plan, the actual delivered dose to the patient is in close agreement with the planned dose. In such a scenario, a new treatment plan with the merged study set is not required.
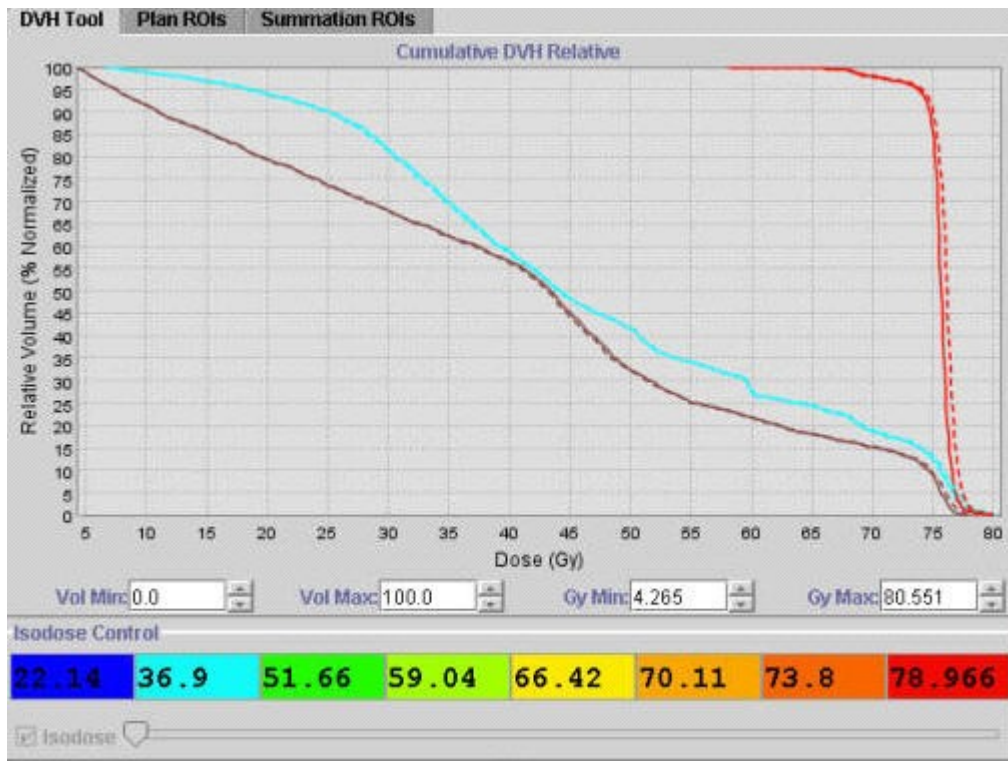
Figure 2.9 Good Agreement between planned and delivered doses using Planned Adaptive software; Dashed line: summation dose. Solid line: planned dose. Cyan line: bladder. Brown line: Rectum. Red line: Prostate.

Scenario II - minimal differences between planned and delivered dose (less than 10% difference between planned and delivered mean doses)

For this patient, the cumulative DVH derived from the summation of verification doses is given below in Figure 10. As shown in Figure 10, the cumulative rectal DVH (dashed line) is less than the planned DVH for the rectum. The cumulative target DVH is less than the planned DVH for the target with the target receiving slight under-dosage even though the prescription dose is still covered by the 95% isodose line. Even though the planned doses and delivered doses differ slightly (less than 10% threshold limit), a plan

modification using the merged study set would not be considered necessary in this scenario.
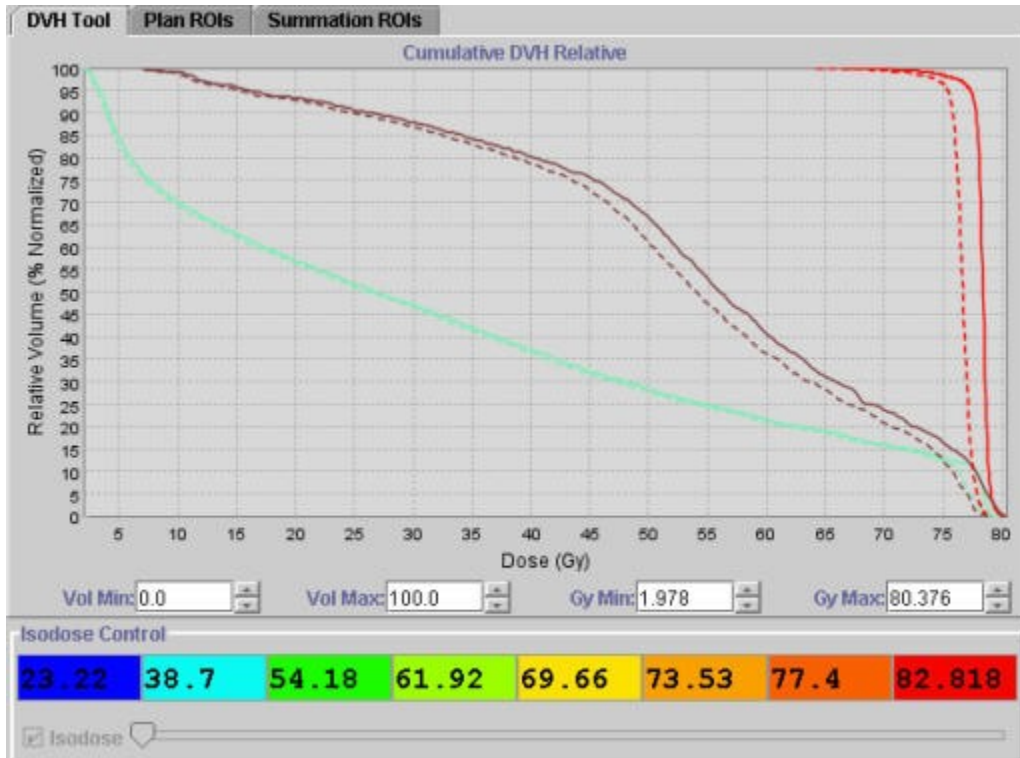
Figure2.10 Minimal differences between planned and delivered doses using Planned

Adaptive software; Dashed line: cumulative DVH. Solid line: planned DVH. Cyan line:

bladder. Brown line: Rectum. Red line: Prostate.

Scenario III: delivered dose NOT in agreement with planned dose (Greater than 10%

difference between planned and delivered mean doses)

Figure 11 shows a patient for whom a Tomotherapy boost of 28.8 Gy over 16 fractions

had been prescribed to be delivered to the prostate. In this particular patient there was a

large variation in dose delivered to the rectum when compared with the planned dose.

The large variation was a result of the patient having a distended rectum during planning

which caused the volume of rectum irradiated during actual treatment delivery to be

smaller in most fractions. A 10% difference between planned and delivered mean doses

was used as our threshold limit in deciding whether or not to re-optimize the plan based on the actual dose delivered. For this particular patient, after reviewing the cumulative DVH, the patient plan was modified off-line by choosing a different optimization scheme to account for the volume changes in the rectum from daily MVCT scans.
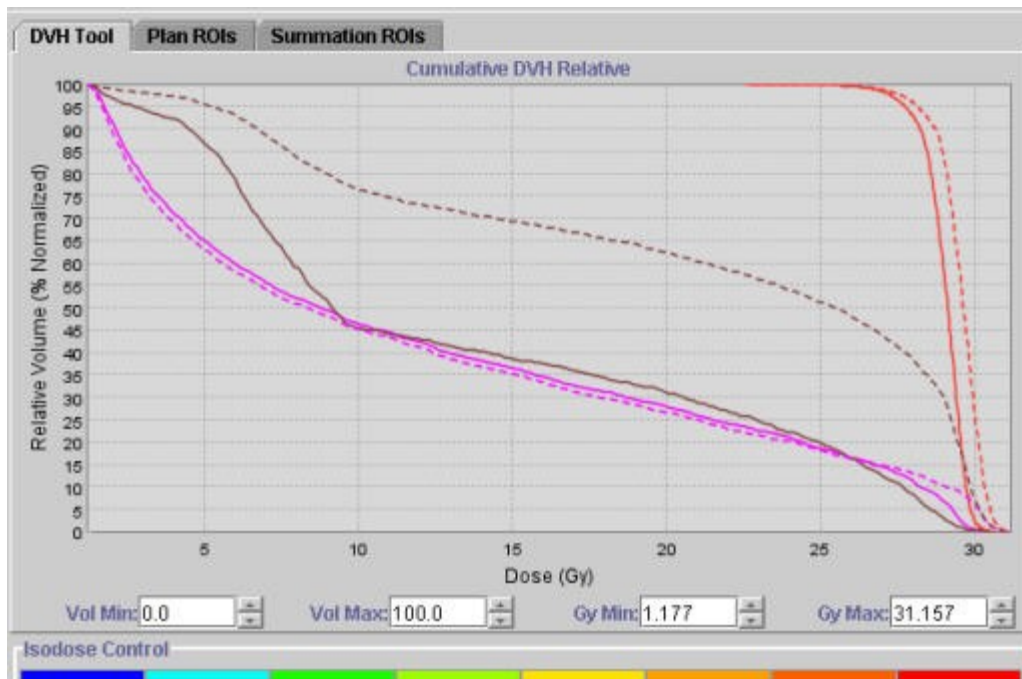
Figure 2.11 Large Differences between planned and delivered doses using Planned Adaptive software; Dashed line: cumulative DVH. Solid line: planned DVH. Pink line: bladder. Brown line: Rectum. Red line: Prostate.

The resulting adapted plan is given below in Figure 12, displaying that the planned and delivered doses to target, bladder and rectum are now in close agreement.
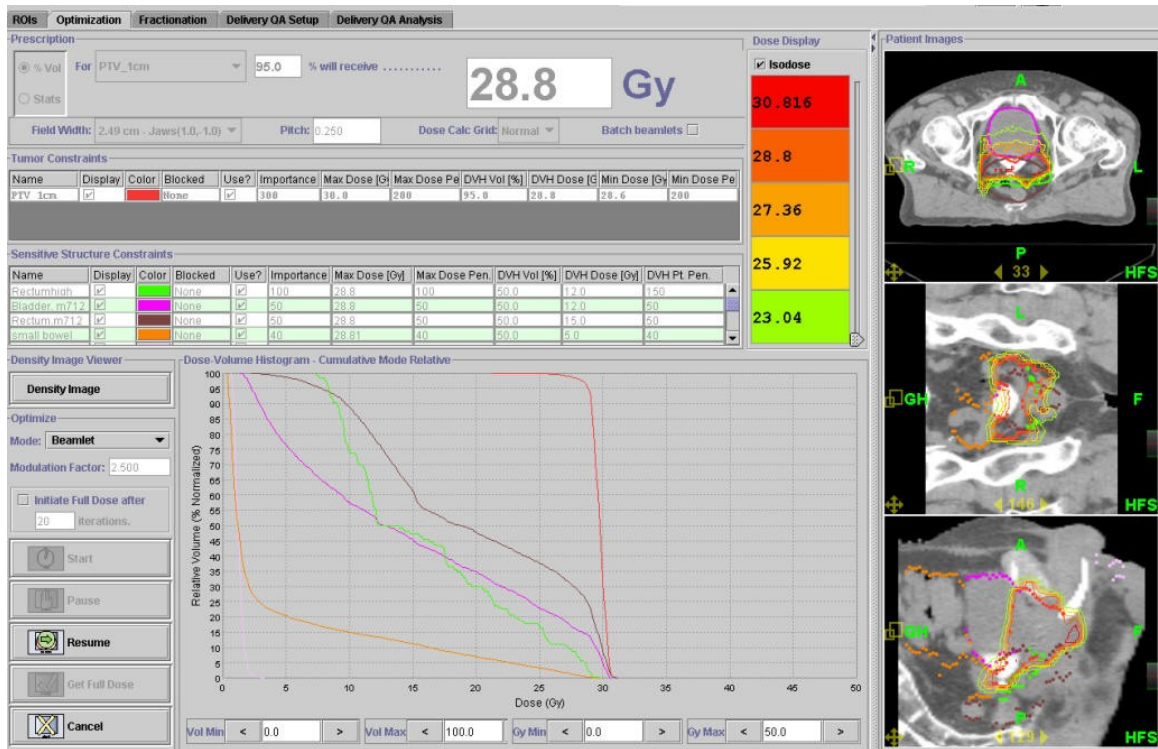
Figure 2.12 Re-optimized plan from the adaptive information whereby planned and delivered doses are now in agreement.

2.4 DISCUSSION

Positional variation of prostate gland in the treatment of prostate cancer has been extensively studied and various Image Guided Technologies which can potentially correct for these variations have also been reported. [46-59].

Several studies recently in the literature [60-62] [63-65] have shown that dose escalation is necessary and leads to an improved clinical outcome in the treatment of prostate cancer. Dose escalation, however, leads to increased dose to the critical structures, namely bladder and rectum, even with the IMRT treatment modality. There have also

been studies which have demonstrated the efficacy of hypofractionated treatments for prostate cancer [66-68]given the low $^\alpha/_\beta$[69-72] value suggested for prostate cancer. In this scenario, the precision and accuracy of the dose delivered to the target and critical structures takes on a greater significance. The evaluation of actual dose delivered to the prostate, bladder and rectum based on the anatomy of the day may become a clinical necessity for these treatments.

Our study involving kvCBCT with Elekta Synergy system clearly demonstrates that in the absence of any special protocol that involves bowel preparation, daily soft tissue imaging with the kvCBCT scans show large variations in delivered dose to bladder and rectum with the confirmation that the dose delivered to the prostate is satisfactory. Thus while clearly IGRT with daily soft tissue imaging improves the accuracy of dose delivered to prostate it also has the potential to document and monitor changes in anatomy and dose to the critical structures (i.e. bladder and rectum)

The changes in bladder and rectal volume were random in nature and the clinical impact of such variations cannot be well understood unless we quantify the changes and sum the doses from one CT scan to the other using a deformable registration model which were not done in this study. The variations of bladder and rectal volumes from weekly kvCBCT scans are displayed on the treatment planning CT scan in Figure 13. Currently there are no commercial treatment planning systems that have the ability to carry out such an analysis in an automated manner. Consequently, even in this study which takes into account only a weekly kvCBCT scan for each patient, the time required to do a dosimetric analysis of this nature is not practical in a busy clinical setting. Working with

the Radiation Oncologist, the physicists in this study spent approximately 3 hours per patient to contour bladder and rectum on each 3D kvCBCT studyset.

Various strategies have been suggested for off-line adaptive radiotherapy using kvCBCT scans in the literature [8, 73-77]. Most involve the creation of a modified target and rectum based on the evaluation of daily kvCBCT scans from the first few fractions and a modified treatment plan created for the rest of the treatment course based on these structures.

We have shown that the maximum variation in rectum and bladder volumes in our kvCBCT study receiving the percentage of prescribed dose was 12% and 40% respectively. These large variations could be clinically significant. Clearly the challenge is to create cumulative DVH information to interpret the volume changes occurring during IGRT.

This was our motivation to perform the study with the Tomotherapy system using the Planned Adaptive software tool. As stated before, 5 patient plans were evaluated with this adaptive planning method to determine whether treatment plan improvements could be dosimetrically significant and to distinguish between clinically significant and clinically insignificant anatomy changes.

Figure 2.13 kvCT superimposed with kvCBCT contours showing variation in bladder and rectal volumes for a patient over 9 week period.

The cumulative DVH information from the merged MVCT-kvCT images also gives us re-planning options should a significant discrepancy exist between planned dose and delivered dose. Our analysis of 5 patients treated on the Tomotherapy Hi-ART system found that there was a significant improvement in the treatment plan for one patient based on the cumulative DVH analysis from planned adaptive software and subsequent reoptimization of the plan.

Deformation of organs is a complicated process if organ wall changes are to be quantified. The deformation of the organ wall was not included in our analysis for bladder and rectum using the MVCT images. The bladder and rectum were assumed to be

"filled" organs while re-contouring on the MVCT and kvCBCT study sets. The soft tissue contrast was found to be insufficient for organ wall delineation. A sample MVCT image with and without the original kvCT contours are given below in Figures 14a and 14b to illustrate this point.
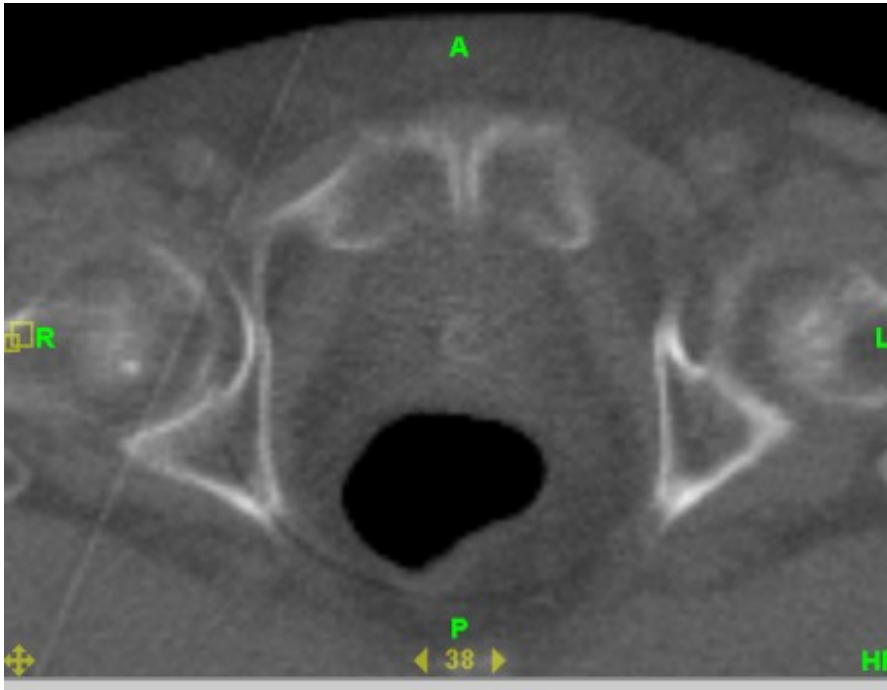
Figure 2.14(a) MVCT scan of patient illustrating lack of sufficient image contrast for rectal wall delineation.
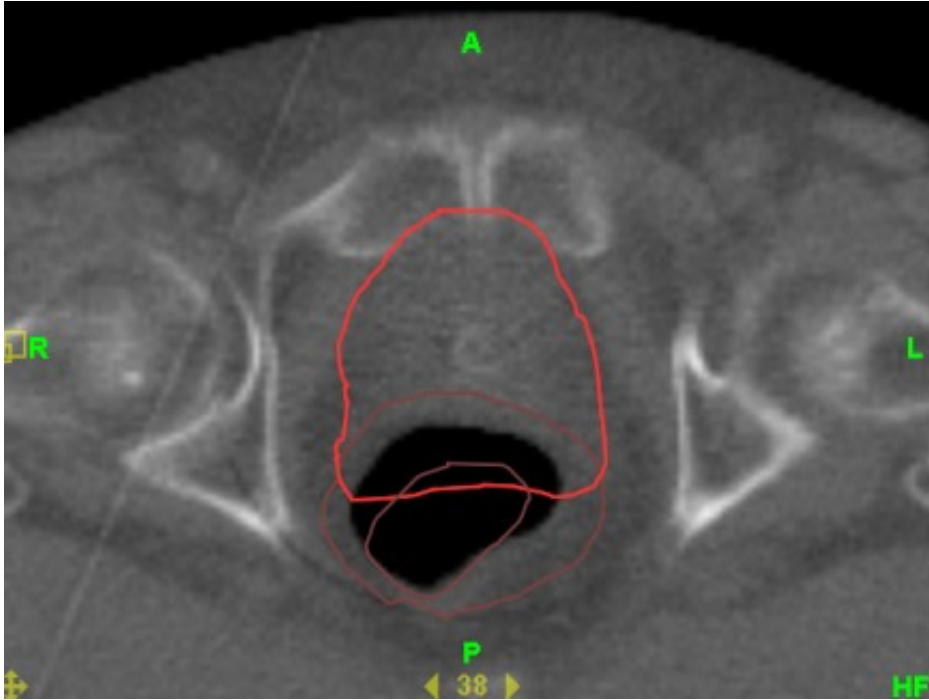
Figure 2.14 b. Outline of MVCT indicating rectum but the rectal wall cannot be visualized.

2.5 Adaptive Re-planning

The re-planning options can be divided into the two broad strategies of off-line and on-line options. The off-line approach is the most practically feasible approach to implement today and a practical implementation strategy is provided here. The off-line approach requires cumulating all of the actual delivered doses by accounting for the daily volume changes of prostate, bladder and rectum. Therefore in principle, an adaptive treatment plan can be created at the end of each week to evaluate for any potential changes in delivered dose as compared to planned dose delivery using the cumulative DVH. If a significant discrepancy occurs (greater than the 10% mean dose difference threshold) as shown in scenario 3, a re-optimization of the plan will be done to account

for these changes. A final plan will then be created which results in a DVH that closely matches or has a superior dose distribution when compared to the original planned distribution based on the feedback from the changed anatomy.

In cases where there are only minimal differences in the cumulative DVH midway through the treatment, the original plan will continue to be used for patient treatment and a final adaptive summation plan will be created at the end of patient treatment with the cumulative DVH demonstrating the planned and actual dose delivered. The Adaptive Tomotherapy plans for these cases will serve as a clinical quality assurance tool to document that the actual delivered doses were in agreement with the planned dose. The main drawback of performing the planned adaptive plans is that they are extremely time consuming because all the contours have to be manually drawn as in our kvCBCT study. An average of 12 hours per patient was spent to contour an entire 42 fraction MVCT study set. The other major drawback is that although the summation dose is computed in the planned adaptive software this only evaluates the summation dose for one MVCT at a time and does not include a deformable registration model which can potentially follow the doses delivered to the voxels creating an overall dose pattern. We are currently actively pursuing deformable registration tools with MVCT to create such models.

The on-line adaptive therapy process accounts for the deformation of the prostate, bladder and rectum using deformable registration tools based on the anatomy whereby DVH is created and compared to the planned DVH while the patient is on the table. Thus any changes to the plan or positioning of the patient is done not just by image registration data but after on-line evaluation of dose. This process can only be implemented if there are automatic software tools which evaluate the deformation of the prostate, bladder and

rectum in real time and feed the information to the optimization engine such that DVH can be generated in real time while the patient is still on table.

2.6 CONCLUSION

Our study involving both kvCBCT and MVCT image guidance have shown the ability to track actual doses delivered to prostate, bladder and rectum based on anatomy of the day. Due to the large variation in CT number on the kvCBCT images with the Elekta Synergy system we conclude that direct dose computation on these images is not feasible. We have also quantitatively evaluated the low contrast resolution, spatial resolution and image uniformity of the 3 imaging modalities of kvCT, kvCBCT and MVCT using CatPhan 600 phantom and have found as expected that the kvCT and kvCBCT images have better contrast resolution than the MVCT images.

Using the planned adaptive software on the Tomotherapy system, our study has demonstrated the ability to sum doses from multiple fractions on the merged kvCT-MVCT study set in order to construct and evaluate a cumulative DVH. We have demonstrated a clinical process where using the adapted plan, an adjustment to treatment plan optimization may be performed whereby actual delivered doses are in agreement with the planned dose based on the information gained from daily MVCT scans. To take this investigation further, one has to develop deformable registration tools which can be used to calculate cumulative doses to organs at risk and target volumes thereby providing a valuable tool for evaluating adapted plans. It is our belief that such evaluations will eventually pave the way for a dose-guided radiotherapy paradigm in the treatment of localized prostate cancer.

Chapter 3 Overview of Deformable Image Registration (DIR)

3.1 Introduction:

The problem of registering medical images has been the subject of active research for many decades. The fundamental science of image registration is determining a spatial transformation – or mapping – that relates positions in one image, to corresponding positions in one or more, other images. The meaning of correspondence varies and takes different significance depending on the application. For example, the user may be interested in structural correspondence [78] (e.g. lining up the same anatomical structures before and after radiation treatment to detect response), functional correspondence (e.g. lining up functionally equivalent regions of the brains of a group of subjects) or structural–functional correspondence (e.g. correctly positioning functional information on a structural image). These have resulted in a variety of different registration algorithms which are continuously evolving based on the application of image registration to a particular area of interest.

From a radiation oncology perspective, there are three broad applications of medical image registration and deformable image registration (DIR) in particular. These are 1) Identifying and correlating tumor or organ of interest across a series of medical scans (e.g. CT, CBCT, or MRI). 2) Matching of images from different patients (inter-patient registration) which has applications in atlas based segmentation, 3) Multi-modal registration which means matching images of the same patient acquired by different imaging modalities.(CT to MRI or CT to PET/CT etc…)

However the basic ingredients on how a DIR algorithm is operational is the same [78] and is reviewed in this chapter. Any DIR algorithm has three basic components i)

similarity measures of how well the images match, ii) deformation model (parametric or non-parametric models) which specifies how a source or moving image can be made to match target or fixed image, iii) optimization process that varies the parameters of a particular deformation model to maximize the matching criterion.

Deformable registration is inherently degenerate and is considered an ill-posed problem because there is generally no unique solution to a registration problem. Usually image registration is presented as an optimization problem. Registration methods can be based on information derived from image intensities or from landmark information (such as contours or points) placed on the images. Hybrid models are possible using a combination of intensities and landmarks. A review of DIR and the algorithm implementation details from the perspective of radiation oncology applications will be presented here. First we review two classical definitions of DIR as an image matching problem borrowed from theoretical imaging science.

3.1.1. DIR definition

 Based on reference [79]deformable image registration can be defined as finding the functions h and g in the following mapping between two 3D images I_1 and I_2:

$$I_2(x, y, z) = g (I_1 (h(x, y, z)))$$

where I_1 is called the source or moving image and I_2 is called the reference or target image. The images I_1 and I_2 can be thought of as mappings from 3D coordinates to image intensities.

The function g is called an intensity mapping function that accounts for a difference in image intensities of the same object in I_1 and I_2. In other words it is used to describe so-called 1D intensity differences. The function h is used to describe geometric differences.

It is a spatial 3D transformation that describes the mapping between the spatial

coordinates (x, y, z) in the reference image to map the coordinates (x', y', z') in the

source or moving image

so that (x', y', z') = h(x, y, z). These transformations take different forms depending

on the registration method used.

2. Alternately way to define DIR matching is presented in the recently published review

paper in IEEE [80] and is described below based on that review paper. Let us consider

source (moving) image as S and fixed or target image as T. The two images are defined

in image domain Ω and are related by a transformation W. The goal of registration is to

estimate the optimal transformation that optimizes energy of the form

M (T, S o W) + R(W).

The objective function defined above comprises two terms. The first term M, quantifies

the level of alignment between a target image T and a source image S . This term is

commonly refereed as similarity criterion in DIR.

The optimization problem consists of either maximizing or minimizing the objective

function depending on how the matching term is chosen. The images get aligned under

the influence of transformation W. The transformation is a mapping function of the

domain Ω to itself, which maps point locations to other locations. In general, the

transformation is assumed to map homologous locations from the target physiology to the

source physiology. The transformation at every position, x ϵ Ω, is given as the addition of

an identity transformation with the displacement field, u , or W(x) = x + u(x)

The second term R, regularizes the transformation (for example smoothing with

Gaussian etc..) aiming to favor any specific properties in the solution that the user

requires, and seeks to tackle the difficulty associated with the problem. Regularization

and deformation models are closely related.

In the case that the transformation is parameterized by a small number of variables and is

inherently smooth, regularization may serve to introduce prior knowledge regarding the

solution that we seek by imposing task-specific constraints on the transformation.

Second, in the case that we seek the displacement of every image element (i.e.,

nonparametric deformation model), regularization dictates the nature of the

transformation. Before we describe deformation models commonly used in radiation

oncology applications, a review of similarity measures is presented

3.2 Similarity measures

The quality of how well the images are matched after deformable image registration is

defined by the similarity measures. The two input images into DIR in reality are never

perfectly matched. Instead a similarity measure is defined, and the optimal registration is

the one that features a transformation which minimizes this measure. The commonly used

similarity measures are discussed below based on Ref [50])

3.2.1 Sum of squared differences (SSD)

The most widely used similarity metric is the sum of squared differences (SSD) measure

defined as: $SSD = 1/N \sum_x \{T(x)-S(t(x))\}^2$

Where $T(x)$ is the intensity at a position x in an image and $S(t(x))$ is the intensity at the

corresponding point given by the current estimate of the transformation $t(x)$. N is the

number of voxels in the region of overlap.

SSD is very sensitive to voxels with large intensity differences (outliers) which makes

SSD only applicable in single-modality registration (e.g. both must be CT or MRI images

etc..) contexts, or more precisely, in cases where the images to be registered only differ

by noise when registered. The least-squares form of *SSD* makes the measure

computationally very attractive since fast optimization schemes can be used.

3.2.2 Correlation Coefficient (CC)

The Correlation Coefficient metric can be written as:

$$CC = \frac{\Sigma x(T(x)-\overline{T})}{\sqrt{\Sigma x(T(x)-\overline{T})2}} * \frac{(S(t(x)-\overline{S})}{\sqrt{\Sigma x(S(t(x)-\overline{S})2}}$$

As this is a quadratic form, the same highly efficient numerical methods can be applied as

for the optimization of *SSD*-based measures. Usually *CC* is not suited for multi-modality

registration since a global linear transformation function of the grey values cannot be

presumed. However, in a number of small neighborhoods the assumption of a linear

relationship is valid and the correlation coefficient can be used as an indicator of image

similarity. This metric has the advantage that it has a reduced dependence on linear

scaling of image intensities. This means that two images can be registered even though

one is brighter than the other.

3.2.3 Mutual Information:

As discussed in review papers [78-80] [81] image registration can also be considered

within an information theoretic framework. The basic idea is to exploit a statistically

significant relationship between the grey values of the input images. This relationship

does not have to be explicitly known but rather only assumes a probabilistic relationship

between intensities. The only fact used is that proper registration means proper alignment

of significant grey value structures that through their statistical relationship lead to

pronounced peaks in the joint grey value distribution detected as maxima of its mutual

information or entropy. The mutual information can be defined in terms of entropies of the intensity distribution

$MI = H_T + H_s - H_{T,S}$

and $H_T = - \Sigma_i P_i \log P_i$, $H_s = - \Sigma_j Q_j \log Q_j$ and $H_{i,j} = - \Sigma_{i,j} p_{i,j} \log p_{i,j}$

where P and Q are probability of intensity i and j occurring in target and source image respectively and $p_{i,j}$ is the joint probability of both occurring at the same time.

MI has evolved into the accepted standard for similarity measures especially in multi-modality imaging.

3.2.4 Normalize Mutual information (NMI)

This is defined as $NMI = (H_T + H_S)/ H_{T,S}$

This metric was proposed to minimize the overlap problems occasionally seen when using the MI metric.

3.3 Deformation Models:

Deformable image registration models can be divided into those using parametric based registration (model based) and those using non-parametric ones. The parametric methods are characterized by featuring a transformation function that is described by a limited number of parameters. The parametric methods are also classified as geometric transformations derived from interpolation theory[80]. These typically include a) Radial basis functions (RBS), b) Elastic body splines (EBS) and Thin plate splines (TPS), c) free form deformation using B-splines etc. Using basis functions with compact support, a change of a parameter only affects the transformation in a spatially limited neighborhood while other parts of the deformation remain unchanged. Hence, with respect to image resampling, only the relevant part of the image has to be resampled, which improves the

computational performance of DIR.

In contrast to this, non-parametric methods typically feature a transformation function that is based on a vector per voxel describing the displacement of the point represented by this voxel. This is converted to a continuous function by interpolation. The non-parametric deformation models are also called as geometric transformations derived from physical models by some authors. These include d) elastic body models that obey Hookes law etc. e) Viscous fluid flow methods that obey Navier stokes equation etc.., f) Diffusion models like demons registration g) optical flow methods like Horn and Schunck algorithm etc.

3.3.1 Parametric or model based deformation models:

A registration method based on a parametric transformation function is usually written as a minimization problem in which an optimal set of parameters must explicitly be found that minimizes the chosen similarity measure. Typically parametric based deformation models rely on constructing a mapping function which maps points from moving (source) image to the corresponding landmark points in fixed (target) image.

The matching of point features in source and target (reference) images can also be done manually by a trained anatomy expert based on fiducial markers placed before image acquisition or image features extracted from images after scanning.

3.3.2 Transformations based on radial basis functions

A generalized way to describe the geometric transformation is creating a global function based on a set of radial basis functions (RBF), which are functions depending only on the distance between two points. Thin plate splines (TPS) are an example of radial basis functions that are derived from minimization of a smoothness

measure based on the partial derivatives of the transformation[82] . A known

synthetically induced deformation using TPS model is used to verify the accuracy of DIR

in this dissertation and is discussed in the next chapter. The name "thin plate" refers to a

physical analogy of bending a thin sheet of metal plate orthogonal to the plate such that

the plate will arrange itself in a configuration where the bending is evenly distributed or

producing radially symmetric transformations.

A number of other basis functions for RBF-based transformations have been

proposed for image registration including elastic body splines (EBS), Wendland

functions[83] and Gaussian functions.

3.3.3 Adaptation of Insight Segmentation Tool Kit (ITK) Thin Plate Spline:

 ITK uses a variation of the elastic body spline [84] to implement the thin plate spline.

The elastic body spline is obtained by solving the Navier equilibrium partial differential

equation for a homogeneous isotropic elastic body subjected to loads [84]:

$$\mu\nabla^2\vec{u}(\vec{x})+(\mu+\lambda)\nabla[\nabla\bullet\vec{u}(\vec{x})]=\vec{f}(\vec{x}) \tag{1}$$

where $\vec{u}(\vec{x})$ is the displacement from the original position $\vec{x}$, ∇^2 and ∇ are respectively

the Laplacian and gradient operators. The force field $\vec{f}(\vec{x})=\vec{c}r(\vec{x})$. Position vector

$\vec{r}(\vec{x})=|\vec{x}|=[x_1^2+x_2^2+x_3^2]^{1/2}$. μ and λ are the coefficients that describe the physical

properties of the materials derived from Young's modulus (E) and poisson ratio, (υ) and

can be written as

$E=\dfrac{\mu(3\lambda+2\mu)}{\lambda+\mu}$ and $\upsilon=\lambda/[2(\lambda+\mu)]$

$\nabla \bullet \vec{u}(\vec{x})$ is the divergence of the $\vec{u}(\vec{x})$. The solution to equation (1) given the force field

is:

$$\vec{u}(\vec{x}) = G(\vec{x})\vec{c} \qquad\qquad (2)$$

$$G(\vec{x}) = [\alpha r(\vec{x})I - 3\vec{x}\vec{x}^{T}]r(\vec{x}) \qquad\qquad (3)$$

The passion ratio $\upsilon = \lambda/[2(\lambda + \mu)]$ and $\alpha = 12(1-\upsilon)-1$. I is the identity matrix. The form

of $G(\vec{x})$ for the ITK TPS implementation is as follows:

$$G(\vec{x}) = Ir(\vec{x}) \qquad\qquad (4)$$

The matrix block element $G(\vec{x})$ in the ITK TPS implementation is a 3x3 matrix. The

"traditional" thin plate spline [82] $G(\vec{x})$ is replaced by 1x1 matrix As noted [84], this

difference derives from the assumption that individual displacements in each coordinate

axis in the "traditional" thin plate spline is independent. The ITK implementation of the

thin plate spline assumes that the displacements in each ordinate are coupled as a direct

consequence of being parts of the solution solving the equation (1). The stiffness of the

splines could be adjusted by the stiffness factor ξ. When ξ is set to zero, one obtains the

interpolating splines [85].

Other ITK kernel splines

The TPS is a member of a family of splines available in ITK for deformable alignment.

Other spline models available are given below.

–Thin Plate Reciprocal Spline: $G(x) = r(x)^2 \log(r(x)) \times I$.   (5)

–Elastic Body Spline (EBS): $G(x) = ((12 \times (1-v) - 1) r(x)^2 \times I - 3xx^T) \times r(x)$ where v is the

Poisson's ratio.   (6)

–Elastic Body Reciprocal Spline: $G(x) = ((8 \times (1-v) - 1) r(x) \times I - 3x x^T / r(x))$.   (7)

–Volume Spline: $G(x) = r(x)^3 \times I$.   (8)

The variants are based on variants plugged into the solution of $G(x)$, see reference [84]

for details.

3.3.4 Transformations based on a grid of control points

B-splines:

B-splines are a commonly used deformation model in radiation oncology applications

and have been used in commercial implementation of DIR software as well (Velocity

AI). A common approach to parameterizing a transformation using basis functions is

to base the transformation on a number of control points arranged in a regular

grid and four basis functions .In short, a function is represented as a linear combination of

basis functions such that

$$\vartheta(x) = \sum_i p_i \beta_i(x)$$

where p_i is a scaling function and $\beta(u)$ is a piecewise cubic polynomial and,

$\beta_0(u) = (1 - u)^3/6$

$\beta_1(u) = (3u^3 - 6u^2 + 4)/6$

$\beta_2(u) = (-3u^3 + 3u^2 + 3u + 1)/6$

$\beta_3(u) = u^3/6$.

The four piecewise polynomials are shown in the figure 3.1 below.
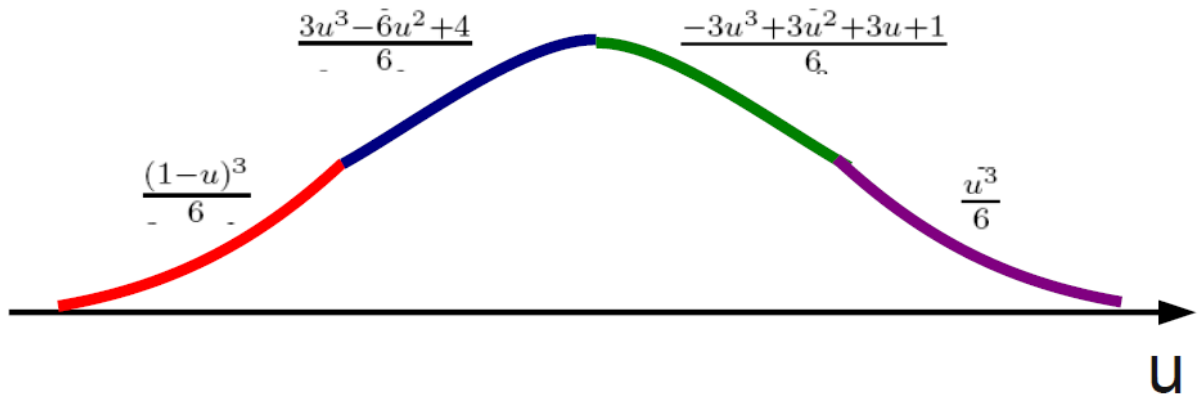
Figure 3.1 Graphical representation of four piecewise polynomials in B-spline algorithm

Using these it is possible to develop a transformation function which is locally

controlled , i.e when a control point is moved the points in the vicinity are transformed

This technique is sometimes called free form deformation (FFD). The compact support of

the BSplines means that when evaluating the effect of moving a control point, only the

vicinity of this point needs to be considered. In a cubic B-spline FFD transformation

approach is applied in registration used in mammography for breast cancer [86]. This

registration is based on MR images and using MI as similarity measure for creation of

external forces.

The B-spline approach combined with Mattes MI similarity metric has been widely used

for several applications in radiotherapy[87-89]

3.3.5 Mesh based models

Mesh based models perform DIR (also known as deformable mesh registration (DMR)

based on dividing the entire image into polygons (2D) or polyhedra (3D), where the

subdivision follows boundaries in the images. This can be used for finite element analysis based methods in image registration.[90, 91]

A number of authors have based their registration approach on using organ segmentations for creating a mesh of points connected by triangles (organ surface), and tetrahedra or hexahedra (entire organ volume). Recently this method was used to verify the accuracy of automatic target registration by comparing tumor and lymph nodes delineated by an anatomy expert on weekly CT scans with those derived from mesh registration[92].

3.4 Non-parametric deformation models

Non-parametric deformation models or transformations are typically described by a field consisting of a displacement vector per voxel of the reference image. A continuous transformation function is defined by interpolation between these vectors and consequently the DVF generated in non-parametric models constitute a vast number of degrees of freedom. The non-parametric deformation models are also sometimes called free form deformation in some of the published work.

3.4.1 Methods for non-parametric registration

Deformation models in parametric approaches to some extent are regularized by the continuous nature the parametric functions. However regularization is crucial when using non-parametric transformations. In this section some examples will be given of non-parametric registration methods which rely on physical properties based on an underlying physics to guide the registration process.

3.4.2 Linear Elastic matching

Hooke's law of elasticity describes the strain, the deformation a body undergoes,

when subjected to a stress, the force per unit area. Under Hooke's law this is a

linear relationship is described by

$F = -kx,$

where x is the change in length of the object, F is the restoring force exerted by the

body, and k is the spring or force constant. Hooke's law can be rewritten, in terms

of stress and strain, as

$\sigma = E^* \varepsilon$, where E is young's modulus and σ and ε are the applied stress and strain . The

deformation along the axis of applied force follows Hooke's law and can be written as

$x = \frac{\Delta L}{L} = \frac{1}{E} * \frac{F}{A}$ where E= Young's modulus of organ and $\frac{F}{A}$(force per unit area) is the

applied load.

In a simple 2 D model the deformation in a direction perpendicular to the direction of

applied force (Δ H) can be written in terms of the Poisson ratio of a particular organ as

follows: $y = \frac{\Delta H}{H} = \frac{\upsilon}{E} * \frac{F}{A}$ where υ is the poisson ratio of the individual organ defined as the

ratio of transverse contraction strain to longitudinal extension strain that describes the

compressibility of a material. Typical organ Young modulus and poisson ratio are given

in Table 3.1below that can be used in biomechanical algorithms based DIR[91].

Organ	Poisson's ratio (υ)	Young's modulus (E) (kPa)
Lung	0.45	5.0
Bladder	0.45	16
Breast	0.45	19
Liver	0.45	7.8

Spleen	0.499	50
Kidney	0.499	24
Stomach	0.499	500
Interior	0.4	1.5(abdomen) to 6.0(thorax)

Table 3.1 Typical Young Modulus and poisson ratio of organs used in DIR

biomechanical algorithms

3.4.3 Demons Algorithm

The demons registration method was introduced by Thirion[93] and has been used in several radiotherapy applications.[94-96]

Optical flow is used to find a driving force at each point based on the intensity gradient of the image. The allowed transformations are described using a vector field where each voxel has an associated deformation vector describing where this voxel is mapped to in the reference image. The main concept here is to drive the voxels of the moving image in the direction of the gradient ∇f if their intensity is higher than the corresponding intensity of voxels in fixed image and in the opposite direction if intensity is lower. To regularize the flow a Gaussian filter is used.

The Demons algorithm defines the deformation fields as

$$\vec{u}(\vec{x}) = \frac{(m\text{-}s)\nabla s}{\nabla s^2 + (m-s)^2} = \frac{F.\nabla s}{\nabla s^2 + F^2}$$

where (m-s) is the external force or the differential force between static and moving images and ∇s is the gradient of the static image.

This method has been validated on a wide variety of radiotherapy applications[94, 95].

3.4.4 Viscous-fluid registration

A registration method designed to handle large geometric displacements between

two images is the viscous-fluid registration method by Christensen [97]. The general idea

in this method is to use a motion model that is derived from continuum physics that

describes the motion of a viscous fluid for regularizing the registration process.

The general equation can be described using Navier-Stokes equation namely

$$\mu \nabla^2 \vec{u}(\vec{x}) + (\mu + \lambda) \nabla [\nabla \bullet \vec{u}(\vec{x})] = \vec{f}(\vec{x})$$

For an incompressible fluid, the conservation of energy, momentum, and mass lead

to the Navier-Stokes equations to describe the motion of a fluid substance. In the

viscous fluid model equation above, μ is set to 1 and λ to 0, resulting in the simplified

equation

$$\nabla^2 \vec{u}(\vec{x}) + \nabla [\nabla \bullet \vec{u}(\vec{x})] = \vec{f}(\vec{x})$$

The driving force in the viscous-fluid registration is a body force vector field that is

derived on the basis of image intensities finding the local direction of steepest

decrease of an SSD similarity measure. The method is very time consuming because it

requires an iterative solution of a partial differential equation (PDE) and in each iteration

another PDE must be solved to find a vector field of velocities.

An example of viscous-fluid registration method extended to include the use of

landmark information was used in cervical cancer registration with patients with CT

compatible intra cavitary applicators[98]. A hybrid model is presented here in which

regions of interest are converted to binary volumes. These volumes are included when

body forces are calculated which makes it easier to assure that structures of importance in

the images are matched.

3.4.5 Optical flow based registration methods

The process of estimating optical flow is the process of finding a mapping between the fixed and moving image that relates in a quantitative manner how image intensity information has changed between the two images. In theory both images are regarded as part of one mathematical function where spatial changes have occurred in the time between acquisitions transforming one image into the other. The optical flow is a vector field consisting of the changes in spatial coordinates. These vectors can be thought of as "optical velocity" vectors showing the direction of image intensity flow.

A well-known method for estimating optical flow is the classical Horn and Schunck algorithm [99]. Here the optical flow field is found by minimizing a cost function that consists of an intensity term and a term penalizing non-smooth optical flow fields. The Horn and Schunck algorithm is available to radiation oncology community through the DI-ART platform in public domain[100]. The optimization is based on the calculus of variations. Because the Horn and Schunck method performs a global optimization it is able to produce very smooth transformations. The method was used for estimating intra-thoracic tumor motion by Guerrero et al.[101]. Further the Horn and Schunck algorithm was found to be the best performing algorithm for dose warp accuracy in stereotactic irradiations and also the best performing algorithm in low contrast DIR accuracy studies using a deformable gel which played the roles of both a dosimeter and image study set [102-104]

An invertibility term can be added to the Horn and Schunck method as done by Yang et al.[105] for obtaining inverse consistent registration (that is registration of moving image to the fixed image is the same as the inverse transformation of the fixed image to the

moving image, the details of inverse consistency are discussed in next chapter). A different approach than the global optimization performed by Horn and Schunck was taken by Lucas and Kanade [106] which is also available to the radiation oncology community through the DI-ART package[100]. Here an assumption of constant flow in a window around the pixel being considered was chosen which can be solved by the least squares method. The Lucas and Kanade method leads to a registration result which is of a more local nature in that the information about displacements at edges does not propagate through areas of uniform intensity.

The two optical flow estimation methods mentioned above as well as the Demons method by Thirion have become the basis for a variety of deformable registration models based on non-parametric mode and have been used widely in radiation oncology community for a variety of clinical applications.

Some authors have used calculus of variations in their work on DIR. For example Lu et al.[107] used calculus of variations to represent the minimization of their registration cost function as a set of elliptic partial differential equations and validated the method on lung and prostate CT images. For applications in head and neck, Zhang et al.[108] used these variational methods in implementing an atlas based segmentation by automatically delineating volumes of interest on 32 CT images from 7 different patients.

3.5 Optimization methodologies

Optimization refers to the manner in which a transformation function is adjusted to improve image similarity metrics discussed in sec 3.2. A good optimizer can be thought of as one which finds the best possible transformation between source and fixed image in a quick and robust manner. Deformable image registration as discussed before is in

general an ill-posed problem. There can be many deformation vector fields (DVF) in a non-parametric registration resulting in the same deformed image and thereby resulting in the same cost value as calculated by the chosen similarity measure. Therefore the similarity metric is usually combined with a regularization term. For parametric transformations the regularization is often achieved using a combination of a regularization energy term on the parameters and the properties of the parameterization function itself. Other transformations (like RBFs) function as interpolators and work by providing a smooth interpolation of prescribed displacements (the matching of landmarks).

For non-parametric methods the smoothness of the resulting transformation is dependent on the regularization chosen. This is related to the harmonic energy of the deformation vector field which is inversely proportional to the smoothness of the DVF. The details of harmonic energy of a deformation field are discussed in next chapter. For some non-parametric methods the regularization imposed is an implicit result of a search strategy instead of a term included in the cost function to optimize.

3.5.1 Hierarchical approaches

Most practical implementations of image registration methods utilize some kind of Hierarchical coarse-to-fine approach. Several possible approaches exist as discussed in Ref[109]:

Multi-resolution approaches:

The deformation is first approximated on low resolution versions of the images to be registered. The result of this coarse registration is then used as a starting point for a registration at a higher resolution. This continues until the deformation has been

approximated at the highest resolution. A multi-resolution strategy enables us to systematically handle modes of deformation at different scales. By finding a minimizing transformation at a low resolution there is a better chance of avoiding local minima at a higher resolution. This approach is used in the commercial DIR platform Mim Software [110].

 It should be noted that most DIR algorithms use different registration methods of increasing complexity as part of the hierarchical approach. Almost every deformable registration method requires an initial global (rigid or affine) registration to be made that reduces the parametric search space before the deformable model is invoked.

3.5.2 Optimization methods for parametric registration models

For parametric methods a number of numerical methods can be used for optimization of the cost function. Gradient descents (GD), conjugate gradients (CG), etc… are commonly used optimizers for parametric models.

A key ingredient in efficient optimization of a cost function is how efficient it is to compute the derivative of the cost function with respect to each of its parameters. If these derivatives cannot be found analytically they may be estimated using finite difference approximations.

3.5.3 Optimization methods for non-parametric registration models.

The non-parametric deformation models discussed before often needs a method to solve the Partial differential equations (PDEs) that arise from various models (Demons, Viscous fluid etc...) There are two primary methods to solve PDEs, the finite element method and finite difference method. The finite element method solves the PDEs by approximating the solution using a mesh to describe the volume and in general leads to a

better solution in more complex geometries because the mesh can be made flexible. The finite element methods are computationally more intensive.

On the other hand the finite difference method approximates the PDEs and a solution is found by finite difference. These equations can then be solved by assigning appropriate boundary conditions applicable to a particular deformation model.

Chapter 4

A framework for deformable image registration validation in radiotherapy clinical applications

This chapter focuses on the details of DIR verification in the context of radiation therapy clinical applications. The DIR verification scheme proposed as part of this chapter was published in Journal of Applied Clinical Medical Physics, Ref [18].

4.1   Introduction:

Image Guided Radiation Therapy (IGRT) has become a widely used treatment modality in recent past with advanced treatment processes. IGRT requires daily or frequent imaging which can lead to treatment planning modification decisions based on patient specific anatomical variations as quantified by the imaging. However, routine IGRT in most clinical departments uses only the vendor supplied rigid registration matching between original treatment planning CT (kvCT) and the daily imaging study set. Deformable image registration (DIR) studies have been advocated to more accurately quantify these anatomical and biological variations [111]. Deformable registration is essential to map the position of each voxel to a reference CT image for dose tracking and to ultimately practice adaptive radiotherapy [6, 9] . The accuracy of deformable registration is particularly important in Intensity Modulated Radiation Therapy (IMRT) and adaptive radiotherapy that deliver differential doses to different parts of the tumor and organs at risk which then sum to a uniform dose. The existing methods of deformable image registration can be classified broadly into two categories, parametric or model based(B-Splines [86], Thin plate splines [112], linear elastic finite element [90] etc..) and non-parametric methods (optical flow [93], viscous fluid [97], etc..)

There have been many techniques proposed to validate the accuracy of various DIR algorithms [95, 108, 113-119]. All DIR evaluation procedures require the use of evaluation data and validation methods. Considering the evaluation data one can separate the methods into two groups: a. those using real patient image data and b. those using phantom image data. In the first set of methods the authors use real patient image that they deform artificially to create the reference and the test study. Alternately multiple imaging acquisitions on different time moments where changes in anatomy are clearly visible and anticipated (e.g. re-planning scans or cone beam CT scans) are used. The use of deformable phantoms has also been explored to validate the accuracy of DIR. However phantoms as described in [120-122] cannot be routinely used in most busy clinical departments because of the lack of resources and time required to build and test these phantoms. Further, it is not practical to build a phantom that will be sophisticated enough to simulate all anatomical deformations that can occur in a clinical environment. It has also been suggested that the presence of uniform intensity regions in the phantom images as opposed to more intensity gradients in clinical CT images may limit the applicability of phantom tests in DIR verification [113].

The validation methods often include using landmark points in regions of interest, as a surrogate tool in verifying accuracy of DIR. A frequent problem with this technique is locating the landmark points, which in real patients anatomy can be time consuming and difficult to identify markers in low contrast regions. The contour based evaluation is useful qualitative verification in contour propagation and also for inspecting anatomical difference among images. Although contour propagation techniques seem to provide a more efficient way of validation compared to markers, including changes in shape

volume and location of a structure, they often do not confirm that the volume within the contour has been properly registered.

In this work we describe a commercial software tool kit, ImSimQA (Oncology Systems Limited, UK) which can serve as a virtual deformable QA tool by simulating clinically observed organ deformations in routine IGRT. In contrast to previous years where deformable registration algorithms where available only in a research based setting, today several commercially available products are available. Most of these commercially available products are "black boxes" in that very little information is known to the medical physicist regarding the overall system accuracy of the implemented algorithm and what the limitations of the deformable registration algorithm could be for a given clinical situation. This is particularly true for IGRT since different organs exhibit varying levels of deformation over the course of radiation therapy. Presumably the algorithm will have different registration settings to accurately register the images over these varying clinical scenarios. Therefore, it is critical that some quantitative validation of the system accuracy of the implemented algorithm and its potential limitations in the commonly encountered IGRT clinical situations exists [123].

This work describes a complete set of metrics and tools and a practical framework to evaluate a deformation field and highlights the importance of selecting an appropriate evaluation tool which is dependent on a given clinical deformation. This will ensure that a false positive conclusion is not reached in validating a particular DIR algorithm.

4.2   MATERIAL AND METHODS.

In order for a complete and thorough validation of DIR performance in a clinical environment the following three characteristics were examined in this study

4.2.1 Anatomical correspondence:

Anatomical correspondence between original and deformed image sets can be identified using markers or contours defined by the users. This validation is important because in radiotherapy clinical applications, the tumor and organs at risk (OAR) volume changes and consequently the partial volume dose received by these structures. The magnitude and location of these changes dictate the need for adaptive radiotherapy. Hence the accuracy of DIR in relation to this is evaluated in this paper by quantitatively comparing the original tumor and OAR segmentation with those obtained from warping the RT structures with the Deformation Vector Field (DVF) derived from registration. Dice Similarity coefficient, Hausdorff distance and average surface distance were used as three metrics to evaluate the accuracy of tumor and OAR segmentation and spatial overlap index.

4.2.2. Deformation field: The physical characteristics of the deformation fields should be investigated. This is because recent applications in Adaptive Radiation Therapy (ART) have used the deformation fields arising from image registration process to warp the RT Dose and display a deformed dose [124-127]. Hence some quantitative information on the physical characteristic of deformation fields is necessary for clinical implementation of ART. It is known that matching of structures based on their intensities alone is not a sufficient condition to produce physically achievable deformations[128].

In this work we used a number of methods to evaluate the characteristics of the DVF. One of the key methods reported in the literature is the concept of inverse consistency [129-131]. Inverse consistency between two images A and B are evaluated as follows in this paper. Image A is deformed to match image B, and image B is separately deformed

to match image A using two different algorithms. A perfect inverse consistent algorithm will produce a true inverse DVF when the roles of source and target images are switched. However in practice this is not the case. The inverse consistency error (ICE) between forward and inverse registration is calculated by compositive accumulation of forward and inverse deformation fields. The magnitude of compositive accumulation will be zero for perfectly inverse consistent algorithm. The details of compositive accumulation are discussed in the next section. The disadvantage of inverse consistency method is that a zero value for ICE is a necessary but not sufficient condition for an accurate algorithm as errors in one DVF may cancel with errors in the other to yield a net zero value during composition of two deformation maps [129].

Diffeomorphism is a necessary condition for deformation fields to be physically feasible [132]. This property is related to the jacobian of the deformation field. Negative jacobians indicate unrealistic physically unachievable organ deformations as organs can only be compressed and deformed but cannot undergo non invertible spatial transformations like folding of structures [133, 134]. This is the primary advantage of diffeomorphic demons over B-Splines algorithm as the jacobian is always non-negative in the former.

In this study, we compute the determinant of the jacobian of the deformation field as a criterion for validating physical behavior of deformation. The harmonic energy of the deformation field is used to quantify the regularity of the spatial transformation obtained by the deformable registration process [135]. The harmonic energy of B-Splines and diffeomorphic demons algorithms are calculated in this study to distinguish displacement fields based on regularity of the transformation.
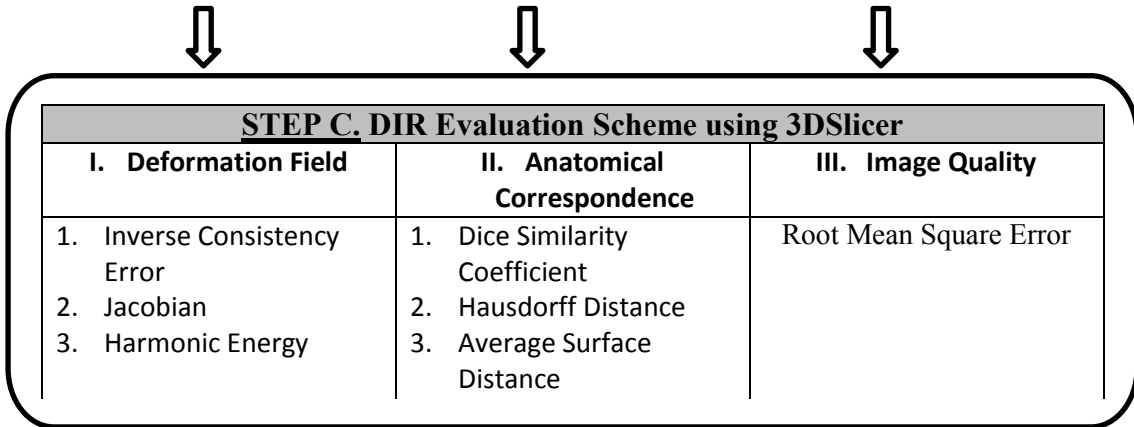
4.2. 3. Image characteristics: Comparison between original and deformably registered images to provide a measure of how well the deformation is recovered in the entire image voxel space.

Mean Square Error (MSE) between registered and original image was computed as a measure of how well the deformation is recovered in the entire image voxel space. Three clinically relevant examples from Prostate, Head & Neck and Lung case are presented and the accuracy of DIR is evaluated using various methods described above and the relative merits of these are discussed.

The workflow and evaluation methods for DIR accuracy used in this paper are summarized in the flow chart below.

STEP A. Prepare CT Test Cases using ImSimQA		
Prostate	Head & Neck	Lung
Apply *Local* Deformation	Apply *Global* Deformation	Apply *Local* Deformation
Products		
1. Warped CT images 2. Warped RT structures 3. Direct and inverse ImSimQA deformation field		

⇩　　　　⇩　　　　⇩

STEP B. Apply DIR between Original and Warped image sets in both forward and inverse direction using 3DSlicer	
Diffeomorphic Demons algorithm	B-Splines algorithm
a. Prostate original. vs. warped b. Head & Neck original. vs. warped c. Lung original. vs. warped	a. Prostate original. vs. warped b. Head & Neck original. vs. warped c. Lung original. vs. warped
Products	
1. Direct and inverse deformation field (B-Splines & Diffeomorphic Demons) 2. Warped RT structures using above deformation fields	

STEP C. DIR Evaluation Scheme using 3DSlicer		
I. **Deformation Field**	II. **Anatomical Correspondence**	III. **Image Quality**
1. Inverse Consistency Error 2. Jacobian 3. Harmonic Energy	1. Dice Similarity Coefficient 2. Hausdorff Distance 3. Average Surface Distance	Root Mean Square Error

4.2.4. Overview of methods of deformation in ImSimQA:

A brief description of the deformation process used in ImSimQA to warp the images to produce clinically observed organ deformation is presented below. In ImSimQA, there are two choices for the geometric deformation of the image data. Both implementations are based on the Radial Basis Function approach with different kernel functions. For the global deformation of the data, the Thin-Plate Spline (TPS)[136] kernel was utilized and the Compact Support Radial Basis functions (CSRBF)[137] as the local deformation scheme. Both algorithms have a closed form solution and their parameters can be computed by solving a linear system through QR decomposition.

Thin-Plate Splines

In ImSimQA the algebraic solution of Bookstein [82, 136] is followed which treats the TPS solution as an interpolation problem. In order to perform the deformation, two sets of landmark points must be chosen which will be referred to as the source points (SP) and the target points (TP) from so on. In case of a 2D image, the surface of the image is treated as a 2D grid with each x, y of the image coordinates being a part of the image grid. The SP and TP are manually inserted on the grid. The vectors, with their origin at

the SP coordinates and directed at the corresponding TP coordinates, show the

deformation direction of the grid. In order to solve this problem a mapping function

$f(x, y)$ is found that will map the SPs to TPs by deforming the underlying grid.

Given a set of n corresponding points on a D dimensioned grid, the TPS warping is

described by $D(n + D + 1)$ parameters which include $D(D + 1)$ global affine transform

parameters and Dn coefficients as the RBF parameters. As an example in $2D$ space, for

any $\mathbf{q} = \begin{bmatrix} x \\ y \end{bmatrix}$ vector in the Image space being SP, the mapping from $\mathbf{q} \to \mathbf{q'}$, where $\mathbf{q'}$ is

the TP, is given by the equation:

$$f(\mathbf{q}) = \begin{bmatrix} f_x(\mathbf{q}) \\ f_y(\mathbf{q}) \end{bmatrix} = \begin{bmatrix} a_1^x \\ a_1^y \end{bmatrix} + \begin{bmatrix} a_2^x \\ a_2^y \end{bmatrix} x + \begin{bmatrix} a_3^x \\ a_3^y \end{bmatrix} y + \sum_{k=1}^{n} U\left(\|\mathbf{P} - \mathbf{q}\|^2\right) \begin{pmatrix} w_{x,k} \\ w_{y,k} \end{pmatrix} =$$

$$\underbrace{\mathbf{A} \begin{bmatrix} \mathbf{q} \\ 1 \end{bmatrix}}_{The \ \ rigid \ \ Part} + \underbrace{\sum_{k=1}^{n} U\left(\|\mathbf{P} - \mathbf{q}\|^2\right) \begin{pmatrix} w_{x,k} \\ w_{y,k} \end{pmatrix}}_{The \ \ non-rigid \ \ Part} \qquad (1)$$

Where P are the target points, $U(d) = d^2 \log d^2$ is the TPS kernel and d the distance

between SP and TP. W are the parameters for the non-rigid part of the function and A

the parameters of the rigid part. The separation of the rigid and the non-rigid parameters

is done through QR decomposition and the solution can be extended in any dimension.

Compact Support Radial Basis Functions (CSRBF)

The TPS deformation affects the whole image and is characterized as a global

deformation procedure. For applications which need local deformation, the CSRBF

model is implemented. The locality effect of the CSRBF is adjusted by calibrating a

scaling parameter. The algebraic solution to the CSRBF is the same as the TPS with only

difference the RBF kernel used. The CSRBF kernel is a Wendland function[83] constructed from piecewise polynomials. In ImSimQA the kernel utilized in the CSRBF implementation is:

$$R(d) = (1 - d)^l$$

where d is the distance between the SP and the TP, $l = D/2 + 3k + 1$. D is the dimension space of the problem, and k is a smoothing parameter (0 in ImSimQA). In this way R returns a value for $0 \le d \le 1$ otherwise returns 0. The deformation is applied in a radius around the SP. There is a spatial scaling parameter $a > 0$ for adjusting the radius. Then the CSRBF is scaled as $R_a(d) \equiv R(d/a)$ and in this way the radius of the deformation is adjustable. In both algorithms anchor markers can be placed inside the dataset in places where the restriction of the deformation is needed. If the SP and the TP are identical then deformation around these markers is restricted. By default, in both algorithms there are anchor points at the border of the dataset, four in the 2D case and eight in the 3D case. This is done to avoid excessive warping of the original dataset.

Simulating and storing deformations in ImSimQA

As mentioned above, ImSimQA can perform global and local deformations or a combination of both. The deformation algorithms are controlled using marker points that are user-defined and can be freely positioned on the image set. The deformation workflow is performed in the following work flow.

a.   The user defines the source control marker points and enables the local (CSRBF) or global (TPS) deformation procedure. The direction of the deformation is given by translating and rotating the control points individually or as a group of points. The control

points can be moved in three dimensions. For the deformation procedure to start, the source and target positions of the control points are used.

b.   A deformation field comprising a three component vector value at each voxel is generated.

c.   The source image is then warped using this deformation field. Tri-linear interpolation is used to correct floating voxel locations during image warping.

For more complex deformations, one can combine TPS over CSRBF deformations and vice versa. In this way the new data set is a deformation based on a complex calculation of deformation. The final deformation field is composed as the addition of both deformations which can be applied only once on the original image set.

For documentation and testing purposes it is possible to export the deformed image set (as a new DICOM set), the deformation field as a binary 3D grid and also deformed RT structures as a new RT-Structure.

In Figures 4.1a -f, a simulated deformation example is illustrated. The original axial image is a virtually generated phantom CT image. Figure 4.1a shows the axial image of quasar phantom [138] The red marker points in figure a illustrate the original marker location. In figure 4.1b, the target location of the markers is a result of marker translation and rotation. Target location and source position are linked with a line. The global deformation (TPS) result is shown in figure 4.1c while the local deformation (CSRBF) result is shown in figure 4.1d. For both deformations the same source and target points were used. The magnitude of the deformation field vectors on an axial slice for the TPS and CSRBF are shown in figure 4.1e & f respectively. As expected, one can observe a

much wider area of iso-contours for the TPS deformation. For the CSRBF, the deformations are limited into a small radius around the target marker location.
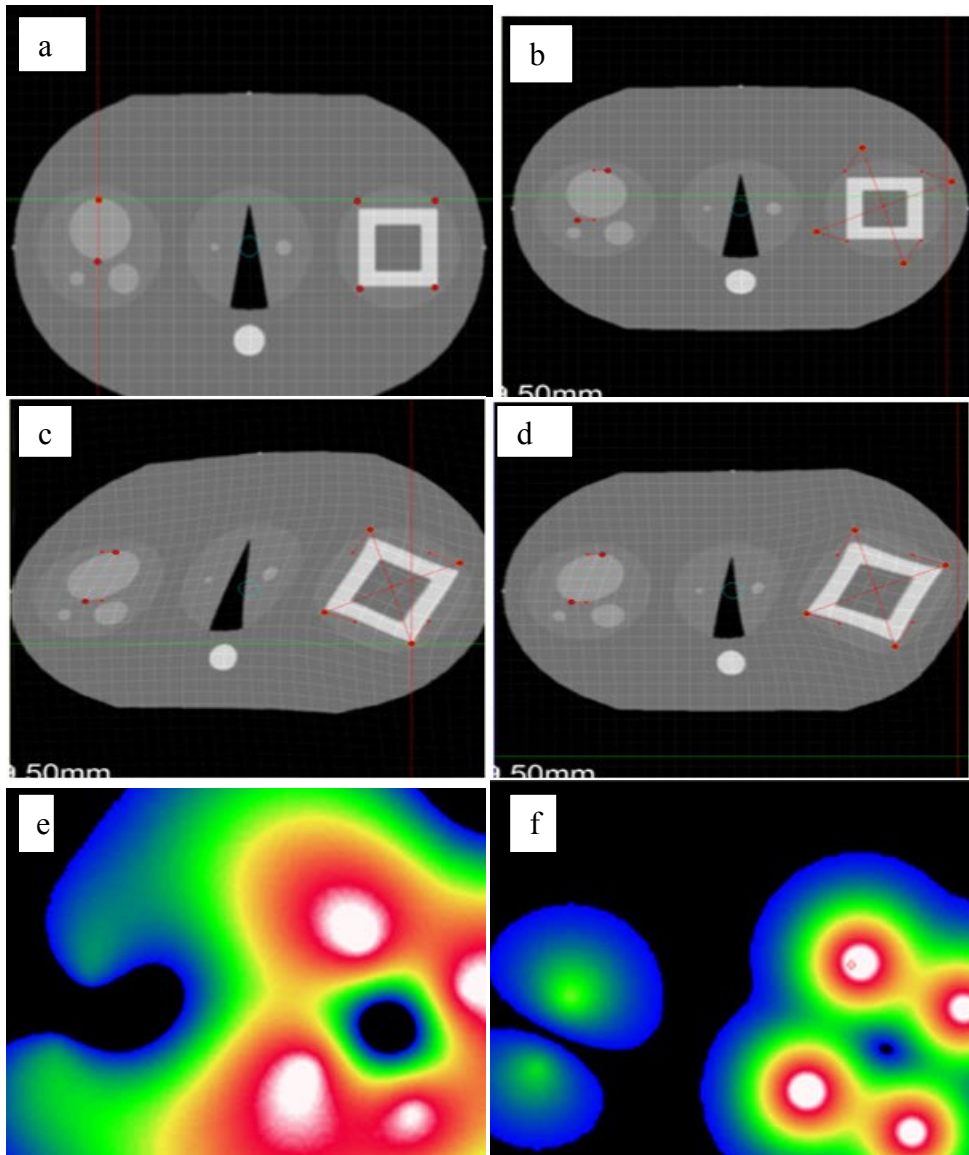
Figure 4.1a: Axial image of quasar phantom with original marker points.

Figure 4.1b   Axial image of quasar phantom with target marker points.

Figure 4.1 c: Axial phantom image after applying the global (TPS) deformation algorithm.

Figure 4.1d: Axial phantom image after applying the local (CSRBF) deformation algorithm.

Figure 4.1e   Magnitude of deformation vector field from TPS on the axial view

Figure 4.1f   Magnitude of deformation vector field from CSRBF on axial view

4.2.5. Clinical rationale and description of applied known deformation in each anatomical site:

a) Prostate: In prostate IGRT, deformation of the prostate due to variations in rectal filling is commonly observed. The need for adaptive radiation therapy for prostate cancer due to inter and intra fraction motion is well documented in the literature [107, 139-148]. We applied a known deformation in the ImSimQA to mimic a distended rectum and introduce rectal gas in the synthetically deformed image. This in turn deforms the prostate as routinely seen in prostate IGRT.

For the CT series of the prostate case (512 × 512 ×74 (median) voxels; 0.86 × 0.86 × 5.0 mm^3) images were acquired on a SIEMENS Sensation 16 CT scanner which included the RT structures used during DIR evaluation. It should be noted all the applied deformation in this study is fully three dimensional although only a particular slice view is shown for illustration. Figure 4.2 below shows axial view of original kvCT image with RT structures, figure 4.3 indicates applied deformation from ImSimQA and figure 4.4 shows the changes in RT structures from the applied ImSimQA DVF when compared to original RT structures.

Gas Pocket
Introduced in Rectum

Applied Local
Deformations
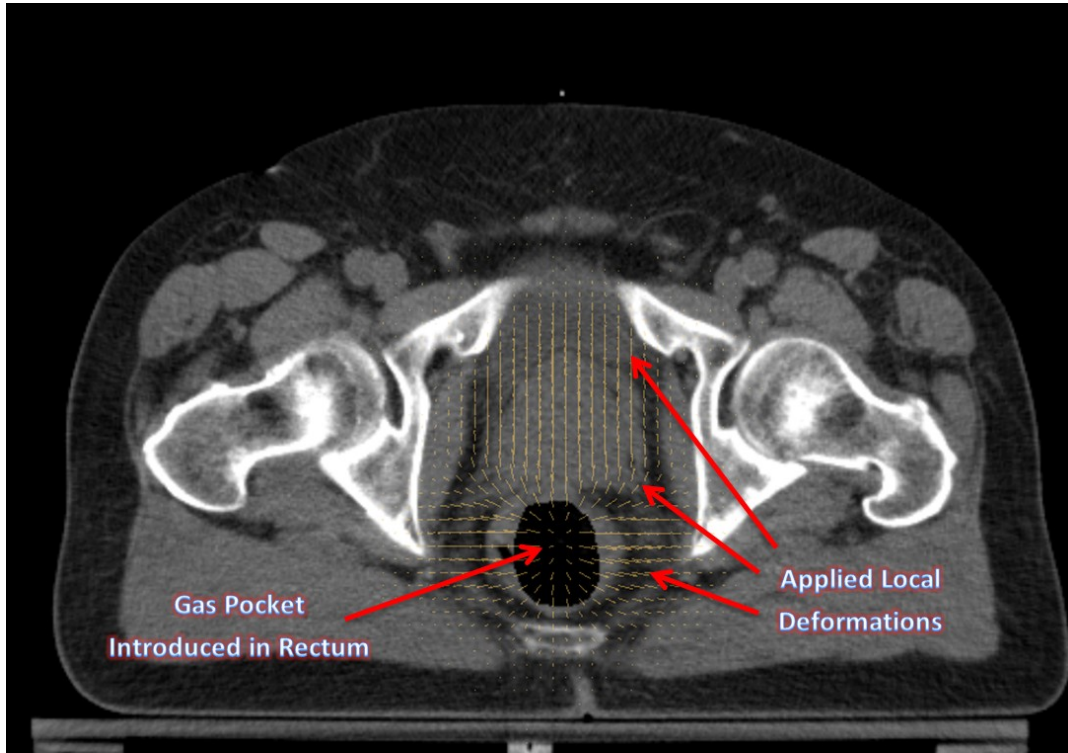
Figure 4.2:   Axial view illustrating the local deformations introduced in the prostate

and rectal region and gas pocket in the rectum.
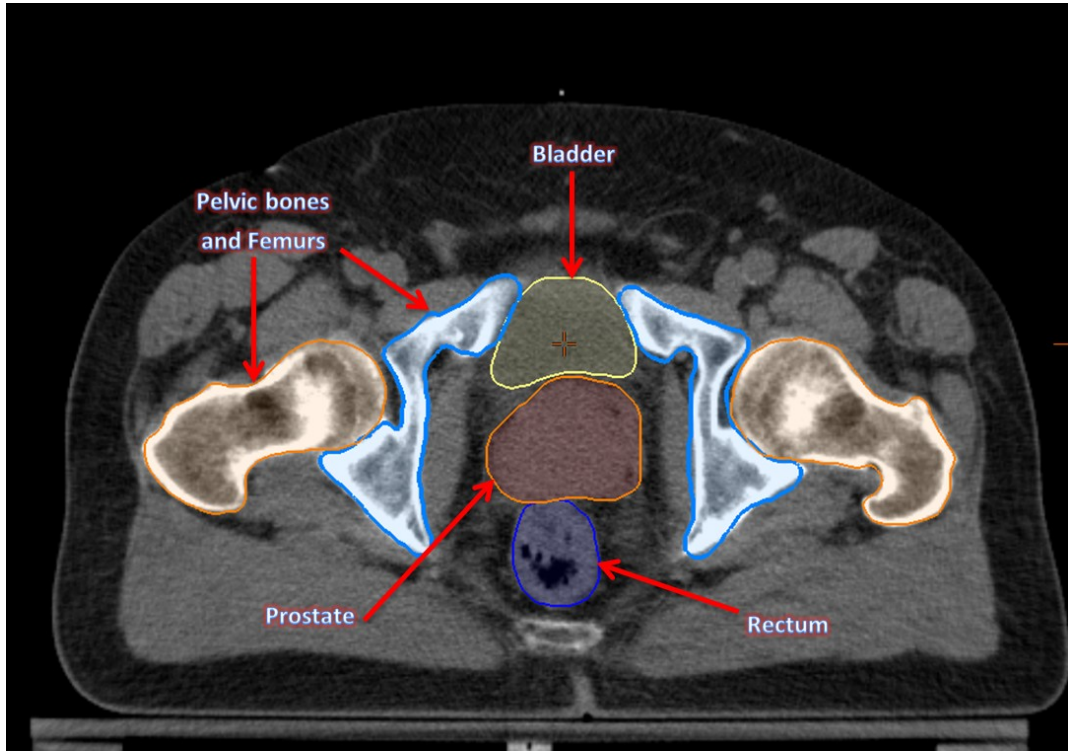
Figure 4.3:   Axial view of the prostate kvCT image with original RT structures namely bladder, prostate, rectum and pelvic bones.
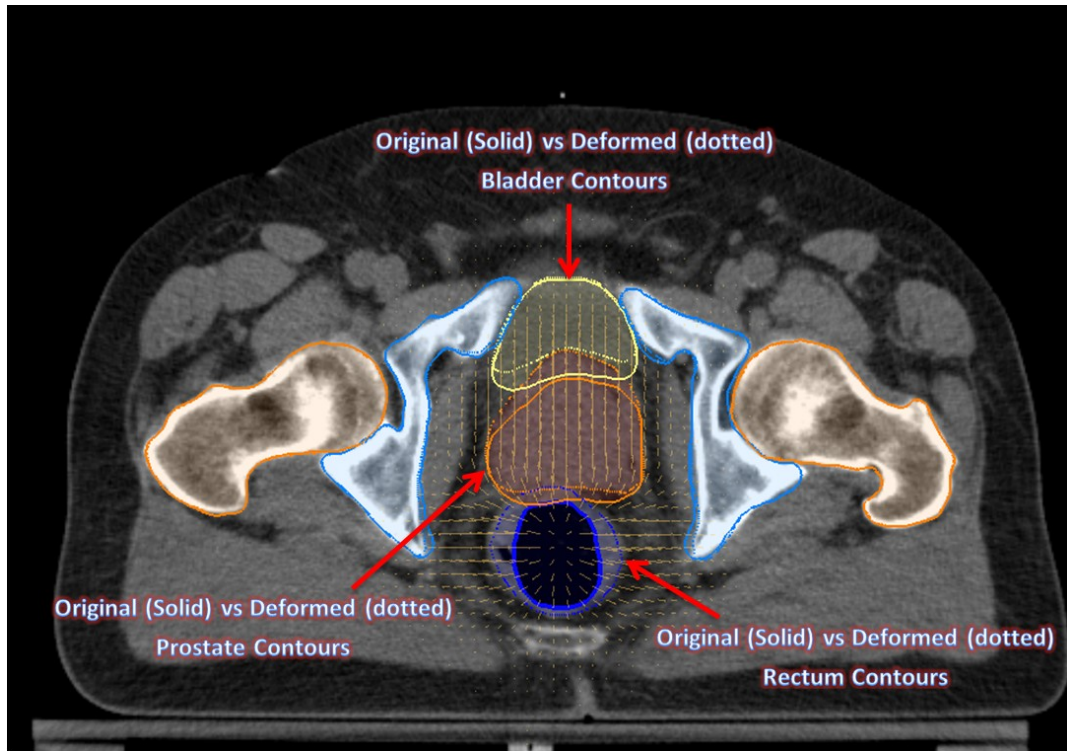
Figure 4.4:   Contour changes in prostate, bladder and rectum from the applied

ImSimQA DVF when compared with original segmentation of these structures. Solid

figures refer to original segmentation done by radiation oncologist on kvCT image and

dotted figures refer to the deformed volumes due to the applied deformation.

b) Head & Neck:

There are significant changes in patient anatomy during the course of Head and Neck

IGRT treatment that are related to decrease of tumor and nodal volumes, patient weight

and alteration in muscle and fat distribution with an average tumor volume reduction of

70% of its initial volume at the end of treatment[149]. Similarly, the parotid glands also

undergo significant volume reduction with an average reduction of 49.8 % and a

translation of 8.1 mm upon completion of treatment [150].

The changes occurring due to patient weight loss could have a significant impact on

Organs at Risk (OAR) like the parotids, since these structures can now be in the high

dose gradient area and tumor could be under dosed. Adaptive radiotherapy has been

advocated to mitigate such volume changes [151-156]. We applied a global deformation

on the ImSimQA software to change the patient neck flexion and studied the deformable

registration algorithm to track these changes as shown in figs 4.5 a, b c. The induced

deformation does not correspond to inter fraction variation that occurs during routine

head and neck IGRT but rather relates to a clinical scenario where the patient was treated

previously with a completely different neck position and is now being evaluated for

radiation therapy in the same area in a different treatment position. The induced

deformation significantly altered the nasal cavity, the alignment of vertebral body, spinal

cord and skull in comparison with the original image.

For the CT series of the head and neck case ($512 \times 512 \times 112$ (median) voxels; $0.94 \times$

0.94×3.0 mm^3) images were acquired on a SIEMENS Sensation 16 CT scanner which

included the complete set of RT planning structures. Figure 4.5 d shows the sagittal view

of original kvCT image with associated RT structures, figure 4.6 shows the deformed

image from ImSimQA after applying the neck flexion and the and the warped RT

structures as result of applied ImSimQA DVF when compared to original RT structures.
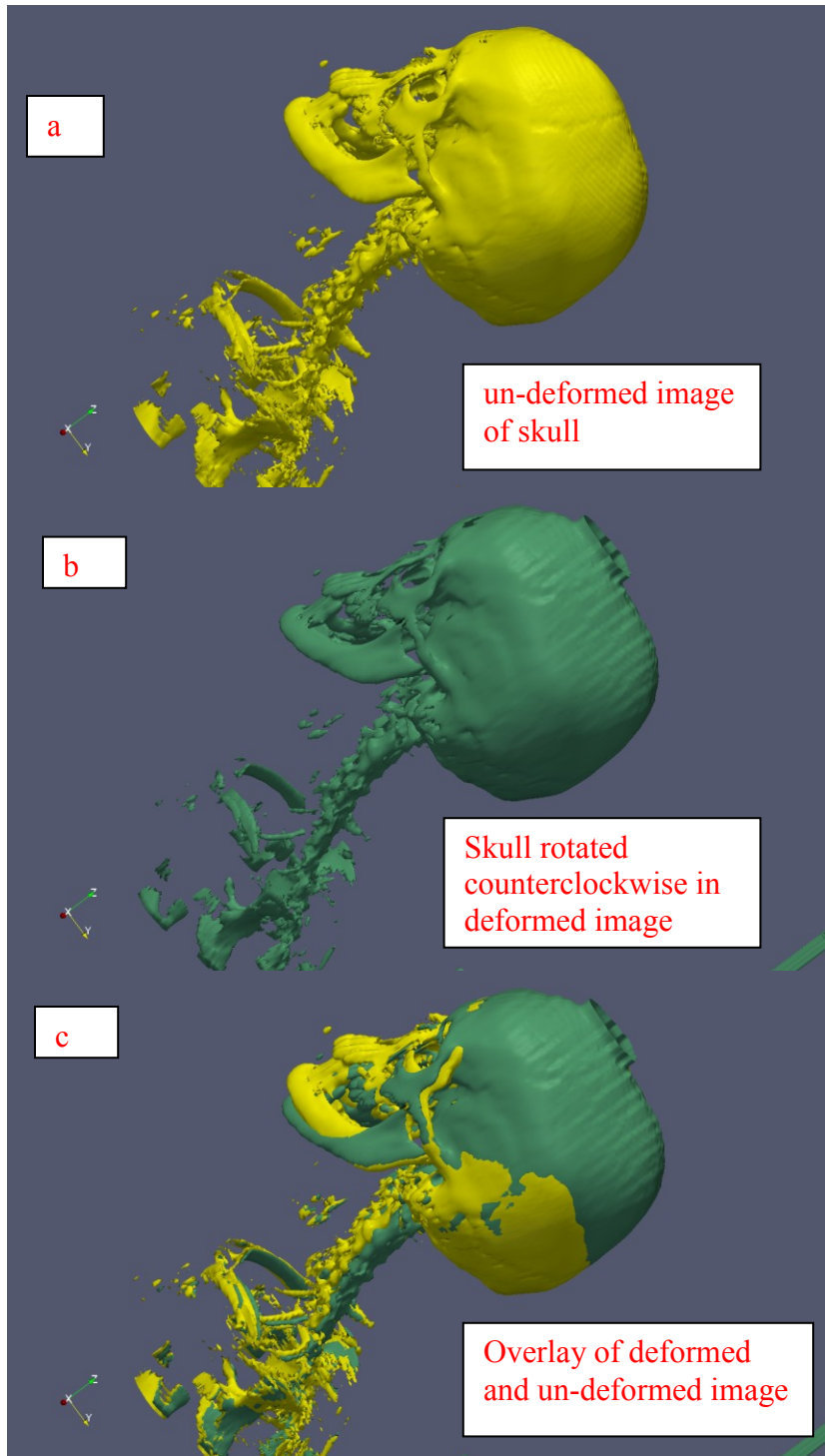
Figure 4.5 a,b,c. Original image of skull, rotated image of skull and overlay of original and rotated skull respectively demonstrating the applied neck flexion for validating DIR
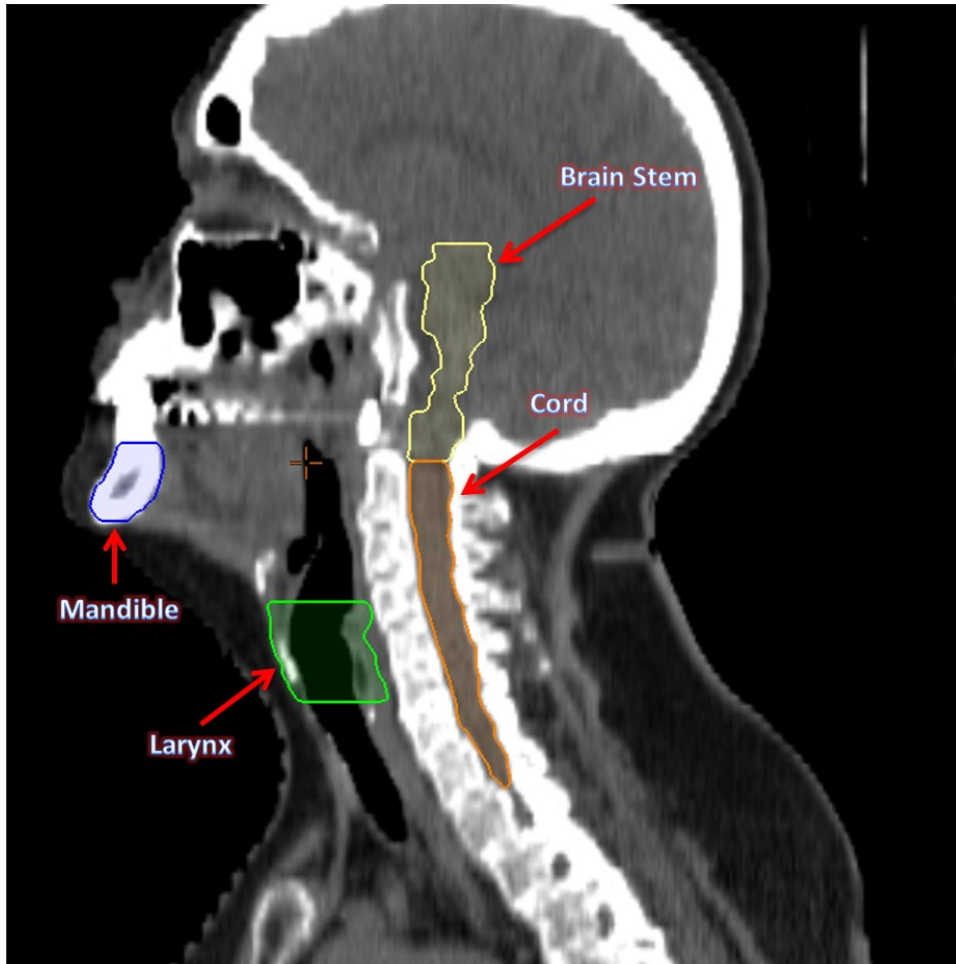
Figure 4.5 d: Sagittal view of the original head & neck CT image with the associated RT structures brain stem, cord, larynx and mandible.
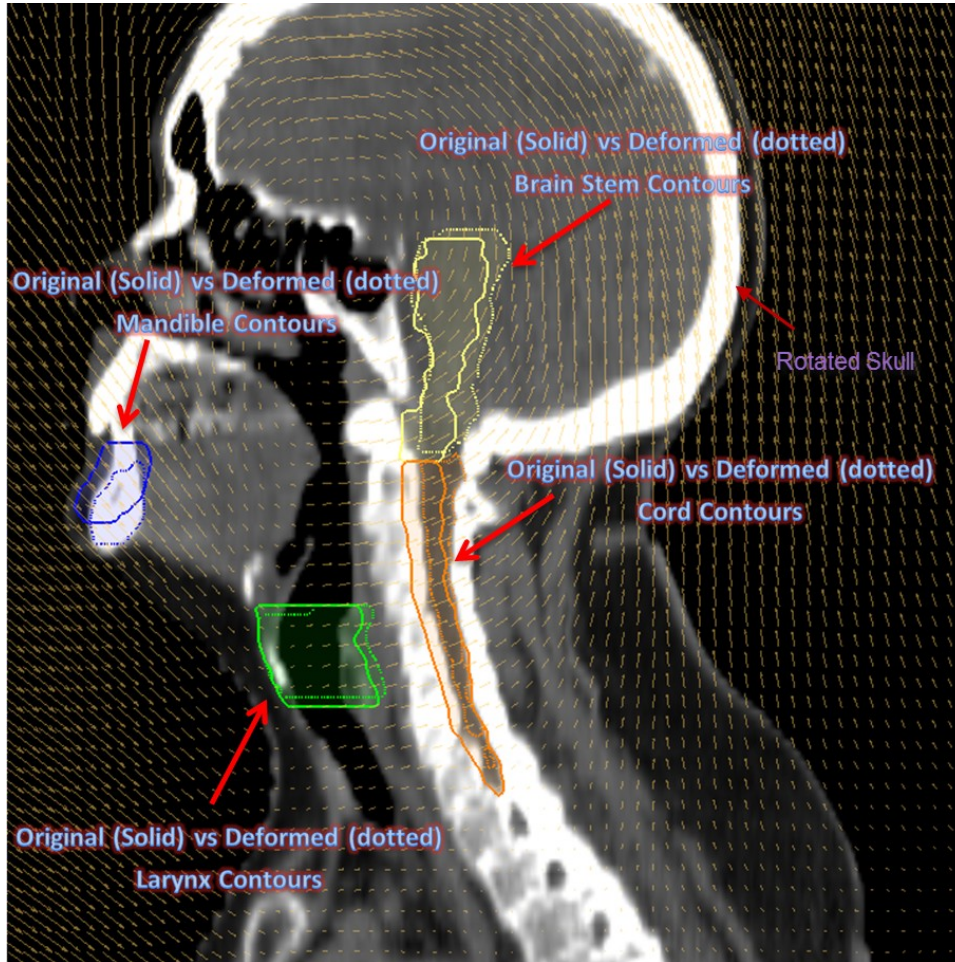
Figure 4.6:Sagittal view of the head and neck image from the applied global deformation mimicking a large neck flexion. The skull is rotated counter clockwise. The deformed RT structures due to the applied deformation are displayed as dotted figures.

c) Lung:

Respiratory motion of the order of 1 cm has been observed for tumors close to the diaphragm [157, 158]. We introduced a deformation in ImSimQA to mimic dataset from inhale and exhale breathing phases of 4DCT. Deformable registration attempted to track this worst case scenario.

In addition to the lung volume changes, we introduce contrast changes in the image to assess the quality of DIR during variable contrast enhancement. The original kvCT

images have contrast in the scan, while in the synthetically deformed images from ImSimQA the contrast has been taken out. This example was chosen to highlight the limitations of diffeomorphic demons algorithm when the intensities of identical tissues and organs are different in the two images.

For the CT series of the lung case (512 × 512 ×123 (median) voxels; 0.98 × 0.98 × 3.0 mm^3) images were acquired on a SIEMENS Sensation 64 unit which included the complete set of RT planning structures.

Figures 4.7, and 4.8, below show the coronal view of original kvCT image with contrast, and the coronal image from ImSimQA without contrast showing diaphragm motion and lung volume changes.
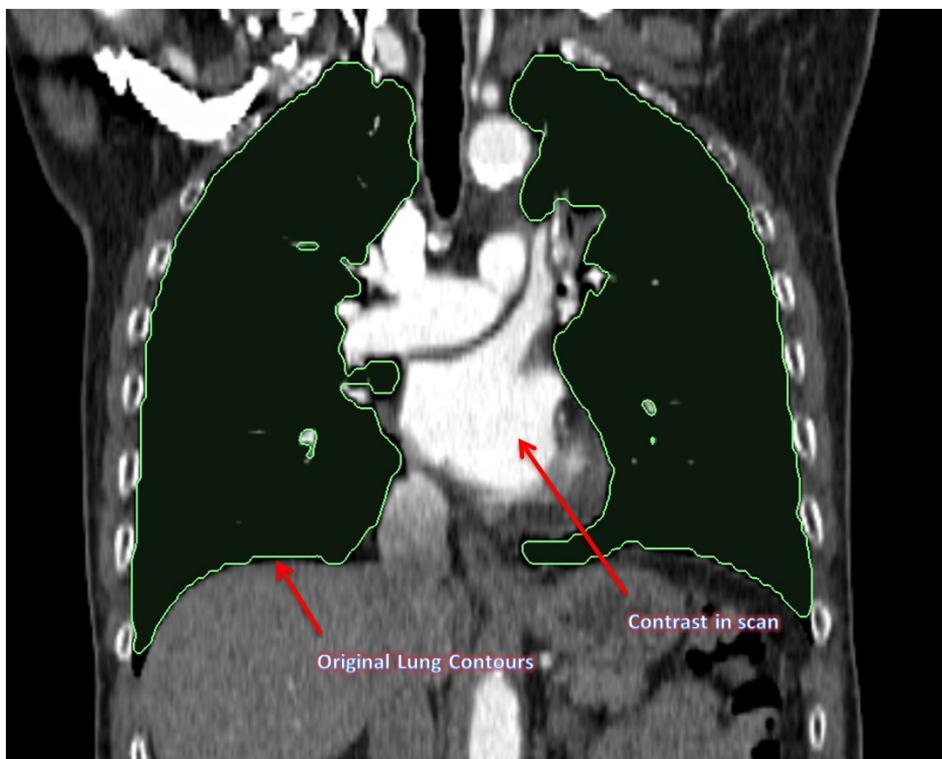
Figure 4.7:   Coronal view of the original lung kvCT image showing the lung contours and contrast in scan.
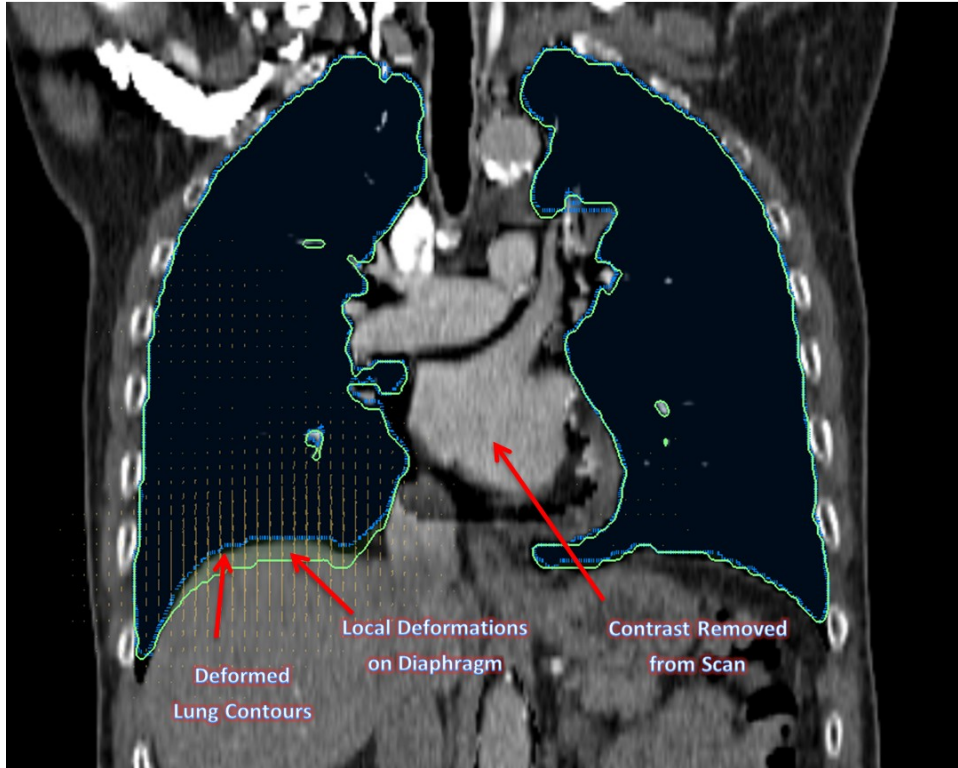
Figure 4.8:   Coronal view of the same lung kvCT image illustrating the applied local deformations on the diaphragm and the changes in lung contour associated with that. This mimics an inhale and exhale breathing phase of respiratory cycle. The contrast is also taken out of this image to validate DIR during variable contrast enhancement.

4.2.6. Deformable Image registration

The Insight Segmentation and Registration Toolkit (ITK) was used to perform (a) free-form parametric deformable registration using a cubic B-Splines [159] and (b) non-parametric registration using diffeomorphic demons. The DIR and all the analysis tools described in this work were integrated into open source platform 3D Slicer [17]via custom developed modules. We used the Mattes Mutual Information (MI) metric [160] with an evolutionary algorithm followed by gradient descent optimizer for optimization [161]. The images are initialized to line up their centers. The evolutionary optimizer

works by searching for the minimum metric value by generating random samples about the current location in parametric space and iteratively growing or shrinking parameters of previous iteration to hone in on the optimum. This process is fairly resilient to noise. After this, a regular step gradient descent optimization is performed, with the transformation parameters incremented in the direction of gradient. The increment is determined in a bipartition manner until it converges on the minimum of the metric. Registration is performed in 3 phases: rigid, followed by affine, followed by deformable registration. A control point spacing of 60 (pixels), 50 maximum iterations and 10% of the image pixels for metric evaluation were used in this study during B-Spline registration to achieve optimal balance between quality of DIR and run time of registration. Registration was completed in 15 minutes on a Windows 7, 64 bit operating system running on Intel quad core 2.8GHz processor with 8GB RAM.

The same manually deformed images are also registered using diffeomorphic demons [162]to provide a smooth and invertible transformation. In general, for non-parametric registration methods such as diffeomorphic demons used in this study, the registration is expressed as an objective function comprising of an image term and regularization term. The image term may be the difference in intensities of two voxels (optical flow as in demons) while the regularization term keeps the deformation field well-behaved. This is usually done by smoothing the deformation field with a Gaussian at each iteration to ensure that it is well-behaved.

Details on the implementation of this algorithm and its advantages over Thirion's demons algorithm [93] are discussed in literature[162]. A diffeomorphism by definition preserves the topology of objects in the image. In other words, it prevents folding of

structures onto itself. Therefore the jacobian is always non-negative. This is a good property to have for medical image registration. The second important property of diffeomorphism is that they are guaranteed invertible by definition.

Registration is typically faster and takes about 10 minutes when using diffeomorphic demons algorithm using the same hardware platform as previously described.

4.2.7. Evaluation Scheme:

I. Deformation Field

a. Inverse Consistency:

For each anatomical site the original kvCT and the synthetically deformed image from ImSimQA were used to test inverse consistency of B-Splines and diffeomorphic demons algorithms. The two images are registered separately both in the forward and inverse directions. A perfect inverse consistent algorithm in theory should give a deformation map which is a true inverse of one another. However in reality this rarely occurs because most algorithms do not produce true inverse deformation maps since deformable registration is inherently degenerative and multiple solutions may exist for a given image matching problem.

We use the concept of compositive accumulation to quantify the inverse consistency error. The details of compositive accumulation as discussed in [129, 163] are summarized below.

The concept of compositive accumulation is used to quantify the inverse consistency error. The warping by a deformation vector field D is associated with its corresponding transformation operation Δ, such that $\Delta \triangleq Id + D$, or $\Delta(x) \triangleq x + D(x)$, where Id is the identity transformation such that $I\ d(x) = x$. Mathematically given two images A and B

during DIR, the objective is to find a deformation vector field D such that warping of

image B by D is close to original image A or A = B o Δ.

 If D_1 and D_2 are two deformation fields, a single warping by compositive addition of D_1

and D_2 is equivalent to successive deformation of an image by D_1 and then followed by

D_2.

The warping by a field D is equivalent to the composition with its corresponding

transformation Δ. One can then use the composition of function in order to replace

successive warpings (*i.e.* by different displacement fields) with a single warping (*i.e.* by

an equivalent displacement field). Mathematically, this compositive operation denoted as

$\oplus$, is defined as follows

$D_1 \oplus D_2 = \Delta_1 \circ \Delta_2 - \text{Id.}$

By construction, the deformation operation linked to the displacement field $D_1 \oplus D_2$ is

therefore Δ_1 o Δ_2. The operation $\oplus$ has some interesting and useful properties. First, the

neutral is of course obtained with the null displacement field, *i.e.* $D \oplus 0 = 0 \oplus D = D$. It

can be shown that the associative relations $(D_1 \oplus D_2) \oplus D_3 = D_1 \oplus (D_2 \oplus D_3) = D_1 \oplus$

$D_2 \oplus D_3$ for three displacement fields D_1, D_2 and D_3.

The composition of two deformation fields makes use of the operation o. This means

$D_1 \oplus D_2 = D2 + D1 \; o \, D2$, meaning that that $D_1 \oplus D_2$ is equivalent to summing deformation field D_2 with the field D_1 warped by D_2 [163] . A simple proof is presented below.

$D_1 \oplus D_2 = \Delta_1 \; o \; \Delta_2 - Id$. By construction the deformation operation linked to $D_1 \oplus D_2$ is $\Delta_1 \; o \; \Delta_2$.

Since $D1 \; o \, D2 = D1 \; o \, \Delta2$, and $D = \Delta - Id$, one can easily see that:

$D2 + D1 \; o \, D2 = D2 + D1 \; o \, \Delta2$

$= \Delta2 - Id + \Delta1 \; o \; \Delta2 - Id \; o \; \Delta2$

$= \Delta1 \; o \; \Delta2 - Id$

$= D1 \oplus D2.$

Further the compositive addition operation $\oplus$ is associative for three deformation fields

D_1, D_2 and D_3 meaning $(D_1 \oplus D_2) \oplus D_3 = D_1 \oplus (D_2 \oplus D_3) = D_1 \oplus D_2 \oplus D_3$

For the warp, we use a linear interpolator, i.e. we add the right field to the interpolated

left field for that pixel as the resulting point x will not land exactly in the grid.

For purposes of inverse consistency, if D_1 and D_2 are deformation fields from forward and

inverse registration, the compositive accumulation of forward and inverse deformation

fields will yield the inverse consistency error (ICE). If the deformation maps are true

inverses, this composition will yield zero. The L2 norm (absolute magnitude) of the

composed fields is used to quantify the magnitude of inverse consistency error.

Further, ICE between the DVF arising from DIR and the synthetic DVF generated from

ImSimQA software which was used to produce clinically relevant organ deformation was

evaluated. The ImSimQA can also output inverse DVF of the applied deformation. This

DVF was compared with the DVF generated from the inverse registration process where

the roles of source and target images were switched. A compositive accumulation of the

ImSimQA DVF and the DVF from registration (B-Spline and diffeomorphic demons)

was done to quantify the ICE between DVFs. If the results of DIR produced a DVF

which is the exact inverse of applied synthetic DVF in ImSimQA, then this composition

of DVFs will be zero. The L2 norm of the composed DVFs is computed to quantify the

ICE between DVFs.

b. Determinant of jacobian of the deformation Field:

The jacobian of the deformation field gives information about the image transformation

consistency[134, 164]. The jacobian is a matrix given by the first partial derivatives of

the transformation with $Ji, j = \frac{\partial \Delta i}{\partial x j} = \partial i j + \frac{\partial D i}{\partial x j}$,

where ∂ij is kronecker delta ($\partial ij = 1 \ if \ i = j$, $0 \ otherwise$) and D_i is the ith component of deformation field.

We computed the determinant of the jacobian of the deformation field in this study to validate the physical behavior of deformation. A negative determinant indicates singularities in the field and corresponds to a physically unrealistic organ deformation. A determinant greater than 1 indicates expansion at that location while a value less than 1 indicates contractions.

c. Mean Harmonic Energy of the Deformation Field:

The harmonic energy captures the non-linearity of the warp i.e. deviation from an affine transformation. The mean harmonic energy is defined as the frobenius norm of the jacobian and is inversely proportional to how smoothness of the deformation field [135]. The harmonic energy at a voxel can be defined based on the first order partial derivatives of the deformation field as follows:

$$HE \ (D) = \frac{1}{2} \int \sum_{i=1}^{n} \sum_{j=1}^{n} \left[\left(\frac{\partial di(x)}{\partial xj} \right] \right)^2 dU$$

where U is the domain of the deformation field.

II. Anatomical correspondence:

In radiotherapy clinical applications the accuracy of tumor and organ at risk (OAR) structures is of paramount importance. Ultimately the changes in the shape and volume of these structures and consequently the dose received by them dictate the need for adaptive radiation therapy.

We use the Dice similarity coefficient, Hausdorff distance and average surface distance as three metrics to evaluate the accuracy of tumor and OAR for each anatomical site

before and after DIR. These metrics have been previously used to compare segmentations in radiotherapy applications and are described below [96, 165-167]. The ImSimQA DVF was used to warp the original RT structures in addition to CT images. The registration DVF from both algorithms was then applied to these RT structures. If the results of DIR were perfect then the RT structures before and after DIR would be the same. The degree of mismatch indicates the quality of DIR from an anatomical correspondence perspective.

a. **Dice Similarity Coefficient:**

The metric computes the number of pixels that overlap between the two volumes and normalizes it by the half the sum of the number of non-zero pixels in the two volumes. The result is a value between 0 (no overlap) and 1 (perfect overlap) as shown in fig 4.9

$$\alpha = \frac{2 \ X \ |A \cap B|}{|A| + |B|}$$

where A is the gold standard segmentation which in our case refers to segmentation in kvCT fixed image, B is the segmentation mapped from the deformably registered image. The metric is symmetric and is sensitive to both differences in scale and position. While volume overlap is a good indicator of mismatch, it is a poor indicator of shape since is not a measure of distance and hence the following metrics are also evaluated to assess the overall accuracy.

b. **Hausdorff distance**:

The Hausdorff distance [168] is defined as the maximum of the closest distance between two volumes where the closest distance is computed for each vertex of the two volumes. The hausdorff distance H(A,B) between 2 sets of points A = {a1, .., am} and B = {b1, .., bm} is given by

H(A,B) = *max*(h(A,B), h(B,A))

where $h(A,B) = max_{a \in A} min_{b \in B} || a\text{-}b ||$

$h(A,B)$ is the directed hausdorff distance from A to B, which unlike the hausdorff distance is not symmetric.

$h(A,B)$ identifies the point a ∈ A that is farthest from any point in B, and then measures the distance of A to its nearest neighbor in B. The point sets A, B in our case, are the centers of the non-zero pixels in the gold standard (original kvCT) and deformably registered segmentations. Thus, the hausdorff distance is a measure of the maximum distance between two surfaces as shown in fig 4.9 a. It obeys all four properties of metric spaces and distance functions.

– Identity: $H(A,A) = 0$

– Positive semi-definiteness: $H(A,B) = 0$

– Symmetricity: $H(A,B) = H(B,A)$

– Triangle inequality: $H(A,C) = H(A,B) + H(A,C)$

The metric is very sensitive to outliers since the most mismatched point is the sole determining criteria of the distance. Some authors use 95% Hausdorff distance (95%HD) as the outliers are rejected in 95%HD.
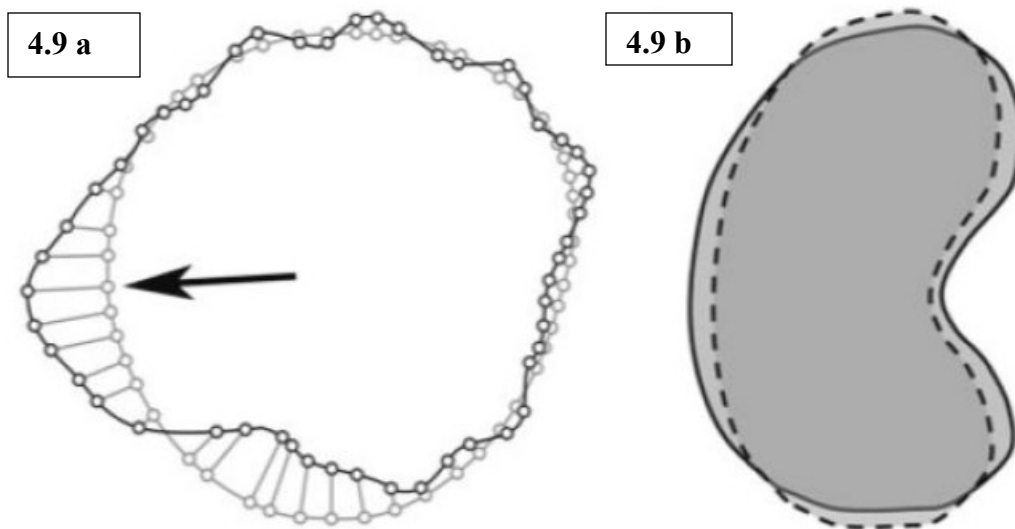
Fig 4.9a Hausdorff Distance is the maximum perpendicular distance between closest

points from two contours of registered images. *Black line* represents an external contour

from one image and *gray line* represents an external contour from another registered

image. *Small circles* represent corresponding closest points between each contour.

Hausdorff distance represents the distance between *small circles* at *black arrow*. **b)** Dice

coefficient similarity (DSC) is an index of overlap of two different volumes. *Solid black*

line represents a volume from one image and *dotted black line* represents a volume from

another image after registration. DSC is a value between 0 (no overlap) and 1 (perfect

overlap). (Diagram above adapted from Reference [169])

c. **Average Surface Distance**:

This metric mitigates the outlier problem exhibited by the Hausdorff distance. The metric

is the average of the absolute distance from each surface pixel in one image to its closest

point on the other image. This metric is not symmetric, although it satisfies the positive

semi-definite and identity properties of distance metrics.

$$M(A, B) = \frac{\sum_{a \in A} min_{b \in B} ||a-b||}{|A|}$$

III. Image Characteristics:

a.   Mean Square Error:

We used metric Mean Squared Error (MSE) to define the extent of mismatch between the

original image A and the deformably registered image B which is the normalized square

difference between the two images A and B [170] . If f *(n)* and g *(n)* represent the value

(intensity) of an image pixel at location **n**. The MSE between

f *(n)* and g *(n)* is defined as:

MSE $= 1/N \Sigma_n$ {f *(n)* - g *(n)*}^{2},

where N is the total number of pixel locations in f *(n)* or g *(n)*.

For a perfect image match between images A and B the MSE error is zero.

The error is reported as Root MSE in this paper where Root MSE $= \sqrt{MSE}$

4.3 Results:

The results of the accuracy of DIR evaluation in three clinical cases namely prostate,

head & neck and lung are presented below

4.3.1 Inverse Consistency Error:

Table 4.1 below lists Inverse Consistency Error (ICE) between various DVFs used in

DIR and ICE between applied ImSimQA DVF and DVF from DIR for the 3 anatomical

sites studied.

Inverse Consistency Error (ICE) comparison
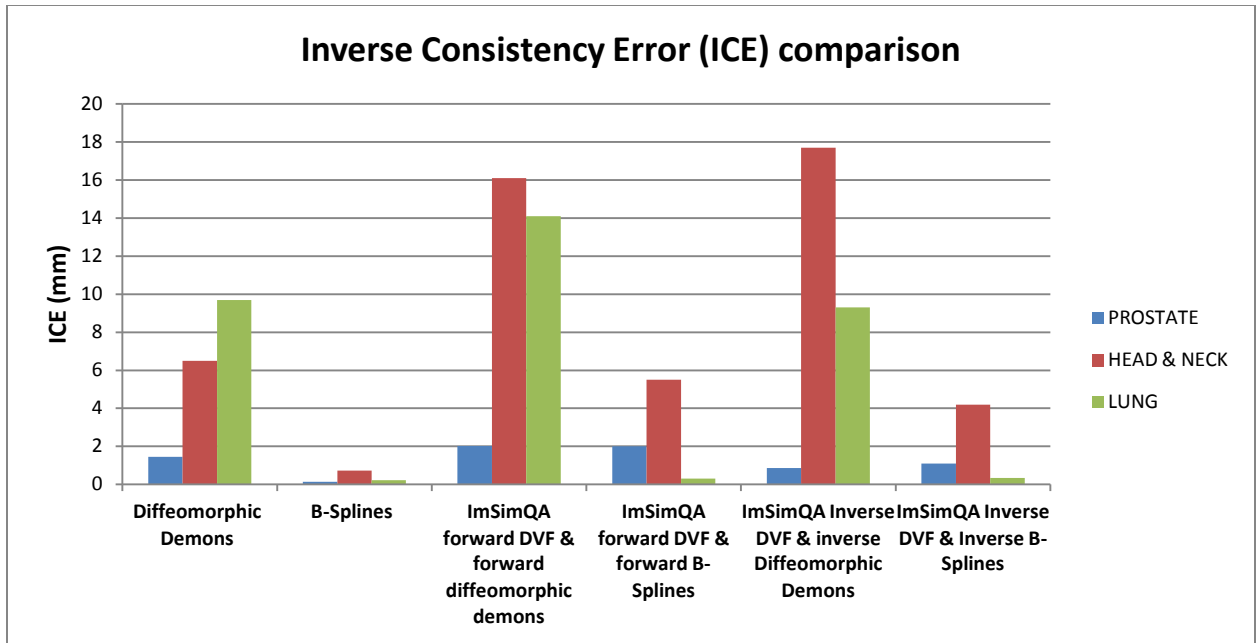
Table 4.1. Inverse consistency error of various DVFs and in comparison with ImSimQA DVF

As an example for the prostate case, the DVF from diffeomorphic demons algorithm is overlaid on the original kvCT image for forward, inverse and compositive addition of forward and inverse DVFs is shown in figures 4.10, 4.11 and 4.12 respectively. Figure 4.13 relates to the quantitative ICE described in Table4.1 (1.45 mm) for diffeomorphic demons algorithm for the prostate case.

Figure 4.10:   Forward diffeomorphic demons DVF from the registration overlaid on the original prostate kvCT image illustrating the local changes due to the DVF. The field vectors are pointing outward.

Figure 4.11:   Inverse diffeomorphic demons DVF when the role of source and target images were switched from previous example, overlaid on the original kvCT image. The field vectors are pointing inward.
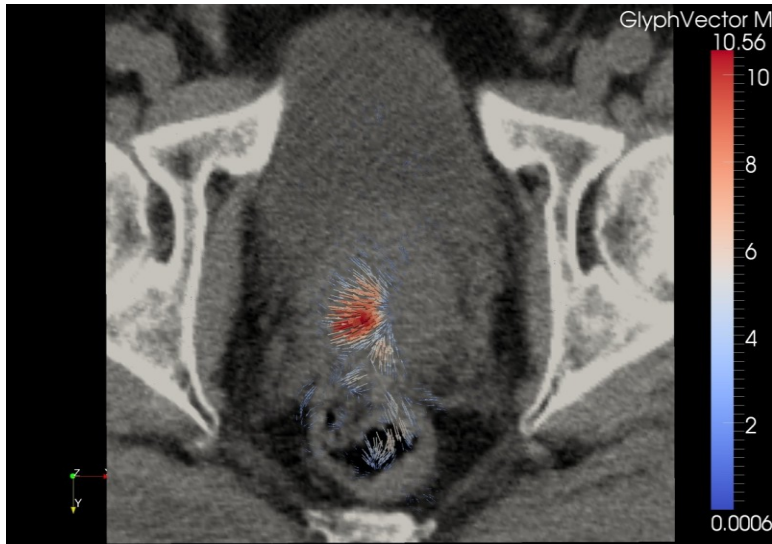
Figure 4.12:   Compositive addition of forward and inverse demons DVF overlaid on the original kvCT image. If the algorithm was truly inverse consistent this composition would yield zero. The magnitude of this compositive addition is 1.45 mm in this example as discussed in Table 4.1.

4.3.2 **MSE, Jacobian and Harmonic energy of DVF**

Table 4.2 below lists Root Mean Square Error, Minimum jacobian and Harmonic Energy of deformation field for registration algorithms both in forward and inverse directions for all 3 anatomical sites:

	PROSTATE				HEAD & NECK				LUNG			
Algorithm	RMSE Before DIR	RMSE After DIR	Harmonic Energy	Minimum Jacobian	RMSE Before DIR	RMSE After DIR	Harmonic Energy	Minimum Jacobian	RMSE Before DIR	RMSE After DIR	Harmonic Energy	Minimum Jacobian
Diffeomorphic Demons Forward	25.9	11.8	0.05	0.12	187	51.9	0.32	0.0005	91.33	853.6	0.53	N/A
Diffeomorphic	25.9	11.6	0.09	0.003	187	66.1	0.43	0.003	91.33	223.3	0.19	N/A

Demons Inverse												
B-Splines Forward	25.9	11.03	0.0006	0.88	187	80.8	0.014	0.53	91.33	68.1	0.0005	0.82
B-Splines Inverse	25.9	10.9	0.0005	0.87	187	51.2	0.005	0.58	91.33	69.2	0.0004	0.87

Table 4.2 Root Mean Square Error, Minimum jacobian and Harmonic Energy of deformation field for registration algorithms both in forward and inverse directions for prostate, head and neck and lung anatomical sites:

4.3.3. Accuracy of RT Structures

Tables 4.3, below evaluates the accuracy of RT structures for the prostate case, after DIR when compared to original segmentation done by the radiation oncologist in kvCT (used as the gold standard) for both diffeomorphic demons and B-Splines algorithms. This was done by applying the registration DVF to RT structures deformed by ImSim DVF. All the evaluation is done on the original fixed image (kvCT) coordinate system.

Table 4.3 Accuracy of RT structures after DIR for Prostate			
Algorithm: Diffeomorphic Demons			
Anatomy	**Dice Similarity Coefficient**	**Hausdorff Distance (mm)**	**Average Surface Distance (mm)**
Prostate	0.85	15.9	2.3
Bladder	0.93	11.1	0.78
Rectum	0.79	12.6	1.2
Femoral Heads	0.99	1.7	0.1

Mean values	0.89	10.3	1.1

Algorithm: B-Splines			
Anatomy	**Dice Similarity Coefficient**	**Hausdorff Distance (mm)**	**Average Surface Distance (mm)**
Prostate	0.91	9.8	1.03
Bladder	0.95	7.7	0.42
Rectum	0.89	10.3	0.8
Femoral Heads	0.99	1.2	0.1
Mean values	**0.94**	**7.3**	**0.59**

Table 4.4 below evaluates the accuracy of RT structures for head & neck case. Although by visually inspecting the images the registration seems to agree qualitatively (the skull and vertebral bodies matched after DIR) the contour comparison statistics are not clinically acceptable especially for organ at risk structures. This is primarily due to large neck flexion introduced as a known deformation in ImSimQA. Based on this analysis, auto registration of images when there is significant neck flexion should be evaluated with caution especially when there is a re-treatment being considered.

Table 4.4 Accuracy of RT structures after DIR for Head & Neck			
Algorithm: Diffeomorphic Demons			
Anatomy	**Dice Similarity Coefficient**	**Hausdorrf Distance(mm)**	**Average Surface**

			Distance(mm)
PTV Primary	0.85	8.9	1.8
PTV Secondary	0.86	9.1	1.5
Spinal Cord	0.51	12.2	2.4
Right Parotid	0.84	4.7	0.8
Left Parotid	0.77	6.6	1.4
Brainstem	0.64	11.9	2.7
Mandible	0.63	40.5	4.6
Larynx	0.86	5.7	1.1
Right Eye	0.74	7.5	1.8
Left Eye	0.79	4.9	1.3
Mean values	**0.75**	**11.2**	**1.9**

Algorithm: B-Splines

Anatomy	Dice Similarity Coefficient	Hausdorrf Distance(mm)	Average Surface Distance(mm)
PTV Primary	0.88	8.2	1.5
PTV Secondary	0.87	8.6	1.4
Spinal Cord	0.52	10.5	2.2
Right Parotid	0.84	3.7	0.8
Left Parotid	0.79	5.9	1.3
Brainstem	0.52	9.7	3.9

Mandible	0.7	13.6	1.9
Larynx	0.86	5.7	1.1
Right Eye	0.59	8.7	2.6
Left Eye	0.83	4.7	0.93
Mean values	**0.74**	**7.9**	**1.7**

Table 4.5 below computes the accuracy of RT structures for the lung example involving variable contrast enhancement. The diffeomorphic demons algorithm produced improper displacement estimation in this case because of the difference in intensities of two images due to the variable contrast enhancement. The mismatch in RT structures is particularly relevant in heart, lung, bronchial tree and vertebral bodies as the hausdorff distance exceeds 10mm and the average surface distance is as large as 11.8 mm for heart. This is because diffeomorphic demons algorithm tries to match structures of same intensity which in our case does not correspond to identical anatomical structures due to the differences in contrast between two images.

Table 4.5. Accuracy of RT structures after DIR for Lung			
Algorithm: Diffeomorphic Demons			
Anatomy	Dice Similarity Coefficient	Hausdorff Distance (mm)	Average Surface Distance (mm)
PTV	0.83	8.8	1.4
Cord	0.95	4.6	0.2

Anatomy	Dice Similarity Coefficient	Hausdorff Distance (mm)	Average Surface Distance (mm)
Heart	0.37	56.7	11.8
Lung	0.99	17.7	0.4
Bronchial Tree	0.49	18	4.2
Trachea	0.91	15	1.3
Vertebral Body	0.92	10.3	0.2
Mean Value	**0.78**	**19.3**	**2.8**

Algorithm: B-Splines

Anatomy	Dice Similarity Coefficient	Hausdorff Distance (mm)	Average Surface Distance (mm)
PTV	0.88	6.9	2.1
Cord	0.94	8.3	0.3
Heart	0.99	4.1	0.2
Lung	0.99	6.3	0.3
Bronchial Tree	0.96	1.4	0.1
Trachea	0.97	1.4	0.2
Vertebral Body	0.93	10.3	0.2
Mean Value	**0.95**	**5.5**	**0.4**

4.4 Discussion:

Deformable image registration will continue to be a key component in the implementation of adaptive radiotherapy with the ultimate goal of dose tracking and dose accumulation based on daily image feedback [126, 127, 146]. Verification of DIR accuracy is an important task in implementation of adaptive radiotherapy. We have presented a framework to test and evaluate the accuracy of DIR using known deformations which are clinically relevant that can be applied to any CT images. The accuracy of DIR was evaluated by comparing anatomical correspondence, physical characteristics of deformation field, and image characteristics. The relative merits of these methods in the final decision making on DIR accuracy for the anatomical sites studied is discussed below.

Prostate:

Our results on prostate case indicate that the ICE was comparable to both algorithms. Also, the MSE values were very similar for both methods. However the B-Splines algorithm had significantly better anatomical correspondence for rectum and prostate than diffeomorphic demons algorithm. So considering the anatomical correspondence of the RT structures one can conclude that the B-Splines algorithm performed better. In this example the MSE and ICE evaluation parameters provide no criteria to determine which method performs better.

Head and Neck:

For the head and neck case, the ICE was much larger for the demons algorithm (6.5 mm) as compared to B-Splines (0.7 mm). The MSE was comparable for both algorithms. However, since the induced neck flexion was large, neither algorithm had a desired

anatomical correspondence for PTV and organs at risk that could make the result clinically acceptable. Similar to the prostate case, this example also indicates that considering only the ICE and MSE methods could lead to false positive conclusions.

Lung:

In the lung case B-Splines algorithm accurately estimated the deformations between images with variable contrast and was clearly superior in all the metrics that were evaluated. The demons algorithm had gross errors in areas of contrast differences between images. This was the only example where all metrics used for the DIR evaluation were in full agreement on the decision making of the DIR algorithm performance.

Verification of absolute accuracy of DIR is a challenging problem as each of the methods studied has its own drawback. In the case of inverse consistency, a zero value for ICE is a necessary but not sufficient condition for an accurate algorithm as errors in one DVF may cancel out errors in the other to yield a net zero value during composition of two deformation maps.

The determinant of the jacobian and the harmonic energy of the deformation field were used to classify the registration strategies based on invertibility and smoothness although they do not give information on the accuracy of DIR. However, one needs to confirm the non-negative value of jacobian of the deformation field to ensure that a given DVF is physically achievable by an organ [133, 134, 163]. The harmonic energy captures the non-linearity of the warp.

The harmonic energy of B-Splines was consistently lower in all our examples and was generally small since it was physically constrained. The parameters that control it are the

maximum deviation the user allows (step length) during registration and the number of nodes specified in the command line. The harmonic energy of the diffeomorphic demons is controlled by the parameter "sigma" used to smooth the deformation field. Increasing sigma will reduce the harmonic energy but will come at the expense of reduced registration accuracy. The harmonic energy from B-Splines registration was consistently lower on all our cases indicating that the deformation field from B-Splines was smoother. An abnormally large value of harmonic energy may indicate problems with DVF as was the case for demons algorithm during registration of images with variable contrast enhancement. However, there is nothing in the B-Splines algorithm that prevents negative jacobians which is physically unrealistic. Deformation fields from diffeomorphic demons on the other hand are guaranteed invertible and the jacobian is always non-negative.

The image quality of a deformed image set and product of a DIR method is significant for the daily clinical routine when used to define OARs and target volumes. However, the use of the MSE as image quality metric is proven to be inadequate for drawing a useful and consistent conclusion. A small value of MSE indicates an overall good accuracy in the entire image voxel space but does not guarantee good accuracy of DVF inside the organs. Another option to address this issue is to make a selective MSE calculation within regions of interest (e.g. OARs) and investigating other image quality metrics. If unsure about the DIR image outcome, the images should be reviewed by a clinical expert. Ultimately the accuracy of DIR also needs to be validated with contour comparison methods as outlined in this study because the registration accuracy of RT structures and hence the partial volume doses received by these structures dictate the need for adaptive

radiotherapy. This evaluation proved to be the most consistent and reliable method in validating DIR accuracy in our study.

DIR results in a daily clinical environment might be very variable and affected from various factors such as patient anatomy, image quality, and registration parameters of the particular algorithm. It should be well appreciated that the evaluation of a DIR algorithm for use in a clinical routine should be conducted in a long term study including a large number of clinical cases.

4.5 Conclusion:

We conclude that the proposed framework offers the application of known deformations on any patient or phantom image sets, that provide clinical medical physicist tools to test, understand and quantify limitations of each algorithm before implementing deformable image registration in the clinic. The evaluation based on anatomical correspondence, physical characteristics of deformation field and image characteristics can facilitate DIR verification with the ultimate goal of implementing adaptive radiotherapy. The suitability of application of a particular evaluation method is strongly dependent on the clinical deformation observed.

Chapter 5. Dose warping and experimental validation of accuracy of dose warping using deformable phantoms.

5.1. Introduction:

Deformable Image Registration (DIR) has gained wide spread acceptance with the availability of several commercial DIR platforms. To properly account for changes in patient anatomy over time, a cumulative dose distribution accounting for the deformations of organs over multiple data sets needs to be implemented. Dose warping or "deformable dose" defined as applying the deformation vector field (DVF) arising from DIR on the original dose distribution has the potential to accumulate doses to ultimately implement adaptive radiotherapy and has been the subject of great interest and controversy in the recent past.[19, 171, 172]. It is known that the accuracy of DIR algorithms can vary depending on the algorithm used and the suitability of application may be site specific[173, 174] potentially leading to errors in dose warping. However, verification of accuracy of dose warp remains a challenging problem as warping the dose with DVF may not represent the physical process of dose deposition in a deformed anatomy.

There have been a number of studies done to validate the accuracy of dose warping using deformable phantoms and dosimeters. [103, 104, 127, 175-178]. Various approaches include 1D (MOSFETs)[179], 2D (film) [176]and 3D (polymer gel)[104, 175] dose measurements in the deformed anatomy and also dose simulation in deformed anatomy using TPS dose have been done[179] and results compared to the warped dose from DIR. For example Yeo et al.,[104] evaluated the accuracy of dose warp for stereotactic irradiations for a range of algorithms available in the public domain using the DIRART

code [100] for 3 different deformation states of the polymer gel. Similarly, Similarly, Niu et al, [175] evaluated dose warp accuracy of the MORFEUS algorithm using a twelve field conformal plan while Juang et al, [180] used Presage-Def radio-chromic 3D dosimeter to verify a commercial B-spline algorithm.

In this context the accuracy of "*deformable dose*" solution provided by commercial DIR algorithms is investigated in this chapter. The "deformable dose" in commercial DIR platforms is derived by applying the DVF from registration to TPS dose and providing the warped dose in the new anatomy.

We illustrate the concept of "deformable dose" using two different methodologies as discussed below.
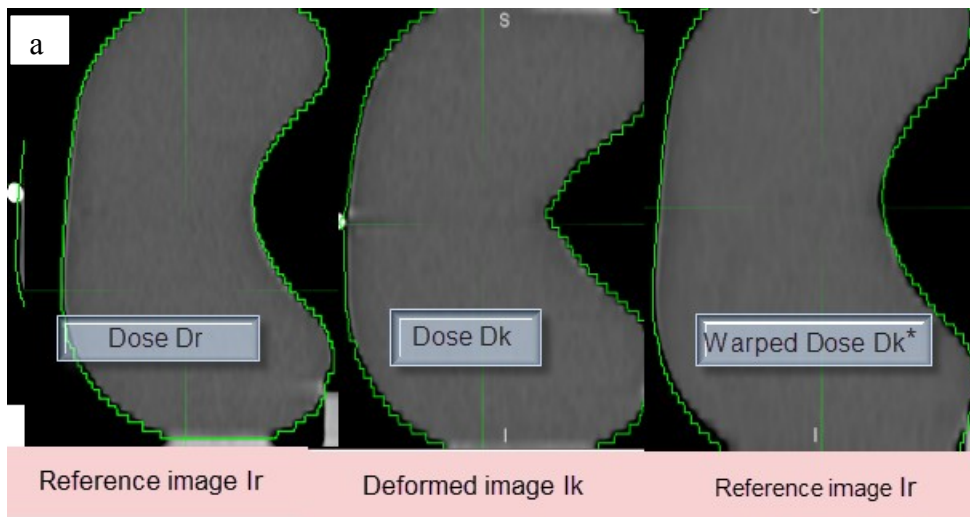
Figure 5.1 a. Representation of the method to illustrate the concept of dose warping in reference image I_r.

Reference I_r Deformed I_k Reference I_r

M_r M_k M_r M_k^{reg}

Planned dose D_r Delivered dose D_k Registered dose D_k^{reg}
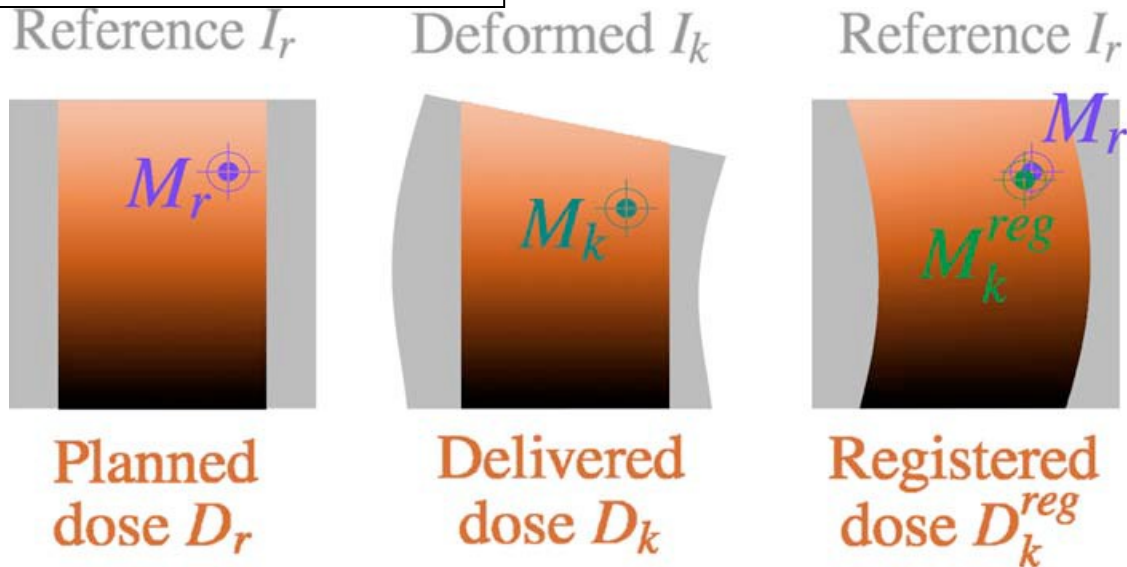
Figure 5.1 b Representation of the method to illustrate the concept of dose warping in the reference image I_r.

a) Let D_r and D_k represent the "true" doses in un-deformed and deformed geometry respectively from TPS. If no dose warping is employed, {D_k-D_r} evaluated in 3D will indicate the magnitude of errors due to organ deformation. Applying the DVF to D_k will result in the warped dose D_k^* in the original CT. If deformable image registration is perfect between images I_r and I_k, then all the voxels deformed in image I_k, will return to the original position when DVF is applied as shown in figure 5.1 b. for a individual marker $M_{k(Reg)} = M_r$. The magnitude of difference between D_k the "true" dose received by the organ in the deformed geometry and D_k^* the warped dose in the reference geometry indicates the agreement of dose warping in 3D. For a perfect dose deformation this difference {Dk-D_k^*} should be zero. This is evaluated systematically by varying the amount of deformation using the deformable bladder phantom designed for this study and the schema is outlined in the flow chart in figure 5.1c below. The details of the phantom and the methods used are discussed in next section.
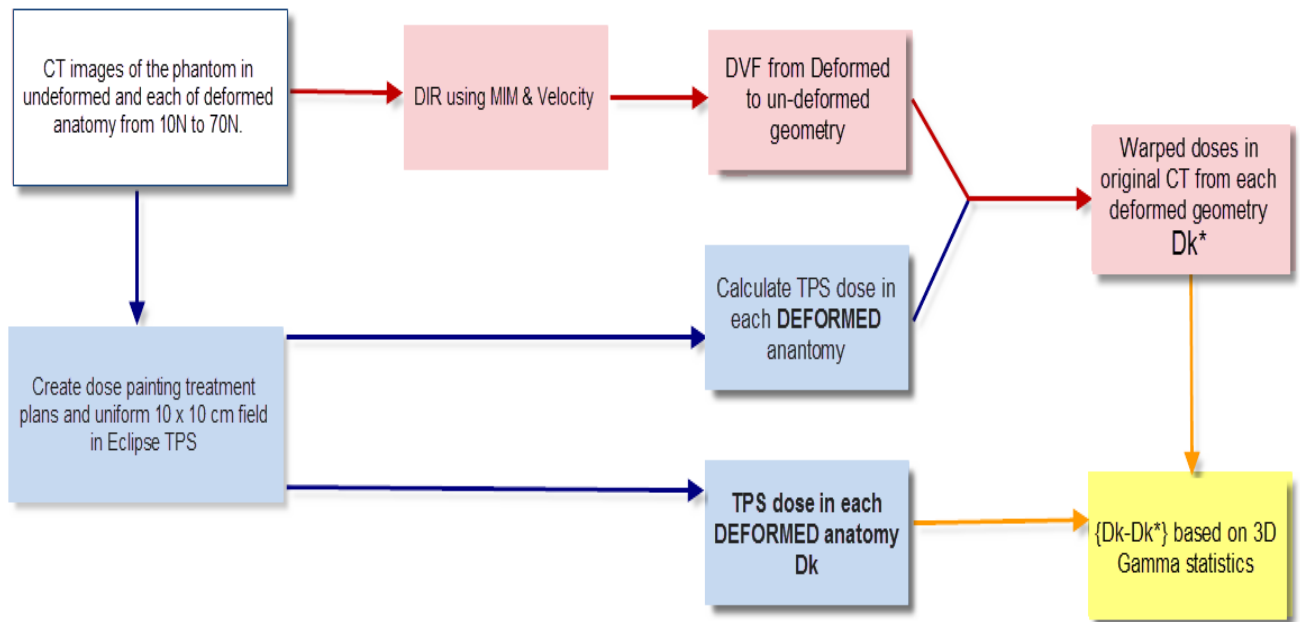
Fig 5.1c Flow chart illustrating the schema used to validate the dose warping in reference image geometry

b) Alternately "dose deformation" can also be viewed from an inverse mapping. Here the roles of source and target images are switched, as one is interested to know what is the magnitude of difference between warped dose on the deformed anatomy, when compared to the true dose received by the organ in deformed anatomy. In this scenario the commercial DIR workflows are propagating D_r* in the deformed geometry. This can be done in less than 2 minutes. However one must recognize D_r* and D_k are in fact two different doses. D_k refers to the "true" dose received by the organ in deformed geometry while D_r* is warped version of dose delivered in un-deformed state. If the warped dose D_r* is accurate, it is potentially very valuable for the radiation oncologist as the dose information (including DVH) can be made available quickly and it has potential

applications in dose accumulation[79, 81, 101]. However if it is not accurate, then it

merely equivalent to "photo shopping" of dose. In general agreement of image

registration does not guarantee accuracy of dose registration and radiation oncologists

should not make clinical judgment based on the erroneous D_r* dose in the deformed

anatomy. Deformable dose is useful to get different doses in the same coordinate system

allowing "voxel" based comparisons to estimate changes in dose received by target and

organs at risk due to organ deformation. Potentially if D_r* = D_k in a clinically relevant

criteria, (3%, 3mm distance to target agreement) then one can propagate the warped

dose to estimate the dose received in deformed geometry without dose recalculation.

However what is not known is, at what level of deformation, dose recalculation in

deformed anatomy may be clinically necessary? This chapter seeks to address that by

systematically evaluating the magnitude of $\{D_r^* - D_k\}$ induced by dose deformation using

the deformable bladder phantom using the schema outlined below in flow chart in figure

5.1d below.
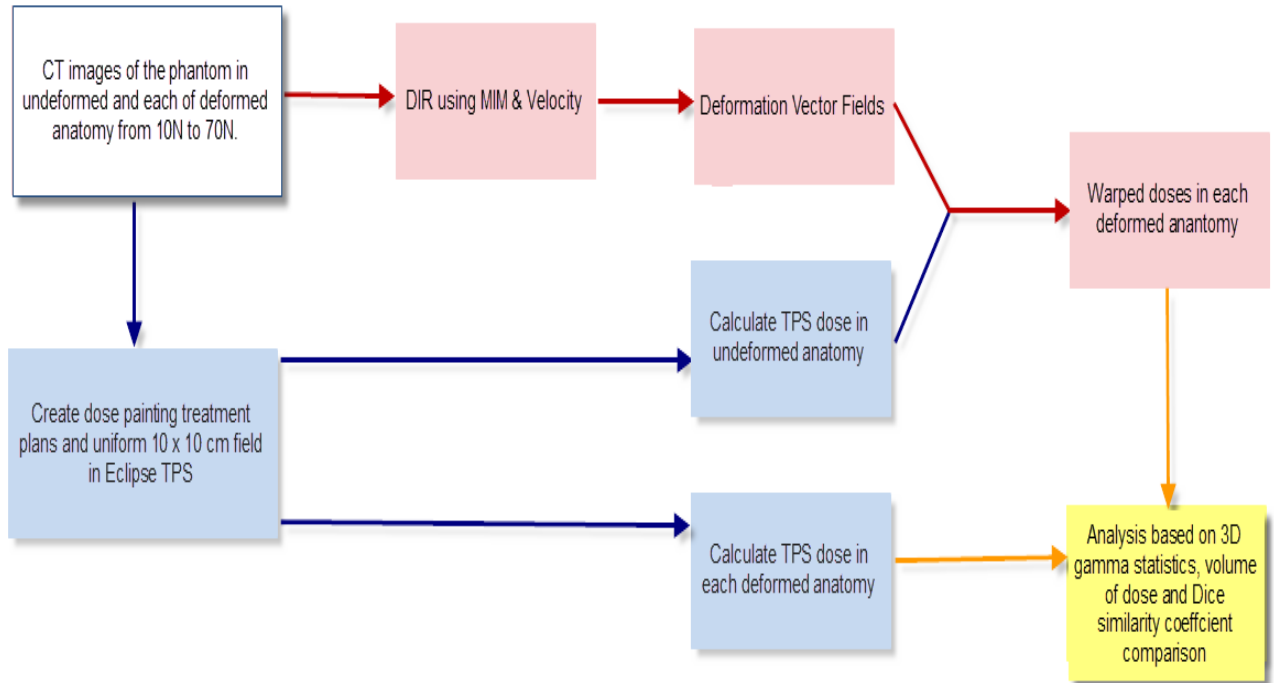
Fig 5.1d Flow chart illustrating the schema used to validate the dose warping in deformed image geometry.

Although deformation has been studied in the context of dose warping, it is mostly used to describe arbitrary deformations for dose delivery verification. The fundamental science of how to properly characterize different levels of deformation with applied force and the limits of applicability of dose warping to a dose painting scenario is not fully understood. A quantitative relationship between force and deformation may give insight into the deformation characteristics of other organs if their biomechanical properties are known and has the potential to create simulated deformations of various organs. A force-deformation relationship of organs has important applications in surgical simulations, optimizing surgical tool design and understanding tissue injury mechanism and damage thresholds[20].

In a clinical context, an increasing number of patient treatment plans are generated with dose painting inside the target volume using Intensity Modulated Radiation Therapy (IMRT) and Volumetric Modulated Arc Therapy (VMAT) techniques for a wide variety of anatomical sites [181-193]. While dose warping may be applicable for a uniform homogeneous dose, its applicability in dose painting geometry has not been validated. The purpose of this study to a) verify the dose warping accuracy with invivo dosimetry using implanted MOSFETs in the deformed anatomy b) characterize the deformation of the organ with applied force, c) ascertain and establish a threshold limit for the dose warp accuracy from various commercial DIR algorithms studied, d) evaluate the efficacy of dose warping in dose painting scenarios and propose suitable validation methods.

Part 1: 1D dose verification using MOSFETs in deformed anatomy.

Methods and Materials:

5.2 Deformable phantom for 1D dose warping verification in deformed anatomy:

The deformable phantom was made from a solid water prototype (figure 5.2 a) with dimensions of 10.5 x 9 x 4.8 cm^3 measuring 386cc in total volume, mimicking human "bladder-like" organ volume and geometry [194]. The solid water prototype was coated with mold release and a silicone rubber compound was poured around the organ. It was then placed in the vacuum chamber at a pressure of 25 inches of mercury for about 20 hours. The mold was filled with Akton visco elastic polymer and the phantom was removed from the mold after hardening (fig 5.2b). The Akton viscoelastic polymer (Action Products, Hagerstown, MD) used is tissue equivalent with relative electron density of 1.02 and physical density of 1.03g/cm^3[195]. The tensile properties of the viscoelastic polymer used are described in more detail in the next section when

describing 3D dose verification. 5 parallel air canals that run along the organ were used

for positioning MOSFET detectors at multiple locations.(Fig 5.3) For measuring the

actual dose delivered in deformed geometry, metal oxide semiconductor field-effective

transistor (MOSFET) dosimeter standard TN-502RD, (Best Medical, Canada) were used.

Dose calculation was performed in un-deformed geometry with varying degree of dose

gradients. The phantom was deformed using a compression plate and the resulting images

before and after deformation along with the location of MOSFETs is shown in Fig 5.4.

The maximum deformation of the organ along the axis of applied force was 15 mm.

Fig 5.2. a   Fig 5.2 b
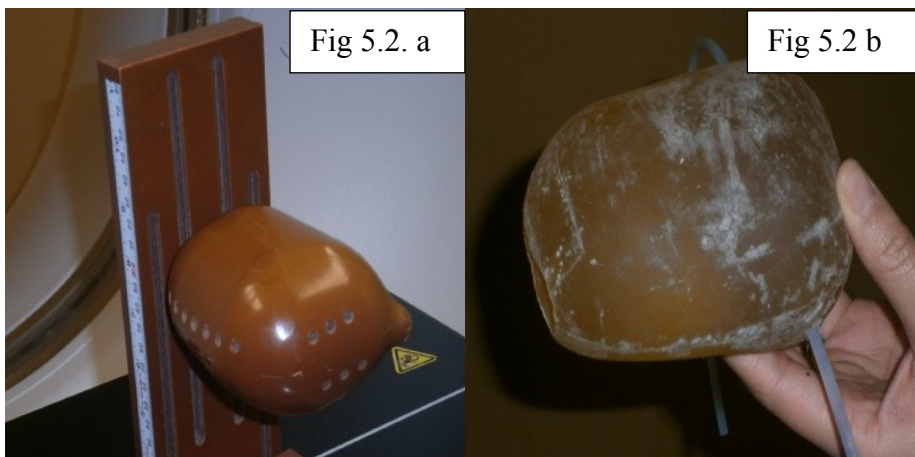
Figures 5.2 a, b showing the solid water prototype, and the viscoelastic polymer based

deformable phantom respectively
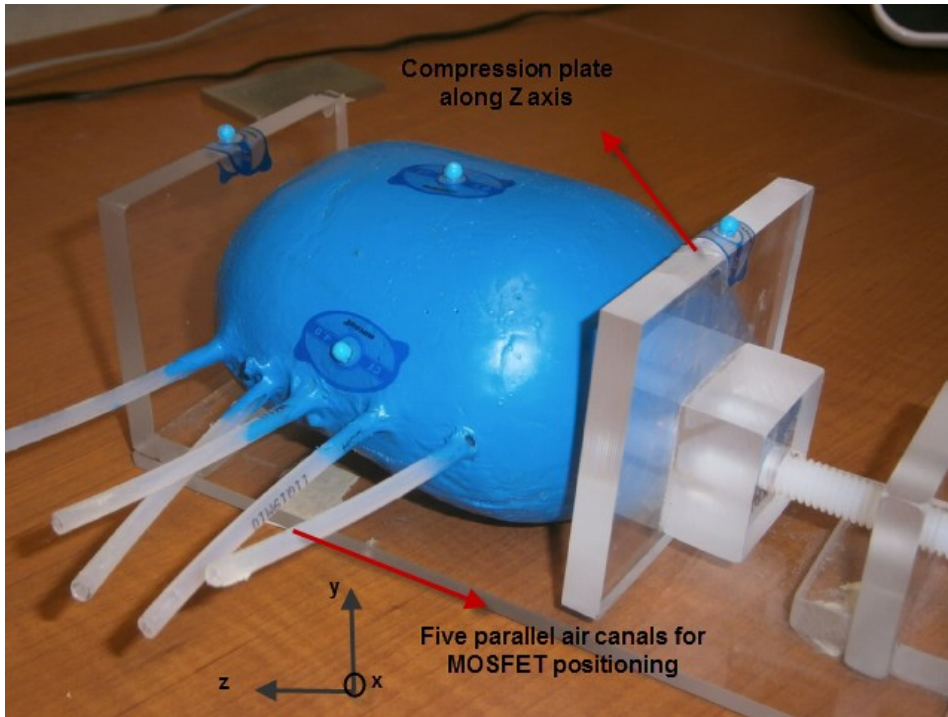
Figure 5.3 Deformable bladder phantom with 5 parallel air canals for 1D dose

verification using MOSFETs
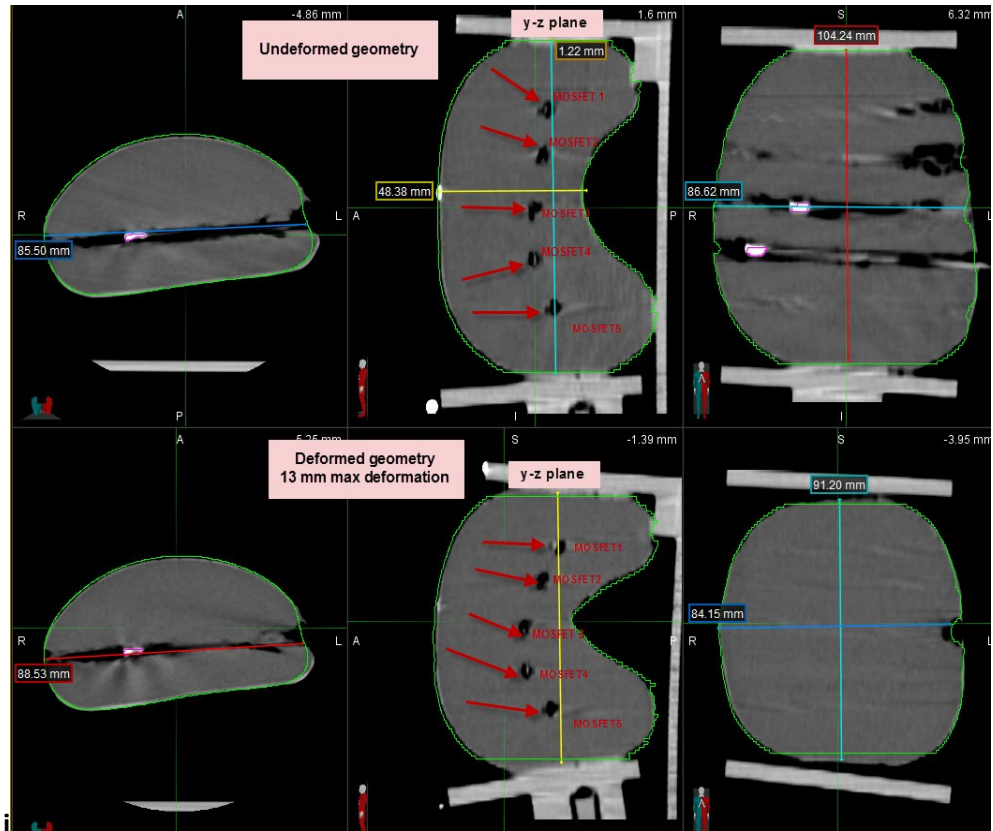
Figure 5.4 CT images of bladder phantom in undeformed and deformed positions along with locations of 5 MOSFETS

5.3 Deformable image registration algorithms studied for 1D dose warping:

In this work we assess the suitability of DIR based dose warping (using 1D point dose measurement with MOSFETs) for the commercially available DIR algorithm namely the free form intensity based deformation from MIM 5.6 (MIM Software, OH) and also the B-spline algorithm found in the open source Slicer-RT platform[196] . MIM software (MIM) uses a free form fully automatic intensity based deformation with a multi-resolution approach[110] and the details of the B-spline algorithm using Slicer-RT were discussed in Chapter 4.

5.4 Beam geometries studied for 1D dose warping:

Five different beam geometries were studied to evaluate the efficacy of dose warping using MOSFETs. They are

1) A uniform 10 x 10 cm^2 field

2) 60 degree Enhanced Dynamic Wedge (EDW 60) with a collimator rotation of 45 degrees.

3) 60 degree Enhanced Dynamic Wedge (EDW 60) with collimator angle of 0 degrees where the induced dose gradient is in an opposite direction to previous example 2. This results in a dose gradient across organ as shown in figure 5.5 below

4) A sweeping MLC gap across the organ with a gap width of 0.5 cm

5) A sweeping MLC gap across the organ with a gap width of 1 cm.

The MOSFETS were moved 3 times along each air canal position and thus a total of 15 MOSFET measurements were performed for each of the five beam geometries studied.
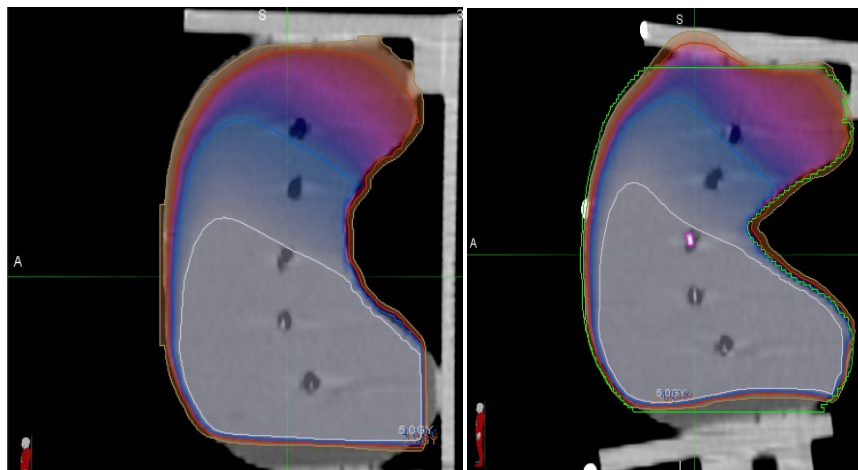
Figure 5.5 Sagittal view of 60 degree Enhanced Dynamic Wedge doses with original dose on original CT (left), and deformed old dose on deformed CT (right).

5.5. Dose warping evaluation Scheme for MOSFETs.

The dose warping accuracy using MOSFETS was evaluated using the following methodology similar to the work in Ref [179]. Accuracy of the dose warping was assessed by using two comparison techniques. The first validation was made using the simulation of dose distribution planning where the warped dose from DIR was compared to the directly calculated dose from Eclipse TPS in the deformed geometry. The second validation was made with the dose directly measured by the MOSFET detectors in the deformed geometry and compared to the warped dose from DIR algorithms. Let $D(r_i)$ denote the dose received by each MOSFET at position r_i in the undeformed state. Under the influence of applied deformation the dose received by each MOSFET is $D(r_k)$ The percentage error in dose warping accuracy for each MOSFET at each beam geometry studied was evaluated using the formulae

Dose warp error using MOSFETS = $\{D^{DIR}(r_k) - D(MOSFET_k)/ D(MOSFET_k)$

where $D^{DIR}(r_k)$ refers to the warped dose of MOSFET in the deformed location r_k. Similarly the dose warp error using Eclipse TPS was evaluated using the formulae

Dose warp error using TPS = $\{D^{DIR}(r_k) - D(TPS_k)\}/ D(TPS_k)$

Where $D(TPS_k)$ refers to the dose directly recalculated at each MOSFET location r_k in the treatment planning system in the deformed geometry

5.6.Results of deformable dose evaluation using MOSFETs

Tables 5.1 to 5.5 detail the 15 individual MOSFET raw data readings and the TPS dose at each MOSFET location for both undeformed and deformed geometry when compared to the warped dose from DIR algorithms for each of the 5 beam geometries studied. The

results of 15 MOSFET measurements were averaged and are summarized in Figures 5.6

for TPS dose simulation and figure 5.7 for MOSFET measurement.
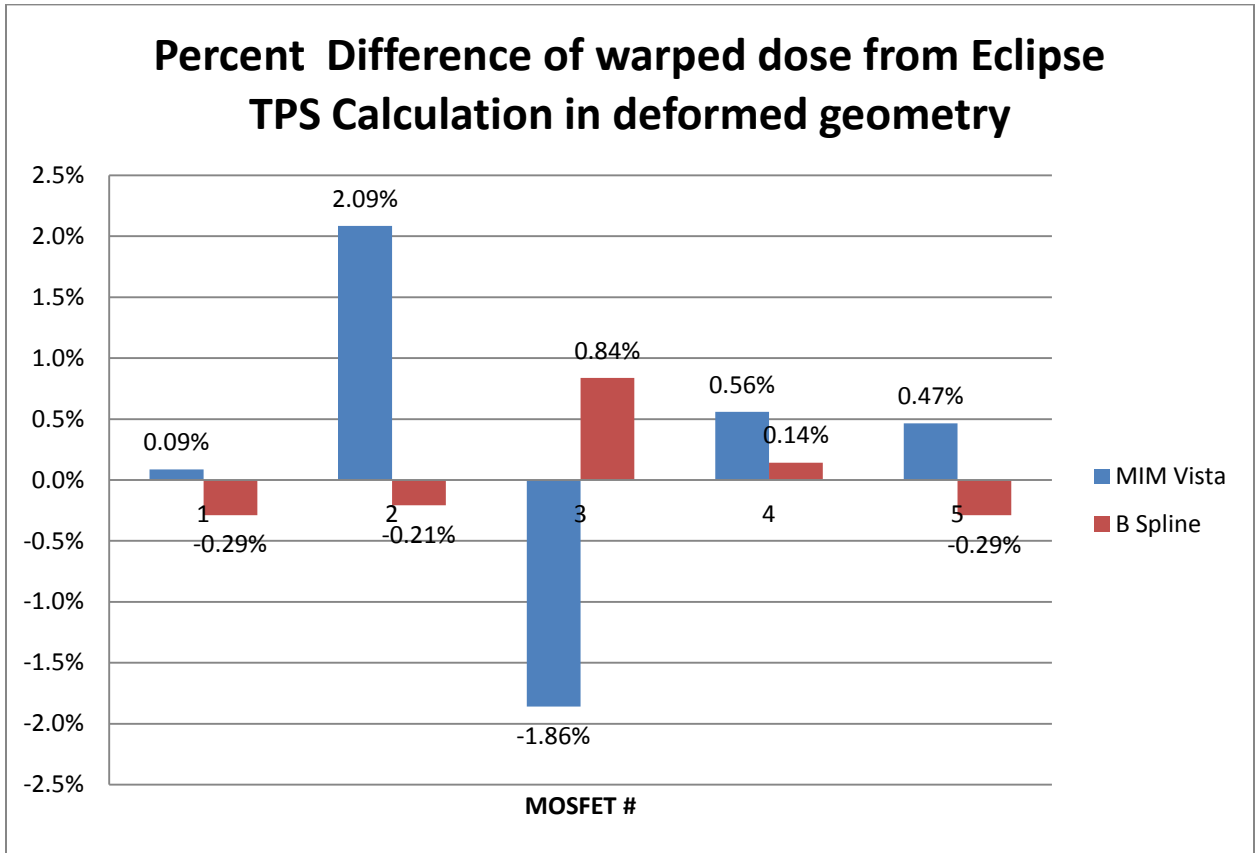
Figure 5.6 illustrating the agreement between warped dose from DIR algorithms and

dose directly recalculated in the TPS in the deformed geometry for each of the 5 beam

geometries given in section C. The data shown represents the average TPS dose at the 15

MOSFET locations in the deformed geometry.

Percent Difference of warped dose from MOSFET Measurement in deformed geometry
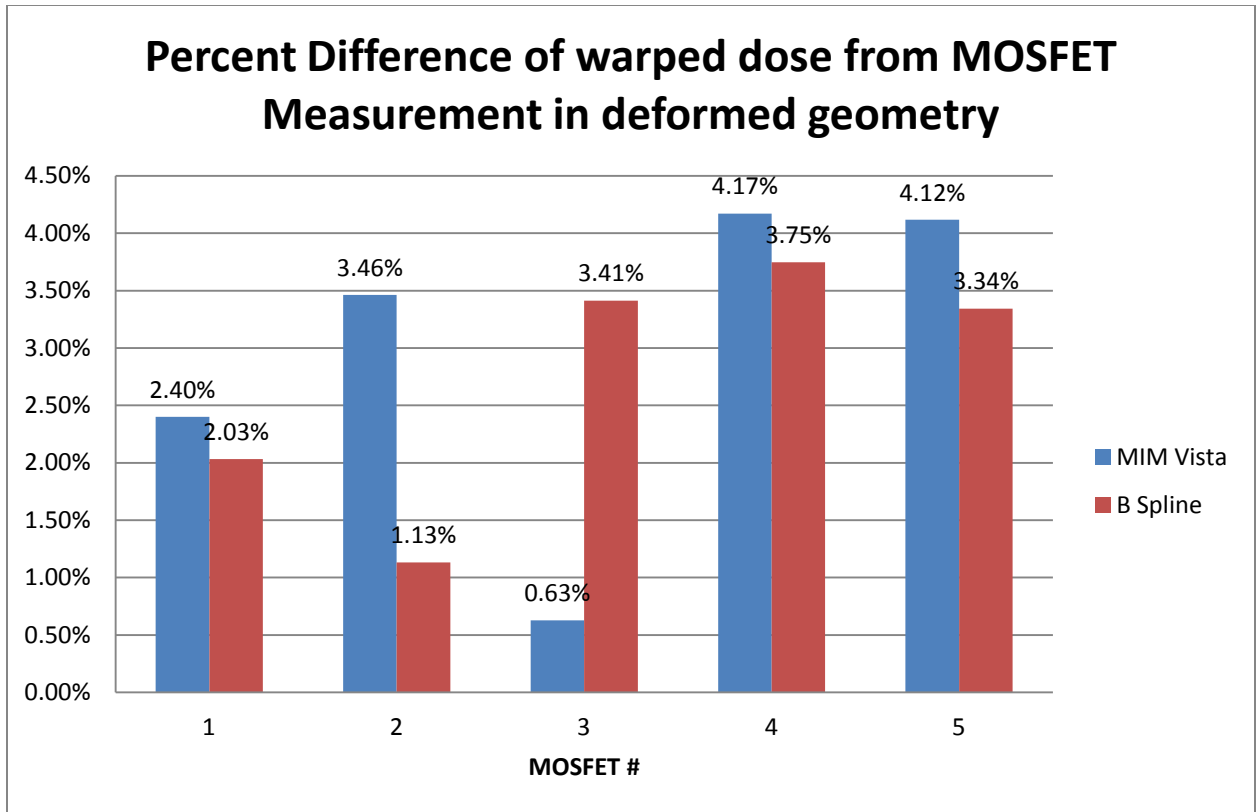
Figure 5.7 illustrating the agreement between warped dose from DIR algorithms and dose directly measured by MOSFETs in the deformed geometry for each of the 5 beam geometries given in section C. The data shown represents the average of the 15 MOSFET readings for each beam geometry.

Table 5.1. MOSFET measurements in deformed anatomy for 10 x10 cm² field

	Baseline MOSFET accuracy- Undeformed					Undeformed Eclipse		Undeformed Measured		Mim			Slicer RT-Bspline		
MOSFET Number	TPS Dose (cGy)	Measured Dose (cGy)	% Diff	TPS Dose (cGy)	Measured Dose (cGy)	TPS Dose (cGy)	%Δ from deformed Eclipse	Undeformed MOSFET Meas (cGy)	%Δ from deformed Meas.	Calculated Dose (cGy)	%Δ from deformed TPS	%Δ from deformed Meas.	Calculated Dose (cGy)	%Δ from deformed TPS	%Δ from deformed Meas.
1	49.4	48.5	1.82	48.3	48.1	49.4	2.28	48.5	0.83	49.3	2.07	2.49	47.3	-2.07	-1.66
2	49.4	48.4	2.02	48.9	48	49.4	1.02	48.4	0.83	48.7	-0.41	1.46	48.8	-0.20	1.67
3	49	48.3	1.43	49.5	48.2	49	-1.01	48.3	0.21	49.1	-0.81	1.87	50.1	1.21	3.94
4	50.2	49.7	1.00	50.3	49.4	50.2	-0.20	49.7	0.61	50.3	0.00	1.82	51.05	1.49	3.34
5	48.5	47.7	1.65	48.2	47	48.5	0.62	47.7	1.49	48.1	-0.21	2.34	48.1	-0.21	2.34
6	49.2	50.4	-2.44	47.8	47.4	49.2	2.93	50.4	6.33	49.4	3.35	4.22	46.5	-2.72	-1.90
7	48.9	47.6	2.66	48.6	48	48.9	0.62	47.6	-0.83	49.4	1.65	2.92	48.3	-0.62	0.62
8	49.6	48.6	2.02	50.2	48.2	49.6	-1.20	48.6	0.83	49.9	-0.60	3.53	50.9	1.39	5.60
9	49.8	48.8	2.01	50.1	49	49.8	-0.60	48.8	-0.41	50.3	0.40	2.65	50.5	0.80	3.06
10	48.5	47.2	2.68	48.2	47.4	48.5	0.62	47.2	-0.42	48.4	0.41	2.11	48.8	1.24	2.95
11	49.8	48.8	2.01	48.9	47.7	49.8	1.84	48.8	2.31	49.4	1.02	3.56	47.5	-2.86	-0.42
12	48.4	47	2.89	49.8	47.6	48.4	-2.81	47	-1.26	49.3	-1.00	3.57	48.5	-2.61	1.89
13	48.8	47.9	1.84	50	48.7	48.8	-2.40	47.9	-1.64	48.9	-2.20	0.41	50.7	1.40	4.11
14	50.8	49.4	2.76	51.1	49.4	50.8	-0.59	49.4	0.00	50.4	-1.37	2.02	50.5	-1.17	2.3%
15	48.7	47.7	2.05	49	48	48.7	-0.61	47.7	0.62	48.5	-1.02	1.04	49.3	0.61	2.71
AVG Percent Change (%)			1.76				0.03		0.55		0.09	2.40		-0.29	2.03

130

Table 5.2. MOSFET measurements in deformed anatomy for EDW 60 with 45 deg collimator angle

MOSFET Number	Baseline MOSFET accuracy- Undeformed			Deformation Comparisons		Undeformed Eclipse		Undeformed Measured		Mim			Slicer RT-Bspline		
	TPS Dose (cGy)	Measured Dose (cGy)	% Diff	TPS Dose (cGy)	Measured Dose (cGy)	TPS Dose (cGy)	%Δ from deformed Eclipse	Undeformed MOSFET Meas (cGy)	%Δ from deformed Meas.	Calculated Dose (cGy)	%Δ from deformed TPS	%Δ from deformed Meas.	Calculated Dose (cGy)	%Δ from deformed TPS	%Δ from deformed Meas.
1	37.8	36.8	2.65	38	37.4	37.8	-0.53	36.8	-1.60	38.4	1.05	2.67	37.7	-0.79	0.80
2	41.4	40.9	1.21	42.1	41.2	41.4	-1.66	40.9	-0.73	43	2.14	4.37	42.5	0.95	3.16
3	50.7	50.1	1.18	51.2	50.5	50.7	-0.98	50.1	-0.79	51.2	0.00	1.39	51.7	0.98	2.38
4	50.5	50	0.99	50	49.8	50.5	1.00	50	0.40	50.6	1.20	1.61	50.4	0.80	1.20
5	57.6	56.8	1.39	56.8	54.7	57.6	1.41	56.8	3.84	60.8	7.04	11.2	55.5	-2.29	1.46
6	43.2	42.6	1.39	43.6	43.5	43.2	-0.92	42.6	-2.07	44.7	2.52	2.76	42.7	-2.06	-1.84
7	47.9	47.2	1.46	48.7	49.2	47.9	-1.64	47.2	-4.07	51.5	5.75	4.67	48.8	0.21	-0.81
8	56.3	56.1	0.36	57.1	56.3	56.3	-1.40	56.1	-0.36	58.2	1.93	3.37	58.3	2.10	3.55
9	63.8	61.7	3.29	64	64.5	63.8	-0.31	61.7	-4.34	66	3.13	2.33	64.04	0.06	-0.71
10	68.1	66.1	2.94	66.2	64.8	68.1	2.87	66.1	2.01	66.3	0.15	2.31	66.1	-0.15	2.01
11		35.5		36.5	35.8			35.5	-0.84	36.7	0.55	2.51	36.7	0.55	2.51
12		35.6		36.8	35.9			35.6	-0.84	36.7	-0.27	2.23	36.4	-1.09	1.39
13		44.7		46.8	45.7			44.7	-2.19	47.1	0.64	3.06	47.3	1.07	3.50
14		46.2		47.3	47.7			46.2	-3.14	47.3	0.00	-0.84	46.2	-2.33	-3.14
15		51.3		53.1	51.7			51.3	-0.77	56	5.46	8.32	52.5	-1.13	1.55

10 x 10 EDW60 Coll45

AVG Percent Change (%)			1.68				-0.22		-1.03		2.09	3.46		-0.21	1.13

Table 5.3. MOSFET measurements in deformed anatomy for EDW 60 field

| MOSFET Number | Baseline MOSFET accuracy-Undeformed | | | Deformation Comparisons | | | | | | | | | | | |
| | TPS Dose (cGy) | Measured Dose (cGy) | % Diff | TPS Dose (cGy) | Measured Dose (cGy) | Undeformed Eclipse | | Undeformed Measured | | Mim | | | Slicer RT-Bspline | | |
						TPS Dose (cGy)	%Δ from deformed Eclipse	Undeformed MOSFET Meas (cGy)	%Δ from deformed Meas.	Calculated Dose (cGy)	%Δ from deformed TPS	%Δ from deformed Meas.	Calculated Dose (cGy)	%Δ from deformed TPS	%Δ from deformed Meas.
1	39.3	38.9	1.02	39.9	38.3	39.3	-1.50	38.9	1.57	38.4	-3.76	0.26	40.7	2.01	6.27
2	44.3	43.9	0.90	45.1	42.8	44.3	-1.77	43.9	2.57	43.7	-3.10	2.10	46.2	2.44	7.94
3	51.8	50.9	1.74	52.8	51.2	51.8	-1.89	50.9	-0.59	51.7	-2.08	0.98	53.9	2.08	5.27
4	60.2	58.2	3.32	60.2	59.7	60.2	0.00	58.2	-2.51	60.2	0.00	0.84	61.3	1.83	2.68
5	66.8	65	2.69	65.6	65.1	66.8	1.83	65	-0.15	66.7	1.68	2.46	64.2	-2.13	-1.38
6	38.8	38.4	1.03	40	39.9	38.8	-3.00	38.4	-3.76	38.1	-4.75	-4.51	40	0.00	0.25
7	43.8	43.1	1.60	45.3	44.1	43.8	-3.31	43.1	-2.27	44.2	-2.43	0.23	46.2	1.99	4.76
8	52.4	51.4	1.91	54.1	53.6	52.4	-3.14	51.4	-4.10	52.4	-3.14	-2.24	55.5	2.59	3.54
9	60.8	59.3	2.47	61.1	59.1	60.8	-0.49	59.3	0.34	60.5	-0.98	2.37	61.8	1.15	4.57
10	67.9	65.8	3.09	66.3	65.4	67.9	2.41	65.8	0.61	67.1	1.21	2.60	66.5	0.30	1.68
11	39.1	38.1	2.56	40.2	39	39.1	-2.74	38.1	-2.31	38.6	-3.98	1.03	40.9	1.74	4.87
12	43.8	42.5	2.97	44.8	42.8	43.8	-2.23	42.5	-0.70	43.9	-2.01	2.57	44.3	1.12	3.50
13	51.3	49.4	3.70	53	50.8	51.3	-3.21	49.4	-2.76	51.3	-3.21	0.98	54.1	2.08	6.50
14	60.6	59.7	1.49	60.8	60.2	60.6	-0.33	59.7	-0.83	60.1	-1.15	-0.17	60	-1.32	-0.33
15	68.6	67.1	2.19	66.9	65.5	68.6	2.54	67.1	2.44	66.8	-0.15	1.98	66.2	-1.05	1.07
AVG Percent Change (%)			2.18				-1.12		-0.83		-1.86	0.63		0.84	3.41

Table 5.4. MOSFET measurements in deformed anatomy for MLC Gap width of 0.5 cm

MOSFET Number	Baseline MOSFET accuracy-Undeformed			Deformation Comparisons		Undeformed Eclipse		Undeformed Measured		Mim			Slicer RT-Bspline		
	TPS Dose (cGy)	Measured Dose (cGy)	% Diff	TPS Dose (cGy)	Measured Dose (cGy)	TPS Dose (cGy)	%Δ from deformed Eclipse	Undeformed MOSFET Meas (cGy)	%Δ from deformed Meas.	Calculated Dose (cGy)	%Δ from deformed TPS	%Δ from deformed Meas.	Calculated Dose (cGy)	%Δ from deformed TPS	%Δ from deformed Meas.
1	42.9	40.9	4.66	41.8	40.6	42.9	2.63	40.9	0.74	42.9	2.63	5.67	41.1	-1.67	1.23
2	42.9	40.5	5.59	42.4	41.1	42.9	1.18	40.5	-1.46	42.3	-0.24	2.92	42.4	0.00	3.16
3	42.7	43.1	-0.94	43	41.4	42.7	-0.70	43.1	4.11	42.7	-0.70	3.14	43.6	1.40	5.31
4	43.7	42	3.89	43.8	42.5	43.7	-0.23	42	-1.18	43.7	-0.23	2.82	44.4	1.37	4.47
5	42.2	41	2.84	41.8	40.1	42.2	0.96	41	2.24	41.8	0.00	4.24	41.9	0.24	4.49
6	42.8	40.4	5.61	41.5	39.5	42.8	3.13	40.4	2.28	43	3.61	8.86	40.5	-2.41	2.53
7	42.5	39.9	6.12	42.1	41.2	42.5	0.95	39.9	-3.16	42.9	1.90	4.13	42.1	0.00	2.18
8	43.3	41.3	4.62	43.6	41.8	43.3	-0.69	41.3	-1.20	43.5	-0.23	4.07	44.4	1.83	6.22
9	43.4	40	7.83	43.5	42.8	43.4	-0.23	40	-6.54	43.7	0.46	2.10	43.9	0.92	2.57
10	42.2	39.7	5.92	41.8	39.5	42.2	0.96	39.7	0.51	42.1	0.72	6.58	42.4	1.44	7.34
11	43.3	41.4	4.39	42.5	41.9	43.3	1.88	41.4	-1.19	42.9	0.94	2.39	41.4	-2.59	-1.19
12	43.3	41.6	3.93	43.3	41.5	43.3	0.00	41.6	0.24	43.2	-0.23	4.10	42.3	-2.31	1.93
13	43.1	41.7	3.25	43.5	41	43.1	-0.92	41.7	1.71	42.9	-1.38	4.63	44.3	1.84	8.05
14	44.3	42.7	3.61	43.3	42.4	44.3	2.31	42.7	0.71	44.2	2.08	4.25	43.9	1.39	3.54
15	42.9	41.1	4.20	42.6	41.1	42.9	0.70	41.1	0.00	42.2	-0.94	2.68	42.9	0.70	4.38
AVG Percent Change (%)			4.37				0.80		-0.15		0.56	4.17		0.14	3.75

	Table 5.5. MOSFET measurements in deformed anatomy for MLC Gap width of 1cm														

	Gap 1cm														
	Baseline MOSFET accuracy- Undeformed			Deformation Comparisons											
						Undeformed Eclipse		Undeformed Measured		Mim			Slicer RT-Bspline		
MOSFET Number	TPS Dose (cGy)	Measured Dose (cGy)	% Diff	TPS Dose (cGy)	Measured Dose (cGy)	TPS Dose (cGy)	%Δ from deformed Eclipse	Undeformed MOSFET Meas (cGy)	%Δ from deformed Meas.	Calculated Dose (cGy)	%Δ from deformed TPS	%Δ from deformed Meas.	Calculated Dose (cGy)	%Δ from deformed TPS	%Δ from deformed Meas.
1	35.8	35.1	1.96	35	33.7	35.8	2.29	35.1	4.15	35.8	2.29	6.23	34.4	-1.71	2.08
2	35.8	35	2.23	35.4	33.5	35.8	1.13	35	4.48	35.3	-0.28	5.37	35.2	-0.56	5.07
3	35.6	35.4	0.56	35.9	34.1	35.6	-0.84	35.4	3.81	35.7	-0.56	4.69	36.2	0.84	6.16
4	36.5	35.2	3.56	36.6	35.5	36.5	-0.27	35.2	-0.85	36.5	-0.27	2.82	36.8	0.55	3.66
5	35.2	33.9	3.69	35	33.9	35.2	0.57	33.9	0.00	34.9	-0.29	2.95	34.8	-0.57	2.65
6	35.7	34.3	3.92	34.7	33.4	35.7	2.88	34.3	2.69	35.8	3.17	7.19	33.8	-2.59	1.20
7	35.5	34.8	1.97	35.2	34.8	35.5	0.85	34.8	0.00	36.2	2.84	4.02	35.1	-0.28	0.86
8	36.2	35.4	2.21	36.4	35.1	36.2	-0.55	35.4	0.85	36.4	0.00	3.70	37.1	1.92	5.70
9	36.3	35.2	3.03	36.3	34.9	36.3	0.00	35.2	0.86	36.6	0.83	4.87	36.7	1.10	5.16
10	35.3	33.9	3.97	34.9	34.4	35.3	1.15	33.9	-1.45	35.4	1.43	2.91	35.4	1.43	2.91
11	36.2	35.2	2.76	35.4	34.2	36.2	2.6%	35.2	2.92	35.8	1.13	4.68	34.5	-2.54	0.88
12	36	35	2.78	35.9	35.1	36	0.28	35	-0.28	35.9	0.00	2.28	34.9	-2.79	-0.57
13	35.9	34.5	3.90	36.3	34.6	35.9	-1.10	34.5	-0.29	35.8	-1.38	3.47	36.9	1.65	6.65
14	36.9	35.8	2.98	37.1	35.2	36.9	-0.54	35.8	1.70	36.8	-0.81	4.55	36.5	1.62	3.69
15	35.8	34.6	3.35	35.6	34.5	35.8	0.56	34.6	0.29	35.2	-1.12	2.03	35.9	0.84	4.06

AVG Percent Change (%)			2.86				0.58		1.26		0.47	4.12		-0.29	3.34

5.7. Conclusion and limitations of MOSFET measurements

The dose warping accuracy studied for the applied deformation (15 mm maximum deformation) yielded acceptable results (< 5% overall disagreement) for all the beam geometries studied. The dose warping accuracy was better when dose simulation from TPS was used as the ground truth. This is due to the inherent uncertainties in MOSFET

measurement in highly modulated geometries like EDW 60 and MLC gap widths studied. It has been shown that the inherent uncertainty in MOSFET measurement in highly modulated fields like IMRT is 4.6%[197]. The dose warping accuracy studies using MOSFETs have two major drawbacks. 1) Although dose warping accuracy studies using 1D point dose measurement using arbitrary deformations give some degree of agreement and validity to DIR based dose warping, they cannot be extrapolated to agreement in other locations within the organ. To meaningfully compare dose warp accuracy, the entire 3D dose matrix has to be evaluated.

2) Dose warp accuracy evaluations using arbitrary deformations as done by vast majority of research groups do not parameterize the deformation of the organ with its causative physical force. To gain scientific insight to the actual deformation of organs, deformation must be linked to the physical force causing the observed deformation as described in Chapter 1. The fundamental relationship between force and deformation of organs has many scientific applications and are discussed in the next section.

To overcome these drawbacks we designed a new deformable phantom and evaluated the dose warp accuracy (3D dose) using a novel methodology which is described in the next section

PART 2: 3D Dose verification

Applicability and Limits of Dose Warping - Are There Islands of Deformation that Fail to Depict Dose Painting?

5.8. Deformable bladder phantom and deformation studied for 3D dose verification:

The deformable phantom for 3D dose verification was made from the same solid water prototype described before, with dimensions of 10.5 x 9 x 4.8 cm^3 measuring 386cc in total volume, mimicking human "bladder-like" organ volume and geometry [194]. The solid water prototype was coated with mold release and a silicone rubber compound was poured around the organ. It was then placed in the vacuum chamber at a pressure of 25 inches of mercury for about 20 hours. The mold was filled with Akton visco elastic polymer and the phantom was removed from the mold after hardening. The Akton viscoelastic polymer (Action Products, Hagerstown, MD) used is tissue equivalent with relative electron density of 1.02 and physical density of 1.03g/cm^3[195]. It has peak tensile strength of 157 kPa and Young's modulus of 17.9 kPa[198]. The mechanical and tensile properties of the phantom are comparable to human bladder with Young's modulus of 16 kPa[199, 200] , density of 1.04 g/cm^3 [201], and peak tensile strength of 270±140 kPa[202] . A coating of blue plastidip, an air-dry synthetic rubber which resists moisture and absorption, was applied on the phantom. The bladder phantom was placed between the apparatus for measuring force-deformation properties (Fig. 5.8). The apparatus made of acrylic has a mechanical piston at one end, and is fitted with a customized miniature load cell with National Institute of Standards and Technology (NIST) traceable calibration. The load cell accurately measured the applied force induced by the piston on the phantom with excellent reproducibility and linearity[203]. The load

cell was connected to a digital process meter and controller which displays the applied

force on the deformable phantom. A precision weight was used to calibrate the accuracy

of the load cell and readout. The applied force on the phantom was varied incrementally

from 10 N to 70N along the longitudinal axis (+z axis) of the phantom, and although the

maximum deformation (compression) is along ±z axis, there is expansion and

compression in other axis and the deformation observed on the organ is three

dimensional. Deformation is quantified both in terms of maximum 1D deformation

observed along the direction of applied force and also the 3D deformation quantified by

the 95 percentile Hausdorff distance (95% HD) [168]. Hausdorff distance measures the

maximum of the closest distance between two volumes where the closest distance is

computed for each vertex of the two volumes. The 95% HD ensures that the outliers are

rejected. To calculate the 95% HD, the external body contour of the deformable phantom

in each deformation state was contoured and compared against the surface contour in

undeformed state using Slicer RT[196].
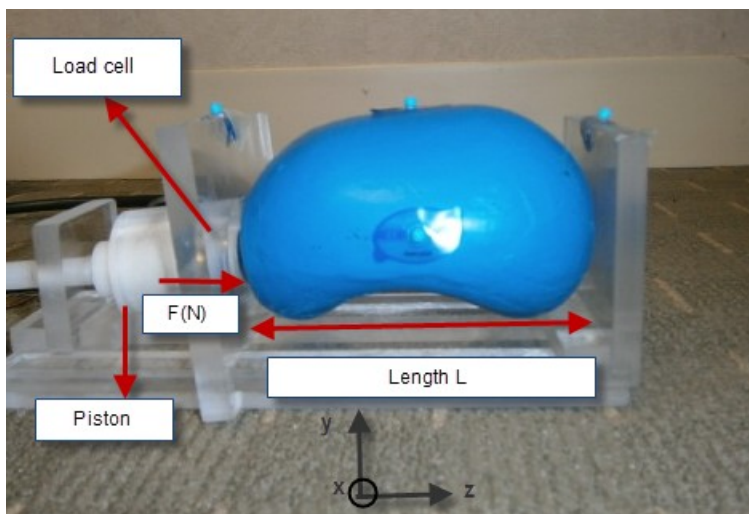
Fig 5.8 Apparatus for investigating force-deformation properties

5.9 Deformable image registration algorithms studied for 3D dose warping

In this work we assess the suitability of DIR based dose warping for the various commercially available DIR algorithms namely the free form intensity based deformation from MIM 6.0.1 (MIM Software, OH) and both the single pass and multi-pass deformation from Velocity AI 3.0 (Velocity Medical Solutions, GA). MIM software (MIM) uses a free form fully automatic intensity based deformation with a multi-resolution approach[110]. The details of the algorithm parameters, including smoothness criteria, are proprietary and are not user-defined. Velocity AI uses a modified B-spline algorithm [87, 89] combined with Mattes mutual information metric[160]. Similar to MIM, the algorithm parameters are not user-defined but are instead inherent to the software. The number of control points in Velocity AI can be varied depending on the choice of multi-pass or single pass registration modes in the software. In the single pass mode, (VEL-SD) the finest grid resolution is applied while in the multi-pass mode(VEL-MD) the grid resolution spacing started at the coarse setting and gradually went down to the finest in multiple steps which potentially helps to make the convergence of the optimizer in a shorter time.

5.10. Dose warping validation for Dose painting:

Dose warping accuracy in deformed anatomy:

The accuracy of dose warp in deformed image is validated in this study using the methodology outlined in the flow chart. (Figure 5.9).The deformable phantom was placed between the compression plate and a CT scan was obtained using a GE Light Speed CT scanner in the undeformed geometry. Using the same imaging acquisition mode, the phantom was successively scanned at various deformed states. The images were processed and cropped to remove the acrylic plate holding the phantom. Both the

commercial DIR platforms have dose deformation work flow navigators which warp the original treatment planning system (TPS) dose in an undeformed state with DVF from DIR to display a warped dose in the deformed or new organ geometry. The warped doses were then exported from the respective DIR platform as DICOM RT Dose files and analyzed for dose warp accuracy. Next, this was compared to the corresponding dose recalculated in TPS. The accuracy of dose warp was evaluated using two different metrics. First, 3D γ analysis[204, 205] which is an extension of the original 2D planar gamma evaluation[206] by considering DTA agreement in 3D was performed by comparing the warped doses from each of the DIR algorithms with dose from TPS using the Slicer RT[196] routines. The passing criteria for all the doses was calculated for those voxels receiving greater than 10% of maximum dose (10 % threshold) as discussed in AAPM Task Group Report 119 [207]. Next, the volumes of high dose paint from various DIR algorithms is compared to the volume of high dose gradient from TPS to evaluate the efficacy of dose warping in a dose painting scenario. As discussed before, in a dose painting scenario the volume of high dose received by the target is of critical importance as one attempts to put localized high dose volume to the target. Hence, the ratio of high dose volumes between true dose received by the target (as calculated from TPS) and warped dose from DIR algorithms is more likely to indicate the accuracy of dose warping in a dose painting scenario. This is because, the usual 3mm distance to target agreement (DTA) used in γ_{3D} analysis may not accurately depict the accuracy of warping due to averaging of low and high dose voxels in the area of interest. Further the Dice similarity coefficient (DSC) and 95% HD was evaluated for the high dose volume surfaces to indicate the spatial agreement of high dose volumes.
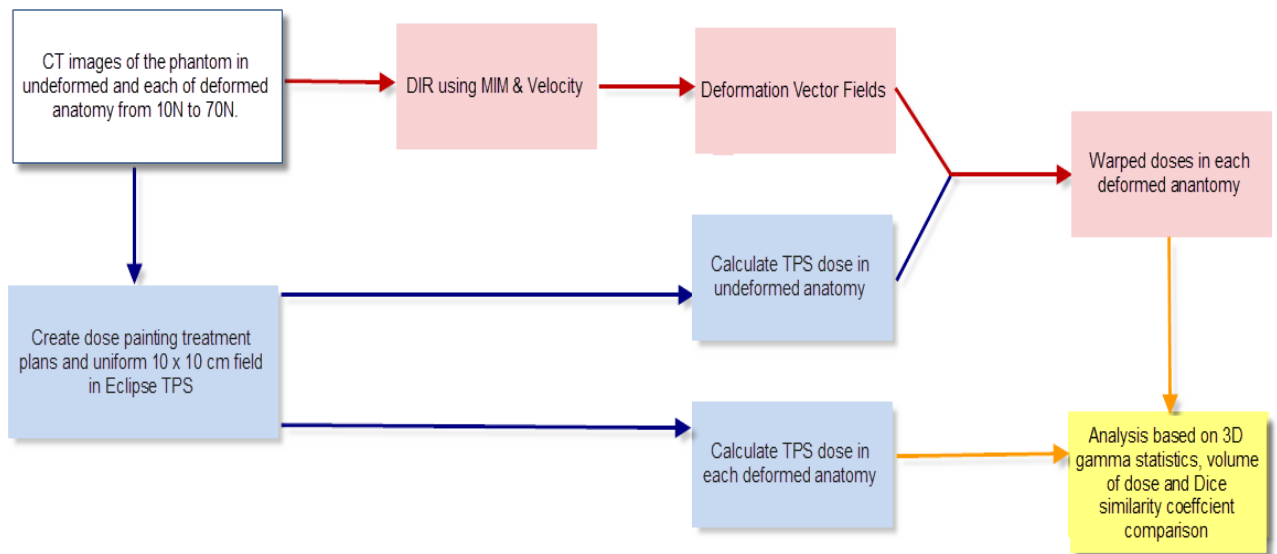
Figure 5.9 Flowchart illustrating the validation of dose warp accuracy in deformed

anatomy

Dose warping accuracy in reference anatomy:

The accuracy of dose warp in reference image is validated in this study using the

methodology outlined in the flow chart. (Figure 5.12). In contrast to the previous work

flow the roles of source and target image are switched here. If DIR and consequently

dose warping was perfect, then the magnitude of difference between $\{D_k - D_k*\}$ would

be zero. As before 3D gamma analysis was used to quantitatively evaluate the agreement

of 3D doses for each of the beam geometries studied.
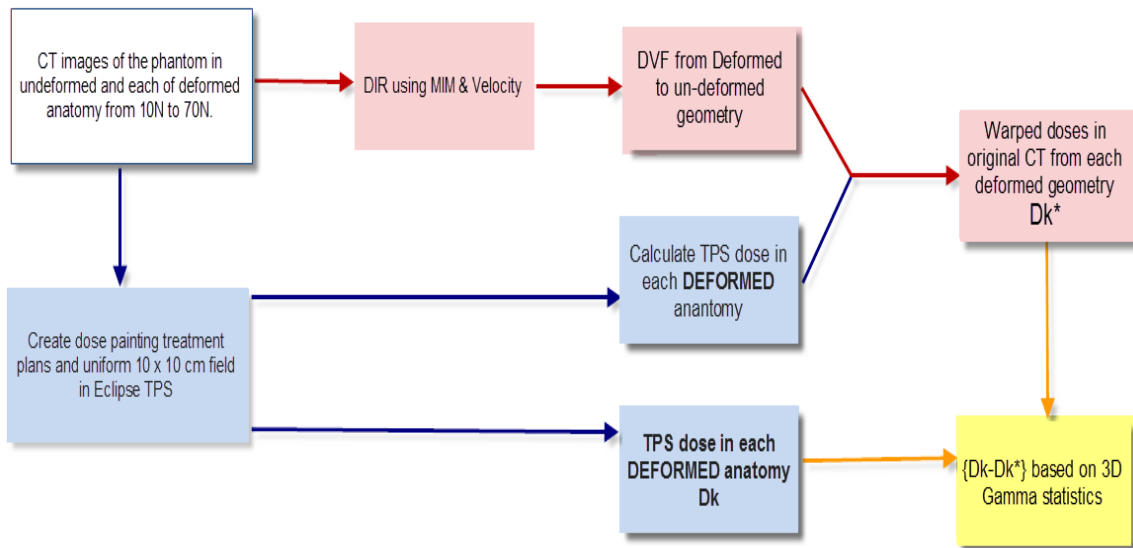
Figure 5.10 Flowchart illustrating the validation of dose warp accuracy in reference image.

5.11 Deformation states and dose paint spatial location beam geometries:

In this study we systematically deform the organ in successive increments by changing the applied force.

In this work we introduced islands of high doses (in addition to a reference 10 x 10 cm^2 field) at different spatial locations of the organ viz. a) along the edges and b) center of the organ to evaluate the accuracy of dose warp. It should be noted that often in a clinical context significant deformation occurs in the area of high dose gradients similar to the ones encountered in the prostate/rectal interface, parotid/tumor etc. Hence in this study we introduced islands of high doses where there is significant deformation as in the edges of the organ and moved the area of high dose paint from edges to the center of organ to study if the DIR based dose warping has any impact on the spatial location of dose paint for each of the deformation states. This was compared to a reference 10 x 10 cm^2 uniform

dose. The dose painting treatment plans were generated using Eclipse TPS by starting

with a standard 10 x 10 cm² field and then adding six sub fields with independent jaws of

varying field sizes to create a localized hot spot. AAA algorithm with 1mmm grid

resolution was used on all the treatment plans. All plans were generated with a fixed

gantry angle of 0 degrees (AP) 6MV photons beams and a prescription dose of 5Gy.

The beam parameters for the respective dose paint geometries are shown in Tables 5.6

and 5.7.

Table 5.6 Beam parameters for dose painting at superior and inferior edges of organ

Beam number	X1 jaw (cm)	X2 jaw (cm)	Y1 jaw (cm)	Y2 jaw (cm)	Monitor units
1	5	5	5	5	430
1.1	5	5	5	-3.0	30
1.2	5	5	5	-2.7	30
1.3	5	5	5	-2.4	30
1.4	5	5	-3.0	5	30
1.5	5	5	-2.7	5	30
1.6	5	5	-2.4	5	30

Table 5.7 Beam parameters for dose painting at center of organ:

Beam number	X1 jaw (cm)	X2 jaw (cm)	Y1 jaw (cm)	Y2 jaw (cm)	Monitor units
1	5	5	5	5	430

1.1	5	5	0.3	5	30
1.2	5	5	0.6	5	30
1.3	5	5	0.9	5	30
1.4	5	5	5.0	0.3	30
1.5	5	5	5.0	0.6	30
1.6	5	5	5.0	0.9	30

The resulting dose paint volumes are given in Figures 5.11 a b with Figure 5.11 c, showing a uniform 10 x 10 cm^2 field.

.
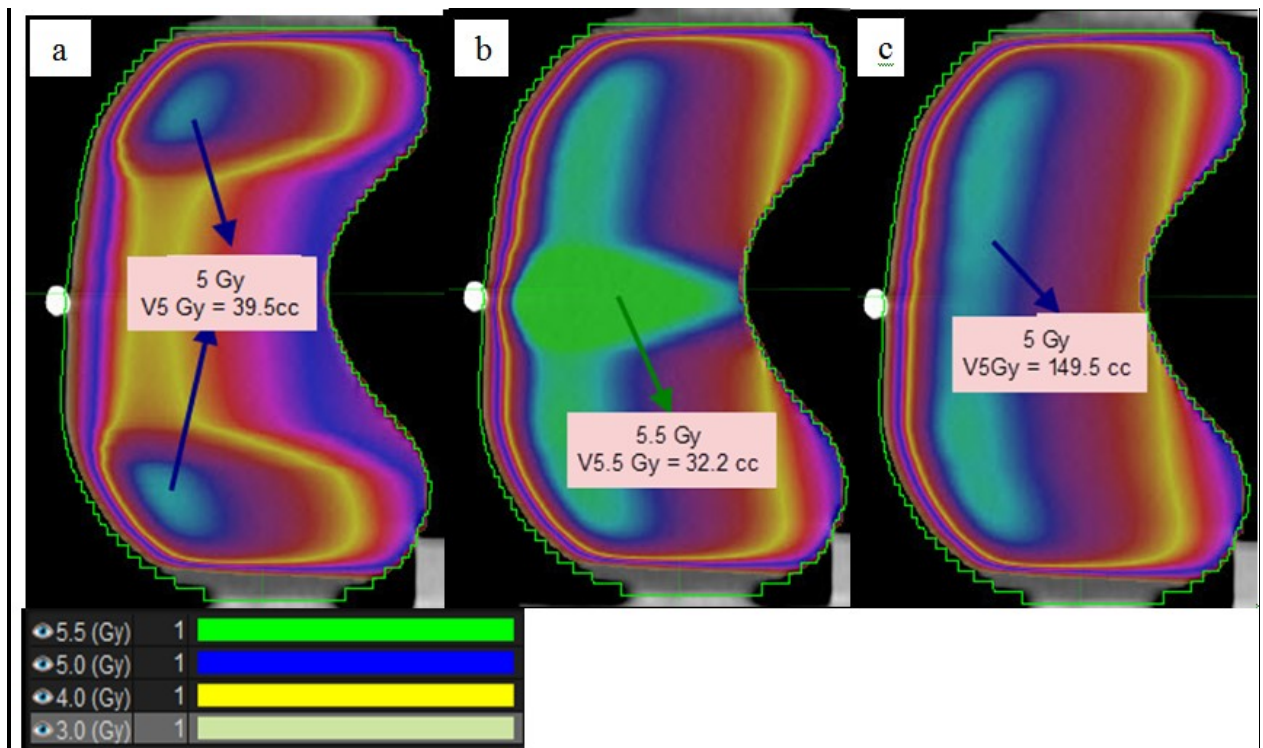
Figures 5.11, a, b, c above representing sagittal view of the phantom in undeformed state showing dose gradient at the edges, center and a uniform 10 x 10 cm field respectively.

5.12 Results of 3D dose warping

5.12.1 Response of applied force vs. deformation:

The applied force on the deformable phantom was incrementally varied from 10N to 70N

along the +z axis, deforming the phantom as shown in Fig. 5.12 a. The Dice similarity

coefficient (DSC) (defined in chapter 4) between the un-deformed organ surface and each

deformed organ surface as a function of applied force is shown in Fig 5.12 b. This gives

the extent of shape changes in volume of organ. As seen in 5.14 b the DSC is ≥ 0.9

between 10N to 30N applied force indicating that external shape changes of organ were

minimal up to 30N. This mass and density preserving deformation ranged from 3mm to

34mm along ±z axis, representing a bilateral compression of equal displacement from

both sides. The deformation showed a linear response to the applied force with $R^2 = 0.99$.

The 3D deformation as quantified by the 95% HD varied from 2mm to 16 mm with $R^2 =$

0.96. This is compared to the predicted deformation along the superior-inferior direction

(±z) using a simple linear elastic model for human bladder that follows Hooke's law, z =

$\frac{\Delta L}{L} = \frac{1}{E} * \frac{F}{A}$ where E= Young's modulus (16 Kpa) and $\frac{F}{A}$ (force per unit area) is the applied

load. (Fig. 5.12c).
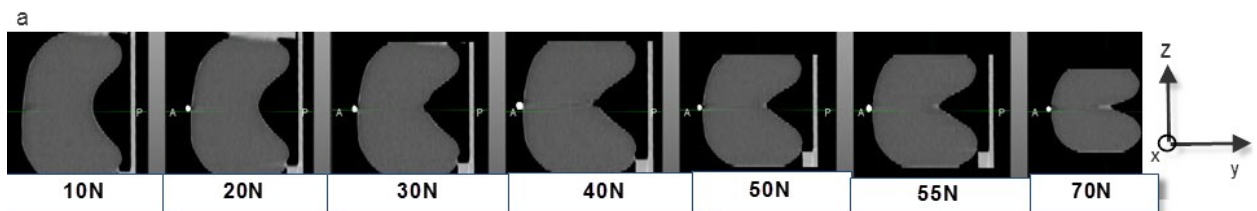
Fig. 5.12 a. Various deformation states of the phantom in response to applied force.
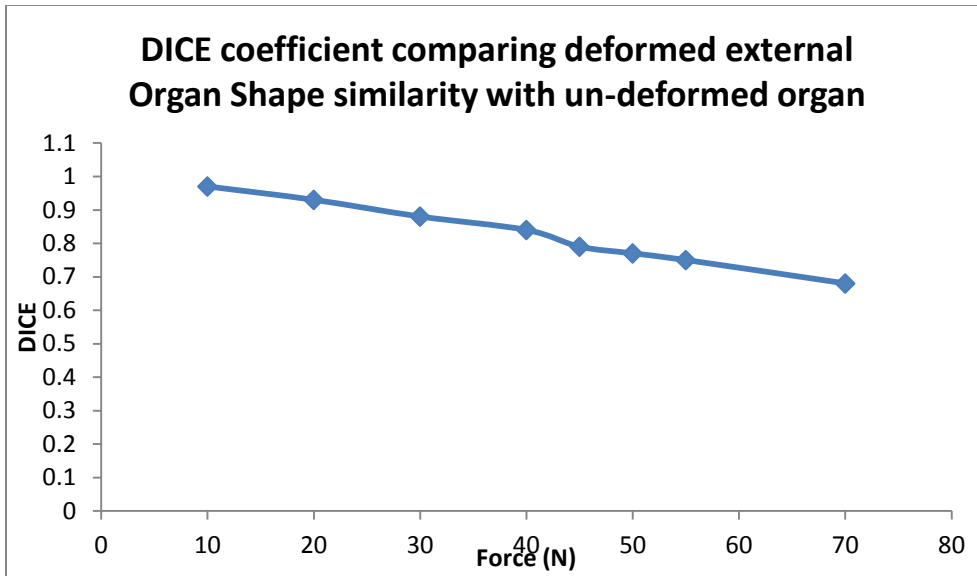
Figure 5.12 b. Dice similarity coefficient of external surfaces between un-deformed

organ and each deformed state of organ as a function of applied force
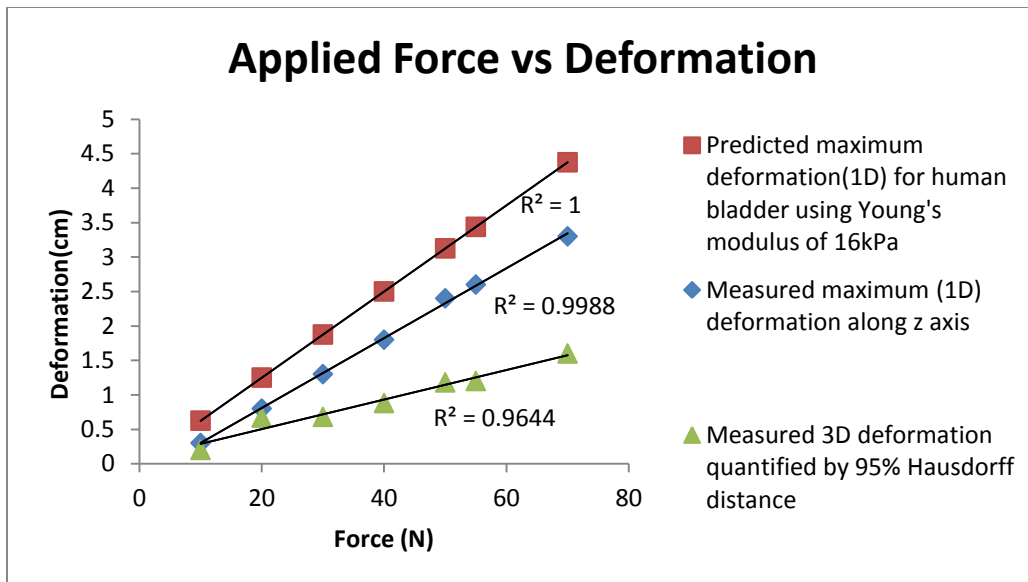
Fig. 5.12 c. Relationship between applied force and deformation observed in the

deformable phantom and predicted in human bladder.

5.12.2 Dose warp accuracy with 3D $\gamma_{3\%3mm}$ statistics:

145

Figs. 5.12 d-f, provide 3D $\gamma_{3\%3mm}$ pass rates at each deformation state for dose painting at the edges, center, and a uniform 10 x 10 cm^2 field respectively. Beyond a threshold applied force of 30N, $\gamma_{3\%3mm}$ pass rates fall below 90% for all commercial DIR algorithms, corresponding to 13 mm maximum organ deformation. For dose painting at the center, the dose warp accuracy yielded better results in the 10N to 40N applied deformation for the B-spline algorithm used by Velocity AI. The volume of high dose at the center was clearly misaligned in MIM beyond 30N as shown in Fig. 5.12 g. Using the $\gamma_{3\%3mm}$ metric, the magnitude of deformation was the sole predictor of the dose warp accuracy.
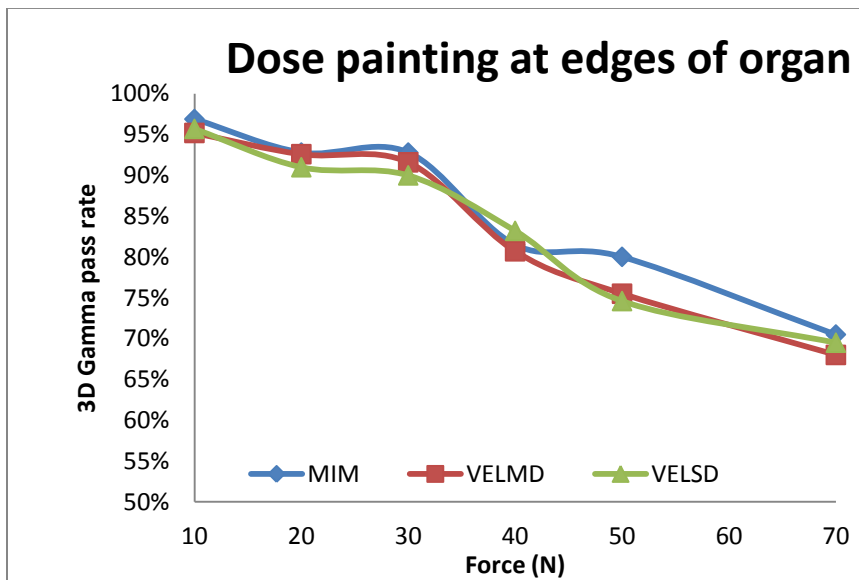
Fig. 5.12d. 3D $\gamma_{3\%3mm}$ pass rates for dose painting at the edges of organ
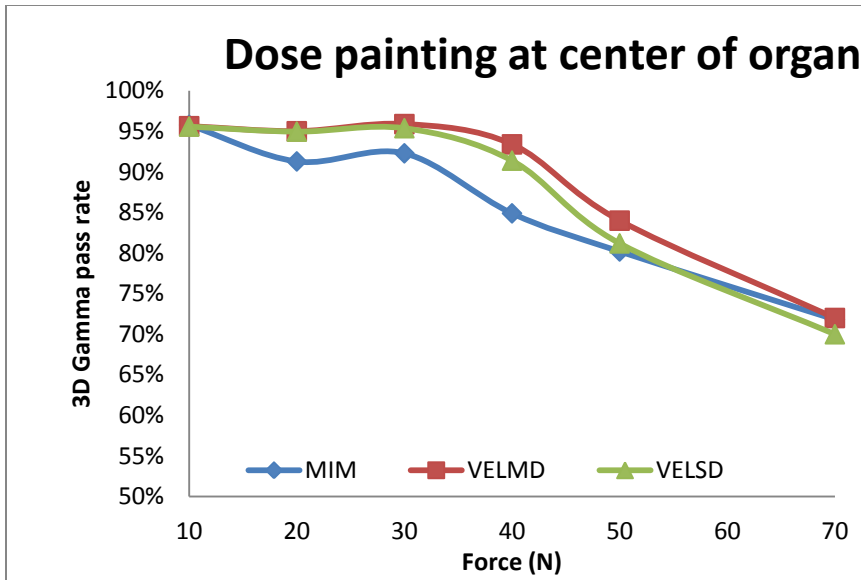
Fig. 5.12e. 3D $\gamma_{3\%3mm}$ pass rates for dose painting at the center of organ
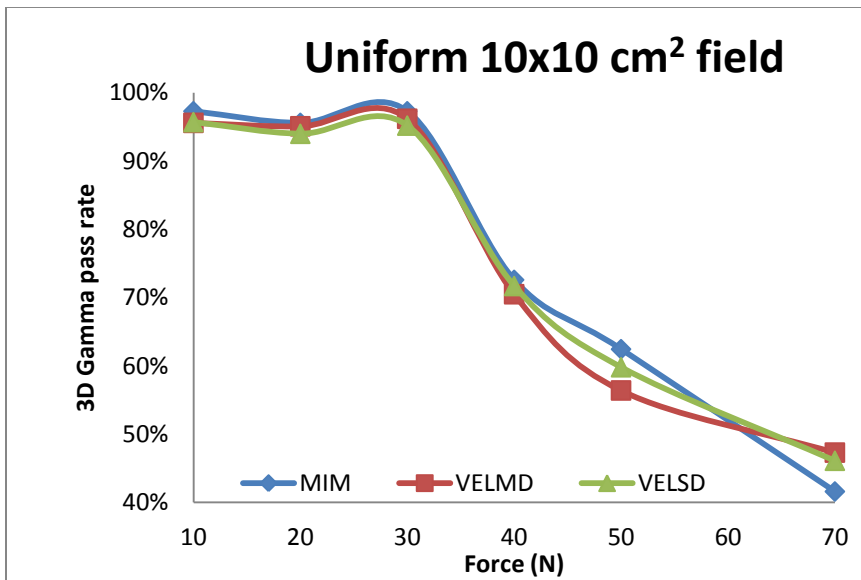
Fig. 5.12f. 3D $\gamma_{3\%3mm}$ pass rates for a uniform 10 x 10 cm^2 field
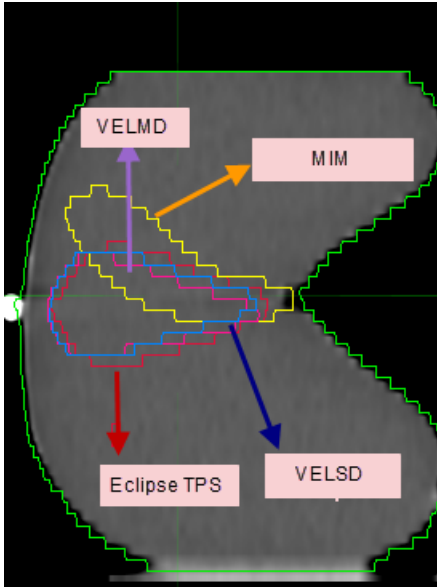
Fig. 5.12g Sagittal view (y-z plane) of bladder phantom displaying calculated dose (from TPS) received by organ at 40N deformation and corresponding warped doses from DIR for center dose painting plan.

5.12.3 Dose warp accuracy using volumes of high dose comparison:

Figs. 5.12 h-j displays the conformity index (defined as the ratio of volume of high dose from DIR to the corresponding volume from TPS) at each deformation state as a function of applied force. A conformity index of 1.0 would indicate perfect agreement between the dose volumes. For dose painting scenarios, none of the DIR algorithms studied were shown to accurately represent the volume of dose received by the organ, even at low deformation levels (Figs. 5.12 h,i).

For a uniform homogenous dose, the conformity index is within ± 2% for applied forces of up to 30N (Fig. 5.12j), indicating results in line with the $\gamma_{3\%3mm}$ pass rates.
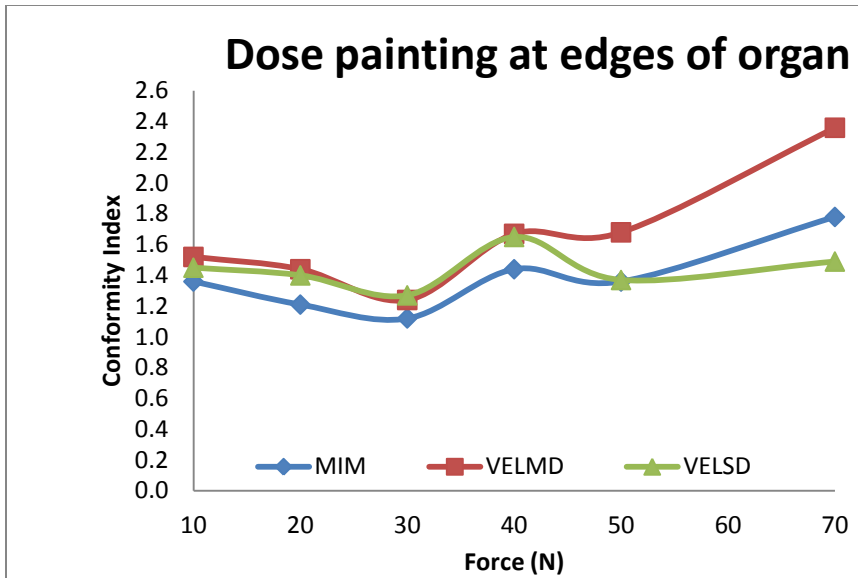
Fig. 5.12h. Conformity index at 5Gy for the dose painting at the edges of the organ
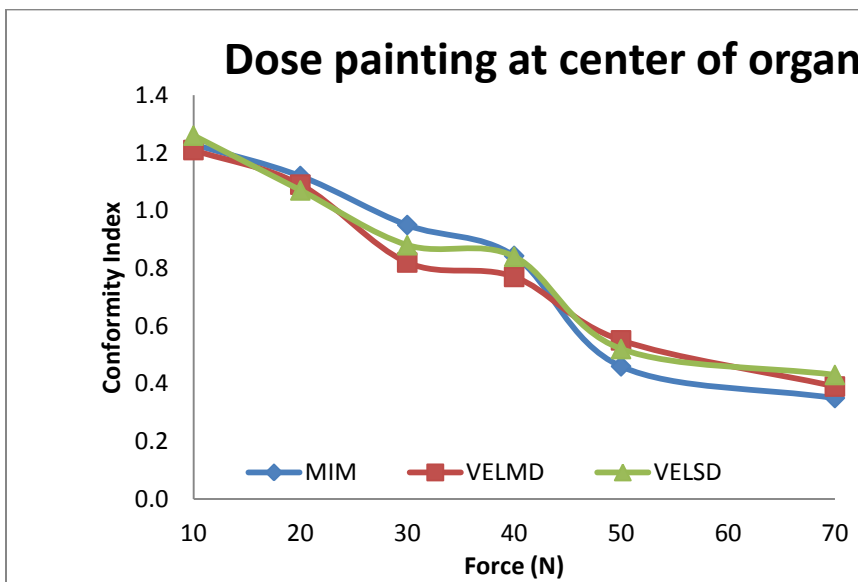
Fig. 5.12i. Conformity index at 5.5 Gy for dose painting at center
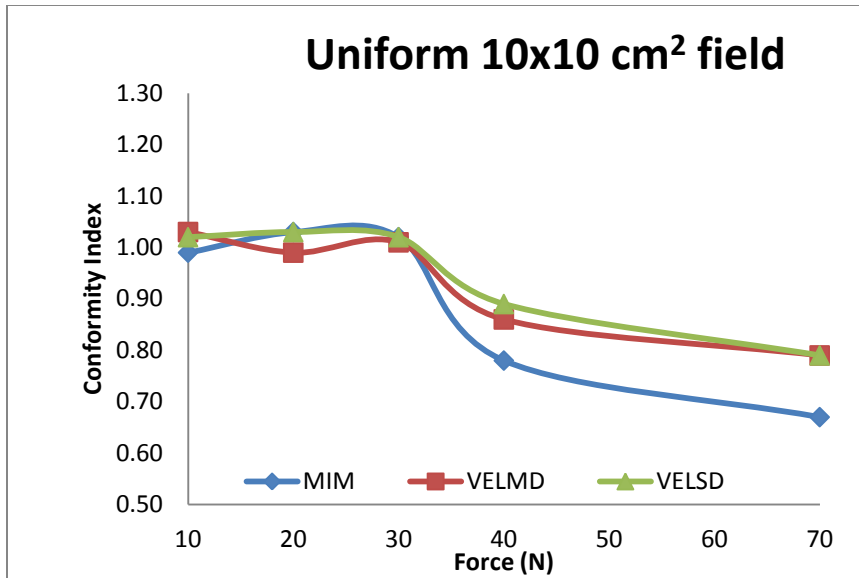
Fig. 5.12j. Conformity index at 5Gy for a uniform 10 x 10 cm^2 field

5.12.4 Dose warp accuracy comparing Dice similarity coefficient between high dose volumes:

Figs. 5.12 k-m displays the Dice similarity coefficient (DSC) at each deformation state as a function of applied force for the high dose volumes. A DSC of 1.0 would indicate perfect agreement between the overlap of dose volumes. For dose painting scenarios, none of the DIR algorithms studied were shown to accurately represent the dose volume overlap at 5Gy and 5.5 Gy doses, even at low deformation levels (Figs. 5.12k,l). For a uniform homogenous dose, (10 x 10 cm^2 field) the DSC is within ± 6% for applied forces of up to 30N (Fig. 5.12m), indicating results in line with the $\gamma_{3\%3mm}$ pass rates.
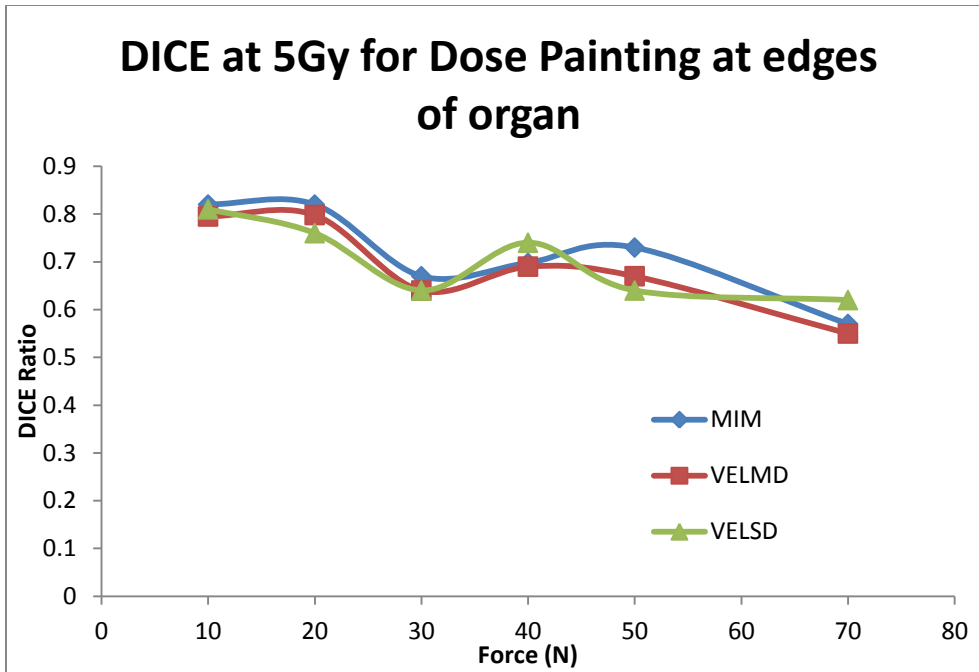
Fig. 5.12k. DSC at 5Gy for the dose painting at the edges of the organ
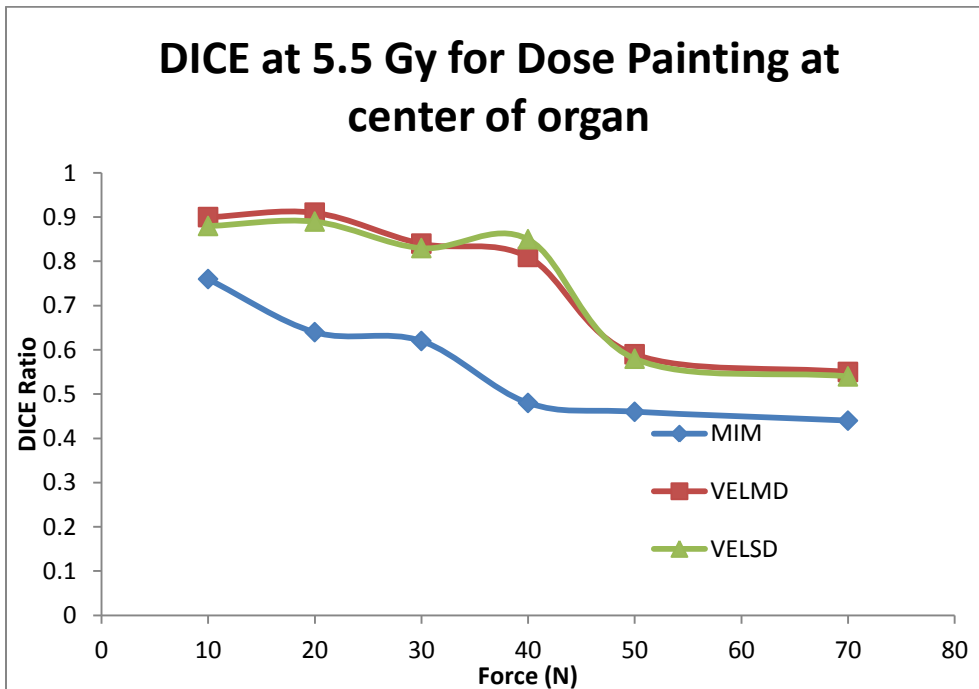
Fig. 5.12l. DSC at 5.5 Gy for dose painting at center
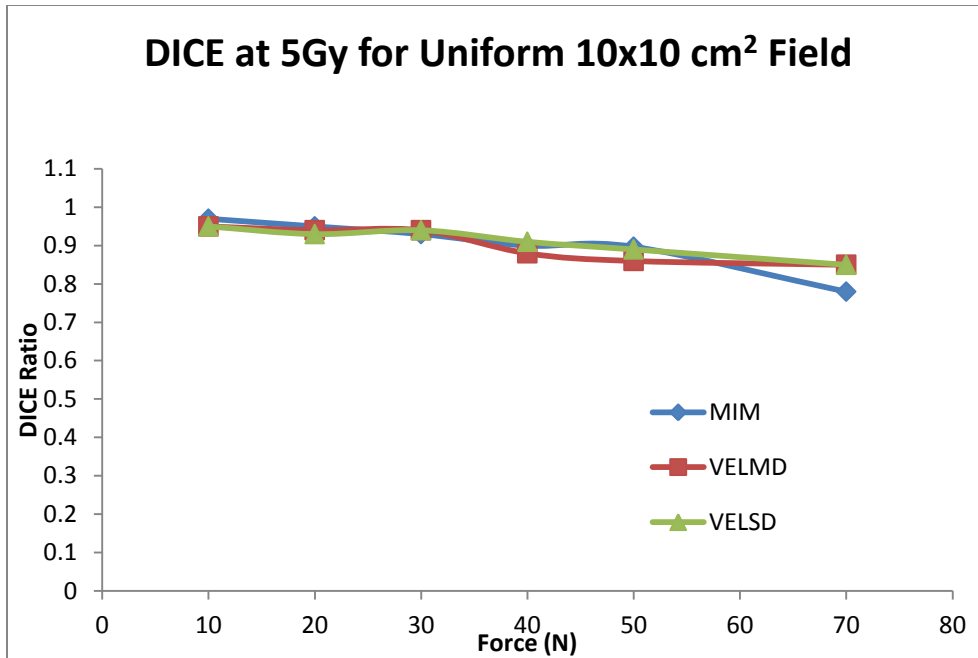
Fig. 5.12m. DSC at 5Gy for a uniform 10 x 10 cm² field

5.12.5 Dose warp accuracy comparing 95% HD between high dose volumes:

Figs. 5.12 n-p displays the 95% HD (mm) compared between dose volumes from DIR algorithms and TPS dose at each deformation state as a function of applied force. This indicates the spatial distance of the high dose volume from DIR algorithms away from true dose received by the organ (TPS).
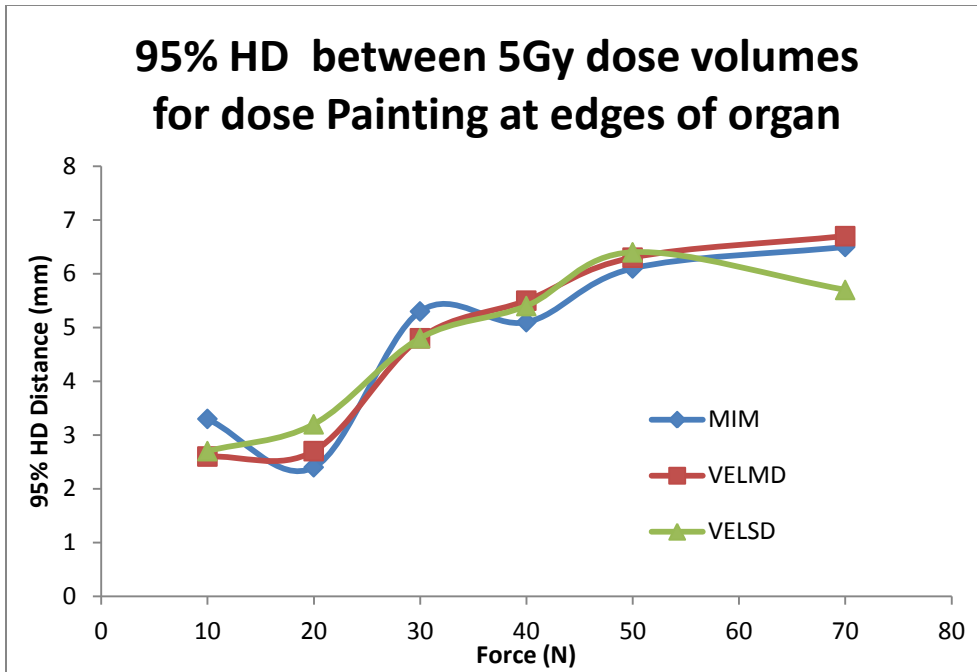
Fig. 5.12n. 95%HD between 5Gy dose volumes for the dose painting at the edges of the organ
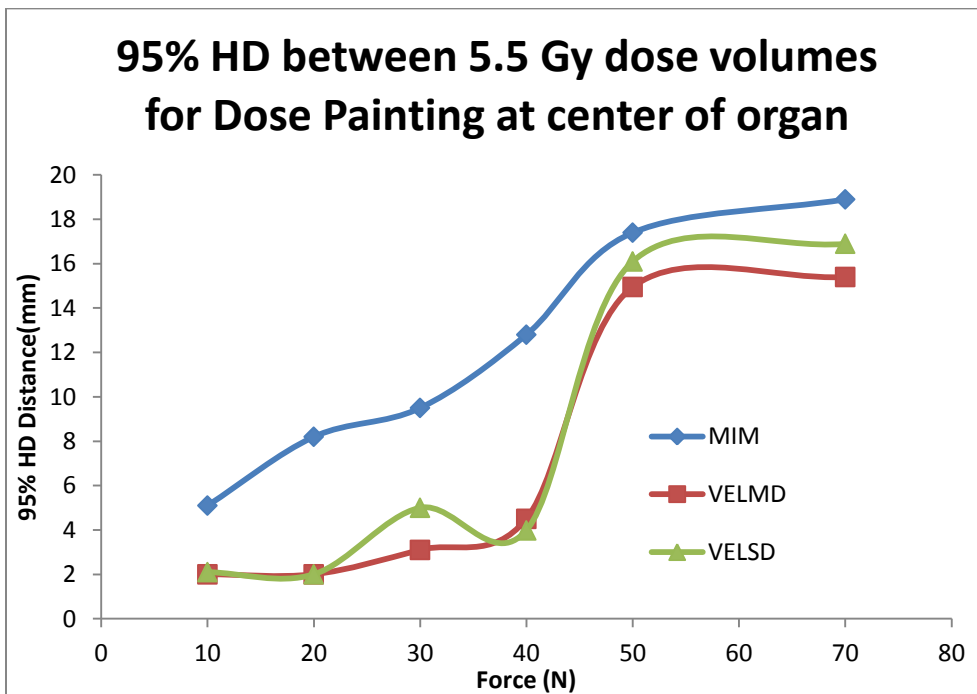
Fig. 5.12o. 95% HD between 5.5 Gy dose volumes for dose painting at center
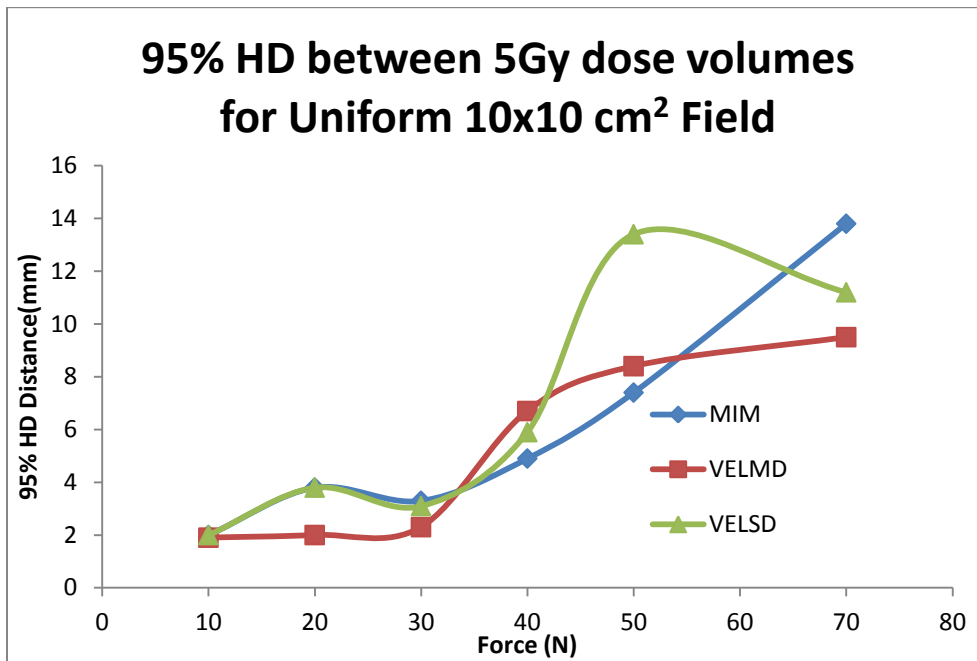
Fig. 5.12p. 95%HD between 5Gy dose volumes for a uniform 10 x 10 cm^2 field

5.13 Dose warp accuracy in reference geometry with 3D $\gamma_{3\%3mm}$ statistics:

Figure 5.13a   below gives the 3D gamma pass rate between un-deformed organ and each

deformed state of the organ as a function of applied force for each beam geometry

studied. This figure illustrates what the dose errors in a deforming organ would result if

dose warping was not employed. As shown in figure, the maximum disagreement and

necessity for dose warping is warranted for dose painting at edges of the organ where

there is maximum dose gradient and deformation.

Figs. 5.13 b-d, provide 3D $\gamma_{3\%3mm}$ pass rates when comparing the warped dose in

reference geometry to the true dose in deformed geometry each deformation state for

dose painting at the edges, center, and a uniform 10 x 10 cm^2 field respectively.

As it can be seen, none of the DIR algorithms performed well in showing an improvement over baseline disagreement induced due to organ deformation.
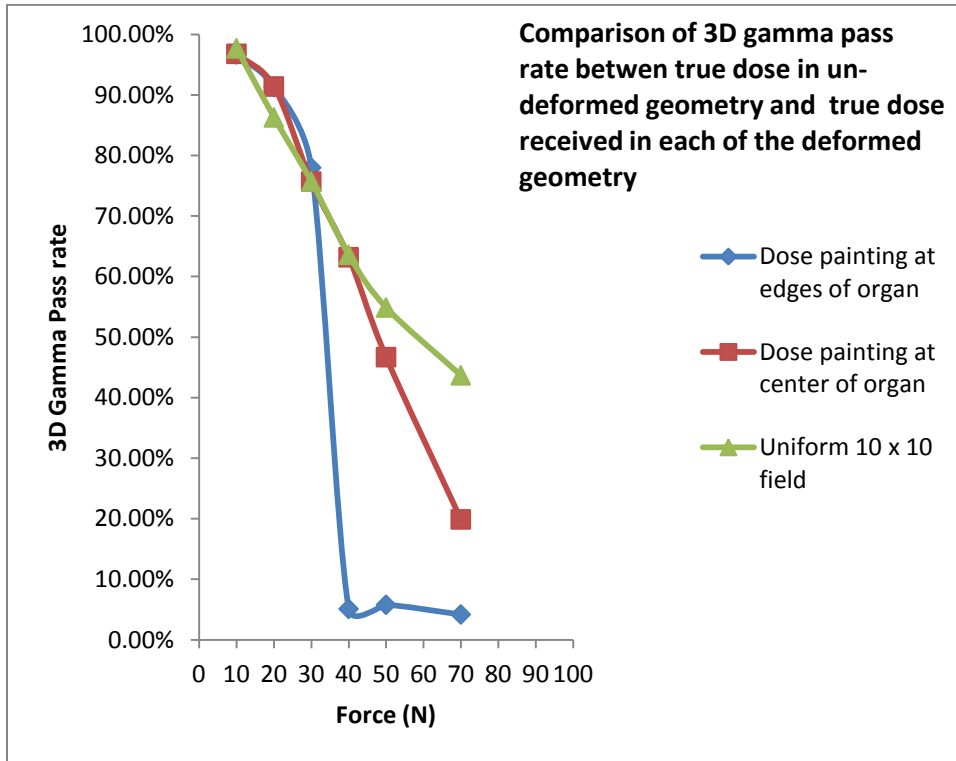
Fig. 5.13a. 3D $\gamma_{3\%3mm}$ pass rates between un-deformed organ and each of the deformed state of the organ as a function of applied force for all the beam geometries
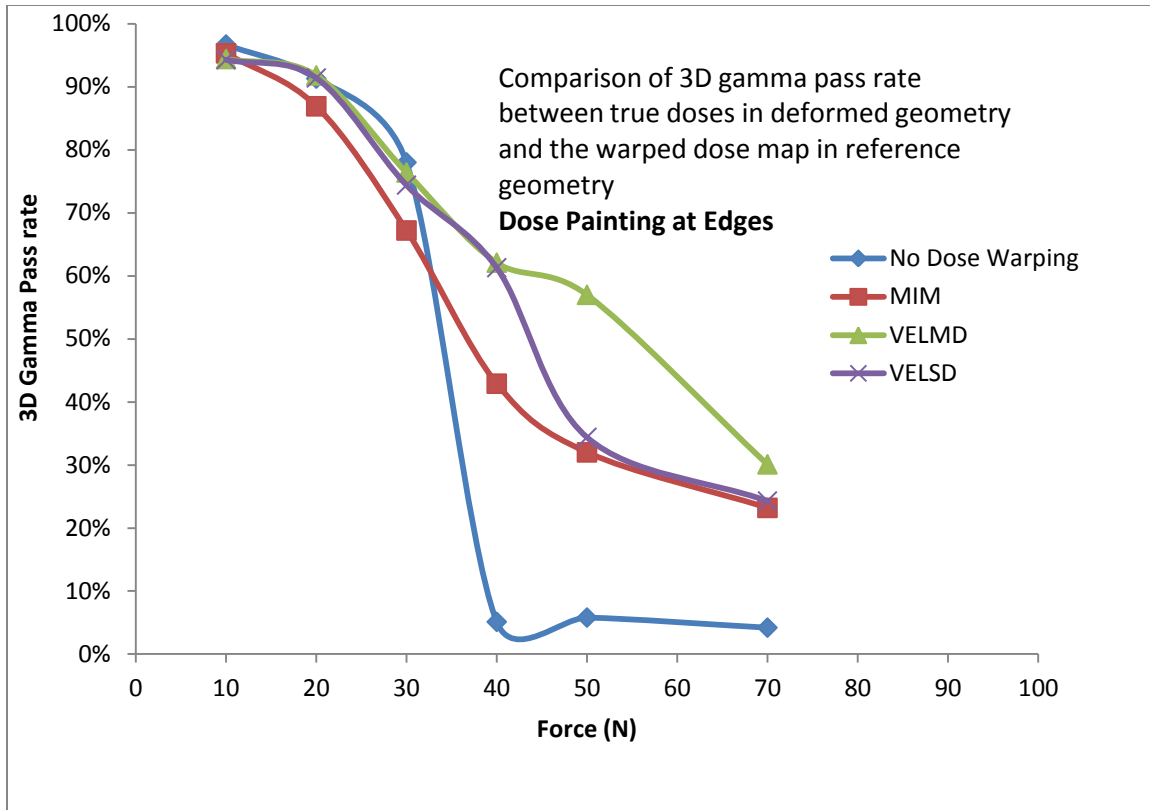
Fig. 5.13 b. 3D $\gamma_{3\%3mm}$ pass rates between warped dose in reference geometry for dose painting at the edges of organ when compared to the true dose received by the organ in deformed geometry
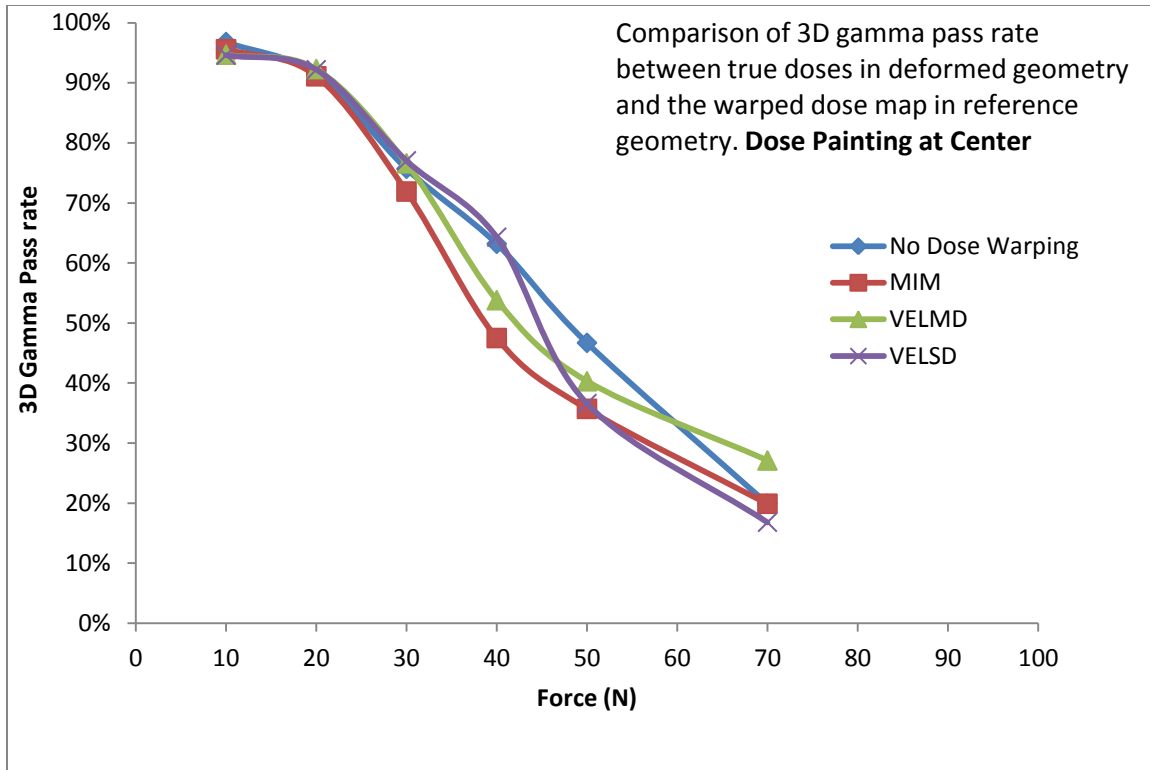
Fig. 5.13 c. 3D $\gamma_{3\%3mm}$ pass rates between warped dose in reference geometry for dose painting at the center of organ when compared to the true dose received by the organ in deformed geometry
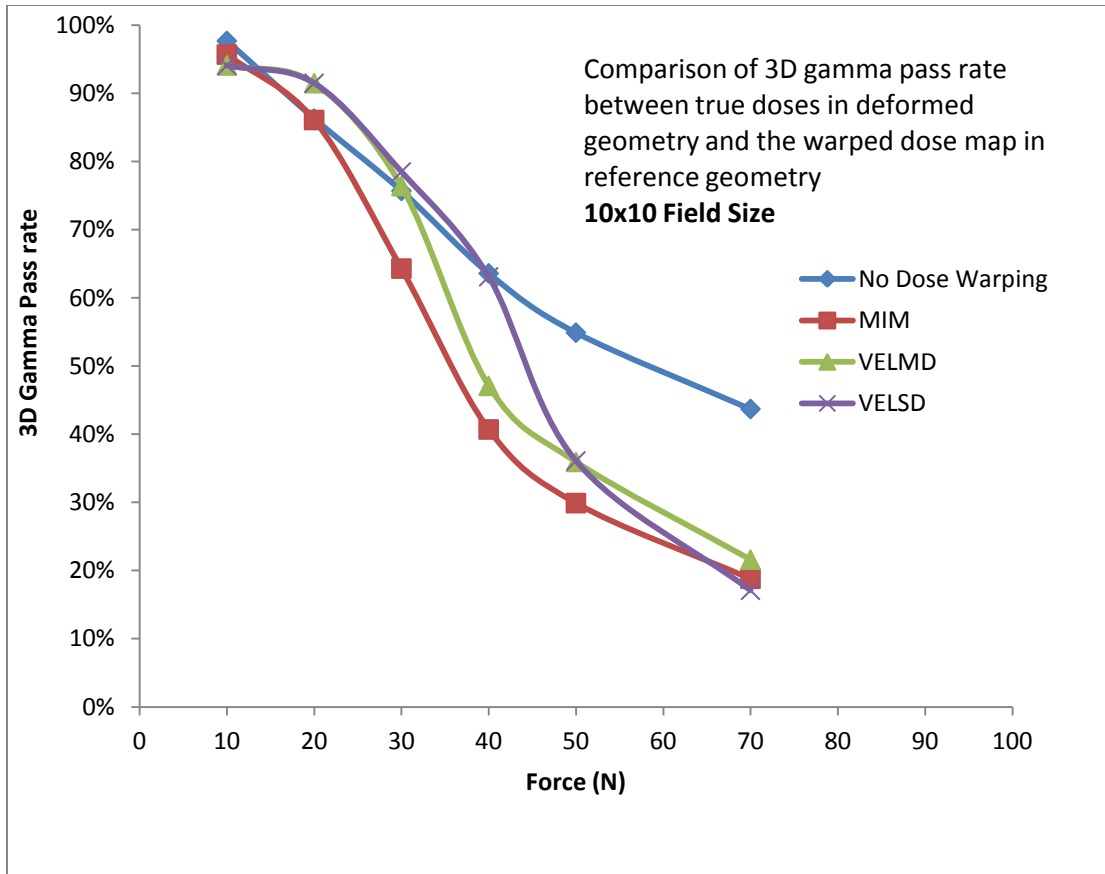
Fig. 5.13 d. 3D $\gamma_{3\%3mm}$ pass rates between warped dose in reference geometry for uniform 10 x 10 cm^2 field when compared to the true dose received by the organ in deformed geometry

5.14 Discussion.

We have established a threshold limit of 13mm maximum 1D and 6.8mm 3D deformation beyond which dose warp accuracy fails for both uniform homogeneous dose and dose painting geometries. The linear response observed in this study between applied force and deformation is typical of the biomechanical properties of human bladder in contrast to other pelvic organs like rectum, vaginal tissue and liver which show increased resistance to deformation with applied force [208, 209] .

Although 3D gamma ($\gamma_{3\%3mm}$) pass rates (in the deformed geometry) are excellent up to 30N for the dose painting geometries studied, the conformity index(average dose volume 30 cc or greater) differs by 20% or larger even for the lowest deformation studied. This is in contrast to a uniform 10 x 10 cm^2 field where the $\gamma_{3\%3mm}$ pass rates and conformity index studied at 5 Gy dose level agree with one another. This is also consistent with Dice similarity coefficient comparison (DSC) between high dose volumes from dose painting. Even at the lowest 10N applied force, the DSC between 5Gy dose volumes is only 0.82 for dose painting at the edges of the organ. Thus, although a uniform homogeneous dose may yield acceptable results in terms of both 3D gamma pass rates and volume of dose received by the organ, this does not apply for dose painting. As a result, while employing dose warping for dose painting scenarios like those encountered in Stereotactic Body Radiation Therapy (SBRT) and other hypofractionated treatments with adaptive radiotherapy potential, the volume of dose received by the target from dose warping needs to be evaluated because dose painting is done under the assumption that high dose gradients are localized to the target.

Further when the warped dose in reference geometry was compared to the true dose received by the organ in deformed geometry (Section 5.13), all the DIR algorithms performed poorly. There was no significant improvement over the baseline disagreement except at greater than 40N induced deformation, for dose painting at the edges of organ. In many instances it was found that dose warping induced more errors than the baseline disagreement.

It should be noted that although boundary matching appears perfect even at 70 N (34mm deformation) between images from all the DIR algorithms, this does not guarantee the

accuracy of dose warping. Dose warp accuracy is a function of registration accuracy and dose gradient at a particular voxel. As a result, a small registration error at a high dose gradient will likely have a greater impact on the overall dose warp accuracy as compared to a larger registration error at a low dose gradient[127]. This effect is shown in the gamma wash color map at 40 N (18 mm deformation) for dose painting at the edges of organ. The maximum disagreement as indicated by the red color wash ($\gamma_{3\%3mm} > 1$) occurs in the area of high dose gradient and large deformation for all the DIR algorithms studied (Fig.5.14 a-c). Although beyond the scope of this study, the high dose islands described at the edges of the bladder phantom are routinely encountered in clinical practice in intensity modulated treatment of prostate cancer. Fig. 5.13d shows a typical patient anatomy with overlap of prostate with bladder and rectal volumes along with the prescribed target dose (75.6 Gy) at the edges of bladder. The deformation of organs and the resultant dose warp accuracy for dose painting as described in this study will have a significant impact on the partial dose volumes received by the organs at risk.
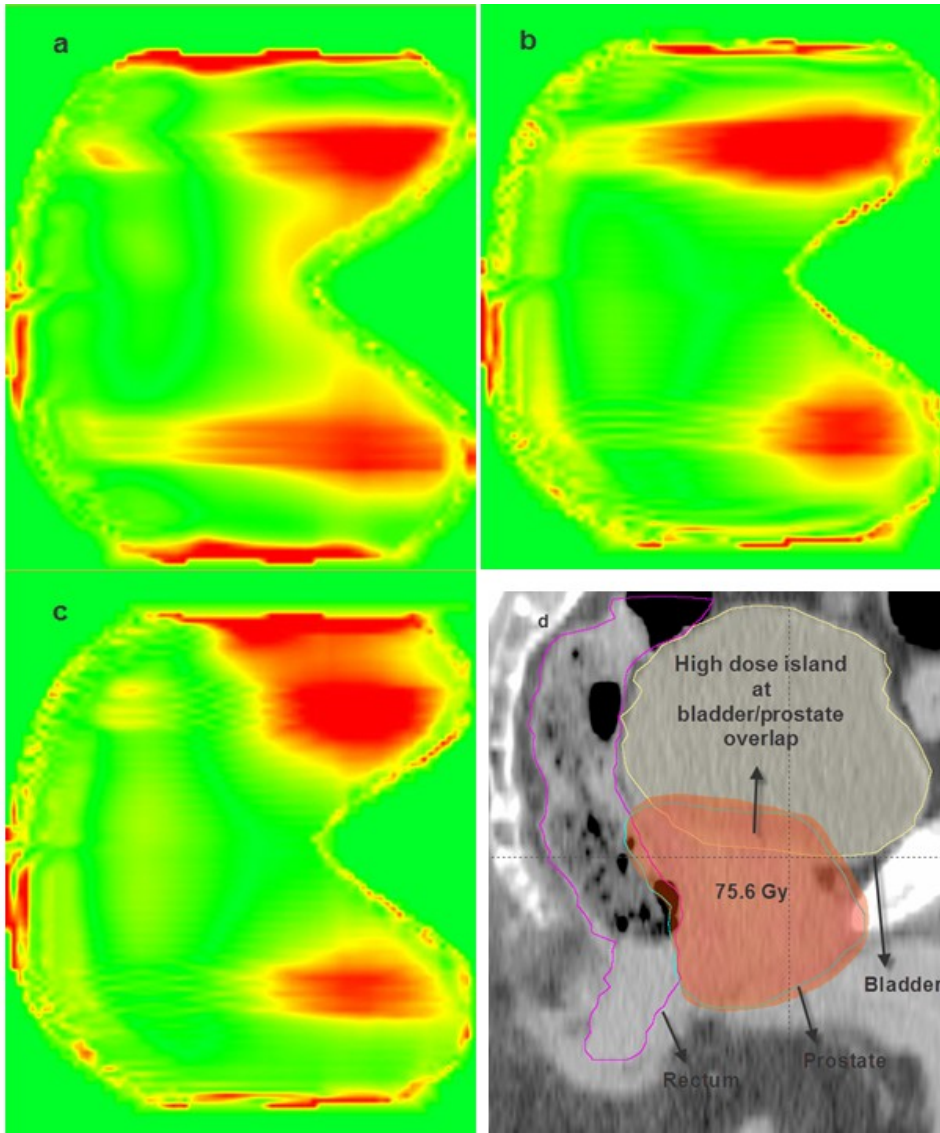
Figs. 5.14 a, b, c showing sagittal view (y-z plane) of gamma volume at 40N deformation for dose painting at the superior and inferior edges of the organ for MIM, VELMD and VELSD DIR algorithms respectively.

Fig 5.14 d Sagittal view of a typical patient anatomy with prostate, bladder and rectal volumes showing high dose islands at the edges of the organs at risk as studied in the deformable bladder phantom

It is known that the smoothing parameters used in DIR algorithms have a significant impact on dose warp accuracy[104]. MIM uses an intensity based algorithm which seeks to minimize the intensity differences between two images while the intensity based B-spline algorithm used by VelocityAI tries to balance both the intensity information regularized by the inherent cost function and the spatial information regularized by the smoothness criteria[174]. The presence of uniform low contrast regions throughout the deformable bladder phantom makes this scenario particularly challenging for both the commercial algorithms studied because of the lack of intensity differences in the internal anatomy of the phantom. In the absence of user ability to edit the deformation parameters in the commercial DIR platforms, both the algorithms interpolated the deformation incorrectly in low contrast regions as the deformation was increased beyond 30N causing the resultant errors in dose warping. It is likely that the registration accuracy and consequently the dose warping accuracy would have been improved in the presence of high contrast features like implanted fiducial markers inside the phantom as found in the study using deformable gel[102] . A similar approach with implanted aluminum fiducial markers will be done in future studies using the deformable bladder phantom.

The deformable phantom used in this study has a uniform CT number (± 10 HU) and density similar to bladder, prostate, pancreas, stomach, kidney, liver, breast, diaphragm etc., in human anatomy[102, 171] and, as such, the results in this study would apply to those organs. The results do not apply to dose warp accuracy in density changing anatomy like the lung or where the mass is not conserved (full vs. empty bladder, organ atrophy, tumor inflammation etc). Although symmetric bilateral compression was studied, future study will include asymmetric compression, changes in the direction of

applied force, and 3D compression. The viscoelastic polymer used can be molded to any organ shape and has the potential to adjust the tensile properties to match other organs in human anatomy which will be subject of future work.

5.15 Conclusion

We have demonstrated the efficacy of dose warping using a tissue equivalent deformable bladder phantom for a range of mass and density preserving deformation states. The deformation observed was correlated with the applied force showing a linear response for both 1D and 3D deformation. A threshold limit of 13mm maximum deformation (1D) along direction of applied force and 6.8 mm 3D deformation was established beyond which deformable dose from DIR algorithms does not agree with true dose received by organ in terms of 3D $\gamma_{3\%, 3mm}$ criteria for the commercial DIR algorithms studied. This illustrates dose recalculation may be necessary for deformations larger than the threshold limit derived. For dose painting, although warped doses from DIR may agree with the TPS dose in the deformed geometry in terms of overall γ_{3D} pass rates, the dose volumes from DIR may be significantly different from the true volume of dose received by the target. None of the DIR algorithms studied were able to accurately model the dose warping in reference image when compared to the true dose received by the organ in deformed geometry due to the uniform low contrast regions present throughout the bladder phantom.

In the absence of user ability to edit the deformation parameters in the commercial DIR platforms, one should carefully evaluate the dose warp accuracy in a clinical context before routine implementation. The accuracy of deformable image registration does not guarantee accuracy of deformable dose.

Chapter 6 Summary and applications for future work

6.1   Summary and general conclusions:

In this dissertation we have presented a framework to include organ deformation in adaptive dose delivery. First, the need for clinical adaptation of treatment plans was demonstrated using daily imaging data from 10 patients treated for localized prostate cancer[16].

It is clear DIR is needed to translate anatomical information between two imaging study sets that exhibit organ deformation. Although there are various DIR algorithms available, there is no universal consensus on how to validate their accuracy in the context of radiotherapy clinical applications.

DIR validation using deformable physical phantoms is an extremely challenging task given the fact no physical phantom can be sophisticated enough to reproduce the various organ deformations occurring in human body. Our work is the first published data that presented a novel way to evaluate DIR performance by synthetically deforming patient CT data to mimic clinically observed organ deformation and using the DVF from that as the ground truth to evaluate the accuracy of DIR[18]. This approach has since gained acceptance in the radiation oncology community as other research groups have used a similar approach to validate the accuracy of DIR [174, 210]. The framework presented in our work based on anatomical correspondence, physical characteristics of deformation field and image characteristics can facilitate DIR verification with the ultimate goal of implementing adaptive radiotherapy. One of the major conclusions of our study[18] was the fact that although there are several methods to evaluate the accuracy of DIR (Inverse consistency error, Mean square error, accuracy of RT structures, etc..) the clinical

applicability of a particular chosen metric to evaluate the accuracy of DIR depends on the deformation observed.

This dissertation also establishes the fundamental relationship between organ deformations with the physical force producing it as in the case of a second generation medical simulator (Fig 1.7 in chapter 1). This work was the first study from a radiation therapy investigation that evaluated the organ deformation and subsequent dose warping accuracy from the "dose deformation "workflows in commercial DIR platforms from the context of applied force. A quantitative relationship between force and deformation has the potential to create simulated deformations of various organs if their biomechanical properties are known and can be potentially used by clinicians to adapt margins in a dose painting scenario. A deformable bladder phantom with mechanical and tensile properties comparable to human bladder was designed which was used to assess dose warp accuracy from various commercial DIR algorithms studied. Our study also highlights the importance of validating the volume of dose from various DIR algorithms as traditionally used 3D gamma pass rates may not accurately describe dose warping for dose painting scenarios. An entire range of organ deformation from 3mm (10N) to 34mm (70N) was studied representing symmetric bilateral compression of equal displacement. Our future study will include asymmetric compression, changes in the direction of applied force, and 3D compression. The viscoelastic polymer used can be molded to any organ shape and has the potential to adjust the tensile properties to match other organs in human anatomy which will be subject of future work.

In the next section we highlight the potential applications of the methods and tools developed as part of this dissertation to other radiotherapy clinical applications which will also be subject of future work.

6.2 Implanted fiducial markers in the deformable bladder phantom

As discussed in section 5.14 in chapter 5, the principal reason for failure of DIR based dose warping was because of the presence of uniform low contrast regions in the deformable bladder phantom where the accuracy of DIR algorithm and the generated DVF is prone to errors because of the lack of information or features that drive the re-distribution of voxels. Consequently any DIR algorithm will work more optimally if there are contrast rich features between the source and target images. To improve the applicability of dose warping and test the results for the same applied deformation as before, we implanted 21 aluminum markers distributed at random locations across the phantom as shown in figure 6.1 below. 18 markers were 1.5mm in size while 3 markers were 2.5 mm in size. The implanted markers will also be used to test the accuracy of image registration by comparing the position of fiducial markers from direct measurement in target image (undeformed) to those obtained from the calculated image obtained by applying the corresponding DVF to each deformed image from 20N to 70N. An example image at 20N deformation is shown in figure 6.2 below.
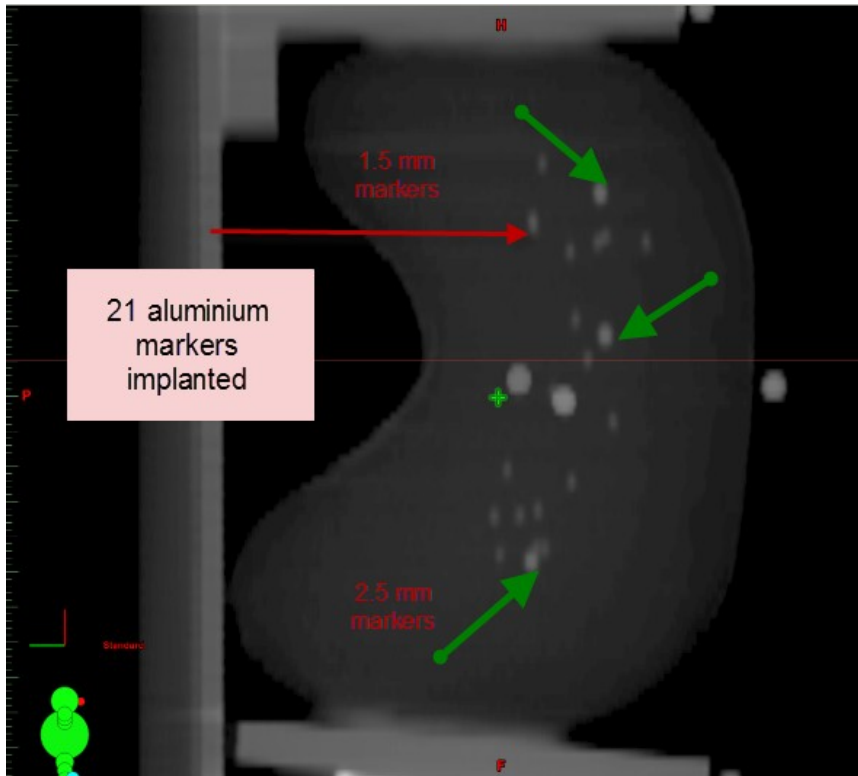
Figure 6.1: 21 implanted aluminum markers in deformable bladder phantom to improve

the accuracy of DIR in low contrast regions
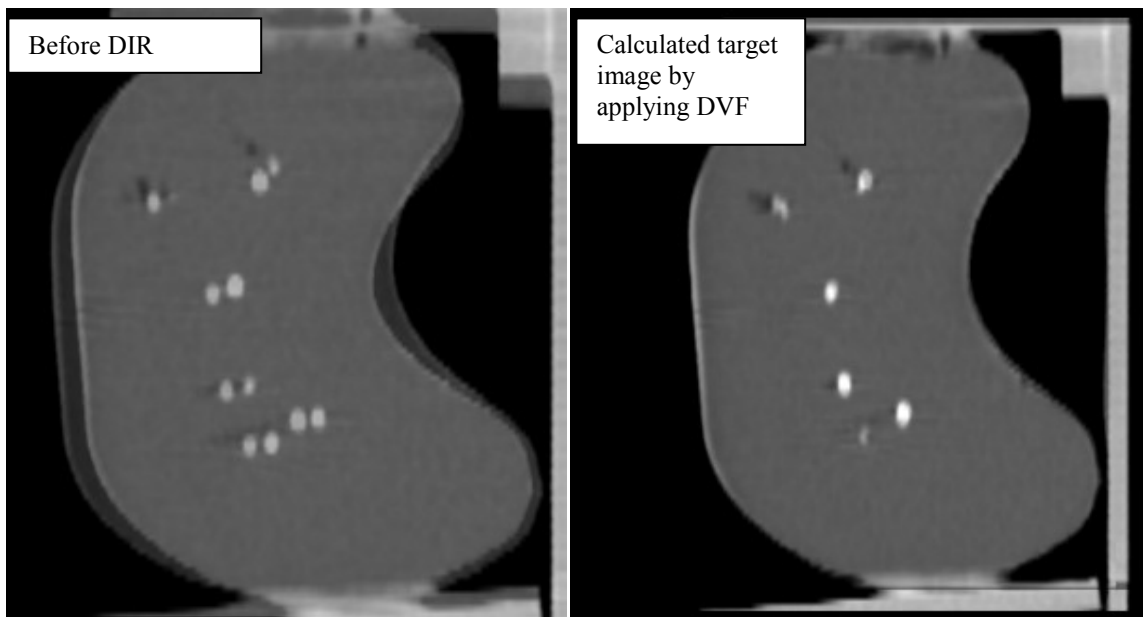
Figure 6.2: Position of fiducial markers before and after applying the DVF at 20N

deformation

6.3 Extension of current project to other radiotherapy clinical applications

In this section the application of tools and methods developed as part of this dissertation to other potential clinical applications will be highlighted.

Lung

It is well known that the chest wall is an important dose limiting structure when treating lung tumor or breast tumor. Understanding the characteristics of chest wall motion is poorly known. As reported in Hui *et al[211].*, inadequate margin around chest wall may under dose to the chest wall. Further, overdosing the ribs can cause chest wall toxicity. Studies have shown that 30 Gy to the chest wall can cause severe fractures to the ribs along with pain.

Several studies have shown rib fractures have been observed with doses as low as 20-26 Gy.[212-214] . For example Stephans et al[213] retrospectively contoured the chest wall for 45 SBRT patients who were treated using treatment plans without specific chest wall avoidance criteria. After a median follow up of 18.8 months, 10 patients were shown to have chest wall toxicity which was correlated to tumor size and the chest wall dosimetry. We studied the motion of the ribs in order to determine the margin that should be placed on the chest wall due to motion, to quantify the dose error at each position[29]. Our procedure includes importing the MIP (Maximum Intensity Projection), AVGERAGE, and non-gated CT scan and contouring a GTV on each image set. The GTV volumes are combined to make the treatment target volume. (ITV,internal target volume). We determined 3 points in the CW by using an x,y,z coordinate on the planning system for 7 patients and observed the motion for each point in the 10 phases. We examined the

diaphragm displacement in each phase (0%-90%, 10% increments) and also at the

corresponding displacement of the chest wall. (See figure 6.3 and 6.4). The motion

during each phase was quantified and averaged for 7 patients. The chest wall motion was

compared to the diaphragm motion and the tumor motion in order to determine the

relationship of the motion and the corresponding dose error to the chest wall due to
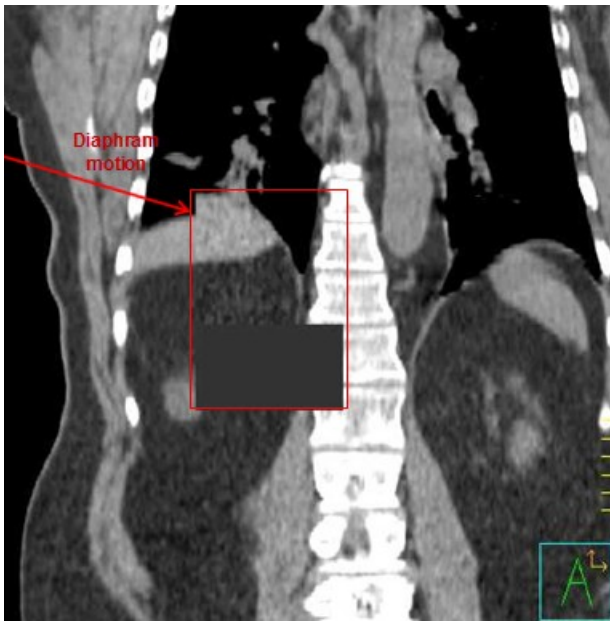
motion

Figure 6.3 illustrating the motion of diaphragm
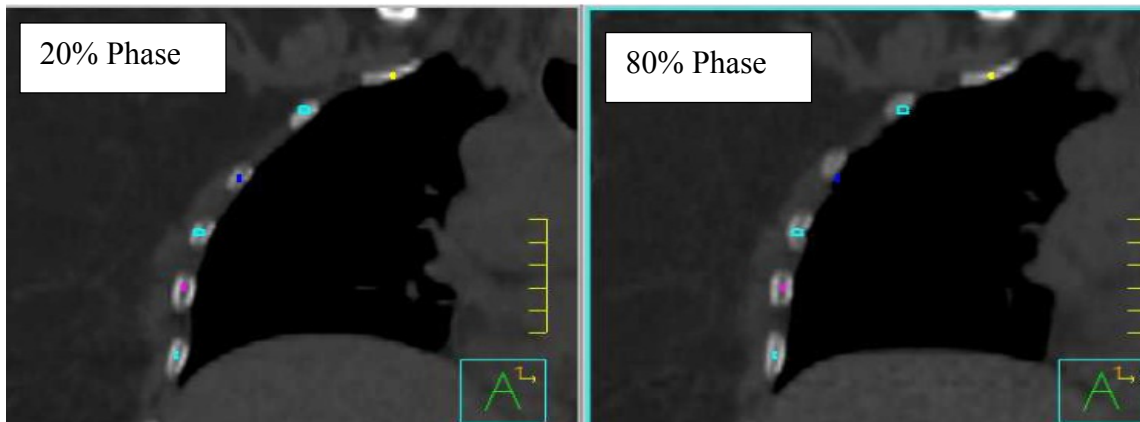
Figure 6.4 illustrating the motion of chest wall in 2 different breathing phases.

6.2.1 Results:

Figure 6.5 shows the displacement of the chest wall for ribs 3, 5, and 7 at each phase of

the breathing cycle and the corresponding diaphragm motion for an average of 7 patients.

Rib 3 moved between 1-3mm with a standard deviation of 0.1mm.

Diaphragm movement was between 4-9mm, with a standard deviation of 1.4mm. Further

the 50% phase showed the largest change in lung volume (cc) when averaged over the

patients we evaluated as shown in figure 6.6.

6.2.2 Conclusions

Quantification of diaphragm motion alone may not be enough to determine chest wall

margin since the chest wall motion is asymmetric with respect to the diaphragm motion.

Due to the asymmetric chest wall motion with respect to the tumor, 4DCT scans should

be considered for breast, lung and TMI to evaluate the tumor and chest wall motion.

6.2.3 Extension of the lung study in the context of this dissertation

Instead of following 3 points on the chest wall manually which is extremely time

consuming and still not comprehensive, the entire ribs from T 1 to T 12 were contoured

and the motion of each rib can be computed using the center of mass displacement.

We deformably registered each of the10 breathing phases of 4D CT with planning CT

using the custom developed open source DIR modules. The deformation matrix from the

image registration is applied to RT Dose from the original plan. Deformed Doses can

then be derived for each breathing phase of 4D CT. This is shown below in figs 6.7 and

6.8 for the 20% and 80% phase respectively. The deformed doses can then be summed

through all the 10 phases of breathing cycle to obtain a "4D Dose" and the DVH from 4D

dose can then compared to original RT Dose. This approach has been used in abdomen

and liver sites.[79, 81]The resultant DVH for each rib from 4D dose is shown in figure 6.9. We are currently analyzing this data and the results will be published soon.
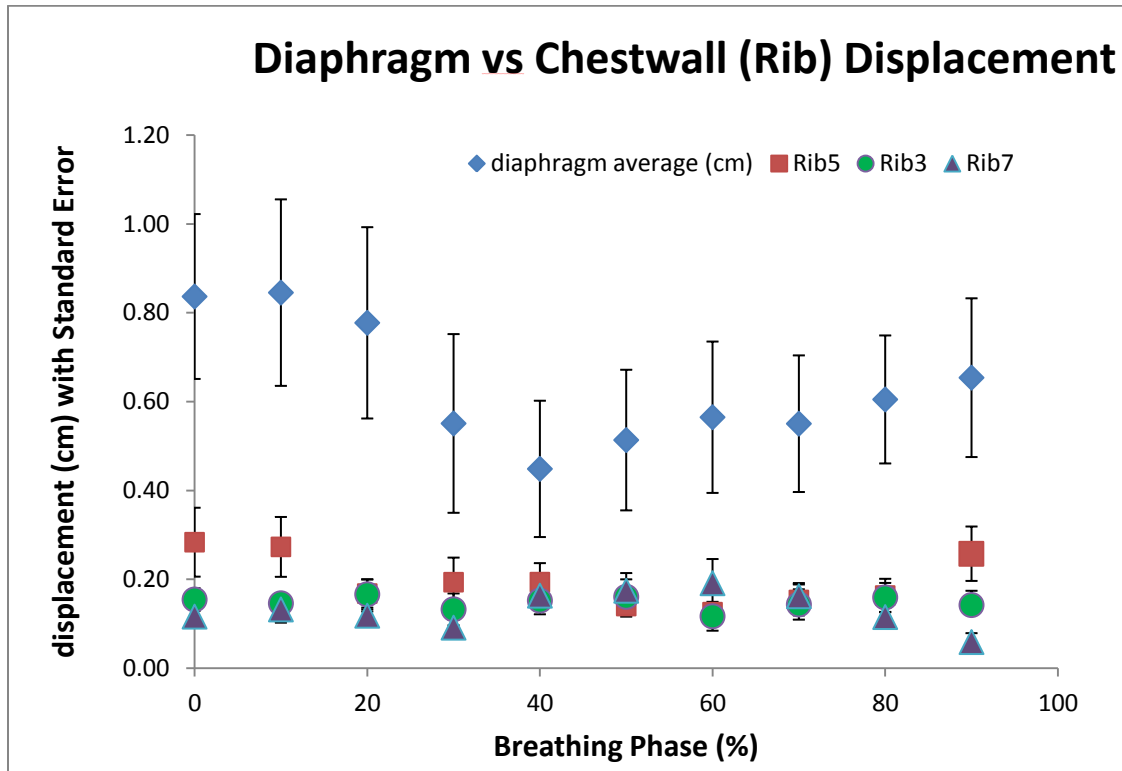
Figure 6.5 showing the motion of diaphragm in comparison to motion of chest wall as quantified by ribs 3, 5, 7
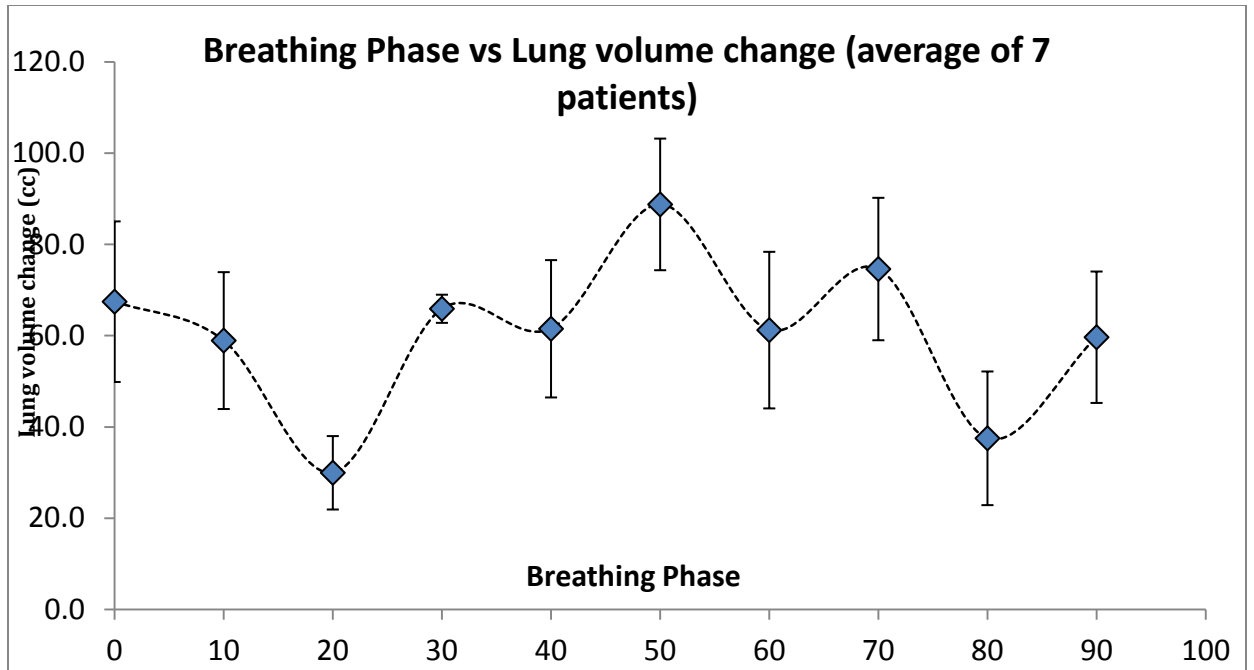
Figure 6.6 Lung volume changes (cc) as function of breathing phase
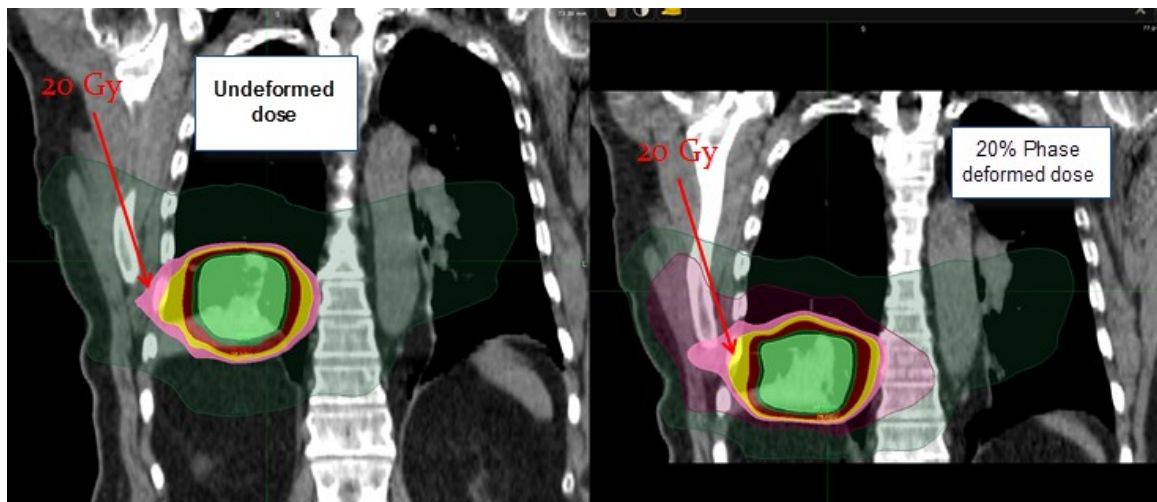
Figure 6.7 illustring the undeformed dose and deformed dose in the 20% breathing phase
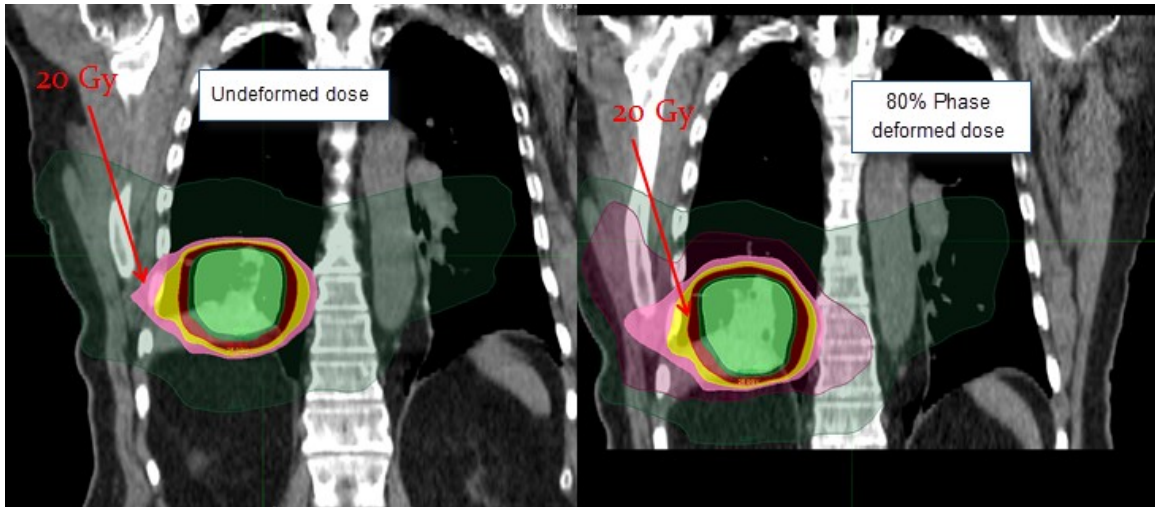
Figure 6.8 illustring the undeformed dose and deformed dose in the 80% breathing phase
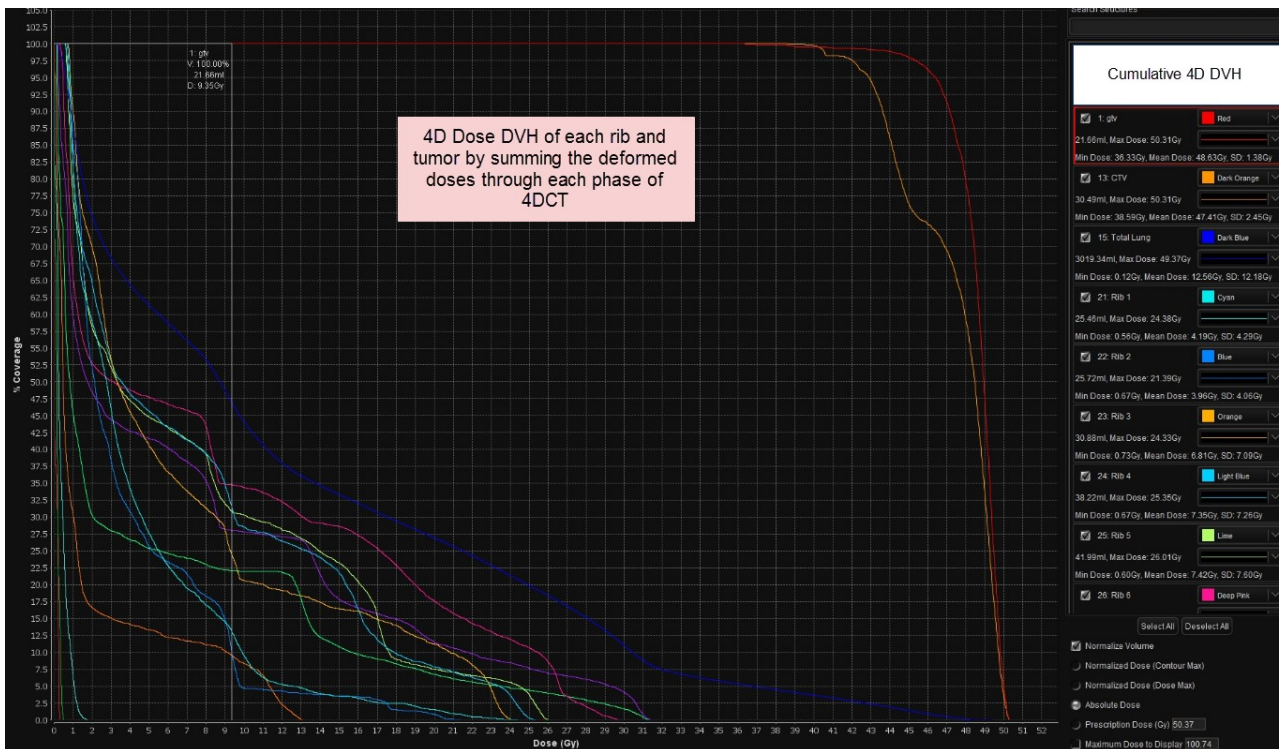
Figure 6.9 illustraing the DVH from 4D dose for all the vertebral bodies (T1 through

T12)

6.2.4 Total Marrow Irradiation (TMI)

The feasibility of using helical tomotherapy for TMI was demonstrated by Hui et al[211].

A TMI work flow methodology can be implemented based on the DIR tools developed as

part of this dissertation similar to the work of Chao et al[215] as shown in figure 6.10.

MVCTs are routinely acquired prior to each TMI treatment. Regions of interest can then

be contoured on each MVCT. The dose for each fraction can be calculated based on the

MVCT using the Tomotherapy workstation. DIR can be used to establish voxel-to-voxel

correspondence between the MVCT and the treatment planning kVCT.

The resultant deformation vector field can be used to map the reconstructed dose from

each fraction to the same point on the plan dose, and a voxel-to-voxel summed dose from

all fractions delivered can be potentially computed

The reconstructed dose distribution and its dosimetric parameters can be compared with

those of the original treatment plan to evaluate the delivery efficacy or modify the plan

during the course of therapy if significant deviations are found.
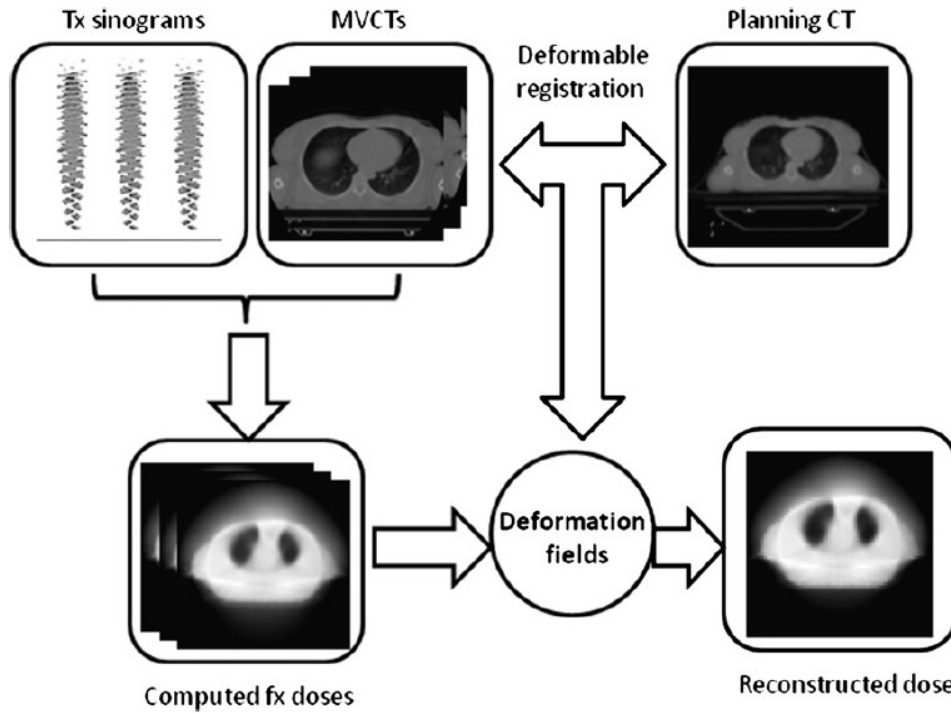
Figure 6.10 Adaptive work flow using DIR in TMI treatment based on Chao etal[215]

6.3 On-line Adaptive Radiation Therapy

On-line ART is a paradigm which attempts to adapt the delivered dose based on daily

soft tissue imaging feedback while the patient is still on table. On-line ART is different

from IGRT beacause IGRT only corrects for positional variation of target and does not

take onto account organ deformation for both target and critical structures. The goal of

on-line ART is to dynamically adapt treatment delivery accounting for organ

deformation. There are two different methods of implementing on-line ART based on

daily volumetric CT imaging. Some research groups have used MLC based tracking[216,

217] whereby MLC aperture shape and leaf sequencing is varied to adapt delivery based

on daily target volume while others have performed a more robust fluence/aperture

optimization based on daily imaging as done for treatment planning CT. The key

requirement for on-line ART in both methodologies is to keep the overall treatment time comprable to conventional IGRT treatment. In that regard, optimization and dose calculation schemes using graphics processing unit(GPU) have shown great promise in implementing on-line ART.[218-220]. GPU computing have access to hundreds of processing cores that can be used for parallel computing thereby providing a very powerful computing platform at a fraction of processing times for various scientific applications in medical physics[221]. For example automatic segmentation of tumor and organs at risk in a 4DCT scan using a Demons algorithm can be achieved in 7 seconds using GPU processors [222]. Similarly a fluence map treatment plan re-optimization for a prostate IMRT plan was done in 2.8 seconds[220] and a direct aperture optimization for prostate and head and neck IMRT plans was done between 0.7 and 3.8 seconds[219] using NVIDIA Tesla C1060 GPU card. It has also been shown that a robust dose calculation using convolution/superposition algorithm can be performed in under 2 seconds using GPU computing.[223]. Thus if image segmentation, re-optimization and dose calculation can be performed in under 2 minutes using GPU computing then on-line ART can be clinically implemented. A work flow model for clinical implementation of on-line ART is given in fig 6.11. and is subject of future research work.
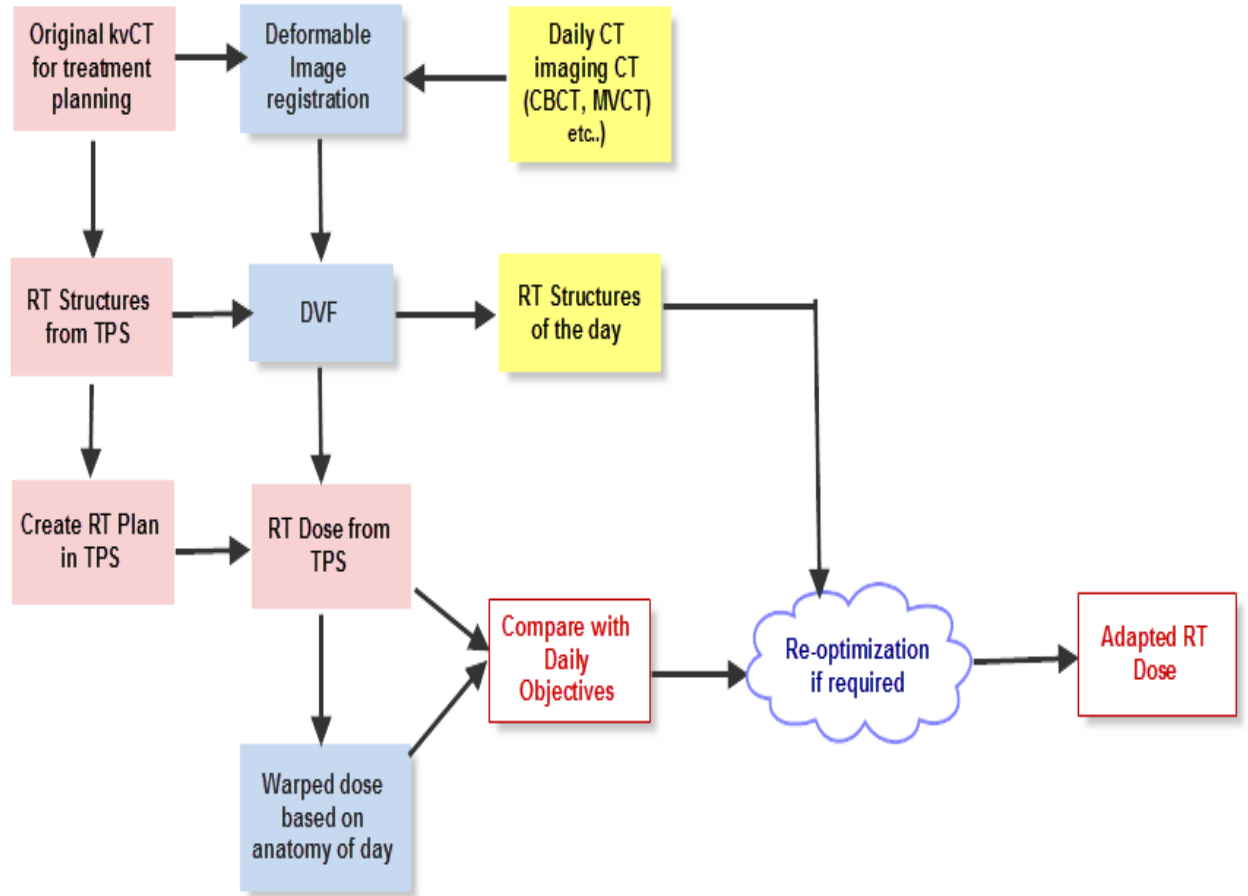
Figure 6.11 An example model for clinical implementation of on-line ART

BIBLIOGRAPHY

1. Wiener JM, Tilly J: **Population ageing in the United States of America: implications for public programmes**. *Int J Epidemiol* 2002, **31**(4):776-781.
2. Purdy JA: **Current ICRU definitions of volumes: limitations and future directions**. *Semin Radiat Oncol* 2004, **14**(1):27-40.
3. **http://www-naweb.iaea.org/nahu/DMRP/imaging.html**
4. van Herk M: **Errors and margins in radiotherapy**. *Semin Radiat Oncol* 2004, **14**(1):52-64.
5. Lee P, Kupelian P, Czernin J, Ghosh P: **Current concepts in F18 FDG PET/CT-based radiation therapy planning for lung cancer**. *Front Oncol* 2012, **2:71.**(doi):10.3389/fonc.2012.00071.
6. Yan D, Vicini F, Wong , Martinez A: **Adaptive radiation therapy**. *Phys Med Biol* 1997, **42**:123-132.
7. Yan D: **Adaptive radiotherapy: merging principle into clinical practice**. *Semin Radiat Oncol*, **20**(2):79-83.
8. Yan D, Wong J, Vicini F, Michalski J, Pan C, Frazier A, Horwitz E, Martinez A: **Adaptive modification of treatment planning to minimize the deleterious effects of treatment setup errors**. *International journal of radiation oncology, biology, physics* 1997, **38**(1):197-206.
9. Yan D: **Adaptive radiotherapy: merging principle into clinical practice**. *Semin Radiat Oncol* 2010, **20**(2):79-83.
10. Peng C, Chen G, Ahunbay E, Wang D, Lawton C, Li XA: **Validation of an online replanning technique for prostate adaptive radiotherapy**. *Phys Med Biol* 2011, **56**(12):3659-3668. doi: 3610.1088/0031-9155/3656/3612/3013. Epub 2011 May 3625.
11. Burridge N, Amer A, Marchant T, Sykes J, Stratford J, Henry A, McBain C, Price P, Moore C: **Online adaptive radiotherapy of the bladder: small bowel irradiated-volume reduction**. *Int J Radiat Oncol Biol Phys* 2006, **66**(3):892-897.
12. Ahunbay EE, Peng C, Godley A, Schultz C, Li XA: **An on-line replanning method for head and neck adaptive radiotherapy**. *Med Phys* 2009, **36**(10):4776-4790.
13. Vos PH: **Decision criteria and correction strategies in the clinical use of electronic digital portal imagers.** In: *Proceedings of the XIIth International Congress of Computers in Radiotherapy.* edn. Edited by Leavitt DD, Starkschall, G. Madison: Medical Physics Publishing; 1997: 33-36.
14. Bel A, Vos PH, Rodrigus PT, Creutzberg CL, Visser AG, Stroom JC, Lebesque JV: **High-precision prostate cancer irradiation by clinical application of an offline patient setup verification procedure, using portal imaging**. *Int J Radiat Oncol Biol Phys* 1996, **35**(2):321-332.
15. de Boer HC, Heijmen BJ: **A protocol for the reduction of systematic patient setup errors with minimal portal imaging workload**. *Int J Radiat Oncol Biol Phys* 2001, **50**(5):1350-1365.
16. Varadhan R, Hui SK, Way S, Nisi K: **Assessing prostate, bladder and rectal doses during image guided radiation therapy--need for plan adaptation?** *J Appl Clin Med Phys* 2009, **10**(3):2883.

17.   Slicer: **3D Slicer, A Visulaization Platform ([http://www.slicer.org)](http://www.slicer.org)**.

18.   Varadhan R, Karangelis G, Krishnan K, Hui S: **A framework for deformable image registration validation in radiotherapy clinical applications**. *J Appl Clin Med Phys* 2013, **14**(1):4066.

19.   Schultheiss TE, Tome WA, Orton CG: **Point/counterpoint: it is not appropriate to "deform" dose along with deformable image registration in adaptive radiotherapy**. *Med Phys* 2012, **39**(11):6531-6533.

20.   Rosen J, Brown JD, De S, Sinanan M, Hannaford B: **Biomechanical properties of abdominal organs in vivo and postmortem under compression loads**. *J Biomech Eng* 2008, **130**(2):021020.

21.   Delp SL, Loan JP: **A graphics-based software system to develop and analyze models of musculoskeletal structures**. *Comput Biol Med* 1995, **25**(1):21-34.

22.   Satava RM: **Medical virtual reality. The current status of the future Medical applications of virtual reality**. *Stud Health Technol Inform* 1996, **29**(3):100-106.

23.   Satava RM: **Medical applications of virtual reality**. *J Med Syst* 1995, **19**(3):275-280.

24.   Decarlo D: **Interactive Technology and the New Paradigm for Healthcare (Studies in Health Technology and Informatics)**: IOS Press and Ohmsha; 1995.

25.   Delingette H: **Toward realistic soft-tissue modeling in medical simulation**. *Proceedings of the IEEE* 1998, **86**(3):512-523.

26.   Fiorino C, Rizzo G, Scalco E, Broggi S, Belli ML, Dell'Oca I, Dinapoli N, Ricchetti F, Rodriguez AM, Di Muzio N *et al*: **Density variation of parotid glands during IMRT for head-neck cancer: correlation with treatment and anatomical parameters**. *Radiother Oncol* 2012, **104**(2):224-229.

27.   Cheung J, Chen Y, Lindberg M, Cannon B, Dong L: **SU-GG-J-146: Evaluation of Parotid Density Changes during IMRT of Head-And-Neck Cancer**. *Medical Physics* 2010, **37**(6):3179-3179.

28.   Varadhan, Hui S: **SU-E-J-204: Experimental Validation of Dose Warping Accuracy From Deformable Image Registration**. *Medical Physics* 2013, **40**(6):198-198.

29.   Chaudhari S, Edlund S, Cho L, Varadhan, Hui S: **SU-E-T-513: Breathing Motion Effects on Chest Wall and Resulting Dose Errors**. *Medical Physics* 2011, **38**(6):3607-3607.

30.   Hui SK, Varadhan R, Dusenbery KD, Levitt SH: **SU-FF-J-109: Conformal Prostate Treatment — a Closer Look at Dose Delivery Uncertainty and Adaptive Options**. *Medical Physics* 2007, **34**(6):2393-2393.

31.   Varadhan, Way S, Nisi K, Hui S: **SU-FF-J-111: Assessing Prostate, Bladder and Rectal Doses During Image Guided Prostate IMRT Using Kilo Voltage Cone Beam CT**. *Medical Physics* 2007, **34**(6):2393-2394.

32.   Varadhan R, Hui S, Roback D: **SU-FF-J-106: Comparison of Image Guided Radiotherapy Technologies: Tomotherapy, Varian Trilogy and Elekta Synergy**. *Medical Physics* 2007, **34**(6):2392-2392.

33.   Galvin JM, Ezzell G, Eisbrauch A, Yu C, Butler B, Xiao Y, Rosen I, Rosenman J, Sharpe M, Xing L *et al*: **Implementing IMRT in clinical practice: a joint document of the American Society for Therapeutic Radiology and Oncology**

and the American Association of Physicists in Medicine. *Int J Radiat Oncol Biol Phys* 2004, **58**(5):1616-1634.

34. Chism DB, Horwitz EM, Hanlon AL, Pinover WH, Mitra RK, Hanks GE: **Late morbidity profiles in prostate cancer patients treated to 79-84 Gy by a simple four-field coplanar beam arrangement**. *Int J Radiat Oncol Biol Phys* 2003, **55**(1):71-77.

35. Ezzell GA, Galvin JM, Low D, Palta JR, Rosen I, Sharpe MB, Xia P, Xiao Y, Xing L, Yu CX: **Guidance document on delivery, treatment planning, and clinical implementation of IMRT: report of the IMRT Subcommittee of the AAPM Radiation Therapy Committee**. *Med Phys* 2003, **30**(8):2089-2115.

36. Levitt SH, Khan FM: **The rush to judgment: Does the evidence support the enthusiasm over three-dimensional conformal radiation therapy and dose escalation in the treatment of prostate cancer?** *Int J Radiat Oncol Biol Phys* 2001, **51**(4):871-879.

37. Tome WA, Fowler JF: **On cold spots in tumor subvolumes**. *Med Phys* 2002, **29**(7):1590-1598.

38. Mackie TR, Kapatoes J, Ruchala K, Lu W, Wu C, Olivera G, Forrest L, Tome W, Welsh J, Jeraj R *et al*: **Image guidance for precise conformal radiotherapy**. *Int J Radiat Oncol Biol Phys* 2003, **56**(1):89-105.

39. Kupelian PA, Langen KM, Zeidan OA, Meeks SL, Willoughby TR, Wagner TH, Jeswani S, Ruchala KJ, Haimerl J, Olivera GH: **Daily variations in delivered doses in patients treated with radiotherapy for localized prostate cancer**. *International journal of radiation oncology, biology, physics* 2006, **66**(3):876-882.

40. Curry TS, Dowdey JE, Murry RC: **Christensen's Physics of Diagnostic Radiology,**, vol. 4th Edition. Malvern, PA: Lea & Febiger,; 1990.

41. Lehmann J, Perks J, Semon S, Harse R, Purdy JA: **Commissioning experience with cone-beam computed tomography for image-guided radiation therapy**. *J Appl Clin Med Phys* 2007, **8**(3):2354.

42. Mutic S, Palta JR, Butker EK, Das IJ, Huq MS, Loo LN, Salter BJ, McCollough CH, Van Dyk J: **Quality assurance for computed-tomography simulators and the computed-tomography-simulation process: report of the AAPM Radiation Therapy Committee Task Group No. 66**. *Med Phys* 2003, **30**(10):2762-2792.

43. Ruchala KJ, Olivera GH, Kapatoes JM, Schloesser EA, Reckwerdt PJ, Mackie TR: **Megavoltage CT image reconstruction during tomotherapy treatments**. *Physics in Medicine and Biology* 2000, **45**(12):3545-3562.

44. Langen KM, Meeks SL, Poole DO, Wagner TH, Willoughby TR, Kupelian PA, Ruchala KJ, Haimerl J, Olivera GH: **The use of megavoltage CT (MVCT) images for dose recomputations**. *Physics in Medicine and Biology* 2005, **50**(18):4259-4276.

45. Schrim M: **Consistency Check of Planned Adaptive Option on Helical Tomotherapy**. *Technology in Cancer Research and Treatment* 2008, **7**(6):425-432.

46. Alasti H, Petric MP, Catton CN, Warde PR: **Portal imaging for evaluation of daily on-line setup errors and off-line organ motion during conformal**

irradiation of carcinoma of the prostate. *Int J Radiat Oncol Biol Phys* 2001, **49**(3):869-884.

47. Birkner M, Yan D, Alber M, Liang J, Nusslin F: **Adapting inverse planning to patient and organ geometrical variation: algorithm and implementation**. *Medical physics* 2003, **30**(10):2822-2831.

48. Britton KR, Takai Y, Mitsuya M, Nemoto K, Ogawa Y, Yamada S: **Evaluation of inter- and intrafraction organ motion during intensity modulated radiation therapy (IMRT) for localized prostate cancer measured by a newly developed on-board image-guided system**. *Radiat Med* 2005, **23**(1):14-24.

49. Chen J, Lee RJ, Handrahan D, Sause WT: **Intensity-modulated radiotherapy using implanted fiducial markers with daily portal imaging: assessment of prostate organ motion**. *Int J Radiat Oncol Biol Phys* 2007, **68**(3):912-919.

50. Happersett L, Mageras GS, Zelefsky MJ, Burman CM, Leibel SA, Chui C, Fuks Z, Bull S, Ling CC, Kutcher GJ: **A study of the effects of internal organ motion on dose escalation in conformal prostate treatments**. *Radiother Oncol* 2003, **66**(3):263-270.

51. Hoogeman MS, van Herk M, de Bois J, Lebesque JV: **Strategies to reduce the systematic error due to tumor and rectum motion in radiotherapy of prostate cancer**. *Radiotherapy and oncology : journal of the European Society for Therapeutic Radiology and Oncology* 2005, **74**(2):177-185.

52. Jani AB: **Organ motion and IMRT in prostate cancer therapy**. *Cancer J* 2003, **9**(4):244-246.

53. Keller H, Tome W, Ritter MA, Mackie TR: **Design of adaptive treatment margins for non-negligible measurement uncertainty: application to ultrasound-guided prostate radiation therapy**. *Physics in Medicine and Biology* 2004, **49**(1):69-86.

54. Landoni V, Saracino B, Marzi S, Gallucci M, Petrongari MG, Chianese E, Benassi M, Iaccarino G, Soriani A, Arcangeli G: **A study of the effect of setup errors and organ motion on prostate cancer treatment with IMRT**. *Int J Radiat Oncol Biol Phys* 2006, **65**(2):587-594.

55. Lattanzi J, McNeeley S, Donnelly S, Palacio E, Hanlon A, Schultheiss TE, Hanks GE: **Ultrasound-based stereotactic guidance in prostate cancer-- quantification of organ motion and set-up errors in external beam radiation therapy**. *Comput Aided Surg* 2000, **5**(4):289-295.

56. Little DJ, Dong L, Levy LB, Chandra A, Kuban DA: **Use of portal images and BAT ultrasonography to measure setup error and organ motion for prostate IMRT: implications for treatment margins**. *Int J Radiat Oncol Biol Phys* 2003, **56**(5):1218-1224.

57. Stroom JC, Koper PC, Korevaar GA, van Os M, Janssen M, de Boer HC, Levendag PC, Heijmen BJ: **Internal organ motion in prostate cancer patients treated in prone and supine treatment position**. *Radiother Oncol* 1999, **51**(3):237-248.

58. van Herk M, Bruce A, Kroes AP, Shouman T, Touw A, Lebesque JV: **Quantification of organ motion during conformal radiotherapy of the prostate by three dimensional image registration**. *Int J Radiat Oncol Biol Phys* 1995, **33**(5):1311-1320.

59. Zhang M, Moiseenko V, Liu M, Craig T: **Internal fiducial markers can assist dose escalation in treatment of prostate cancer: result of organ motion simulations**. *Phys Med Biol* 2006, **51**(2):269-285.

60. Eade TN, Hanlon AL, Horwitz EM, Buyyounouski MK, Hanks GE, Pollack A: **What dose of external-beam radiation is high enough for prostate cancer?** *International journal of radiation oncology, biology, physics* 2007, **68**(3):682-689.

61. Zelefsky MJ, Leibel SA, Gaudin PB, Kutcher GJ, Fleshner NE, Venkatramen ES, Reuter VE, Fair WR, Ling CC, Fuks Z: **Dose escalation with three-dimensional conformal radiation therapy affects the outcome in prostate cancer**. *Int J Radiat Oncol Biol Phys* 1998, **41**(3):491-500.

62. Peeters ST, Heemsbergen WD, Koper PC, van Putten WL, Slot A, Dielwart MF, Bonfrer JM, Incrocci L, Lebesque JV: **Dose-response in radiotherapy for localized prostate cancer: results of the Dutch multicenter randomized phase III trial comparing 68 Gy of radiotherapy with 78 Gy**. *J Clin Oncol* 2006, **24**(13):1990-1996.

63. Cahlon O, Zelefsky MJ, Shippy A, Chan H, Fuks Z, Yamada Y, Hunt M, Greenstein S, Amols H: **Ultra-High Dose (86.4 Gy) IMRT for Localized Prostate Cancer: Toxicity and Biochemical Outcomes**. *International journal of radiation oncology, biology, physics* 2007.

64. Zelefsky MJ, Chan H, Hunt M, Yamada Y, Shippy AM, Amols H: **Long-term outcome of high dose intensity modulated radiation therapy for patients with clinically localized prostate cancer**. *The Journal of urology* 2006, **176**(4 Pt 1):1415-1419.

65. Pollack A, Zagars GK, Starkschall G, Antolak JA, Lee JJ, Huang E, von Eschenbach AC, Kuban DA, Rosen I: **Prostate cancer radiation dose response: results of the M. D. Anderson phase III randomized trial**. *Int J Radiat Oncol Biol Phys* 2002, **53**(5):1097-1105.

66. Loblaw DA, Cheung P: **External beam irradiation for localized prostate cancer--the promise of hypofractionation**. *The Canadian journal of urology* 2006, **13 Suppl 1**:62-66.

67. Miles EF, Robert Lee W: **Hypofractionation for prostate cancer: a critical review**. *Seminars in radiation oncology* 2008, **18**(1):41-47.

68. Madsen BL, Hsi RA, Pham HT, Fowler JF, Esagui L, Corman J: **Stereotactic hypofractionated accurate radiotherapy of the prostate (SHARP), 33.5 Gy in five fractions for localized disease: first clinical trial results**. *International journal of radiation oncology, biology, physics* 2007, **67**(4):1099-1105.

69. Brenner DJ, Martinez AA, Edmundson GK, Mitchell C, Thames HD, Armour EP: **Direct evidence that prostate tumors show high sensitivity to fractionation (low alpha/beta ratio), similar to late-responding normal tissue**. *International journal of radiation oncology, biology, physics* 2002, **52**(1):6-13.

70. Chappell R, Fowler J, Ritter M: **New data on the value of alpha/beta--evidence mounts that it is low**. *International journal of radiation oncology, biology, physics* 2004, **60**(3):1002-1003.

71. Fowler J, Chappell R, Ritter M: **Is alpha/beta for prostate tumors really low?** *International journal of radiation oncology, biology, physics* 2001, **50**(4):1021-1031.

72. Wang JZ, Guerrero M, Li XA: **How low is the alpha/beta ratio for prostate cancer?** *International journal of radiation oncology, biology, physics* 2003, **55**(1):194-203.

73. Nuver TT, Hoogeman MS, Remeijer P, van Herk M, Lebesque JV: **An adaptive off-line procedure for radiotherapy of prostate cancer**. *Int J Radiat Oncol Biol Phys* 2007, **67**(5):1559-1567.

74. Nijkamp J, Pos FJ, Nuver TT, de Jong R, Remeijer P, Sonke JJ, Lebesque JV: **Adaptive Radiotherapy for Prostate Cancer Using Kilovoltage Cone-Beam Computed Tomography: First Clinical Results**. *Int J Radiat Oncol Biol Phys* 2008, **70**(1):75-82.

75. Yan D, Lockman D, Brabbins D, Tyburski L, Martinez A: **An off-line strategy for constructing a patient-specific planning target volume in adaptive treatment process for prostate cancer**. *International journal of radiation oncology, biology, physics* 2000, **48**(1):289-302.

76. Court LE, Dong L, Lee AK, Cheung R, Bonnen MD, O'Daniel J, Wang H, Mohan R, Kuban D: **An automatic CT-guided adaptive radiation therapy technique by online modification of multileaf collimator leaf positions for prostate cancer**. *International journal of radiation oncology, biology, physics* 2005, **62**(1):154-163.

77. Litzenberg DW, Balter JM, Lam KL, Sandler HM, Ten Haken RK: **Retrospective analysis of prostate cancer patients with implanted gold markers using off-line and adaptive therapy protocols**. *International journal of radiation oncology, biology, physics* 2005, **63**(1):123-133.

78. Crum WR, Hartkens T, Hill DL: **Non-rigid image registration: theory and practice**. *Br J Radiol* 2004, **77 Spec No 2**:S140-153.

79. Velec M, Moseley JL, Craig T, Dawson LA, Brock KK: **Accumulated dose in liver stereotactic body radiotherapy: positioning, breathing, and deformation effects**. *Int J Radiat Oncol Biol Phys* 2012, **83**(4):1132-1140.

80. Dice LR: **Measures of the amount of ecologic association between species.** *Ecology* 1945, **26**:297-302.

81. Velec M, Moseley JL, Eccles CL, Craig T, Sharpe MB, Dawson LA, Brock KK: **Effect of breathing motion on radiotherapy dose accumulation in the abdomen using deformable registration**. *Int J Radiat Oncol Biol Phys* 2011, **80**(1):265-272.

82. Bookstein FL: **Principal Warps: Thin-plate splines and the decomposition of deformations**. *IEEE Trans Pattern Analysis Mach Intell 11(6), pp, 1989* 1989, **11**(6):567-585.

83. Wendland H: **Piecewise Polynomial, Positive Definite and COmpactly Supported Radial Functions of Minimal Degree**. *Advances in Computational Mathematics* 1995, **4**:389-396.

84. Davis MH, Khotanzad A, Flamig DP, Harms SE: **A physics-based coordinate transformation for 3-D image matching**. *Medical Imaging, IEEE Transactions on* 1997, **16**(3):317-328.

85. Sprengel R, Rohr D, Stiehl H: **Thin-Plate Spline Approximation for Image Registration**. In: *18th International Conference of the IEEE Engineering in Medicine and Biology Society: 1996*; 1996.

86. Rueckert D SL, Hayes C, Hill DL, Leach MO, Hawkes DJ.: **Nonrigid registration using free-form deformations: application to breast MR images**. *IEEE Trans Med Imaging* 1999, **Aug;18**(8):712-721.

87. Lawson JD, Schreibmann E, Jani AB, Fox T: **Quantitative evaluation of a cone-beam computed tomography-planning computed tomography deformable image registration method for adaptive radiation therapy**. *J Appl Clin Med Phys* 2007, **8**(4):2432.

88. Mattes D, Haynor DR, Vesselle H, Lewellen TK, Eubank W: **PET-CT image registration in the chest using free-form deformations**. *IEEE Trans Med Imaging* 2003, **22**(1):120-128.

89. Schreibmann E, Fox T, Crocker I: **Dosimetric effects of manual cone-beam CT (CBCT) matching for spinal radiosurgery: our experience**. *J Appl Clin Med Phys* 2011, **12**(3):3467.

90. Zhong H, Peters T, Siebers JV: **FEM-based evaluation of deformable image registration for radiation therapy**. *Phys Med Biol* 2007, **52**(16):4721-4738.

91. Brock KK, Sharpe MB, Dawson LA, Kim SM, Jaffray DA: **Accuracy of finite element model-based multi-organ deformable image registration**. *Med Phys* 2005, **32**(6):1647-1659.

92. Robertson S, Weiss E, Hugo GD: **Deformable mesh registration for the validation of automatic target localization algorithms**. *Med Phys* 2013, **40**(7):071721. doi: 071710.071118/071721.4811105.

93. Thirion JP: **Image matching as a diffusion process: an analogy with Maxwell's demons**. *Med Image Anal* 1998, **2**(3):243-260.

94. Wang H, Dong L, Lii MF, Lee AL, de Crevoisier R, Mohan R, Cox JD, Kuban DA, Cheung R: **Implementation and validation of a three-dimensional deformable registration algorithm for targeted prostate cancer radiotherapy**. *Int J Radiat Oncol Biol Phys* 2005, **61**(3):725-735.

95. Wang H, Dong L, O'Daniel J, Mohan R, Garden AS, Ang KK, Kuban DA, Bonnen M, Chang JY, Cheung R: **Validation of an accelerated 'demons' algorithm for deformable image registration in radiation therapy**. *Phys Med Biol* 2005, **50**(12):2887-2905.

96. Wang H, Garden AS, Zhang L, Wei X, Ahamad A, Kuban DA, Komaki R, O'Daniel J, Zhang Y, Mohan R *et al*: **Performance evaluation of automatic anatomy segmentation algorithm on repeat or four-dimensional computed tomography images using deformable image registration method**. *Int J Radiat Oncol Biol Phys* 2008, **72**(1):210-219.

97. Christensen GE, Rabbitt RD, Miller MI: **Deformable templates using large deformation kinematics**. *IEEE Trans Image Process* 1996, **5**(10):1435-1447.

98. Christensen GE, Carlson B, Chao KS, Yin P, Grigsby PW, Nguyen K, Dempsey JF, Lerma FA, Bae KT, Vannier MW *et al*: **Image-based dose planning of intracavitary brachytherapy: registration of serial-imaging studies using deformable anatomic templates**. *Int J Radiat Oncol Biol Phys* 2001, **51**(1):227-243.

99. Horn BKP, Schunck BG: **Determining optical flow**. *Artificial Intelligence* 1981, **17**:185-204.

100. Yang D, Brame S, El Naqa I, Aditya A, Wu Y, Goddu SM, Mutic S, Deasy JO, Low DA: **Technical note: DIRART--A software suite for deformable image registration and adaptive radiotherapy research**. *Med Phys* 2011, **38**(1):67-77.

101. Hoon Jung S, Min Yoon S, Ho Park S, Cho B, Won Park J, Jung J, Park J-h, Hoon Kim J, Do Ahn S: **Four-dimensional dose evaluation using deformable image registration in radiotherapy for liver cancer**. *Medical Physics* 2013, **40**(1):-.

102. Yeo UJ, Supple J, Taylor ML, Smith RL, Kron T, Franich RD: **Performance of 12 DIR algorithms in low-contrast regions for mass and density conserving deformation**. *Medical Physics* 2013, **40**(101701).

103. Yeo UJ, Taylor ML, Dunn L, Kron T, Smith RL, Franich RD: **A novel methodology for 3D deformable dosimetry**. *Med Phys* 2012, **39**(4):2203-2213.

104. Yeo UJ, Taylor ML, Supple JR, Smith RL, Dunn L, Kron T, Franich RD: **Is it sensible to "deform" dose? 3D experimental validation of dose-warping**. *Med Phys* 2012, **39**(8):5065-5072.

105. Yang D, Li H, Low DA, Deasy JO, El Naqa I: **A fast inverse consistent deformable image registration method based on symmetric optical flow computation**. *Phys Med Biol* 2008, **53**(21):6143-6165. doi: 6110.1088/0031-9155/6153/6121/6017. Epub 2008 Oct 6114.

106. Lucas BD, Kanade T: **An Iterative Image Registration Technique with an Application to Stereo Vision (DARPA).** In: *Proceedings of the 7th international joint conference on artificial intelligence: 1981*; 1981: 674-679.

107. Lu W, Chen ML, Olivera GH, Ruchala KJ, Mackie TR: **Fast free-form deformable registration via calculus of variations**. *Phys Med Biol* 2004, **49**(14):3067-3087.

108. Zhang T, Chi Y, Meldolesi E, Yan D: **Automatic delineation of on-line head-and-neck computed tomography images: toward on-line adaptive radiotherapy**. *Int J Radiat Oncol Biol Phys* 2007, **68**(2):522-530.

109. Lester H, Arridge SR: **A survey of hierarchical non-linear medical image registration**. *Pattern Recognition* 1999, **32**(1):129-149.

110. Piper J: **Evaluation of an intensity-based free-form deformable registration algorithm**. *Medical Physics* 2007, **34**:2353.

111. Sarrut D: **Deformable registration for image-guided radiation therapy**. *Z Med Phys* 2006, **16**(4):285-297.

112. Venugopal N, McCurdy B, Hnatov A, A. D: **A feasibility study to investigate the use of thin-plate splines to account for prostate deformation**. *Physics in Medicine and Biology* 2005, **50**(12):2871-2885.

113. Zhong H, Kim J, Chetty IJ: **Analysis of deformable image registration accuracy using computational modeling**. *Med Phys* 2010, **37**(3):970-979.

114. Kashani R, Hub M, Balter JM, Kessler ML, Dong L, Zhang L, Xing L, Xie Y, Hawkes D, Schnabel JA *et al*: **Objective assessment of deformable image registration in radiotherapy: a multi-institution study**. *Med Phys* 2008, **35**(12):5944-5953.

115. Schaly B, Bauman GS, Battista JJ, Van Dyk J: **Validation of contour-driven thin-plate splines for tracking fraction-to-fraction changes in anatomy and radiation therapy dose mapping**. *Phys Med Biol* 2005, **50**(3):459-475.
116. Brock KK: **Results of a multi-institution deformable registration accuracy study (MIDRAS)**. *Int J Radiat Oncol Biol Phys* 2009, **76**(2):583-596.
117. Kaus MR, Brock KK, Pekar V, Dawson LA, Nichol AM, Jaffray DA: **Assessment of a model-based deformable image registration approach for radiation therapy planning**. *Int J Radiat Oncol Biol Phys* 2007, **68**(2):572-580.
118. Ostergaard Noe K, De Senneville BD, Elstrom UV, Tanderup K, Sorensen TS: **Acceleration and validation of optical flow based deformable registration for image-guided radiotherapy**. *Acta Oncol* 2008, **47**(7):1286-1293.
119. Castillo R, Castillo E, Guerra R, Johnson VE, McPhail T, Garg AK, Guerrero T: **A framework for evaluation of deformable image registration spatial accuracy using large landmark point sets**. *Phys Med Biol* 2009, **54**(7):1849-1870.
120. Serban M, Heath E, Stroian G, Collins DL, Seuntjens J: **A deformable phantom for 4D radiotherapy verification: design and image registration evaluation**. *Med Phys* 2008, **35**(3):1094-1102.
121. Kashani R, Hub M, Kessler ML, Balter JM: **Technical note: a physical phantom for assessment of accuracy of deformable alignment algorithms**. *Med Phys* 2007, **34**(7):2785-2788.
122. Kirby N, Chuang C, Pouliot J: **A two-dimensional deformable phantom for quantitatively verifying deformation algorithms**. *Med Phys* 2011, **38**(8):4583-4586.
123. Yan D: **Developing quality assurance processes for image-guided adaptive radiation therapy**. *Int J Radiat Oncol Biol Phys* 2008, **71**(1 Suppl):S28-32.
124. Rosu M, Chetty IJ, Balter JM, Kessler ML, McShan DL, Ten Haken RK: **Dose reconstruction in deforming lung anatomy: dose grid size effects and clinical implications**. *Med Phys* 2005, **32**(8):2487-2495.
125. Orban de Xivry J, Janssens G, Bosmans G, De Craene M, Dekker A, Buijsen J, van Baardwijk A, De Ruysscher D, Macq B, Lambin P: **Tumour delineation and cumulative dose computation in radiotherapy based on deformable registration of respiratory correlated CT images of lung cancer patients**. *Radiother Oncol* 2007, **85**(2):232-238.
126. Schaly B KJ, Bauman GS, Battista JJ Van Dyk J.: **Tracking the dose distribution in radiation therapy by accounting for variable anatomy**. *Phys Med Biol* 2004, **49**(5):791-805.
127. Janssens G, JO. dX, S. F, A. D, B. M, P. L, W. vE: **Evaluation of nonrigid registration models for interfraction dose accumulation in radiotherapy.** *Medical Physics* 2009, **36**(9):4268-4276.
128. Rohlfing T: **Transformation model and constraints cause bias in statistics on deformation fields**. *Med Image Comput Comput Assist Interv* 2006, **9**(Pt 1):207-214.
129. Bender E, Tome W: **The utilization of consistency metrics for error analysis in deformable image registration**. *Physics in Medicine and Biology* 2009, **54**:5561-5567.

130. Yang D LH, Low D, Deasy J and Naqa I: **A fast inverse consistent deformable image registration method based on symmetric optical flow computation**. *Physics in Medicine and Biology* 2008, **53**:6143-6165.

131. Christensen GE, Johnson HJ: **Consistent image registration**. *IEEE Trans Med Imaging* 2001, **20**(7):568-582.

132. Arsigny V, Commowick O, Pennec X, Ayache N: **A log-Euclidean framework for statistics on diffeomorphisms**. *Med Image Comput Comput Assist Interv* 2006, **9**(Pt 1):924-931.

133. Chen M, Lu W, Chen Q, Ruchala KJ, Olivera GH: **A simple fixed-point approach to invert a deformation field**. *Med Phys* 2008, **35**(1):81-88.

134. Rey D, Subsol G, Delingette H, Ayache N: **Automatic detection and segmentation of evolving processes in 3D medical images: Application to multiple sclerosis**. *Med Image Anal* 2002, **6**(2):163-179.

135. Jost J (ed.): **Riemannian geometry and geometric analysis**. New York, NY: Springer; 2005.

136. Bookstein FL: **Principal Warps: Thin-Plate Splines and the Decomposition of Deformations**. *IEEE Transactions on Pattern Analysis and Machine Intelligence* 1989, **11**(6):567-585.

137. Wachowiak MP, Xiaogang W, Fenster A, Peters Tm: **Compact Support Radial Basis functions for soft tissue deformation**. *International Symposium on Biomedical Imaging: Nano to macro* 2004, **2**:1259-1262.

138. Craig T, Brochu D, Van Dyk J: **A quality assurance phantom for three-dimensional radiation treatment planning**. *Int J Radiat Oncol Biol Phys* 1999, **44**(4):955-966.

139. Kupelian P, Meyer JL: **Image-guided, adaptive radiotherapy of prostate cancer: toward new standards of radiotherapy practice**. *Front Radiat Ther Oncol*, **43**:344-368.

140. Li T, Thongphiew D, Zhu X, Lee WR, Vujaskovic Z, Yin FF, Wu QJ: **Adaptive prostate IGRT combining online re-optimization and re-positioning: a feasibility study**. *Phys Med Biol*, **56**(5):1243-1258.

141. Li T, Zhu X, Thongphiew D, Lee WR, Vujaskovic Z, Wu Q, Yin FF, Wu QJ: **On-line adaptive radiation therapy: feasibility and clinical study**. *J Oncol*, **2010**:407236.

142. Lian J, Xing L, Hunjan S, Dumoulin C, Levin J, Lo A, Watkins R, Rohling K, Giaquinto R, Kim D *et al*: **Mapping of the prostate in endorectal coil-based MRI/MRSI and CT: a deformable registration and validation study**. *Med Phys* 2004, **31**(11):3087-3094.

143. Liu H, Wu Q: **Evaluations of an adaptive planning technique incorporating dose feedback in image-guided radiotherapy of prostate cancer**. *Med Phys* 2011, **38**(12):6362-6370.

144. Liu H, Wu Q: **A "rolling average" multiple adaptive planning method to compensate for target volume changes in image-guided radiotherapy of prostate cancer**. *J Appl Clin Med Phys*, **13**(1):3697.

145. Liu H, Wu Q: **Dosimetric and geometric evaluation of a hybrid strategy of offline adaptive planning and online image guidance for prostate cancer radiotherapy**. *Phys Med Biol*, **56**(15):5045-5062.

146. Lu W OG, Chen Q, et al.: **Deformable registration of the planning image (kvCT) and the daily images (MVCT) for adaptive radiation therapy**. *Phys Med Biol* 2006, **51**(17):4357-4374.

147. Murthy V, Shukla P, Adurkar P, Master Z, Mahantshetty U, Shrivastava SK: **Dose variation during hypofractionated image-guided radiotherapy for prostate cancer: planned versus delivered**. *J Cancer Res Ther*, **7**(2):162-167.

148. Ghilezan M, Yan D, Martinez A: **Adaptive radiation therapy for prostate cancer**. *Semin Radiat Oncol*, **20**(2):130-137.

149. Barker JL, Jr., Garden AS, Ang KK, O'Daniel JC, Wang H, Court LE, Morrison WH, Rosenthal DI, Chao KS, Tucker SL *et al*: **Quantification of volumetric and geometric changes occurring during fractionated radiotherapy for head-and-neck cancer using an integrated CT/linear accelerator system**. *Int J Radiat Oncol Biol Phys* 2004, **59**(4):960-970.

150. Vakilha M **Changes in position and size of parotid glands assessed with daily cone beam CT during image-guided IMRT for head and neck cancer: implications for dose received**. *Int J Radiat Oncol Biol Phys* 2007, **69**:S 438-439.

151. Ahn PH, Chen CC, Ahn AI, Hong L, Scripes PG, Shen J, Lee CC, Miller E, Kalnicki S, Garg MK: **Adaptive planning in intensity-modulated radiation therapy for head and neck cancers: single-institution experience and clinical implications**. *Int J Radiat Oncol Biol Phys*, **80**(3):677-685.

152. Ahunbay EE, Peng C, Godley A, Schultz C, Li XA: **An on-line replanning method for head and neck adaptive radiotherapy**. *Med Phys* 2009, **36**(10):4776-4790.

153. Castadot P, Lee JA, Geets X, Gregoire V: **Adaptive radiotherapy of head and neck cancer**. *Semin Radiat Oncol*, **20**(2):84-93.

154. Schwartz DL, Dong L: **Adaptive radiation therapy for head and neck cancer-can an old goal evolve into a new standard?** *J Oncol*, **2011**.

155. Schwartz DL, Garden AS, Thomas J, Chen Y, Zhang Y, Lewin J, Chambers MS, Dong L: **Adaptive Radiotherapy for Head-and-Neck Cancer: Initial Clinical Outcomes from a Prospective Trial**. *Int J Radiat Oncol Biol Phys*.

156. Wu Q, Chi Y, Chen PY, Krauss DJ, Yan D, Martinez A: **Adaptive replanning strategies accounting for shrinkage in head and neck IMRT**. *Int J Radiat Oncol Biol Phys* 2009, **75**(3):924-932.

157. Pantarotto JR, Piet AH, Vincent A, van Sornsen de Koste JR, Senan S: **Motion analysis of 100 mediastinal lymph nodes: potential pitfalls in treatment planning and adaptive strategies**. *Int J Radiat Oncol Biol Phys* 2009, **74**(4):1092-1099.

158. Seppenwoolde Y, Shirato H, Kitamura K, Shimizu S, van Herk M, Lebesque JV, Miyasaka K: **Precise and real-time measurement of 3D tumor motion in lung due to breathing and heartbeat, measured during radiotherapy**. *Int J Radiat Oncol Biol Phys* 2002, **53**(4):822-834.

159. Ibanez L SW, Ng L, Cates: **"ITK software guide", Kitware Inc**.

160. D.Mattes DRH, H.Vesselle. T.K.Lewellen, and W.Eubank: **PET-CT image registration in the chest using free form deformations**. *IEEE Transactions on Medical Imaging* 2003, **22**(1):120-128.

161. Styner M, Brechbuhler C, Szekely G, Gerig G: **Parametric estimate of intensity inhomogeneities applied to MRI**. *IEEE Trans Med Imaging* 2000, **19**(3):153-165.

162. Vercauteren T, Pennec X, Perchant A, Ayache N: **Diffeomorphic demons: efficient non-parametric image registration**. *Neuroimage* 2009, **45**(1 Suppl):S61-72.

163. Janssens G, Jacques L, Orban de Xivry J, Geets X, Macq B: **Diffeomorphic registration of images with variable contrast enhancement**. *Int J Biomed Imaging*, **2011**:891585.

164. Leow AD, Yanovsky I, Chiang MC, Lee AD, Klunder AD, Lu A, Becker JT, Davis SW, Toga AW, Thompson PM: **Statistical properties of Jacobian maps and the realization of unbiased large-deformation nonlinear image registration**. *IEEE Trans Med Imaging* 2007, **26**(6):822-832.

165. Guyon J, Foskey M, Kim J, Firat Z, Davis B, Haneke K, Aylward SR: **VETOT, Volume Estimation and Tracking Over Time: Framework and Validation**. In: *Medical Image Computing and Computer Assisted Intervention Society, MICCAI: 2003*; 2003: 142-149.

166. Shekhar R, Lei P, Castro-Pareja CR, Plishker WL, D'Souza WD: **Automatic segmentation of phase-correlated CT scans through nonrigid image registration using geometrically regularized free-form deformation**. *Med Phys* 2007, **34**(7):3054-3066.

167. Zou KH, Warfield SK, Bharatha A, Tempany CM, Kaus MR, Haker SJ, Wells WM, 3rd, Jolesz FA, Kikinis R: **Statistical validation of image segmentation quality based on a spatial overlap index**. *Acad Radiol* 2004, **11**(2):178-189.

168. Huttenlocher DP, Klanderman GA, Rucklidge WA: **Comparing images using the hausdorff distance,**. *IEEE Trans Pattern Anal MachIntell* 1993, **15**:850-863.

169. Oguro S, Tuncali K, Elhawary H, Morrison PR, Hata N, Silverman SG: **Image registration of pre-procedural MRI and intra-procedural CT images to aid CT-guided percutaneous cryoablation of renal tumors**. *Int J Comput Assist Radiol Surg*, **6**(1):111-117.

170. Gonzalez RC, Woods RW: **Digital Image Processing**: Addison-Weseley, New York; 1992.

171. Taylor ML, Yeo UJ, Kron T, Supple J, Siva S, Pham D, Franich RD: **Comment on "it is not appropriate to 'deform' dose along with deformable image registration in adaptive radiotherapy" [Med. Phys. 39, 6531-6533 (2012)]**. *Med Phys* 2013, **40**(1):017101.

172. Schultheiss TE, Tome WA: **Response to "comment on 'It is not appropriate to "deform" dose along with deformable image registration in adaptive radiotherapy'" [Med. Phys. 39, 6531-6533 (2012)]**. *Med Phys*, **40**(1):017102.

173. Kirby N, Chuang C, Ueda U, Pouliot J: **The need for application-based adaptation of deformable image registration**. *Med Phys* 2013, **40**(1):011702.

174. Nie K, Chuang C, Kirby N, Braunstein S, Pouliot J: **Site-specific deformable imaging registration algorithm selection using patient-based simulated deformations**. *Med Phys* 2013, **40**(4):041911.

175. Niu CJ, Foltz WD, Velec M, Moseley JL, Al-Mayah A, Brock KK: **A novel technique to enable experimental validation of deformable dose accumulation**. *Med Phys* 2012, **39**(2):765-776.

176. Vinogradskiy YY, Balter P, Followill DS, Alvarez PE, White RA, Starkschall G: **Comparing the accuracy of four-dimensional photon dose calculations with three-dimensional calculations using moving and deforming phantoms**. *Med Phys* 2009, **36**(11):5000-5006.

177. Huang TC, Liang JA, Dilling T, Wu TH, Zhang G: **Four-dimensional dosimetry validation and study in lung radiotherapy using deformable image registration and Monte Carlo techniques**. *Radiat Oncol* 2010, **5**:45.

178. Zhang GG, Huang TC, Forster KM, Lin KP, Stevens C, Harris E, Guerrero T: **Dose mapping: validation in 4D dosimetry with measurements and application in radiotherapy follow-up evaluation**. *Comput Methods Programs Biomed* 2008, **90**(1):25-37.

179. Janssens G, de Xivry JO, Fekkes S, Dekker A, Macq B, Lambin P, van Elmpt W: **Evaluation of nonrigid registration models for interfraction dose accumulation in radiotherapy**. *Med Phys* 2009, **36**(9):4268-4276.

180. Juang T, Das S, Adamovics J, Benning R, Oldham M: **On the need for comprehensive validation of deformable image registration, investigated with a novel 3-dimensional deformable dosimeter**. *Int J Radiat Oncol Biol Phys* 2013, **87**(2):414-421.

181. Galvin JM, De Neve W: **Intensity modulating and other radiation therapy devices for dose painting**. *J Clin Oncol* 2007, **25**(8):924-930.

182. Chang JH, Lim Joon D, Lee ST, Gong SJ, Anderson NJ, Scott AM, Davis ID, Clouston D, Bolton D, Hamilton CS *et al*: **Intensity modulated radiation therapy dose painting for localized prostate cancer using (1)(1)C-choline positron emission tomography scans**. *Int J Radiat Oncol Biol Phys*, **83**(5):e691-696.

183. Dirscherl T, Rickhey M, Bogner L: **Feasibility of TCP-based dose painting by numbers applied to a prostate case with (18)F-choline PET imaging**. *Z Med Phys*, **22**(1):48-57.

184. Jouyaux F, De Crevoisier R, Manens JP, Bellec J, Cazoulat G, Haigron P, Chira C, Le Prise E, Lafond C: **[High dose for prostate irradiation with image guided radiotherapy: contribution of intensity modulation arctherapy]**. *Cancer Radiother*, **14**(8):679-689.

185. Niyazi M, Bartenstein P, Belka C, Ganswindt U: **Choline PET based dose-painting in prostate cancer--modelling of dose effects**. *Radiat Oncol*, **5**:23.

186. Supiot S, Lisbona A, Paris F, Azria D, Fenoglietto P: **["Dose-painting": myth or reality?]**. *Cancer Radiother*, **14**(6-7):554-562.

187. Chang JH, Wada M, Anderson NJ, Lim Joon D, Lee ST, Gong SJ, Gunawardana DH, Sachinidis J, O'Keefe G, Gan HK *et al*: **Hypoxia-targeted radiotherapy dose painting for head and neck cancer using (18)F-FMISO PET: A biological modeling study**. *Acta Oncol* 2013.

188. Berwouts D, Olteanu LA, Duprez F, Vercauteren T, De Gersem W, De Neve W, Van de Wiele C, Madani I: **Three-phase adaptive dose-painting-by-numbers**

for head-and-neck cancer: initial results of the phase I clinical trial. *Radiother Oncol* 2013, **107**(3):310-316.

189. Olteanu LA, Madani I, De Neve W, Vercauteren T, De Gersem W: **Evaluation of deformable image coregistration in adaptive dose painting by numbers for head-and-neck cancer**. *Int J Radiat Oncol Biol Phys*, **83**(2):696-703.

190. Madani I, Duprez F, Boterberg T, Van de Wiele C, Bonte K, Deron P, De Gersem W, Coghe M, De Neve W: **Maximum tolerated dose in a phase I trial on adaptive dose painting by numbers for head and neck cancer**. *Radiother Oncol*, **101**(3):351-355.

191. Yang JC, Wexler LH, Meyers PA, Happersett L, La Quaglia MP, Wolden SL: **Intensity-modulated radiation therapy with dose-painting for pediatric sarcomas with pulmonary metastases**. *Pediatr Blood Cancer* 2013, **60**(10):1616-1620.

192. Tunceroglu A, Park JH, Balasubramanian S, Poppe M, Anker CJ, Poplin E, Moss RA, Yue NJ, Carpizo D, Gannon CJ *et al*: **Dose-painted intensity modulated radiation therapy improves local control for locally advanced pancreas cancer**. *ISRN Oncol*, **2012**:572342.

193. Bentzen SM, Gregoire V: **Molecular imaging-based dose painting: a novel paradigm for radiation therapy prescription**. *Semin Radiat Oncol* 2011, **21**(2):101-110.

194. Lukacz ES, Sampselle C, Gray M, Macdiarmid S, Rosenberg M, Ellsworth P, Palmer MH: **A healthy bladder: a consensus statement**. *Int J Clin Pract* 2011, **65**(10):1026-1036.

195. Moyer RF, McElroy WR, O'Brien JE, Chamberlain CC: **A surface bolus material for high-energy photon and electron therapy**. *Radiology* 1983, **146**(2):531-532.

196. Pinter C, Lasso A, Wang A, Jaffray D, Fichtinger G: **SlicerRT: radiation therapy research toolkit for 3D Slicer**. *Med Phys* 2012, **39**(10):6332-6338.

197. Varadhan R, Miller J, Garrity B, Weber M: **In vivo prostate IMRT dosimetry with MOSFET detectors using brass buildup caps**. *J Appl Clin Med Phys* 2006, **7**(4):22-32.

198. **American Society for Testing and Materials (ASTM) D412-98a Rubber Properties in Tension Report, Smithers Scientific Services Inc, Akron, OH**. In.; 2000.

199. Ejofodomi OA, Zderic V, Zara JM: **Tissue-mimicking bladder wall phantoms for evaluating acoustic radiation force-optical coherence elastography systems**. *Med Phys* 2010, **37**(4):1440-1448.

200. van Mastrigt R, Coolsaet BL, van Duyl WA: **Passive properties of the urinary bladder in the collection phase**. *Med Biol Eng Comput* 1978, **16**(5):471-482.

201. F.A.Duck: **Physical Properties of Tissue: A Comprehensive Reference Book**: Academic, New York; 1990.

202. Dahms SE, Piechota HJ, Dahiya R, Lue TF, Tanagho EA: **Composition and biomechanical properties of the bladder acellular matrix graft: comparative analysis in rat, pig and human**. *Br J Urol* 1998, **82**(3):411-419.

203. [http://www.omega.com/Pressure/pdf/LCKD.pdf]

204. Persoon LC, Podesta M, van Elmpt WJ, Nijsten SM, Verhaegen F: **A fast three-dimensional gamma evaluation using a GPU utilizing texture memory for on-the-fly interpolations**. *Med Phys*, **38**(7):4032-4035.

205. Wendling M, Zijp LJ, McDermott LN, Smit EJ, Sonke JJ, Mijnheer BJ, van Herk M: **A fast algorithm for gamma evaluation in 3D**. *Med Phys* 2007, **34**(5):1647-1654.

206. Low DA, Harms WB, Mutic S, Purdy JA: **A technique for the quantitative evaluation of dose distributions**. *Med Phys* 1998, **25**(5):656-661.

207. Ezzell GA, Burmeister JW, Dogan N, LoSasso TJ, Mechalakos JG, Mihailidis D, Molineu A, Palta JR, Ramsey CR, Salter BJ *et al*: **IMRT commissioning: multiple institution planning and dosimetry comparisons, a report from AAPM Task Group 119**. *Med Phys* 2009, **36**(11):5359-5373.

208. Rubod C, Brieu M, Cosson M, Rivaux G, Clay JC, de Landsheere L, Gabriel B: **Biomechanical properties of human pelvic organs**. *Urology* 2012, **79**(4):968 e917-922.

209. Sparks JL, Dupaix RB: **Constitutive modeling of rate-dependent stress-strain behavior of human liver in blunt impact loading**. *Ann Biomed Eng* 2008, **36**(11):1883-1892.

210. Pukala J, Meeks SL, Staton RJ, Bova FJ, Mañon RR, Langen KM: **A virtual phantom library for the quantification of deformable image registration uncertainties in patients with cancers of the head and neck**. *Medical Physics* 2013, **40**(11):-.

211. Hui SK, Kapatoes J, Fowler J, Henderson D, Olivera G, Manon RR, Gerbi B, Mackie TR, Welsh JS: **Feasibility study of helical tomotherapy for total body or total marrow irradiation**. *Med Phys* 2005, **32**(10):3214-3224.

212. Mutter RW, Liu F, Abreu A, Yorke E, Jackson A, Rosenzweig KE, Stephans KL, Djemil T, Tendulkar RD, Robinson CG *et al*: **Dose-volume parameters predict for the development of chest wall pain after stereotactic body radiation for lung cancer Prediction of chest wall toxicity from lung stereotactic body radiotherapy (SBRT)**. *Int J Radiat Oncol Biol Phys* 2012, **82**(5):1783-1790. doi: 1710.1016/j.ijrobp.2011.1703.1053. Epub 2011 Aug 1723.

213. Stephans KL, Djemil T, Tendulkar RD, Robinson CG, Reddy CA, Videtic GM: **Prediction of chest wall toxicity from lung stereotactic body radiotherapy (SBRT)**. *Int J Radiat Oncol Biol Phys* 2012, **82**(2):974-980. doi: 910.1016/j.ijrobp.2010.1012.1002. Epub 2011 Feb 1016.

214. Andolino DL, Forquer JA, Henderson MA, Barriger RB, Shapiro RH, Brabham JG, Johnstone PA, Cardenes HR, Fakiris AJ: **Chest wall toxicity after stereotactic body radiotherapy for malignant lesions of the lung and liver**. *Int J Radiat Oncol Biol Phys* 2011, **80**(3):692-697. doi: 610.1016/j.ijrobp.2010.1003.1020. Epub 2011 Feb 1011.

215. Chao M, Penagaricano J, Yan Y, Moros EG, Corry P, Ratanatharathorn V: **Voxel-based dose reconstruction for total body irradiation with helical tomotherapy**. *Int J Radiat Oncol Biol Phys* 2012, **82**(5):1575-1583. doi: 1510.1016/j.ijrobp.2011.1501.1021. Epub 2011 Apr 1574.

216. Court LE, Dong L, Lee AK, Cheung R, Bonnen MD, O'Daniel J, Wang H, Mohan R, Kuban D: **An automatic CT-guided adaptive radiation therapy technique**

by online modification of multileaf collimator leaf positions for prostate cancer. *Int J Radiat Oncol Biol Phys* 2005, **62**(1):154-163.

217.	Court LE, Tishler RB, Petit J, Cormack R, Chin L: **Automatic online adaptive radiation therapy techniques for targets with significant shape change: a feasibility study**. *Phys Med Biol* 2006, **51**(10):2493-2501. Epub 2006 Apr 2426.

218.	Samant SS, Xia J, Muyan-Ozcelik P, Owens JD: **High performance computing for deformable image registration: towards a new paradigm in adaptive radiotherapy**. *Med Phys* 2008, **35**(8):3546-3553.

219.	Men C, Jia X, Jiang SB: **GPU-based ultra-fast direct aperture optimization for online adaptive radiation therapy**. *Phys Med Biol* 2010, **55**(15):4309-4319. doi: 4310.1088/0031-9155/4355/4315/4008. Epub 2010 Jul 4320.

220.	Men C, Gu X, Choi D, Majumdar A, Zheng Z, Mueller K, Jiang SB: **GPU-based ultrafast IMRT plan optimization**. *Phys Med Biol* 2009, **54**(21):6565-6573. doi: 6510.1088/0031-9155/6554/6521/6008. Epub 2009 Oct 6514.

221.	Pratx G, Xing L: **GPU computing in medical physics: a review**. *Med Phys* 2011, **38**(5):2685-2697.

222.	Gu X, Pan H, Liang Y, Castillo R, Yang D, Choi D, Castillo E, Majumdar A, Guerrero T, Jiang SB: **Implementation and evaluation of various demons deformable image registration algorithms on a GPU**. *Phys Med Biol* 2010, **55**(1):207-219. doi: 210.1088/0031-9155/1055/1081/1012. Epub .

223.	Jacques R, Wong J, Taylor R, McNutt T: **Real-time dose computation: GPU-accelerated source modeling and superposition/convolution**. *Med Phys* 2011, **38**(1):294-305.

APPENDIX-Documentation of custom modules developed in this project and implemented in 3DSlicer

<u>**Slicer modules for dosimetric verfication**</u>

A. Preliminaries

We used 3D Slicer (www.slicer.org) as our visualization platform. Several organizations are involved   in the development of Slicer. Slicer is open source and supports loadable modules, both of which favor us in this regard.

A.1 Installing Slicer

We use a custom, modified version of Slicer, to support RT Dose files.(although since developing these modules, Slicer RT was developed in open source format and can import RT dose files) Uninstall any existing versions of slicer you may have on your computer. Then get this custom version from author, Raj Varadhan. Please send email to rvaradhan@mropa.com for more details. Please use windows 7, 64-bit O/S with minimum of 8GB RAM.

Install, following the usual options. If you are using Windows Vista, it may be preferable to not install it in "Program Files", since log files are written out by modules in the installed folder, where write access may be denied to non-administrative users.

A.2 Installing Custom Modules

We package functionality in the form of Slicer modules. These may be invoked both from within Slicer, or from the   command line. Typically command line invocation is verbose, giving you lots of log messages as you go along, while the   GUI invocation is silent. Functionally, they remain the same.

Get the modules from author Raj Varadhan

Unzip. Place the command line (.exe) and plugin (.dll) files in

<YourSlicerInstallPath>/lib/Slicer3/Plugins/ . This is typically

c:\Program Files\Slicer3\ 3.5.2009-12-05\lib\Slicer3\Plugins

B. Loading data

Extensive documentation on Slicer can be found at www.slicer.org. A minimal description

on getting started with loading the KVCT is below.

B.1 Loading the KVCT data

While Slicer can load DICOM data, our DICOM library is still somewhat primitive. It

requires that each series is isolated to a single folder. Lets create a folder kvctdata/ .

Please all the CT data that correspond to this series in the folder. Be sure to leave out any

scout files or the Dose and RT Plan files out

Our example data folder contains 102 files ...

HeadNeckCase/kvctdata/CT.1.3.12.2.1107.5.1.4.51607.30000009092113454260900000346.dcm

...

HeadNeckCase/kvctdata/CT.1.3.12.2.1107.5.1.4.51607.30000009092113454260900000447.dcm


Select File ->Add Volume and navigate to HeadNeckCase/kvctdata/ . Select "Parse

Directory". Select the series "Rad therapy planning" that shows up with 102 files. Enter a

meaningful name to remember it by. Let's type in "kvct" on the "Name" field and hit

apply.

B.2 Basic functionality

Window / level functionality may be accessed from the "Volumes" module. Volume

Rendering may be accessed from the "Volume Rendering" module. Fiducials from the

"Fiducials" module. Measurements / rulers etc from the "Measurements" module.
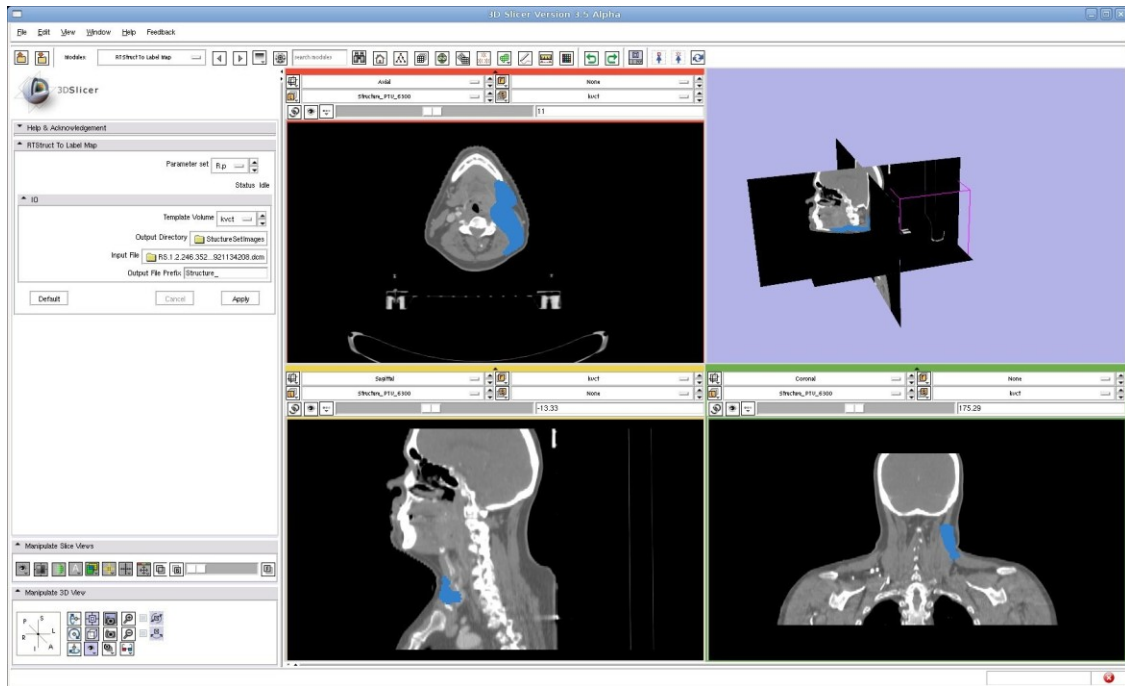
Each image tab allows one to specify the Orientation (Axial/cornal/sagittal), the label

image of any, the foreground image if any and the background image. This allows one to

overlay label maps (in this case the PTV) or overlay a registered image. One can toggle /

fade between the background and foreground
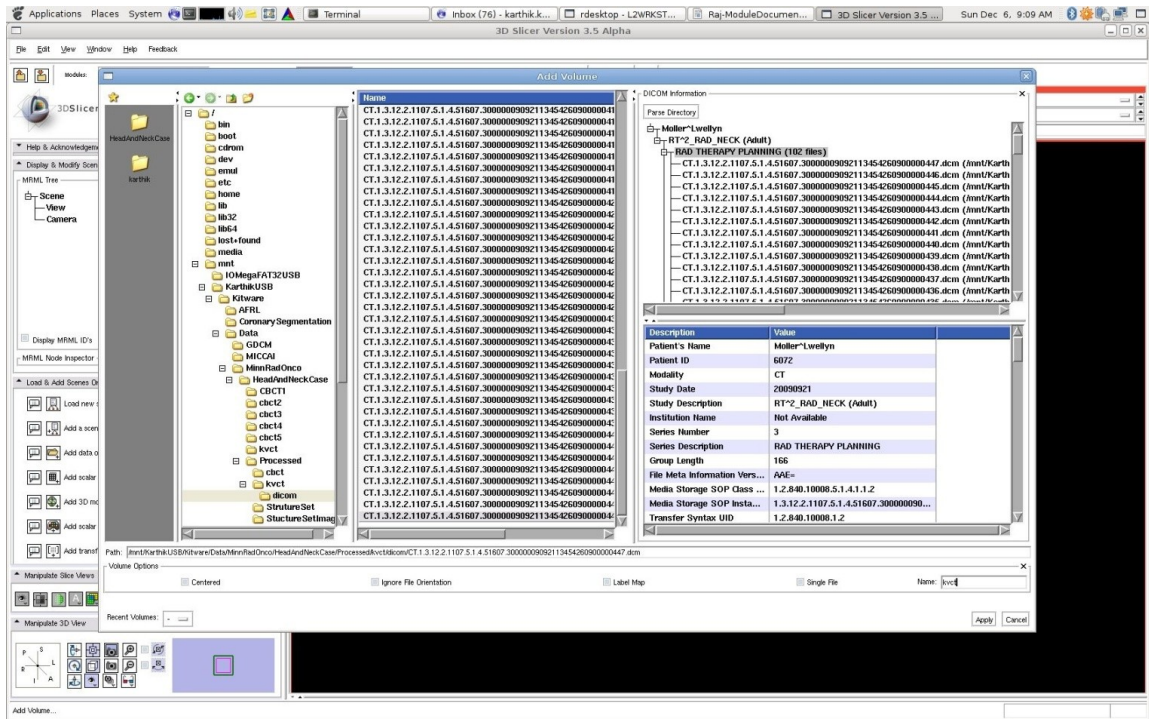
Each image tab allows one to specify the Orientation (Axial/cornal/sagittal), the label

image of any, the foreground image if any and the background image. This allows one to

overlay label maps (in this case the PTV) or overlay a registered image. One can toggle /

fade between the background and foreground

C. Converting RT contours to binarized label map images

Let's convert the DICOM RT contours to a label map image. Let's create a directory to

hold these label map files :

HeadNeckCase/StructureSetImages/

Select Modules from the toolbar above. Navigate to the group "Raj" and select the

module→ "RTStruct to label map"   On the module tab, Select the following parameters:

-       Template Volume : kvct

-       OutputDirectory ...../HeadNeckCase/StructureSetImages/

-       InputFile is the RT structure set file : RS.......dcm

Hit Apply. The module should take about 20 minutes to run. You should find 40

Structure_<NAME>.mha images in your   OutputDirectory.

The same module can be invoked from the command line as well and this reports

progress....

D. *Loading / Overlaying the RTContour label maps.*

Select File → Add Volume. Navigate to the OutputDirectory. Let's load one of the structures, the PTV : (Structure_PTV_6300.mha). Check "Label Map" ON. Perhaps, key in a meaningful name. Hit Apply.

You should see the label map overlaid on the KVCT data as shown above

E. **Registration**

E.1 Loading the CBCT data

Let's now load the CBCT image as well in Slicer. Follow the same process as the KVCT. ie. Isolate the CBCT files in a directory. Select File → AddVolume. Navigate to the folder. Hit "Parse Directory". Select the appropriate series , in this case, "Unknown Series (58 files)".

E.2 Dilation of the PTV mask

We will attempt to restrict our registration to the PTV and its vicinity. This may not be necessary always. Let's Select the module "Raj → ImageManipulation → BinaryDilateFilter".

- Select the label overlay : "Structure_PTV_6300" as the Input Volume.

- On Output Volume, select "Create New Volume". You may wish to name it as "Structure_PTV_6300_dilated".

- Select a "Kernel Radius of "6".

- Hit Apply

The resulting displayed volume is the resampled volume.

E.3 Registration of the CBCT to the KVCT

We first look at the match between the unregistered CBCT and the KVCT. To do this, select KVCT as the "background image", and the CBCT as the foreground image. This aligns the images using their origin (derived from the DICOM image position patient tag). Toggle/fade the background and foreground. As can be seen, the two images are quite misaligned
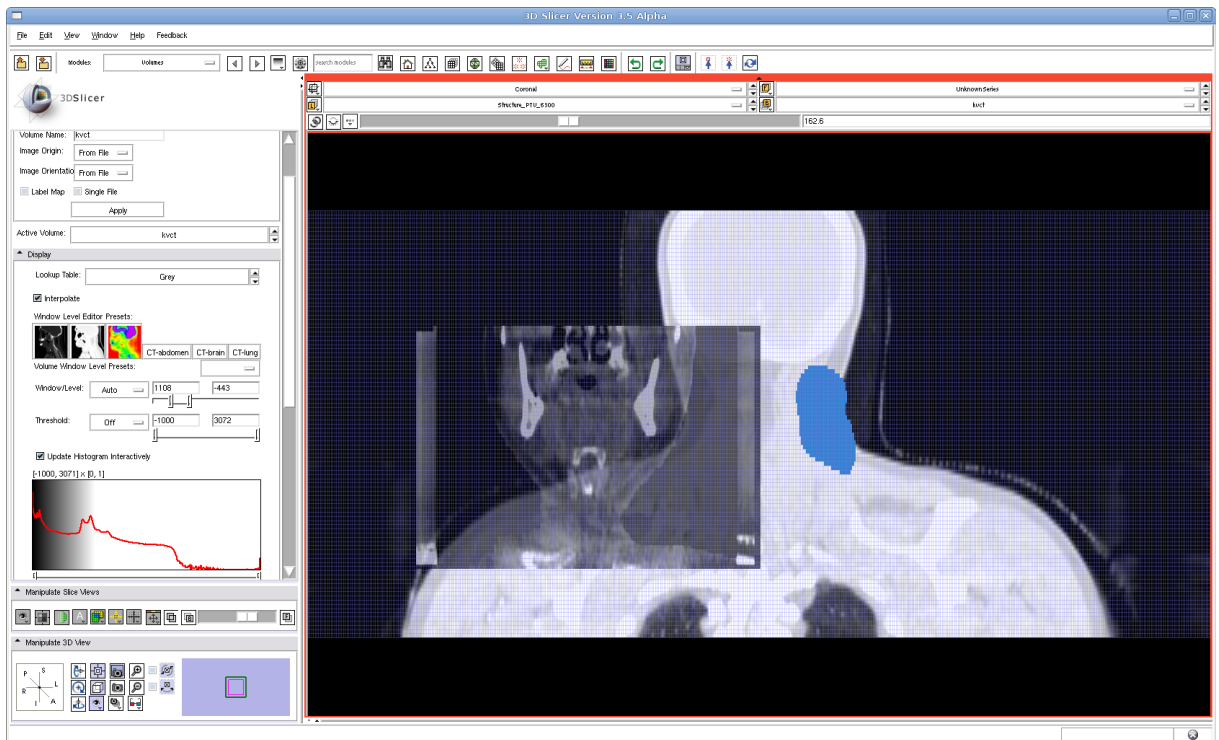
Unregistered images (KVCT background and CBCT foreground)

We will first do a rigid registration of the CBCT to the KVCT. Traverse to the Modules →

Raj → Registration → RegisterImages. Use the following parameters :

IO

FixedImage: KVCT MovingImage: CBCT

Resample Image: Create New Volume (Give a meaningful name, say CBCT-

RigidRegToKVCT)

Registration Parameters Load Transform : None

Save Transform: Create New Transform (Give a meaningful name, say CBCT-

RigidRegToKVCT-Tfm) Initialization: Image Centers

Registration: Pipeline Rigid Metric: Mattes MI

Advanced Registration Parameters: Verbosity level: Verbose

Fixed Image Mask: None Interpolation: Linear

Advanced Rigid Registration Parameters: Rigid Max Iterations : ~200

Rigid Sampling Ratio : ~0.02

(The larger these parameters are, the more time it takes and the more accurate registration

typically is). Hit Apply....

After about 2-3 minutes, you should have a rigid registration.

This initializes the image based on their centers and then performs a rigid registration. The

resulting symmetric rigid registration transform matrix (composed of a rotation and a

translation) can be viewed on the "Transforms" tab. You may   overlay the two images to see the results of the rigid registration.

One can also use the "Checkerboard filter", from Modules → Filtering → Checkerboard filter to view a NxMxR   checkerboard of the two images.
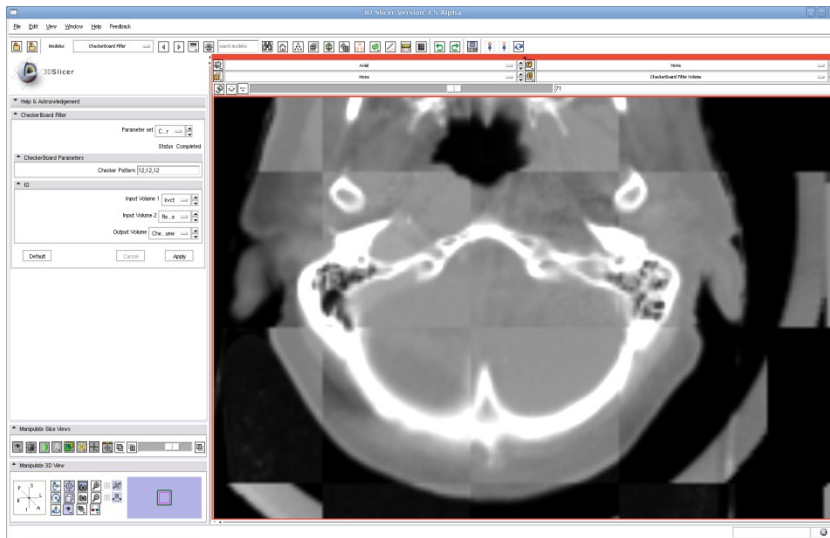
The resulting metric and transform values at each iteration of registration can be seen from the output log, retrieved by   hitting the "X" button at the bottom right and looking at the results on the "Register Images Standard Output".

E.3.2 ***Deformable registration using B-spline algorithm.***

Note: Since the development of these modules Slicer RT supports B-spline registration

in their latest version Slicer 4.3

Deformable registration is typically performed as the second pass once you are satisfied

with the results of the rigid   registration. We will use the same "Register Images" Module.

We will also restrict the deformable registration to the   dilated PTV region. Use the

following parameters

IO

FixedImage: KVCT MovingImage: CBCT

Resample Image: Create New Volume (Give a meaningful name if you like, say CBCT-

DeformableRegToKVCT)

Registration Parameters

Load Transform : CBCT-RigidRegToKVCT-Tfm

Save Transform: Create New Transform (Give a meaningful name if you like, say CBCT-

DeformableRegToKVCT-Tfm)   Initialization: None (We initialize based on the transform

resulting from rigid registration)

Registration: Pipeline BSpline Metric: Mattes MI

Advanced Registration Parameters: Verbosity level: Verbose

Fixed Image Mask: Structure_PTV_6300_dilated Interpolation: Linear

Advanced Rigid Registration Parameters:

Rigid Max Iterations : ~50 (we've already performed a global rigid registration. This does

a rigid registration with samples   drawn from the mask, which really is not necessary)

Rigid Sampling Ratio : ~0.02 <u>Advanced Bspline Registration Parameters:</u> Bspline Max Iterations : 40

Bspline Num Levels: 1 Bspline Sampling Ratio : 0.02 Control point spacing: 60

The deformable registration will typically take 15~ 30 min, depending on the parameters on the Bspline tab. The smaller the control point spacing, the larger the sampling ratio and the larger the number of iterations, the more the time taken.

The log of the B-spline registration along with the computed transform is written out to a file bspline-registrationlog.txt. This contains the transform and the current metric value and could be used as some indicator of progress.

One should be able to view the registered results in the same manner as above.

Future work:

We should confine the B-spline grid to the mask. At the moment the grid is defined and computed over the entire image, although the samples used for computation of the metric is restricted to the mask. This is wasteful. We expect to achieve a 4x speedup by restricting the B-spline grid in addition to the metric, to the masked region.

### E.3.3 Running RegisterImages from the command line

One can run RegisterImages from the command line. An example is shown for the
uploaded lung cancer case : (In addition you specify the directory path in the below
command line on where the input and output files reside)

RegisterImages --resampledImage AfterDeformationRegisteredToBeforeDeformation.mha

--registration PipelineBSpline --initialization ImageCenters --verbosityLevel Verbose

--metric MattesMI --minimizeMemory --interpolation Linear --rigidSamplingRatio 0.02

--rigidMaxIterations 200 --affineSamplingRatio 0.02 --affineMaxIterations 100

--controlPointSpacing 64 --bsplineSamplingRatio 0.05 --bsplineMaxIterations 40

--bsplineNumberOfLevels 1 BeforeDeformation.mha AfterDeformation.mha

The parameters --controlPointSpacing , --bsplineSamplingRatio ,
--bsplineMaxIterations have a direct impact on the run-time. The larger the
controlPointSpacing, sampingRatio and the smaller the number of iterations, the faster the
execution.

At the end of the registration, you should have a DeformationField.mhd and a
DeformationField.raw file in your directory. You may   load these in Paraview to
visualize the deformation.

The figure below shows the overlay of the two images in VolView using the "Merge
Volumes" plugin
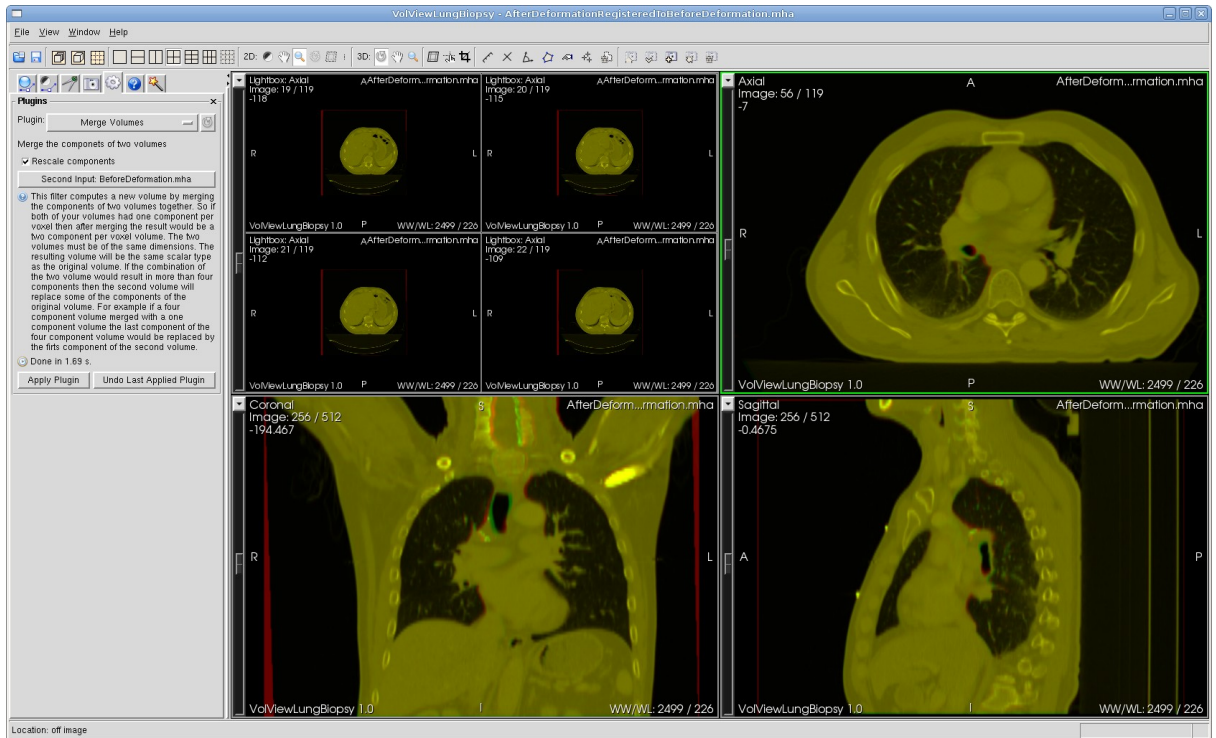
F. *Visualizing the deformation field in Paraview*

(a) Load the dataset using File->Open. Paraview cannot load DICOM data. One must convert it to a MetaImage or VTI.

(b) Filters -> Glyph should show you the deformation field. By default a reasonable masking of the points is done so as to avoid cluttering the display. You may want to see the effect of disabling "Mask Random Points" and setting the "Maximum   number of points" to manually control the number of displayed glyps

(c) One can also load the Input data and overlay the field on the data. File → Open followed by Filters → Slice. One can change the color mapping of the displayed slice by clicking on the slice nodes' "Display" tab → "Edit Color Map" → "Choose Preset" → Grayscale.
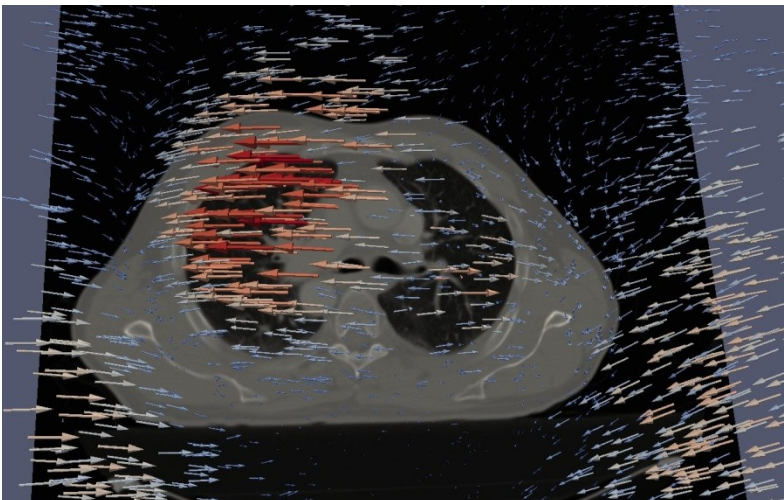
G. Warping the dose file using the registration results

The plugin takes a 3D image and warps it using a deformation (vector) field image. The loaded image is expected to be the image to be warped (also known as the moving image). The module has one parameter namely: the deformation field. The field is expected to have the same size, origin, spacing as the warped volume.

If you supply the moving image as the input to the Warp plugin, and set the deformation field as that resulting from the registration (in Section E.3.3), you should get the same output as the registered volume. This plugin may be run from Slicer or invoked from the command line :

WarpImageUsingDeformationField --field DeformationField.mhd

AfterDeformation.mha AfterDeformationWarpedUsingDeformationField.mha

The file AfterDeformationWarpedUsingDeformationField.mha should be identical to AfterDeformationRegisteredToBeforeDeformation.mha

Similarly one may warp the dose file

H. *Warped dose accumulation*

The plugin takes two dose images and simply adds them to produce a new result. This can be done with each successive warped dose image to get the cumulated dose. (One would read in the dose images are read via the ImportRTDose plugin and warp them with the plugin in Section G.). The plugin may also be invoked from the command line, for instance as :

CumulateDose   DoseKvct.mha WarpedDoseCBCT1.mha DoseKvctAndCBCT1.mha

CumulateDose   DoseKvctAndCBCT1.mha WarpedDoseCBCT2.mha

DoseKvctAndCBCT1AndCBCT2.mha

I. *Compare deformation field to reference field*

For dense deformation fields, this is equivalent to computing the MSE between the registered and the source image. The   plugin MSE found in Raj $\rightarrow$ ImageManipulation computes this. The plugin expects as input the fixed image and the moving image. Slicer does not yet support reporting of results on the UI. Hence the output is written to a file. The output directory where the MSE between the source and target are stored is expected as input on the UI. The file MSEInfo.txt should contain the Sum of Squared Differences, the MSE and Root MSE.

The displayed image should show the absolute difference between the two images (| Image1 $-$ Image2|). As usual the plugin may be invoked from the command line :

MSE --outputdirectory c:/tmp c:/Data/BeforeDeformation.mha

c:/Data/AfterDeformationRegisteredToBeforeDeformation.mha

c:/Data/Output/DifferenceImage.mha

J. Converting ImSimQA field to a metaimage

The ImSimQA field cannot be loaded directly into paraview. To make it readable by

paraview, use the "ReadImSimQAFieldWriteMetaImageField" plugin. This takes as

input the ImSimQA dfm file and writes as output the field as a metaimage.

The plugin may also be invoked from the command line as follows :

ReadImSimQAFieldWriteMetaImageField --inputfile

c:/Data/TPSDeformationField_20100316.762690.dfm --outputfile c:/tmp/field.mha

### K. Importing an RT Dose file

To import an RTDose file into Slicer, use the ImportRTDose plugin.

The dose values are read from the DICOM file and multiplied by the DoseGridScaling

(0x3004|000E) attribute. The resulting image will have dose values with units specified

in DoseUnits attributes via DICOM tag (3004|0002). This is typically Gy. The plugin may

also be invoked from the command line as follows :

ImportRTDose –InputFileName

RD.1.2.246.352.71.7.1455740796.52337.20090923160357.dcm Dose.mha
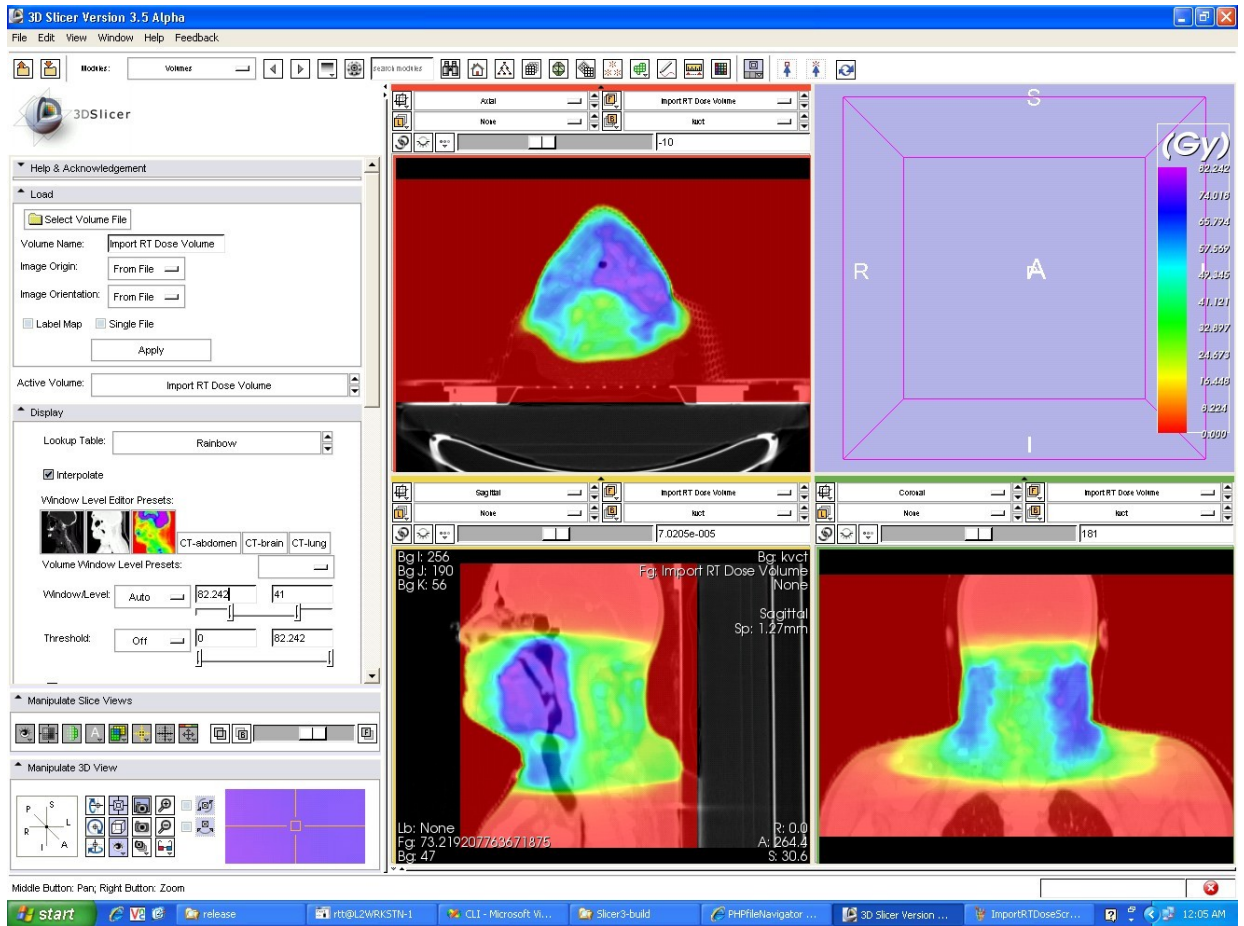
One can also contour the converted dose file in Paraview (see option to generate a series

of values the range) and overlay it on the registered CBCT image along with the

deformation field as shown below.
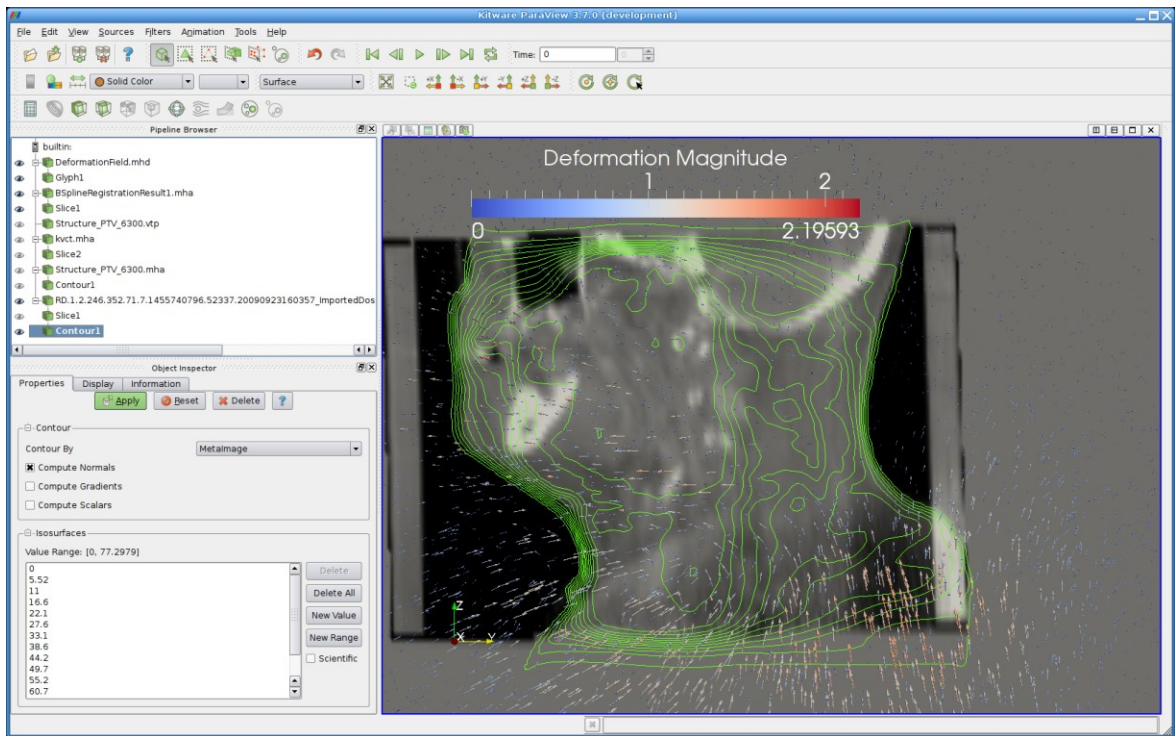
L. *Compute the determinant of the jacobian*

- The jacobian of the transform or of a vector field is an MxN matrix, where M is the dimensionality of the transform and N is the dimensionality of the image. In our case, its a 3x3 matrix.

- The sign of the determinant should tell you if the field is well behaved. If the negative, it indicates singularities in the field.   Typically, if you looked at the deformation grid , one could see the misbehavior,   usually the grid looping back on itself (thick of a figure 8).

- The jacobian matrix itself tells you the local scale change or shearing or rotation involved in the deformation, if you   factorized the matrix.

- A determinant greater than 1 means its diverging. A determinant less than 1 means convergence. We have a Tumor change   tracker module that essentially measures

212

volumetric change between scans at two time points by adding the jacobian   determinants (of the deformation field) on all voxels in the tumor segmented mask region.

- The min and max of determinant is an indicator of how smooth the spatial transformation is. The harmonic energy   captures this metric well. It the Frobenius norm of the jacobian, and hence is inversely related to how smooth the   deformation field is. The plugin expects the deformation field as the input and generates a floating point image representing the determinant of   the jacobian. You may also run it from the command line as follows :

ComputeDeterminantOfJacobian   DeformationField.mhd

Jacobian_DeformationField.mha

The figure below shows a slice of the jacobian field and the corresponding in-plane components of the deformation field in   paraview. Note that the deformation field is well behaved; has a scalar range of [0.95, 1.04]. You will notice the larger   vectors (red) diverging out of the bright regions in the image (regions with $|J(T(x)|>1$) and converging into darker regions   (regions with $|J(T(x)|<1$) as shown below.
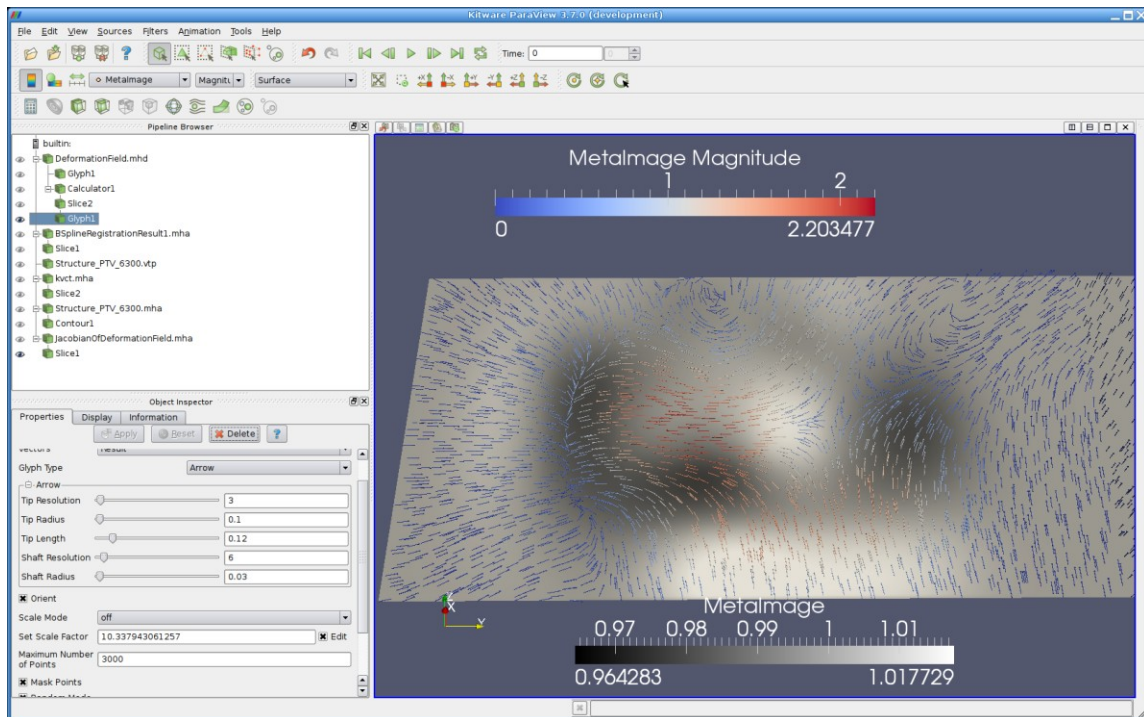
M. *Compute the harmonic energy in the field*

The min and max of determinant of the jacobian is an indicator of how smooth the spatial

transformation is. The harmonic   energy captures this metric well. It the Frobenius norm

of the jacobian, and hence is inversely related to how smooth the   deformation field is.

The neighborhood size used in computing the harmonic energy is 1.

The plugin expects the deformation field as the input and generates a text file containg the

result. You may also run it from   the command line as follows :

ComputeHarmonicEnergy   DeformationField.mhd

HarmonicEnergy_DeformationField.txt   Harmonic energy of deformation field :

DeformationField.mhd is 8.30813e-05

<u>APPENDIX</u>

<u>Troubleshooting:</u>

(a) I am trying to run the plugin from the command line, but I get "Error while loading shared libraries: ....dll"

You need to add the SlicerInstallationDirectory\bin to your path, so as to enable your application to find additional ITK / Slicer libraries.

For instance:

PATH=%PATH%;c:\Program Files\Slicer3 a3.5.2009-12-05\bin